The Role of Helium on Cavity Growth and Swelling at High Damage Levels in Ferritic-Martensitic Steels

by

David Alexander Woodley

A dissertation submitted in partial fulfillment
of the requirements for the degree of
Doctor of Philosophy
(Nuclear Engineering and Radiological Sciences)
in the University of Michigan
2020

Doctoral Committee:

Professor Gary S. Was, Chair
Professor Fei Gao
Professor Amit Misra
Associate Research Scientist Kai Sun

David Woodley

dawoodle@umich.edu

ORCID iD: 0000-0002-5145-7970

Dedication

To my family and friends

Acknowledgements

First, I would like to thank my advisor, Dr. Gary Was, for providing his insights, suggestions and input throughout my years as a Ph.D. student. Without his help, I would not be the scientist that I am today. I would also like to thank the members of my committee, Dr. Fei Gao, Dr. Amit Misra and Dr. Kai Sun for their input which greatly improved this thesis.

I would also like to thank the members of the Was research group, past and present, including Dr. Tyler Moss, Dr. Kale Stephenson, Dr. Stephen Raiman, Dr. Elizabeth Getto, Dr. Anthony Monterrosa, Dr. Justin Hesterberg, Dr. Stephen Taller, Gerrit VanCoevering, Drew Johnson, Katey Thomas, Dr. Peng Wang, Dr. Miao Song, Dr. Mi Wang, Dr. Calvin Lear, Dr. Wenjun Kuang, Dr. Donghai Du, Dr. Kai Chen, Valentin Pauly, and Logan Clowers. Their mentorship, help in the lab, moral support and camaraderie have been one of the highlights of my graduate studies.

Thank you to the past and present staff members at the Michigan Ion Beam Laboratory, Dr. Ovidiu Toader, Dr. Fabian Naab, Dr. Ethan Uberseder, Thomas Kubley, Robert Hensley, and Dr. Prabir Roy. Without their experience, and hard work, these experiments would not have been possible. I also want to thank the staff at the Michigan Center for Materials Characterization for help with FIB liftouts, TEM, and STEM and care of the associated equipment. Thank you to the NEUP Graduate Fellowship Program for providing funding for some of this work along with the DOE NE IRP program DE-NE0000639.

Without the support of Dr. Micah Hackett, formerly at TerraPower, LLC., and Dr. Cheng Xu at TerraPower, LLC., this work never would have happened. Their insights, support and ideas helped shape the initial irradiations and provided the basis for the work that started this dissertation.

To my parents, Ed and Debbie Woodley, who formed the backbone of my support throughout the years. I am forever grateful for all of your encouragement, love and prayers, even when I did not call or visit as often as you would have liked. I would not have been able to complete this without your love and support. Thank you to the rest of my siblings, Edward, Brooke, Richard, Katherine and Leslie for always being loving and supportive.

Table of Contents

List of Tables

List of Figures

List of Appendices

Abstract

The desire for cleaner energy sources for baseload power generation drive an interest in new nuclear power plant designs. The development of radiation-tolerant materials for new nuclear power plants requires extensive research programs. Traditionally, radiation effects studies have been conducted using materials test reactors followed by expensive and time-consuming post-irradiation examination due to the neutron induced radioactivity. Additionally, the damage rate, temperature and helium generation rate within a reactor are all correlated with each other and dependent on the flux of neutrons and gamma rays in a reactor making the analysis for the underlying mechanisms of cavity growth and swelling difficult. Ion irradiation experiments allow for the separation of single variable dependencies to uncover the processes and understand the mechanisms underlying cavity growth and swelling with orders of magnitude higher damage rates compared to reactor irradiations and no induced radioactivity.

The objective of this thesis is to understand the process by which cavity growth and swelling changes with helium content across a wide range of damage levels. Alloys HT9, heat 84425, and T91, heat 30176, were irradiated with 5.0 MeV Fe^{2+} ions with 2.03-2.85 MeV He^{2+} ions at helium co-injection rates of 0 to 4 appm He/dpa at 460°C (HT9) and 445°C (T91) at damage levels from 17 to 650 dpa in the Michigan Ion Beam Laboratory.

The swelling and dislocation evolution for all irradiation conditions were characterized. Scanning transmission electron microscopy (STEM) was used to characterize the cavities greater

than 5 nm in diameter and dislocations. Transmission electron microscopy (TEM) was used to characterize the cavities less than 5 nm in diameter.

The peak in swelling was observed at the highest examined helium-to-dpa ratio at the lowest damage level. The location of the peak was demonstrated to be due to the enhanced nucleation of cavities at higher helium co-injection rates. As the damage level was increased, cavity growth started to dominate swelling, so the increased bubble density and resulting increase in sink strength caused a shift in the peak swelling toward lower helium-to-dpa ratios. The results of the shift were that at an intermediate damage level of 50 dpa, the maximum swelling was observed to occur at an intermediate helium co-injection rate of 0.2 appm He/dpa. At damage levels greater than 150 dpa, the peak swelling was observed to occur without the co-injection of helium.

Examining helium effects in existing literature, the mode of helium injection was demonstrated to not have an influence on the effect of helium. Specifically, at low damage levels, swelling is driven by the nucleation of cavities. As the damage level increases, higher helium levels correspond to higher cavity densities and higher sink strengths which retard swelling and shift the maximum swelling location to lower helium concentrations. At high damage levels, the peak in swelling as a function of helium concentration is observed to occur at 0 appm He.

This work provides substantial insight into the impact of helium on the evolution of cavities.

Chapter 1 Introduction

With increasing global demand for clean energy, Generation IV reactor designs have continued to be an attractive alternative to coal, natural gas, and current nuclear power plants. These reactor designs enable higher energy yield, produce less waste, allow the breakdown of existing radioactive waste, and improve safety. However, the extreme conditions of these reactors (both in temperature and radiation) require the use of highly resilient structural materials. The degradation of the structural materials is closely related to changes in their irradiated microstructure. Components in Generation IV fast reactors will experience damage levels in excess of 200 displacements per atom (dpa) and up to about 600 dpa in some designs [1]. Understanding how these high doses affect the microstructure in reactor conditions is critical to determining the correct material for use.

Ferritic-martensitic steels have been identified as a prime candidate for high dose application. Their high strength at elevated temperatures, swelling resistance, thermal stress resistance, and low activation makes them very desirable for high dose applications in reactor environments [2]. However, high dose neutron irradiated samples are few, due to the long irradiation times required. A typical dose rate for neutrons is on the order of 10^{-8}-10^{-6} dpa/s [3]. Therefore, both proton and heavy ion irradiations (10^{-5} and 10^{-3} dpa/s respectively) are being used to emulate neutron damage in a much faster and cost-effective way. The major damage effects under irradiation include radiation-induced segregation, radiation-induced precipitation, dislocation evolution, and void swelling.

One of the principle reasons ferritic-martensitic alloys are being pursued for high dose applications is their resistance to swelling. The complex microstructure of F-M steels provides strong sink strength for point defects generated during irradiation. If these point defects are annihilated at sinks rather than accumulate in the matrix, then it will become more difficult for voids to form. The driving force of void nucleation is the supersaturation of vacancies (C_v/C_v^0), where C_v is the concentration of vacancies in the matrix and C_v^0 is the thermal equilibrium concentration of vacancies [4]. Thermodynamic analysis indicates that there is a critical void embryo size required to nucleate a void. This occurs when the vacancy supersaturation overcomes the surface and volume energies required to create the cavity. After a cavity has nucleated, its growth is determined by the flux of point defects and helium toward and away from it. A flux of vacancies and helium into the cavity will cause it to grow, while a flux of interstitials will cause it to shrink.

The addition of gases, most importantly helium from transmutation, affects all aspects of bubble formation and growth. In terms of nucleation, the addition of helium to a bubble serves to reduce the free energy of formation. This makes nucleation easier increasing the density of bubbles. After a bubble has formed, the continued absorption of helium allows the bubble to continue to grow. Once the bubble grows large enough, it transitions to a void and is able to grow due to the vacancy supersaturation without the assistance of additional helium.

As mentioned previously, heavy ion irradiation is an attractive alternative to traditional in-reactor tests due to several factors. However, one limitation of the technique is the absence of transmutation gases, such as helium. Under neutron irradiation, some isotopes (particularly isotopes of boron and nickel) undergo (n, α) reactions in which a neutron is absorbed and an alpha particle is emitted. Two general methods have been used to account for the production of helium:

pre-injection and co-injection. Pre-injection is relatively simple to perform in that the helium is injected before the material is irradiated. Generally, this can be done at either room temperature (cold pre-injection) or at the irradiation temperature (hot pre-injection). To limit the potential variation associated with injection (specifically, the rate and time at temperature), only cold pre-injection will be discussed moving forward. The benefits of pre-injection are that they are relatively quick and easy to perform and can be done in most ion beam laboratories. However, because all of the helium is injected before the irradiation starts, the helium-to-dpa ratio is constantly changing and does not directly match what would be expected in reactor. This limitation is addressed by co-injection of helium. Under co-injection, helium is injected into the sample concurrently with the radiation damage. This allows the helium injection to more closely match the helium generation expected in reactor. However, because this process requires hitting a sample with two beams concurrently, it is much more difficult to perform. Because of this difficulty, fewer ion labs are able to perform co-injection experiments. Because of the significant differences in the injection methods and the limited capability to perform co-injection experiments, it is important to understand the differences in microstructure caused by helium injection mode.

Chapter 2 Background

Structural components in Generation IV fast reactors will be subjected to high fluences and temperatures. Although there is an expanding database of knowledge of material behavior under these conditions, the full extent of radiation effects is still not well understood. Significant material degradation has occurred under these conditions via radiation-induced segregation (RIS), nucleation and growth of dislocation loops, secondary phase formation and dimensional change through creep and cavity swelling.

Ferritic-martensitic (FM) alloys are leading candidates for future reactors because of their improved radiation resistance relative to stainless steels that have historically been used in light water reactors and previous fast reactor designs. While the dataset has been expanding recently using both test reactors and heavy ion irradiation, the effects of helium on swelling at high damage levels is not well understood in FM steels. This process is further complicated by the fact that helium generation and damage rate are closely linked in reactor and most of the work with self-ion irradiation has been performed with pre-injected helium rather than co-injected helium.

This chapter will explain the background necessary to understand the results of this work and place them in the context of existing literature. A general overview of FM steels will be provided followed by a comprehensive review of the existing experimental and theoretical framework of swelling and other irradiation-induced phenomena that may influence cavity swelling. Particular attention will be given to the effects of helium on both nucleation and growth of cavities.

2.1 Ferritic-Martensitic Steels

Ferritic-martensitic steels considered for use in reactors are high chromium steels with 7-12% chromium and complex microstructures with a body centered cubic (bcc) or, slightly, body centered tetragonal (bct) structure. To produce these steels, the metal is heated to an austenitizing temperature of 850 to 1200°C to produce either a fully austenitic or duplex structure with austenite and δ-ferrite phases. The material is then rapidly cooled by air cooling or quenching to transform the austenite to martensite. The metal is subsequently tempered to develop a good combination of strength, ductility and toughness. The metallurgy and development of high chromium FM steels have been reviewed extensively. The factors determining the properties of FM steels are briefly covered here.

2.1.1 Physical Metallurgy

The primary components of ferritic-martensitic (FM) steels are iron with smaller amounts of chromium and some carbon. The phase diagram relevant for FM alloy formation is shown in Figure 2.1. Typically, austenitizing occurs when the alloy is heated up to between 850 to 1200°C for 9 to 12 wt% Cr alloys. The austenitizing temperature can be shifted by the addition of austenite (γ-phase) stabilizers which typically lower the temperature required for complete austenitization or ferrite (δ-phase) stabilizers which typically increase the temperature required. While carbon and nitrogen greatly enhance austenite stability, inclusion of significant amounts can lead to the formation of carbo-nitrides. These carbo-nitrides can be dissolved by austenitizing at higher temperatures. However, it also results in coarser prior austenite grains (PAG). Austenitizing temperatures for HT9 are typically around 1050-1100°C. If enough ferrite stabilizers are included, some the metal could retain δ-ferrite after austenitizing. If enough austenite stabilizers are added, some of the metal could retain the austenite after quenching. The typical alloying elements and their effect on the stability of delta ferrite are shown in Table 2.1. Depending on the composition

and heat treatment, HT9 may contain all three phases, but an effort is made to minimize both retained austenite and ferrite. The martensite produced is very brittle and prone to fracture due to the high dislocation density.

Martensite forms in thick sections known as laths due to inhibition of pearlite transformation and absence of bainite. A continuous cooling transformation (CCT) diagram is shown in Figure 2.2. Laths tend to be low in carbon with dimensions of ~0.5-1 μm by 5 μm in length. As long as the cooling rate is fast enough, the austenite phase will transform into martensite, but when the start of the martensite transformation is close to room temperature, some of the austenite can be retained. The typical microstructure consists of PAGs with packets of parallel martensitic laths. Laths within a single packet occupy the same habit plane, have similar orientations and often have closely aligned crystallography.

The final step as mentioned previously, tempering, is required to improve toughness by refining the microstructure. Tempering causes both the annealing of dislocations in the martensitic phase, which increase toughness and ductility, and the formation of carbides, which improves toughness and reduces softening. The tempering is performed at a temperature below austenitization to prevent re-austenitizing the martensite. Typical temperatures are 760-850°C and 870-960°C for reduced activation steels [2]. The effects of tempering temperature are:

<350°C – A fine dispersion of M_3C (Fe_3C) precipitates forms and grows to a dendritic morphology

450-500°C – Fine needles of M_2X nucleate on the dislocations within the martensitic laths, retarding softening

500-550°C – M_7C_3 and M_2X phases coarsen with a rapid decrease in hardness

>550°C – M_7C_3 and M_2X are replaced by Cr-rich $M_{23}C_6$ precipitates on martensite lath and PAG boundaries

>650°C – $M_{23}C_6$ precipitates grow, reducing dislocation density and forming sub-grains

>750°C – Sub-cells grow into equiaxed sub-grains and $M_{23}C_6$ continues to grow

[2]

During tempering, the dislocation networks rearrange into a lower energy configuration with the laths forming small subgrains. Thermally activated dislocation climb and glide results in dislocation motion and rearrangement into grains with small misorientation angles. Even after tempering and the formation of subgrains, the martensitic phase has laths with high dislocation densities. Typical network dislocation densities are on the order of 10^{14}-10^{15} m^{-2} [2,5]. A schematic of the typical microstructure is presented in Figure 2.3 [2,6].

Tempering also results in the precipitation of carbon out of the matrix. As mentioned above, the precipitates at low temperature form fine dispersions which gradually transition to larger $M_{23}C_6$. $M_{23}C_6$ can be found on all boundaries but tend to grow coarser on PAGBs due to the increased diffusion rate along high angle boundaries [6,7].

2.2 Radiation Damage in Ferritic-Martensitic Steels

Radiation damage can occur in ferritic-martensitic steels from nearly any source of radiation, whether it is neutrons, ions, electrons, or gamma rays. All of these forms of radiation have the capability to displace atoms from their lattice sites. The effect of irradiation on materials is rooted in the initial event in which an energetic projectile strikes a target. While the event is made up of several steps or processes, the primary result is the displacement of an atom from its lattice site. The kinetics of the projectile strike on a target lattice atom are discussed in detail in a number of sources [4,8], and will not be reproduced here. Irradiation displaces an atom from its

site, leaving a vacant site behind (a vacancy) and the displaced atom eventually comes to rest in a location that is between lattice sites, becoming an interstitial atom. The vacancy-interstitial pair, known as a Frenkel pair, makes up the basis for radiation effects in crystalline solids. Irradiation events can produce many Frenkel pairs as damage from a single event cascade. The accumulation and diffusion of the resulting point defects form the foundation for the observed effects of irradiation on the physical and mechanical properties of materials.

The formation, growth and dissolution of defect aggregates such as cavities, dislocation loops, and other features, depend upon the diffusion of point defects and their reaction with the defect aggregates. They also depend upon the concentration of point defects in the solid. The concentration at any point and time is a balance between the production rate, and the loss rate of point defects and is adequately described by the point defect balance equations. The increase in diffusion or enhancement of atom mobility in an irradiated metal is due to two factors: the enhanced concentration of the defects from the damage cascade, and the creation of new defect species. The development of radiation-induced vacancy and interstitial concentrations occurs due to competing processes. Frenkel defects are created from the collisions between high-energy particles and lattice atoms. These defects can be lost either through recombination of vacancies and interstitials or by reaction with a defect sink, such as cavity, dislocation, dislocation loop, grain boundary or precipitate. The local change in defect concentration of the various defect species can be written as the net result of the local production rate, reaction with other species, and diffusion into or out of the local volume.

The point defect balance equations can be broken up into four cases [4]: (1) low temperature, low sink density, (2) low temperature, intermediate sink density, (3) low temperature, high sink density, and (4) high temperature. While all of these cases are relevant to the general

effects of concentrations of defects on solids, ferritic-martensitic steels, having a complex microstructure of grain boundaries, lath boundaries, precipitates, dislocations, and other features, fall into the third category for most reactor relevant conditions. The main effect of a high sink density is that interstitials find the sinks before they find vacancies. The time relationship with the concentration of defects can be broken into four regions. In the first region, both interstitials and vacancies buildup without reactions. In the second region, the concentration of vacancies continues to increase while the interstitials reach a semi-steady state as they arrive at sinks. The concentration of interstitials decreases when the concentration of vacancies is high enough to lead to mutual recombination in the third region. Eventually, both the interstitial and vacancy concentrations will reach steady states and begin to form extended defects. These extended defects are responsible for many of the macroscopic changes observed from irradiation.

The first of these extended defects is the dislocation. The interactions of dislocations, a line of either interstitials or vacancies that forms a boundary between a region of the crystal that has slipped and one that has not, with intrinsic point defects are of importance in understanding the processes of plasticity, hardening, and irradiation creep. Plasticity is enabled through the presence of dislocations, which lower the stress needed to deform a material. Additionally, dislocations act as sinks for point defects, affecting dislocation growth and the subsequent swelling of irradiated materials. Although this section is dedicated to dislocation microstructure, the effects of dislocations on ferritic-martensitic steels are important to nearly every radiation induced change in the material. During the early stages of irradiation of ferritic-martensitic steels, defect clusters appear to be rather uniformly distributed within grains, and a saturation density is quickly reached. However, with further irradiation, self-ordering alignment of defect clusters was found in some grains at doses as low as 3 dpa whereas in other grains the defect spatial distribution remained

uniform. Once the aligned structure was created, it was stable up to 15 dpa. The stress caused by a high density of loops would be minimized by the regular arrangement of defects clusters. The preferred crystallographic orientation of defect arrays may be driven by the minimization of elastic interaction energy between defect clusters.

Cavities in ferritic-martensitic steels are also one of the extended defects that form during irradiation and lead to irradiation induced swelling. In the radiation damage process, equal numbers of vacancies and interstitial atoms are created as Frenkel pairs. The dislocations in most ferritic-martensitic steels have a slightly higher preference for the interstitials, leaving the concentration of vacancies higher in the metallic lattice. The excess vacancies can migrate and form clusters. These clusters are stabilized by the diffusion of gases, such as helium produced by (n, α) transmutation reactions, to form three dimensional cavities with a preferential spherical shape. Austenitic stainless steels, having been heavily used in the nuclear industry extensively, are well researched. The major and minor elemental components in austenitic steels, as well as the heat treatment, have been shown to influence the incubation and transient doses before swelling continues at a near constant rate of about 1% per dpa, with the length of the transient regime varying. Body centered cubic materials, such as pure iron, iron alloys, ferritic, bainitic, and martensitic steels with varying levels of chromium, have also been researched heavily and show a much greater resistance to cavity swelling than the austenitic steels, having a face centered cubic structure. The swelling rates for bcc steels are lower than austenitic stainless steels, closer to ~0.1% per dpa or lower compared to 1% per dpa [9].

Another large factor in the microstructural evolution of ferritic-martensitic steels under irradiation is radiation-induced segregation and precipitation. The strong interaction between solutes and the point defects, generated during irradiation, results in coupled transport of the solute

atoms by the point-defect fluxes to and away from sinks, such as grain boundaries, free surfaces, dislocations loops, and cavity surfaces. The magnitude of the solute-point defect binding energy determines whether the solute flow is towards or away from the sinks. A Modified Inverse Kirkendall Effect has been shown to be the primary mechanism for Cr RIS in ferritic-martensitic steels [10]. This segregation also leads to new irradiation induces phases in the ferritic-martensitic steels. These phases are most commonly chromium-rich ferrite (α'), M_6X (η), G phase, and sigma phase (σ). These are primarily formed by the enrichment of chromium (α'), nickel and silicon (G phase), with phosphorus (σ). These changes in phases, along with the growth of dislocations and cavities simultaneously, make the evolving microstructure of ferritic-martensitic steels under irradiation complex.

As a result of these microstructural changes, the macroscopic properties of the ferritic-martensitic steels also see alteration. The loss of ductility in ferritic-martensitic steels during irradiation can be caused by many factors, including hydrogen and helium. It has been concluded from discussions of the mechanisms responsible for the hydrogen embrittlement in the high-chromium martensitic steels that hydrogen is transported to microstructural features and regions of triaxiality during tensile testing by lattice diffusion and mobile dislocation sweeping and is eventually trapped at interfaces and dislocations. The embrittlement then results from either one or a combination of the following processes: the interaction of the hydrogen with dislocations such that plastic flow is localized on specific slip planes, with cross slip possibly being inhibited, and leading to shear modes of failure, and the lowering of the cohesive strength of the interfaces on which the hydrogen has accumulated, thereby promoting brittle modes of fracture. The most widely accepted model of helium embrittlement is based on the stress-induced growth of voids nucleated from helium bubbles at the grain boundaries. The helium bubbles of a certain radius are

initially at equilibrium with the internal gas pressure being balanced by the surface tension. The bubbles on the grain boundaries orthogonal to the applied tensile stress become unstable and grow by grain boundary vacancy condensation if the stress exceeds a critical value. Intergranular helium bubbles of nanometer dimensions have been observed to nucleate voids that enlarge and coalesce to form cracks on the transverse grain boundaries in irradiated austenitic steels and alloys in a manner analogous to the growth of voids during thermal creep. Irradiation creep, however, involves stress-induced processes that enhance the annihilation of irradiation-produced point defects.

In general, the deformation processes involve the stress-induced absorption of irradiation-produced point defects on dislocations that cause the dislocations to climb, which can subsequently lead to glide of the dislocations. For irradiation creep to occur, the absorption of point defects at dislocations must be asymmetric, for if vacancies and interstitials were partitioned equally, annihilation would occur without climb, and there would be no creep. Proposed mechanisms for irradiation creep include swelling-driven creep (I-creep), Stress Induced Preferential Absorption (SIPA) creep, and Preferred Absorption Glide (PAG) creep. I-creep involves climb-enabled glide that occurs because dislocations have a slight bias for interstitials, and these interstitials induce dislocation climb; the excess vacancies are incorporated in cavities. Under the influence of a stress, pinned dislocations can bow out to give an increment of elastic strain. The bias-driven interstitials at dislocations can cause them to climb around the pinning obstacles and glide until they encounter another obstacle and are again pinned. Each time this process is repeated, an increment of creep strain occurs, with the creep rate depending on the climb velocity. In SIPA creep, dislocations are assumed to be sinks for both vacancies and interstitials, but there is a slight bias for interstitials to be absorbed by dislocations with their Burgers vectors aligned with the stress axis. This

preferential absorption due to the stress-induced higher capture efficiency of the dislocations with properly aligned Burgers vectors causes dislocation climb and deformation in the stressed direction. PAG creep is due to climb-enabled glide; that is, first, the dislocations climb around obstacles by the SIPA process, after which the dislocations can glide under the influence of the applied stress until they are again stopped by an obstacle.

In conclusion, the point defects created as part of the radiation damage process provide the basis for the changes of ferritic-martensitic steels under irradiation. The point defects gather to form clusters and from there, agglomerate into extended defects, such as dislocations, cavities, precipitates. They can also cause segregation of elements in the material. These extended defects cause macroscopic changes in ductility, creep strength, hardness, tensile behavior, etc. All of these macroscopic and microscopic changes in ferritic-martensitic steels make predicting the full behavior under irradiation complex.

2.3 Swelling in Ferritic-Martensitic Steels

Since the initial observation of cavities in irradiated materials [11], they have been the subject of much research. The theory of nucleation and cavity growth, as well as the thermodynamics of gas containing cavities, has been published [12–14] and reviewed [15]. Modeling efforts have also been done to understand the behavior of point defects in ferritic steels [16,17]. The primary objective of this section is to provide a review of the experimental undertakings over the years and the conclusions of these studies. This section follows a similar logic and approach to the work done by Klueh and Harries [2] and Garner et al. [9] with additional material added.

In the radiation damage process, equal numbers of vacancies and interstitial atoms are created as Frenkel pairs. The dislocations in most ferritic-martensitic steels have a slightly higher preference for the interstitials, leaving the concentration of vacancies higher in the metallic lattice.

The excess vacancies can migrate and form clusters. These clusters are stabilized by the diffusion of gases, such as helium produced by (n, α) transmutation reactions, to form three dimensional cavities with a preferential spherical shape. The formation of these cavities is partially influenced by the temperature of the material. At low temperatures, defined as 30% of the melting temperature, T_m, the vacancies are slow to diffuse, allowing for recombination with the relatively more mobile interstitials. At relatively high temperatures, greater than 50% of T_m, the thermal vacancy concentration exceeds that caused by the irradiation environment. Thus, the stability of these three dimensional defects is limited to the temperature range 0.3-0.5 T_m [4].

The swelling to damage relation is typically represented as being composed of three regimes, an incubation regime, a transient regime, and a linear swelling regime. In the incubation regime, the swelling is very low, less than 0.1%, and can be considered negligible up to an incubation dose. In the linear swelling regime, the total swelling can be described by a linear relation with the difference between the total dose and the incubation dose multiplied by a swelling rate. Between these two regimes is a transient period to merge the incubation and linear swelling regimes into a continuous function [14,18].

2.3.1 Neutron Irradiation of Ferritic-Martensitic Steels

Under neutron irradiation, helium production via (n, α) reactions is controlled by the neutron energy spectrum of the reactor and the energy dependent cross sections based on the elemental components of the material. Typical helium production has been estimated for fast reactors from ~0.1 appm helium/dpa [19] to ~1.0 appm helium/dpa [20] but varies strongly with composition. This section attempts to gather relevant neutron irradiation experiments to elucidate the effect of helium/dpa on the cavity evolution.

Little [21] presented a general overview of the microstructural evolution of ferritic-martensitic steels under irradiation. For swelling, Little described the viability of using ferritic-martensitic steels for their superior swelling resistance as compared with austenitic steels. Figure 2.4 shows how swelling in ferritic-martensitic steels is much lower compared to swelling in austenitic stainless steels for a given damage level under a variety of irradiation spectrums.

In general, it is observed that increasing amounts of Cr from pure iron tend to increase the swelling resistance. Little continues to propose that ferritic-martensitic steels with 9-12% Cr exhibit the highest swelling resistance at dpa values >100. However lower levels of swelling (<0.5%) are also observed for higher Cr steels (14-22%). The resistance to swelling is also coupled with a large increase in incubation period.

Vitek *et al.* [20] irradiated a 9Cr-1MoVNb steel in HFIR at 300°C, 400°C, 500°C, and 600°C to about 36 dpa with an estimated helium/dpa ratio of 0.83 appm helium/dpa. Few cavities of roughly 4-6nm in diameter were observed at 300°C, 500°C, and 600°C with a homogenous distribution at 300°C and heterogeneously nucleated at dislocations and lath boundaries at 500 and 600°C. At 400°C, the cavities have an average size of 15 nm with a density of 1.1×10^{21} m^{-3} and swelling of 0.19%.

The work of Wakai *et al.* [22,23] explored the effects of helium on cavity development in the reduced activation ferritic-martensitic steel F82H doped with natural boron, boron-10, nickel-58, and nickel-60 to produce helium/dpa ratios of ~0.5 to ~10 appm helium/dpa when irradiated in HFIR to 51 dpa at 300°C and 400°C. At the lower temperature, cavities were observed only in the highest helium/dpa ratios of 6.5 and 9.9 appm helium/dpa. At 400°C, however, cavities were observed in nearly all variations of F82H. As the helium/dpa ratio was increased, the average

cavity size decreased, but the number density came to a peak in the F82H tailored with boron-10 (6.5 appm helium/dpa).

For comparison to the works presented previously, several studies done in FFTF are presented with an assumed nominal helium/dpa ratio of 0.2 appm helium/dpa. Kai *et al.* [24] irradiated a 9Cr-1MoVNb, 9Cr-2WV, 9Cr-2WVTa, and a 12Cr-1MoVW to about 35 dpa at 420°C resulting in cavity densities ranging from 0.05-6 x 10^{20} m^{-3} and average sizes from 25-30nm. Kimura *et al.* [25] irradiated several Fe9Cr-2(1)W alloys to about 40 dpa at 420°C, resulting in average cavity sizes from 20-31nm and densities from 1.6-8.2 x 10^{20} m^{-3}. Sencer *et al.* [26] examined a duct of HT9 used in the FFTF reactor that reached an estimated 155 dpa at 443°C with an average cavity size of 28nm and density of 2.5 x 10^{20} m^{-3}. Van den Bosch *et al.* [27] examined FFTF irradiated T91 irradiated at about 413°C to 184 dpa resulting in an average cavity size of 29nm and 8.3 x 10^{20} m^{-3}. Finally, T91, HT9, MA 956 and MA 957 were examined in the work of Gelles *et al.* [28] at about 200 dpa. The average cavity sizes ranged from 21-35nm and densities from 1.9-48 x 10^{20} m^{-3}. Examining the data from FFTF there is a little concern that the cavity sizes are all in the same range despite the large differences in damage level. However, as the cavities are influenced by the entire microstructure, there are many complicating factors that cannot be sorted out without additional information.

In a recent paper, Getto *et al.* [29] provided a review of swelling in the ferritic-martensitic steels HT9 and T91 irradiated in-reactor up to 208 dpa at temperatures ranging from 400°C to 443°C, reproduced in Figure 2.5. There is a significant amount of scatter in the swelling reported, but in general as the damage level increases, the amount of swelling also increases. There are also variations in different heats of the same alloy, and single heats undergoing different heat

treatments. Up to the high damage level of 208 dpa though, the amount of swelling is still < 3%, highlighting the overall swelling resistance of ferritic-martensitic steels.

2.3.2 Heavy Ion Irradiation of Ferritic-Martensitic Steels

In order to understand the radiation responses of material at an accelerated rate compared to neutron irradiation, ion irradiation experiments have been performed at high damage rates with both pre-injected and co-injected helium to simulate the effects of damage seen in reactor at high damage levels.

A ferritic steel (Fe2.25Cr-1 Mo) was studied by Sindelar *et al.* [30]. The focus of this studying was to determine the microstructural response to irradiation at various damage levels and in different phases of the material. Irradiation was performed up to 350 dpa at 500°C using 14 MeV nickel ions. No cavities were present in any of the samples unless helium was pre-injected at 100 appm.

The ferritic-martensitic alloy T91 was studied by Gigax et al. [31] using 3.5 MeV iron ions at 475°C up to 550 dpa at the region examined. The swelling response indicated low swelling (< 3%) up to 410 dpa but a sudden increase to 22% swelling at 550 dpa for a rate of 0.11%/dpa. Maximum swelling occurred at approximately half of the projected ion range, supposedly due to the defect imbalance effect [32]. Swelling of T91 had an incubation period of swelling of ~400 dpa at the depth of peak swelling, greater than incubation periods from neutron irradiated T91. However, in reactor the production of helium will drive cavity nucleation and therefore, decrease the incubation period for swelling. This ion irradiation study was conducted without considering the effects of helium and this may account for the delay in the incubation period.

The swelling and microstructure evolution of ferritic-martensitic alloys HT9, T91, and T92 were investigated by Getto et al. [29] using iron ions and 10 appm helium pre-injected to obtain

systematic evolution from 75 to 650 dpa. Contrary to the previous study, for the least swelling resistant alloy (HT9), a swelling rate of 0.033%/ dpa was observed from 188 to 650 dpa. Swelling resistance was higher in T91 at a rate 0.007%/ dpa. The decrease in swelling/swelling rate in T91 was primarily due to suppression of cavity nucleation, rather than growth, which proceeded at approximately 0.1 nm/dpa. Swelling resistance was highest in T92, which had not yet reached steady state swelling by 650 dpa due to a low density of small cavities, indicating suppression of both nucleation and growth. Analysis of additional heats of T91 indicated that alloy composition was not the primary factor in determining swelling resistance. In addition to swelling increasing with damage level, the volume fraction of G-phase precipitates and line length of dislocation were found to evolve in the microstructure up to 650 dpa as shown in Figure 2.6. The use of ion irradiations has been instrumental in determining that the microstructure of ferritic-martensitic steels will continue to evolve with damage level beyond intended reactor lifetimes.

2.4 Factors Affecting Cavity Nucleation and Growth

In assessing the current state of knowledge of swelling in ferritic-martensitic steels, it is important to consider both the theoretical models and available body of experimental evidence. Swelling results from the formation of cavities, a term which is inclusive to both voids and bubbles. Voids are formed without the pressure of a residual gas, and bubbles are defined as cavities with gas pressure in mechanical equilibrium with the lattice. Cavity evolution is very sensitive to changes in temperature, dislocation microstructure, and gas content (usually in the form of helium). The expected changes in swelling behavior due to changes in these parameters can be assessed analytically. The experimental studies performed either refute or support these models to some extent. The following analyzes, in sequence, the effect of changes in temperature, dislocation microstructure, helium content, and carbon contamination on the cavity evolution of ferritic-

martensitic steels. Each section first discusses the analytical models, and then proceeds to discuss the relevant body of experimental evidence. Conclusions on the state of knowledge of each effect are summarized at the end of each section.

2.4.1 Impact of Temperature

Cavity nucleation rate is strongly dependent on the vacancy super-saturation. Therefore, changes in temperature which affect the super-saturation of vacancies will affect the length of the nucleation region as well. Theory has shown that swelling follows a bell-curve temperature dependence based on the melting temperature of the material, T_m [33]. Cavity formation and swelling tends to prevail at irradiation temperatures from about $0.3T_m$ to about $0.5T_m$. Below this temperature range, vacancies are unable to diffuse and cluster together to form cavity embryos. Nucleation of cavities decreases with increasing temperature outside of this range due to a higher emission of vacancies from clusters. In this intermediate temperature range, there is a temperature where the vacancy flux to a cavity embryo is largest compared to the vacancy emission. Vacancies have limited mobility at these temperatures and will recombine with interstitials before clustering into cavities. This behavior can be described by the number of vacancies required for a critically stable cavity to form [34]:

$$n = \frac{36\pi\gamma^3\Omega^2}{3(kT)^3\left[ln\left(\frac{B_v(n)-B_i(n+1)}{B_v^0(n)}\right)\right]^3}, \qquad \text{Eq. 2.1}$$

where $\gamma$is the surface energy, Ω is the atomic volume, k is Boltzmann's constant, T is temperature and $\frac{B_v(n)-B_i(n+1)}{B_v^0(n)}$ represents the vacancy super-saturation. Both temperature and vacancy super-saturation appear in the denominator. At low temperatures and low vacancy super-saturations, the number of vacancies n becomes extremely large, and cavity nucleation is an unlikely event. At high temperatures, the vacancy super-saturation is reduced, from the increase in thermal vacancies

and emission of vacancies to be lost to other sinks and therefore $n$will also become prohibitively large.

Dvoriashin and colleagues [35] studied a ferritic-martensitic steel EP-450 after irradiation in a fast reactor. Swelling was studied as a function of temperature in the range of 275ºC - 690ºC. Figure 2.7 shows swelling rate as a function of temperature demonstrating the characteristic bell-curve dependence. A peak is observed around 420ºC. Considering the lower damage data points at 11 dpa have a larger swelling rate than those at either 46 dpa or 89 dpa, it is likely that these swelling rates are representative are more representative of a nucleation rate rather than a growth rate, and therefore demonstrating that nucleation follows a similar bell-curve.

Ayrault [36] studied the effect of irradiation temperatures above 450°C on a 9Cr-1Mo steel. No swelling peak was found, but the highest swelling occurred at 450ºC. This may suggest that the tail-end of a temperature peak was caught in this study and the peak would appear somewhere close to 450ºC.

Hide *et al.* [37] studied the response to irradiation of six different ferritic alloys with 200keV C^+ and 3 MeV Ni^+: MA957 (an ODS alloy), HT9, Fe-12Cr, 12Cr-2Mo, 9Cr-8Mo-4Ni (solution anneal), 9Cr-8Mo-4Ni (aged). These metals were studied at damage levels ranging from 50 – 200 dpa and temperatures from 425-625°C. All of the samples were pre-injected with helium to a fixed ratio of 0.1 appm/dpa. All alloys exhibited peak swelling at 575°C. Although this value is higher than the previously suggested values between 400-500°C, the higher damage rate is expected to shift the swelling bell-curve to higher temperatures [14,38].

Kai and Kulcinski [39] studied HT9 irradiated with nickel ions at three different temperatures: 400ºC, 500ºC , and 600ºC. Cavities were only observed at 500ºC. The intermediate temperature seemed the only temperature which allowed for cavity nucleation.

Schmidt *et al*. [40] observed a peak swelling temperature of 500ºC in HT9 and 550ºC in EM-12 after irradiation with 2.8 MeV Fe^{+} ions up to 250 dpa. The dependence of swelling as a function of temperature is shown in Figure 2.8.

Sencer *et al.* [26] irradiated HT9 in FFTF and found a peak swelling temperature at about 443ºC. However, it must be noted that the damage level was also highest at this temperature (155 dpa compared to 28 dpa at 384ºC), which may cloud the effect of temperature.

Wakai *et al*. [41] showed highest swelling at 470ºC, which then decreased with increasing temperature. Ferritic-martensitic steel F82H was irradiated with a triple beam system (Fe^{+}, He^{+}, and H^{+}) at temperatures from 470ºC to 600ºC. It is likely that a peak swelling temperature is present at a temperature lower than that studied in this paper.

Getto *et al.* [42] studied swelling in HT9 at temperatures ranging from 400°C to 480ºC after irradiation up to 375 dpa using Fe^{2+} ions and 10 or 100 appm helium pre-injected. The peak swelling temperature was determined to be near 460ºC. At lower and higher temperatures 480ºC and 440ºC, it was determined that the onset of swelling was delayed relative to experiments performed at 460ºC. The swelling behavior as a function of temperature at 188 dpa is shown in Figure 2.9. This set of experiments suggested that cavity nucleation was enhanced closer to the peak swelling temperature.

Toloczko *et al*. [43] performed a study on a MA957 tube up to 500 dpa at a variety of temperatures, 400ºC, 420ºC, 450ºC, and 500ºC. The peak swelling temperature was determined to be near 450ºC. The swelling results are shown in Figure 2.10. The study compared the swelling behavior at damage levels of 100 and 500 dpa. However, the coarseness of these doses does not allow for the determination whether steady-state swelling was achieved. It does, however, provide further evidence that nucleation was enhanced at doses closer to the peak temperature.

The authors compared the swelling behavior of MA-957 to that of HT9 and EP-450. The swelling as a function of dose are shown up through about 500 dpa in Figure 2.11. A steady-state swelling value of 0.2%/dpa was determined for HT9 and EP-450. However, it is important to note that EP-450 was irradiated at a different temperature (480°C) compared to MA-957 and HT9. MA-957 exhibited the lower swelling up to 500 dpa and the achievement of steady-state has not yet been confirmed. This is further supported by the cavity size distributions in the paper, which are skewed to smaller sizes.

Per both theory and the studies described here; a swelling peak is expected at an intermediate temperature range. For neutron irradiations, this peak may be approximately centered at 420°C-440ºC. For ion irradiations, it may be higher from ~460ºC-500ºC. This swelling peak is usually referred to as occurring at steady state, however since the processes affecting the growth of cavities also govern nucleation behavior (i.e. super-saturation of vacancies), these concepts can also be extended to cavity nucleation. Therefore, the swelling at low damage levels would also be expected to have a peaked behavior at an intermediate temperature.

Qualitatively, there is evidence that swelling follows the expected bell-curve behavior, and so it is reasonable to assume that nucleation behavior will follow, due to its large role in determining overall swelling behavior. However, there is a very little direct experimental evidence that suggests this is the case. This is due to the difficulty in determining the transition from nucleation to growth dominated behavior. Garner [9] postulated that there exists a "universal steady-state swelling rate" independent of temperature, but this has not been experimentally confirmed. A systematic set of experiments at incremental temperatures and incremental damage levels would be required to identify the location of the peak swelling temperature and possible changes during the transition from nucleation to growth dominated swelling.

2.4.2 Effects of Damage Rate and Helium Co-Injection Rate

From the neutron and dual ion irradiated ferritic-martensitic steels, a picture of the overall effect of the helium/dpa ratio can be attempted. Several assumptions have been made going into this picture, such as the assumption that any FFTF irradiated material had a helium/dpa ratio of about 0.2 appm helium/dpa and the assumption that materials irradiated in the same reactor have the same nominal damage rate. Consolidating all of the available cavity information from neutron irradiations performed between 400-500°C and 12-200 dpa [19,20,22–28,44] and dual ion irradiations from 10-125 dpa between 360-600°C [45–52], the trends of cavity density, Figure 2.12b, average cavity size, Figure 2.12a, and swelling, Figure 2.12c with the helium/dpa ratio can be obtained. Because of the high sink density in ferritic-martensitic steels, the damage rate and the vacancy concentration are expected to be linearly dependent, and thus Figure 2.12 an also be viewed as the helium/vacancy ratio.

As the helium/dpa ratio increases, the average cavity diameter appears to decrease. The cavity density also appears to increase with increasing helium/dpa ratio up to about 30 appm helium/dpa. The swelling appears to decrease with increasing helium/dpa ratio. Although the trends are visible, there is still significant scatter in the available data. Given the possible variations in cavity evolution with temperature, material composition, heat treatment, and across damage rates, these trends have still emerged. Graphing the same set of cavity data as a function of the irradiation damage rate, Figure 2.13, similar trends do not emerge. While the cavity densities can be considered similar between the low damage rates of neutron irradiation and the high damage rates of ion irradiation, the significant differences in the helium/dpa ratio, and therefore helium/vacancy ratio, make the comparison questionable. The dependence of damage rate on

cavity evolution is not discernable from the literature included in this review. This is likely in part from the lack of reporting on the damage rate for many of the neutron irradiation studies.

2.4.3 Helium Effects

Neutron Irradiation of Ferritic-Martensitic Steels

Under neutron irradiation, helium production via (n,α) reactions is controlled by the neutron energy spectrum of the reactor and the energy dependent cross sections based on the elemental components of the material. Typical helium production has been estimated for fast reactors from ~0.1 appm helium/dpa [19] to ~1.0 appm helium/dpa [20] but varies strongly with composition. This section attempts to gather relevant neutron irradiation experiments to elucidate the effect of helium/dpa on the cavity evolution.

Vitek *et al.* [20] irradiated a 9Cr-1MoVNb steel in HFIR at 300°C, 400°C, 500°C, and 600°C to about 36 dpa with an estimated helium/dpa ratio of 0.83 appm helium/dpa. Few cavities of roughly 4-6nm in diameter were observed at 300°C, 500°C, and 600°C with a homogenous distribution at 300°C and heterogeneously nucleated at dislocations and lath boundaries at 500 and 600°C. At 400°C, the cavities have an average size of 15 nm with a density of 1.1×10^{21} m^{-3} and swelling of 0.19%.

Complimenting the previous study, Hashimoto *et al.* [44] irradiated a 9Cr-1MoVNb steel and 9Cr-2WVTa and additional alloys with 2Ni added to increase helium generation during irradiation in HFIR to about 12 dpa at 400°C with about 2-2.5 appm helium/dpa in the base alloys and 12-13 appm helium/dpa in the nickel doped alloys. Irradiation of the nickel doped alloys resulted in smaller cavities on average and a larger density of cavities compared to the non-nickel doped alloys. However, the amount of swelling was still small in both cases with the largest swelling occurring in the 9Cr-1MoVNb at 0.17%.

The work of Wakai *et al.* [22,23] explored the effects of helium on cavity development in the reduced activation ferritic-martensitic steel F82H doped with natural boron, boron-10, nickel-58, and nickel-60 to produce helium/dpa ratios of ~0.5 to ~10 appm helium/dpa when irradiated in HFIR to 51 dpa at 300°C and 400°C. At the lower temperature, cavities were observed only in the highest helium/dpa ratios of 6.5 and 9.9 appm helium/dpa. At 400°C, however, cavities were observed in nearly all variations of F82H. As the helium/dpa ratio was increased, the average cavity size decreased, but the number density came to a peak in the F82H tailored with boron-10 (6.5 appm helium/dpa).

For comparison to the works presented previously, several studies done in FFTF are presented with an assumed nominal helium/dpa ratio of 0.2 appm helium/dpa. Kai *et al.* [24] irradiated a 9Cr-1MoVNb, 9Cr-2WV, 9Cr-2WVTa, and a 12Cr-1MoVW to about 35 dpa at 420°C resulting in cavity densities ranging from 0.05-6 x 10^{20} m^{-3} and average sizes from 25-30nm. Kimura *et al.* [25] irradiated several Fe9Cr-2(1)W alloys to about 40 dpa at 420°C, resulting in average cavity sizes from 20-31nm and densities from 1.6-8.2 x 10^{20} m^{-3}. Sencer *et al.* [26] examined a duct of HT9 used in the FFTF reactor that reached an estimated 155 dpa at 443°C with an average cavity size of 28nm and density of 2.5 x 10^{20} m^{-3}. Van den Bosch *et al.* [27] examined FFTF irradiated T91 irradiated at about 413°C to 184 dpa resulting in an average cavity size of 29nm and 8.3 x 10^{20} m^{-3}. Finally, T91, HT9, MA 956 and MA 957 were examined in the work of Gelles *et al.* [28] at about 200 dpa. The average cavity sizes ranged from 21-35nm and densities from 1.9-48 x 10^{20} m^{-3}. Examining the data from FFTF there is a little concern that the cavity sizes are all in the same range despite the large differences in damage level. However, as the cavities are influenced by the entire microstructure, there are many complicating factors that cannot be sorted out without additional information.

Dual Ion Irradiation of Austenitic Steels and FCC Alloys

Although ferritic-martensitic steels are the focus of this work, the studies of Katoh *et al.* [53,54] combined together experimental and modeling information on dual ion irradiated solution annealed Type 316 stainless steel to examine the effects of the helium/dpa ratio on the cavity density (separated into bubbles and voids), cavity radius, and swelling. For the voids shown in Figure 2.14, the number density exhibited a bell curve behavior with regards to the helium/dpa ratio with a peak near 15 appm helium/dpa at 25 dpa. For the same level of damage, the average void size decreased with increasing helium/dpa ratio. For bubbles observed at 25 dpa, the density increased with increasing helium/dpa ratio. This study also examined the effect of the damage rate dependence of the helium/dpa ratio on swelling using a rate theory model. For the same temperature, see Figure 2.15, the model predicts as the damage rate is increased, the helium/dpa ratio needed for peak swelling also increased. However, there is no experimental data presented to validate this prediction.

The effects of helium and its relationship with damage rate have been presented in [55] and discussed in a review by Abromeit [56]. Using dual ion irradiation, the effects of the He/dpa ratio on swelling across a range of damage rates from 10^{-4} to 10^{-2} dpa/s were investigated. As shown in Figure 2.17, increasing the helium/dpa ratio increased the swelling overall. However, for the same He/dpa ratio, as the damage rate increased, the amount of swelling decreased. The exact reasons for this decrease are not discussed as no microstructural information is presented. Speculation could suggest an increase in the density of cavities and lower growth of any individual cavity as the damage rate is increased.

Similar behavior can be found in other austenitic stainless steels [57–62] and in simple FCC materials such as copper [63,64] and nickel [65,66]. In these materials, a monotonic increase

in cavity density and corresponding decrease in cavity size with increasing He/dpa ratio at a given irradiation temperature and damage was observed. The peak cavity swelling has been reported to occur near 10-30 appm He/dpa in neutron-irradiated FCC metals, such as copper in Figure 2.18 from references [63,67–72].

Dual Ion Irradiation of Ferritic-Martensitic Steels

Asano *et al.* [45] performed a study on the ferritic-martensitic steel HT9 using dual ion irradiation to 25 dpa with 15 appm helium/dpa at several temperatures (350°C, 410°C, 470°C, 530°C, and 600°C), and up to 100 dpa with 5 appm helium/dpa or 15 appm helium/dpa. At 25 dpa, the highest swelling occurred at 470°C with a bimodal cavity size distribution. At higher temperatures of 530°C and 600°C, the cavities were associated with dislocations and grain boundaries. For the HT9 irradiated to 100 dpa at 450°C, a helium/dpa ratio of 15 appm helium/dpa resulted in a bimodal cavity distribution while the lower helium/dpa ratio of 5 appm helium/dpa formed only small cavities.

In the work of Kupriiyanova *et al.* [51], the ferritic-martensitic steel EP-450 was dual ion irradiated at 480°C up to 200 dpa with up to 160 appm helium/dpa. At 50 dpa, as the helium/dpa ratio was increased from zero, the average size decreased and number density of cavities increased resulting in increased swelling with increased helium/dpa ratio. However at 200 dpa, the swelling decreased with increasing helium/dpa ratio from the decrease in cavity size. Similar trends at 200 dpa were observed in other ferritic-martensitic steels F82H and EK181 also studied in this work.

Ogiwara *et al.* [46] dual ion irradiated two reduced activation ferritic-martensitic steels JLF-1 and JLS-1 from 40-100 dpa with 15 appm helium/dpa at 470°C and 550°C. Significant swelling was observed only at 470°C in both alloys.

The work of Wakai *et al.* [47] irradiated the ferritic-martensitic F82H to 50 dpa with 18 appm helium/dpa at 470°C, 510°C, and 600°C. With increasing temperature the cavity density was reduced but not significantly, such as 5.2 x 10^{21} m^{-3} at 470°C to 4.6 x 10^{21} m^{-3} at 600°C and average cavity sizes ranging from 5.2 to 6.7 nm. From this information, it is likely that all of the cavities observed are stabilized by the co-injected helium and have limited growth from the high temperature.

The work of Hiwatashi *et al.* [48] explored the effects of dual ion irradiation on several reduced activation ferritic-martensitic steels JLF1, JLF3, JLF4, JLF5, and two model alloys Fe9Cr2Mo and Fe2.25Cr1Mo up to 125 dpa and 0, 1, and 15 appm helium/dpa at 450°C. In both JLF4 and the model alloy Fe2.25Cr1Mo, the average cavity size decreased and density increased with increasing helium/dpa ratio with the highest swelling occurring at the intermediate value of 1 appm helium/dpa.

Yamamoto *et al.* [49] performed several dual ion irradiations on a ferritic-martensitic alloy, F82H3 and two nanostructured ferritic alloys MA957 and 14YWT-PM2 at 500°C and 650°C from 15-55 appm helium/dpa with significant characterization at 10 dpa and 26 dpa in F82H3 and MA 957. This work found no significant systematic trend in the cavity density, average cavity density, or swelling with helium/dpa, but found a systematic increase in average cavity diameter with increasing helium content.

Although the materials used in the work of Bhattacharya *et al.* [52] were not commercial ferritic-martensitic steels, the model iron-chromium alloys (Fe, Fe3Cr, Fe5Cr, Fe10Cr, Fe12Cr, Fe14Cr) dual ion irradiated to 128 dpa with 13 appm helium/dpa at 500°C provided insight into the effect of chromium addition on swelling. The Fe10Cr alloy displayed the highest amount of

swelling, primarily from its increased cavity density, as the sizes for all model alloys had similar cavity sizes.

The study of Brimbal *et al.* [50] performed dual ion irradiation on Fe and Fe5Cr to 100dpa with 0, 2.5, and 26 appm helium/dpa at 500°C to examine the effects of helium and chromium on swelling. As the helium/dpa ratio was increased in the pure iron, the average cavity size decreased and the cavity density increased. However, cavities were only observed in the Fe5Cr at the highest helium/dpa ratio of 26 appm helium/dpa with a very high density of cavities and small average size.

2.4.4 Effects of Helium Injection Mode

In accelerator experiments, helium may be injected into the metallic lattice, rather than created through transmutation to simulate reactor environments. The injection of helium is known to shorten the incubation period for cavity nucleation by stabilizing small clusters of vacancies and allowing them to more easily reach critical size. Farrell [58,59] studied the effect extensively. The work is heavily theoretical, backed by some experiments, but explains in detail the role helium plays in cavity nucleation and growth, and effects on dislocations and precipitates. While the work is not specific to F-M steels, it still provides valuable insight into the formation and growth of cavities.

Gasses facilitate nucleation of cavities, especially non-reactive and insoluble gasses such as helium. Helium tends to reduce the incubation period required for the nucleation of cavities, and tends to result in higher densities of smaller sized cavities. The injection process also will affect the behavior of cavities. Pre-injected helium at room temperature seems to be more effective at nucleating cavities than injected helium during the irradiation or helium injected at the

irradiation temperature. High amounts of helium can actually depress growth and retard swelling. If cavities become the dominant sink, then they will tend to reduce cavity growth.

Hot helium injection tends to result in a larger cluster but smaller densities. The less mobile cold pre-injection results in vacancies being trapped on a smaller scale and thus creates a high concentration of smaller cavities. Cold pre-injection and co-injection both tend to result in bimodal distribution of cavities with a large group smaller than the critical radius and a group that has stabilized beyond the critical radius.

Lastly, grain boundaries can serve as traps for helium, thus forming grain boundary bubbles. These bubbles are not bias driven, as the concentration of point defects near grain boundaries is usually very low so supersaturation of vacancies at these sites is very rare.

The most comprehensive work which explored the effects of the method of helium pre-injection was performed by Packan and Farrell [73] on 316 stainless steel. Doses up to 70 dpa were explored with helium either simultaneously injected at 20 appm/dpa (to a total of 1400 appm), or pre-injected at room temperature or 627°C at 1400 appm. The highest swelling was observed in the helium-free material (18%), with simultaneous injection resulting in 11% and pre-injection at 627°C resulting in 4% and only 1% at room temperature. These results are summarized in Table 2.2 below.

From the images of the cavity microstructure (Figure 2.18) it is clear that the higher swelling in the helium-free case is due to the fact that the cavities were allowed to grow unimpeded. The addition of helium through any method resulted in lower swelling, likely due to the high cavity sink strength resulting from the very high density of nucleation.

While the addition of helium causes a reduction in swelling in all cases, it should be noted that only relatively high amounts of helium were studied—likely resulting in excessive cavity

nucleation which inhibited growth. It remains unclear whether the addition of a smaller amount of helium would enhance the swelling beyond that of the helium-free condition. However, the difference in swelling behavior between the room temperature injection and the 627°C injection is likely due to a coarsening effect of the pre-injected helium clusters. The higher temperature pre-injection created fewer but larger cavity nuclei.

The authors suggest that for the room temperature pre-injection the cavities were the overwhelming dominant sink and cavities and dislocations were approximately equal in the co-injected and no helium cases. The defect partitioning ultimately determines whether the cavities will grow unimpeded or not, but a thorough comparison of the Q ratios is not presented in the paper. Based on the results, it is likely that hot pre-injection pushes the microstructure to a more dislocation-favored regime.

It is also postulated that the high levels of helium served to bind many vacancies, preventing them from clustering and promoting recombination. These helium-vacancy complexes served as non-biased sinks for point defects resulting in a decrease in the super-saturation and ultimately repressing the nucleation and growth of stable clusters. However, while this theory is postulated, there is no confirmation that this is the cause of repressed swelling. Furthermore, there is no comparison with other levels of pre-injected helium, to be able to determine whether this is caused from pre-injection, or just the high level of helium included.

2.4.5 Theoretical Considerations

Russell [12,13,74] presents the thermodynamics of voids and gas-containing cavities in metals. For the cavity to be in equilibrium with the solid around it, the external pressure of the solid on the cavity must be equal to the internal pressure from the gas atoms with the surface energy taken into account as well. This theory presents that the size of the cavity is proportional

to the density of the gas occupying the cavity, and the volume of the cavity itself. The internal pressure of a gas in any individual cavity is difficult to measure, but has been estimated by using Electron Energy Loss Spectroscopy [75], as done in [76–79] for helium bubbles in aluminum and ferritic-martensitic alloys.

The production of inert gas atoms in reactors acts to stabilize subcritical cavities, and from this process, encourage nucleation of stable cavities. Helium is the focus of many inert gas studies as it is commonly produced in reactor materials through nuclear transmutation reactions. Helium is thought to enhance the nucleation of cavities by lowering the free energy requirement to create a critical cavity embryo. The free energy equation for voids without any gas is driven by the supersaturation of vacancies (S_v) and countered by the energy required to form an interface in the material:

$$\Delta G = -nkT\, ln(S_V) + (36\pi\Omega^2)^{1/3}\gamma n^{2/3}. \qquad \text{Eq. 2.2}$$

In the presence of helium, the free energy equation for cavities becomes:

$$\Delta G = -nkT\, ln(S_V) + (36\pi\Omega^2)^{\frac{1}{3}}\gamma n^{\frac{2}{3}} - xkT\, ln\left(\frac{MHn\Omega}{xkT}\right), \qquad \text{Eq. 2.3}$$

where *x* corresponds to the number of helium atoms in the cavity, *M* is the concentration of helium atoms in the solid (usually in atoms/cm^3 or equivalent), and *H* is the Henry's Law constant for the dissolution of helium in the metal. From comparing Equations 2.2 and 2.3, the presence of helium lowers the free energy required to form a stable cavity, with the added term being the free energy required to move the helium from the solid into the cavity. This lower free energy results in a smaller critical cavity nucleus, and thus enhancing nucleation relative to a gas-free environment.

Hishinuma [34] and Mansur [80] discuss the effect of helium in terms of a critical radius required for a cavity to stabilize and grow. These works highlight a derivation of the critical radius, the radius at which the net flux of vacancies to the cavity is zero, to include the functional

dependences on gas pressure, dislocation and cavity capture efficiencies, temperature, damage rate, and other variables. By examining the critical radius, the emergence of a bimodal cavity size distribution is discussed with one distribution around the radius of a gas-stabilized bubble and the other distribution arising from cavities with a large enough inward flux of vacancies to grow.

To investigate the importance of helium to cavity nucleation, Stoller and Odette [81] studied the effect of the cluster composition (helium vs. vacancy) on the nucleation path of cavities. Two paths emerge to limit cavity formation: one limited to growth by helium accumulation alone, the other limited by stochastic fluctuations in the vacancy cluster population. The accumulation of gas seemed to be the generally dominant mechanism. Specific cluster compositions and distributions are not analyzed, however. This work was also analyzed in the context of austenitic stainless steels, and its applicability to ferritic-martensitic steels has still not fully emerged.

Stoller and Osetsky [82] evaluated the behavior of helium in bcc iron using molecular dynamics. This work found that when a helium bubble is in mechanical equilibrium with the iron lattice, the helium/vacancy ratio decreases as the bubble increases in size. The compressibility of the helium also decreases with increasing bubble size, leading to ideal gas behavior for the helium. However, the bubbles presented in these simulations are less than 5 nanometers in size and would result in barely visible structures under TEM. The simulations found that the helium to vacancy ratio for equilibrium bubbles large enough to be visible is in the range of 0.3-1.0, consistent with electron energy loss spectroscopy results in ferritic-martensitic steels [76,77].

One mechanism of helium related to swelling is the generation of Frenkel pairs via a loop punching mechanism [83–85]. Small clusters of helium atoms produce lattice distortions and lead to lattice atoms being pushed into interstitial sites. In BCC materials, the helium interstitial activation energy is lower than in FCC materials. Since the binding energies of helium interstitials

to each other in BCC materials are even greater than in FCC, self-trapping of helium will also occur. The concentration of helium–helium clusters increases in the initial evolution phase under irradiation but decreases to a negligible amount at longer times. The concentration of helium–vacancy clusters shows three distinct stages of evolution [86,87]. At lower times, the helium–vacancy cluster concentration increases, it remains fairly constant for several orders of magnitude of time and then decreases at higher time scales. The initial increase is due to very small helium–vacancy clusters. Once the free helium is depleted, the size of the clusters grows by incorporating more vacancies. At longer time scales, point defects dissociate from smaller clusters and form larger clusters. These large clusters serve as sinks to absorb point defects and grow into cavities.

2.4.6 The Critical Bubble Model of Cavity Nucleation

Many aspects of cavity formation have been modeled approximately using the critical bubble model (CBM) concept [88,89]. A critical bubble is one that has grown to a radius (r^*) and helium (m^*) content such that upon the addition of a single helium atom or vacancy, the bubble immediately transforms into an unstably growing cavity without the need for statistical nucleation. More generally, the CBM is one of the possible solutions to the cavity growth rate equation when the growth rate is equal to zero:

$$\frac{dr}{dt} = \frac{\Omega}{r}\left[D_v C_v - D_i C_i - D_v C_{v,T} \exp\left(\frac{2\gamma}{r} - p_g\right)\right]. \quad \text{Eq. 2.4}$$

The three major terms of the equation are the growth of the cavity through the arrival of vacancies to the cavity ($D_v C_v$), the reduction in cavity radius from interstitial arrival to the cavity ($D_i C_i$), and the thermal emission of vacancies using the capillary approximation to account for the gas pressure inside the cavity ($D_v C_{v,T} \exp\left(\frac{2\gamma}{r} - p_g\right)$). In general, the roots of the cavity growth rate equation strongly depend on the helium gas pressure and can result in four possible states with increasing helium concentration in the cavity, illustrated in Figure 2.20 [90]. Without helium, there

is only one root (r_v^*) and it corresponds to when a cavity embryo becomes large enough through statistical fluctuations in the number of vacancies in the cavity to grow through bias driven growth. With some helium atoms in the cavity and below the critical helium content, the growth rate equation has two roots corresponding to the stable bubble radius (r_b^*) and the size to convert from a bubble to an unstably growing cavity (r_v^*). With the critical amount of helium, as described previously for the CBM, there is only one root (r^*) and it corresponds to the critical bubble radius. With a helium content greater than the critical number of helium atoms, there are no roots to the growth rate equation and all cavities grow unstably.

A significant advantage of the CBM and the cavity growth rate equation is that it requires a relatively modest number of parameters, and parameter combinations, that are generally reasonably well known including for defect production, recombination, dislocation bias, sink strengths, interface energy, and defect diffusion rates. One key prediction of the CBM is the prediction of a bimodal cavity size distribution, composed of growing voids and stable bubbles. It is with this prediction and advantage that the cavity growth rate equation used with the CBM is the primary context for the discussion around cavity nucleation.

Table 2.1: Effects of alloying addition on the constitution of high chromium steels [2].

Element	Change in δ-ferrite Content, % per Mass % Alloy Addition
N	−220
C	−210
Ni	−20
Co	−7
Cu	−7
Mn	−6
W	+3
Mo	+5
Si	+6
Cr	+14
V	+18
Al	+54

Table 2.2: The swelling resulting from different methods of helium injection at 70 dpa and 627°C from [73].

Injection Condition	Swelling (%)
None	18
Co-injection (20 appm He/dpa)	11
627°C Hot Pre-injection (1400 appm)	4
Room Temperature Pre-injection (1400 appm)	1

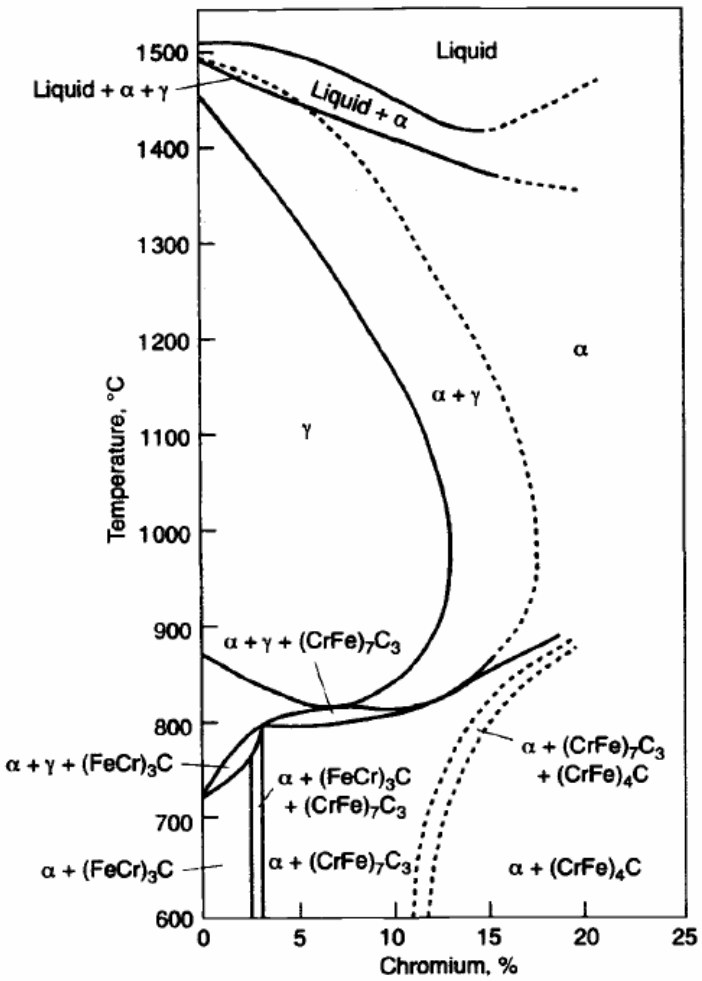

Figure 2.1: Effect of chromium on Fe-Cr-C steels containing 0.1% carbon. $(CrFe)_4C$ is the $M_{23}C_6$ carbide [2].

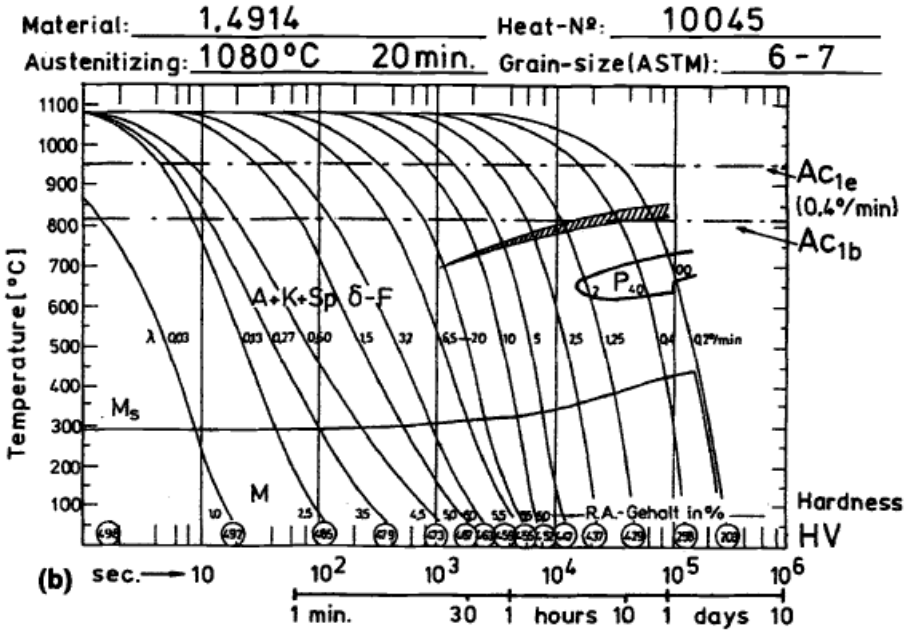

Figure 2.2: Continuous cooling transformation (CCT) diagrams for 1.4914 (12Cr-MoVNb) martensitic steel (A = Austenite, K = Carbide, Sp δ-F=Trace of ferrite, M = Martensite, P = Pearlite, Ac_{1b} = Start of austenite formation on heating, Ac_{1e} = Completion of austenite formation on heating, λ = Cooling rate (°C/min) from 800-500°C [2].

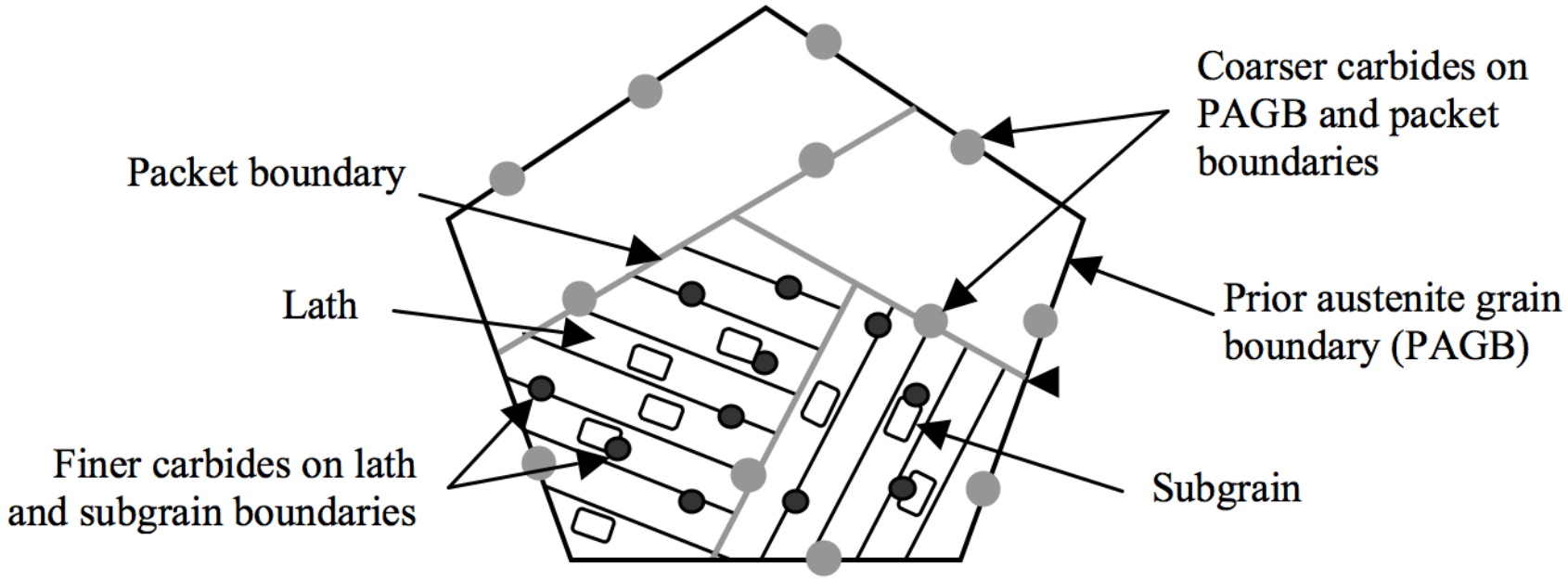

Figure 2.3: Typical F-M microstructure following tempering [6].

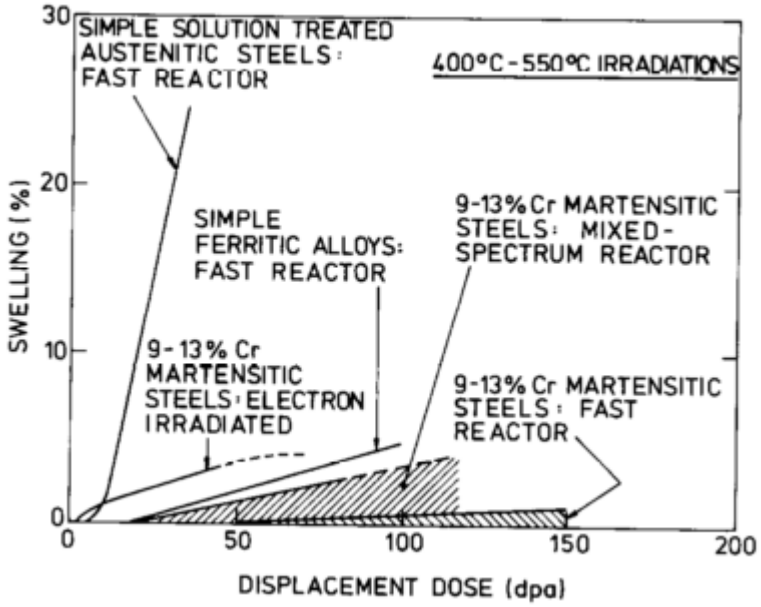

Figure 2.4: Swelling of ferritic-martensitic and austenitic alloys are displayed under a variety of irradiation spectrums.

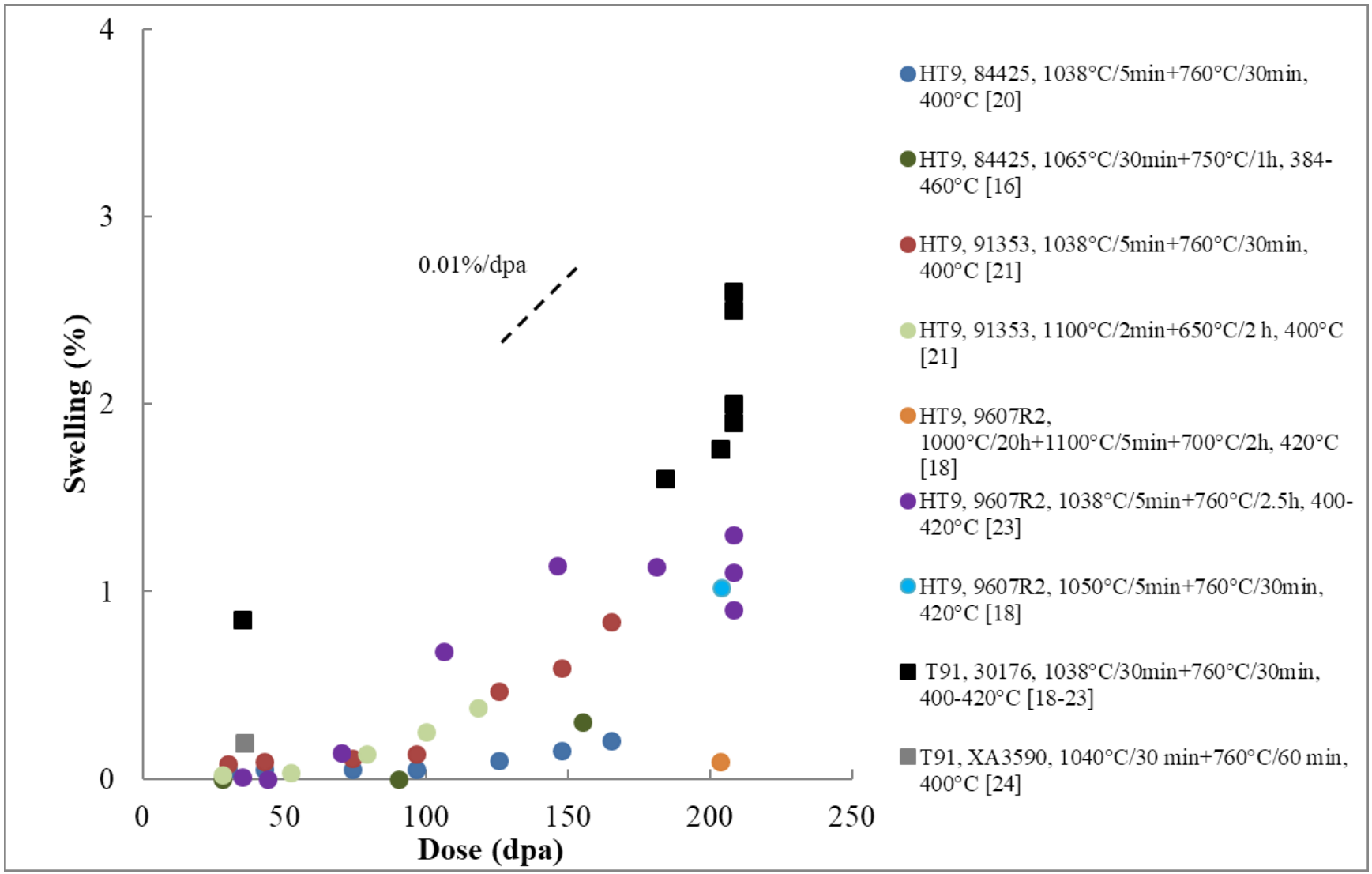

Figure 2.5: Summary of ferritic-martensitic steels irradiated in-reactor up to 208 dpa at temperatures varying from 440°C to 443°C, reproduced from [29].

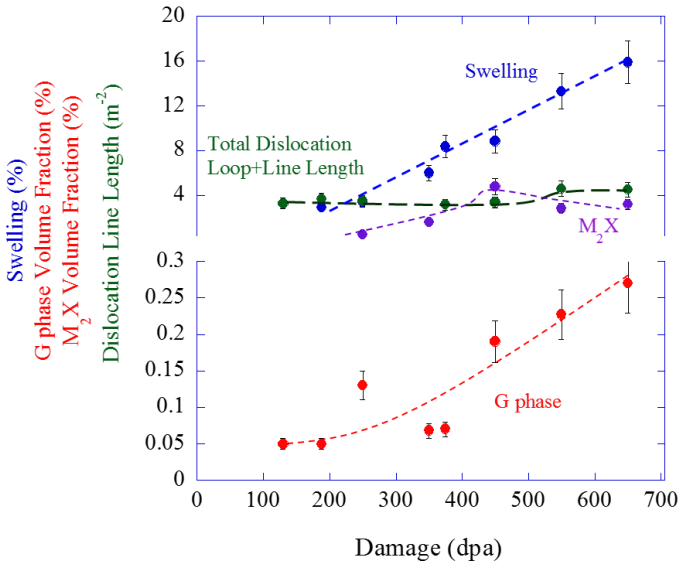

Figure 2.6: Microstructural evolution of HT9 irradiated with 5 MeV iron ions at 460°C from 130 to 650 dpa from [29].

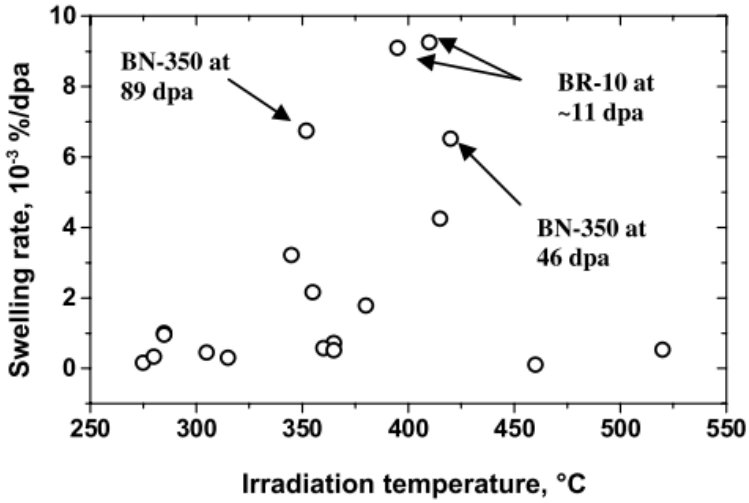

Figure 2.7: Temperature dependence of swelling rate in EP-450 [91].

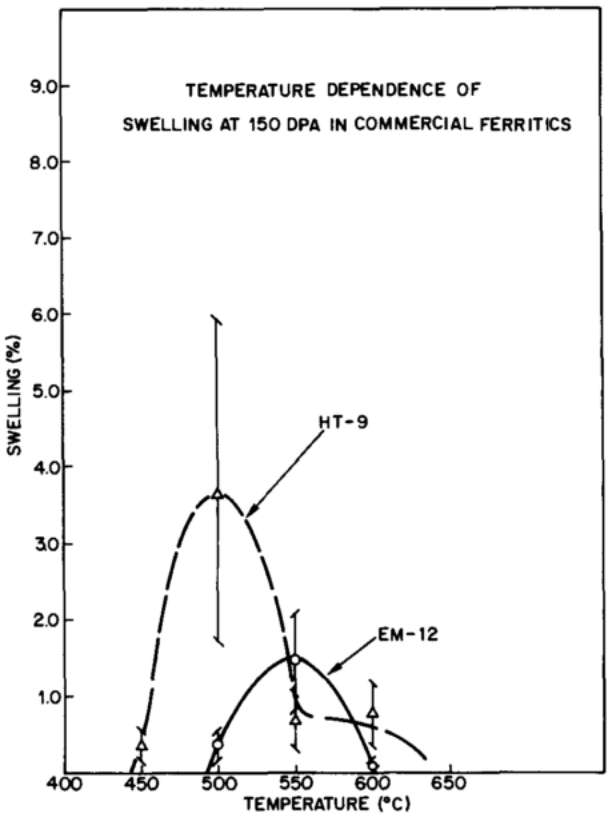

Figure 2.8: Temperature dependence of swelling at 150 dpa for EM-12 and HT9 [40].

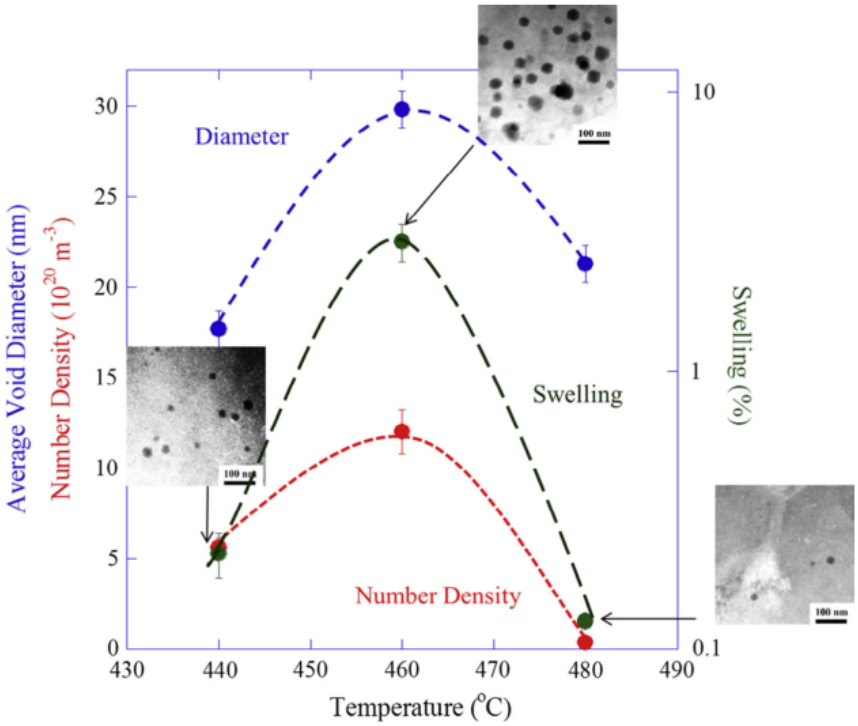

Figure 2.9: Temperature dependence of swelling, diameter and number density at 188 dpa for HT9 [42].

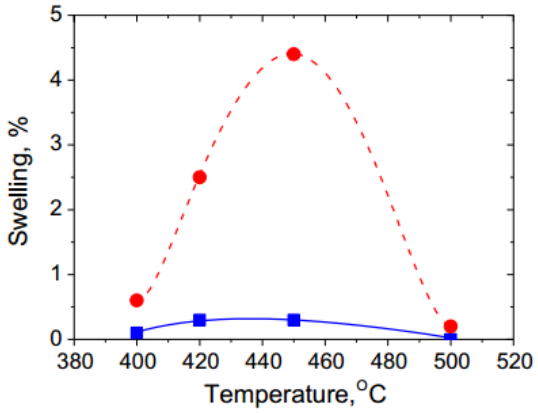

Figure 2.10: The temperature dependence of swelling is shown for MA957 at 500 dpa (red curve) and 100 dpa (blue curve) from [43].

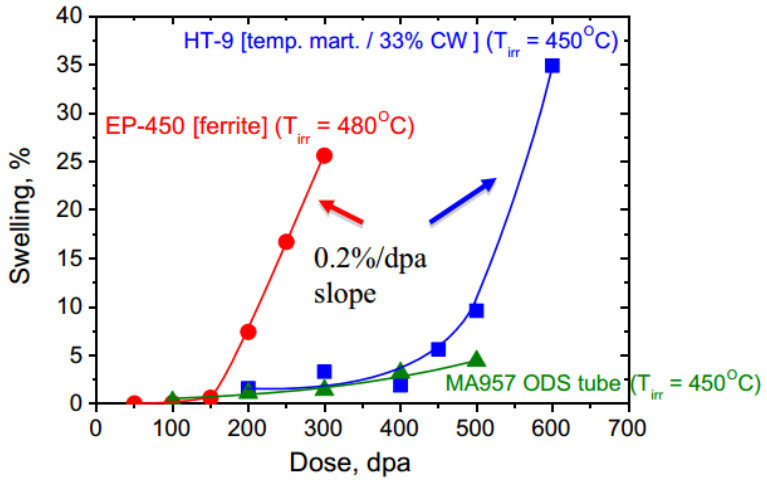

Figure 2.11: The swelling dependency for MA957, HT9 and EP-450 are shown through ~600 dpa from [43].

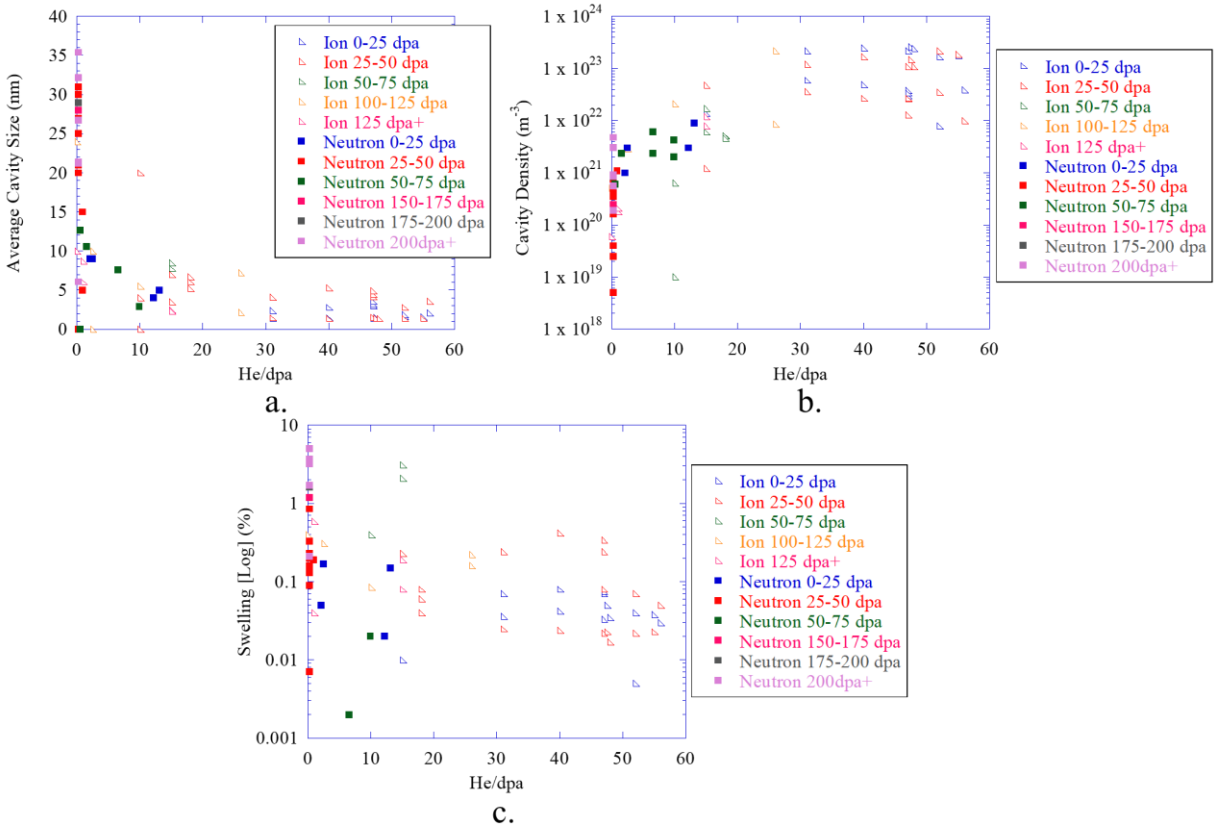

Figure 2.12: Compilation of literature data to show the effect of the helium/dpa ratio on (A) average cavity size, (B) average cavity density and (C) swelling from [90].

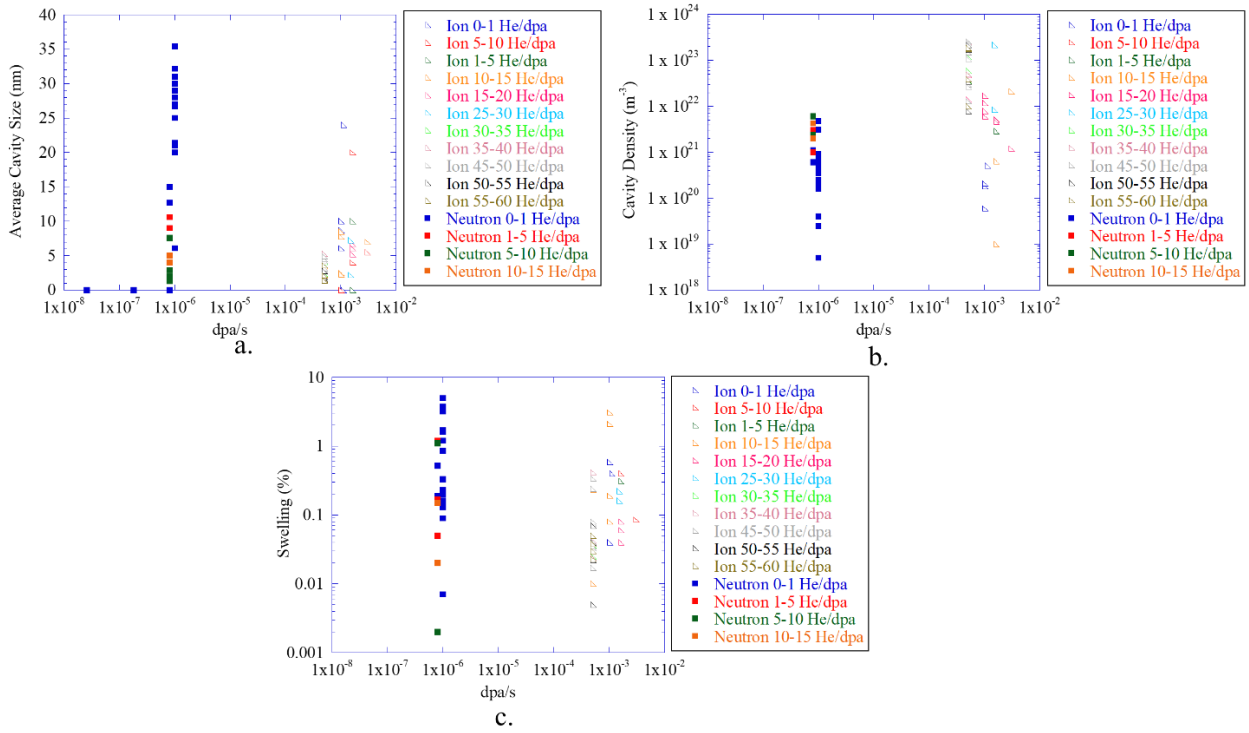

Figure 2.13: Compilation of literature data to show the effect of the damage rate on (A) average cavity size, (B) average cavity density and (C) swelling from [90].

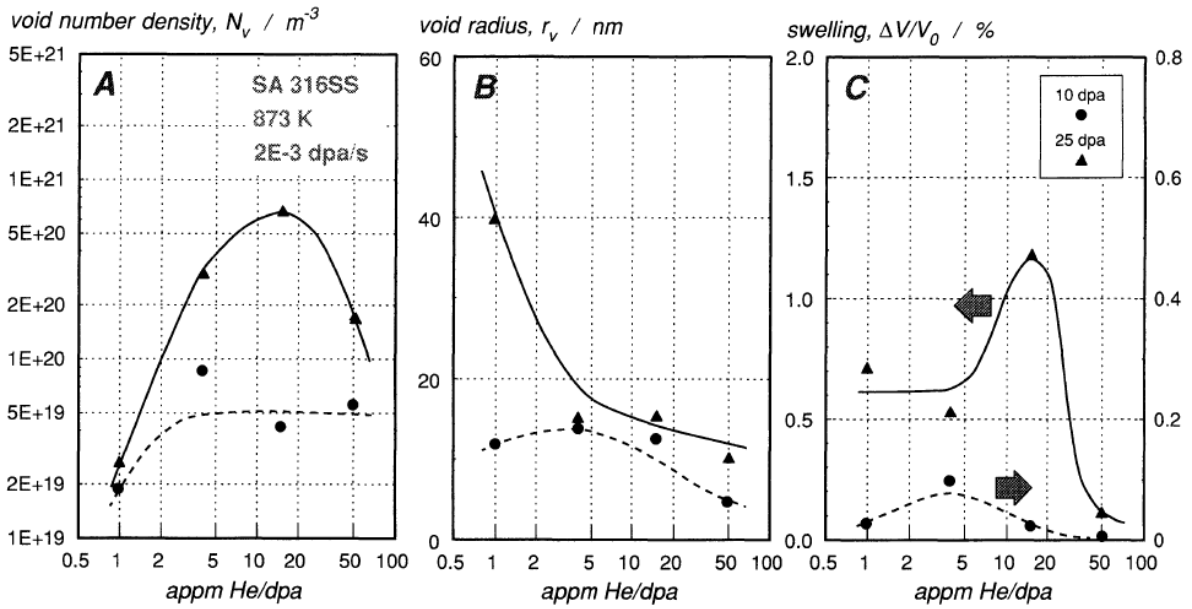

Figure 2.14: He/dpa dependence of (A) void number density, (B) mean void radius and (C) swelling in dual-ion irradiated 316 stainless steel from [53,54].

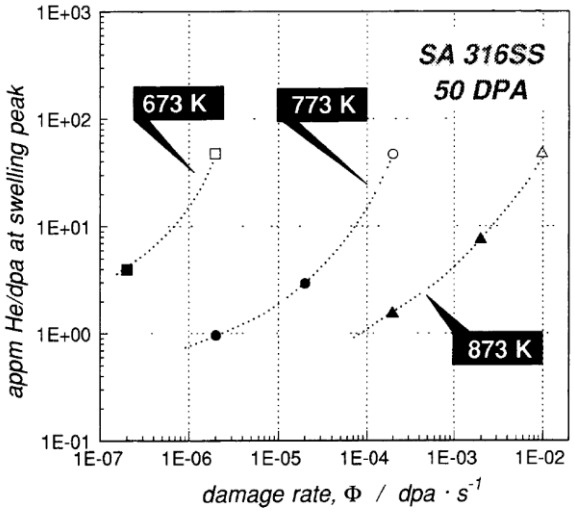

Figure 2.15: Predicted damage rate dependence of the He/dpa ratio at which peak swelling occurs from [53].

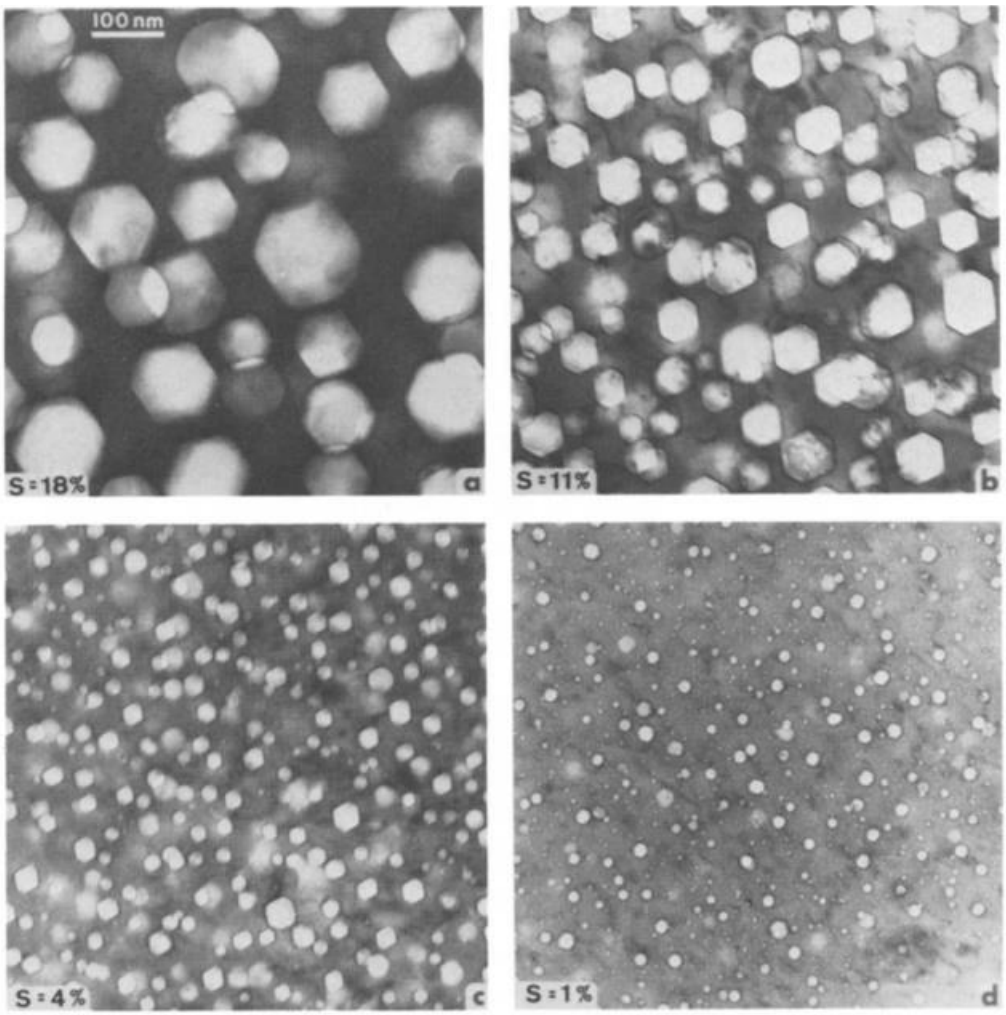

Figure 2.16: Void microstructure produced at 70 dpa at 627°C with (a) no helium, (b) co-injection, (c) pre-injection at 627°C and (d) pre-injection at room temperature [73].

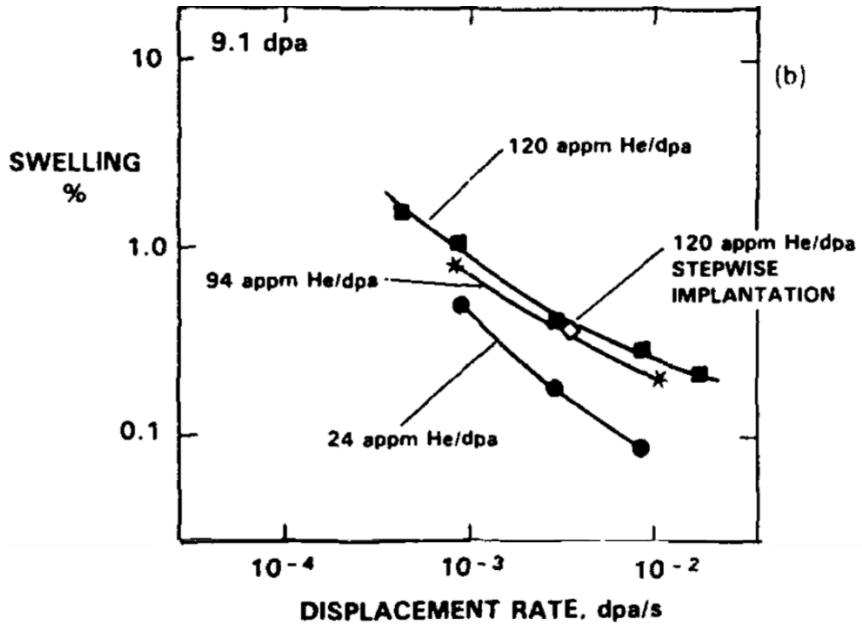

Figure 2.17: The influence of helium and displacement rate on nickel-ion induced swelling from [56].

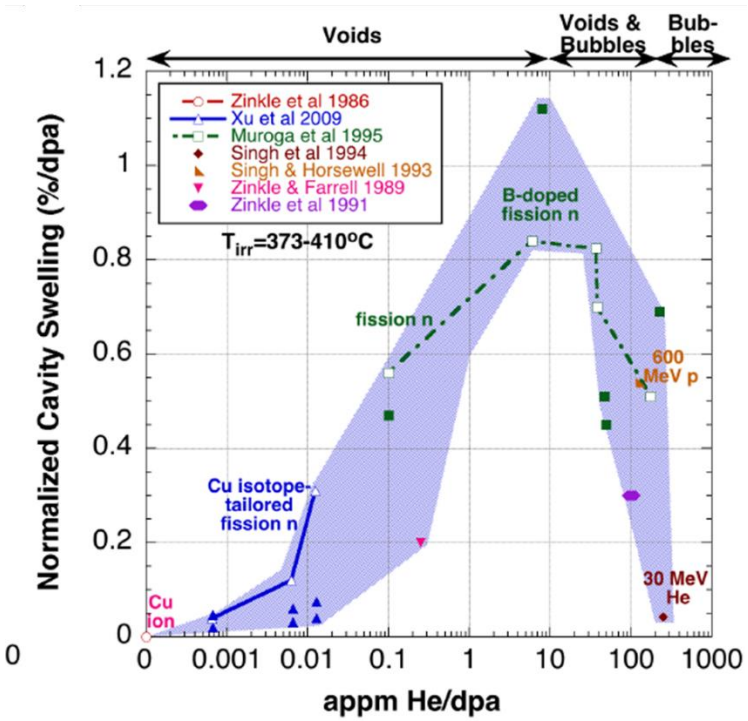

Figure 2.18: Normalized cavity swelling as a function of He/dpa ratio for copper irradiated between 373 and 410°C. Figure produced by S. Zinkle from [63,67–72].

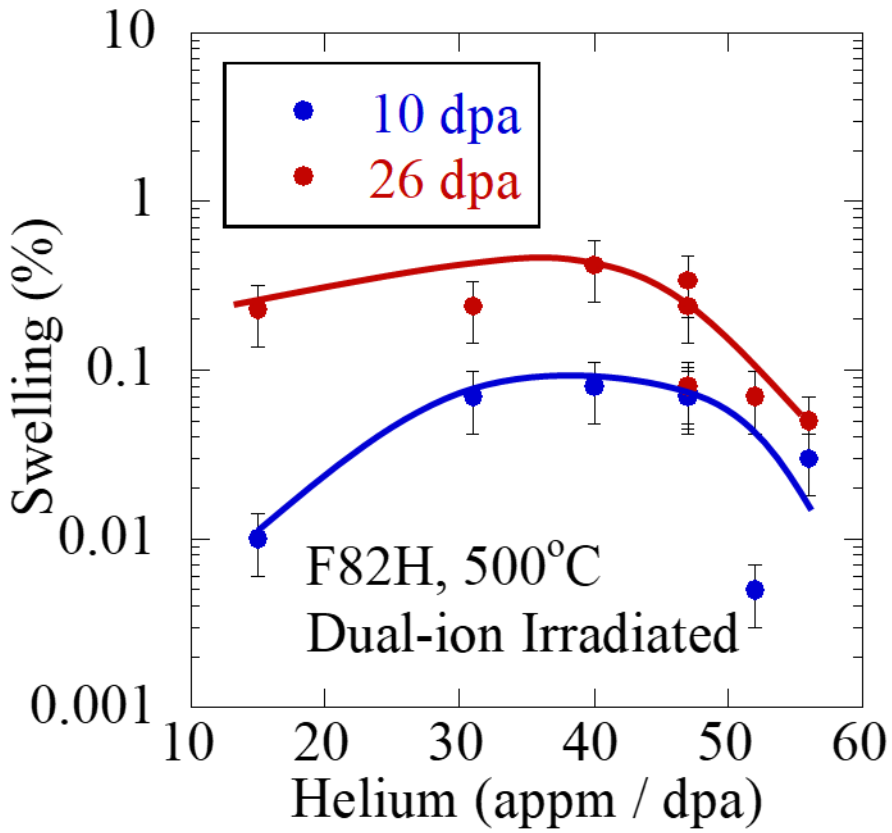

Figure 2.19: Swelling as a function of helium-to-dpa ratio for F82H under dual-ion irradiation at 500°C [49].

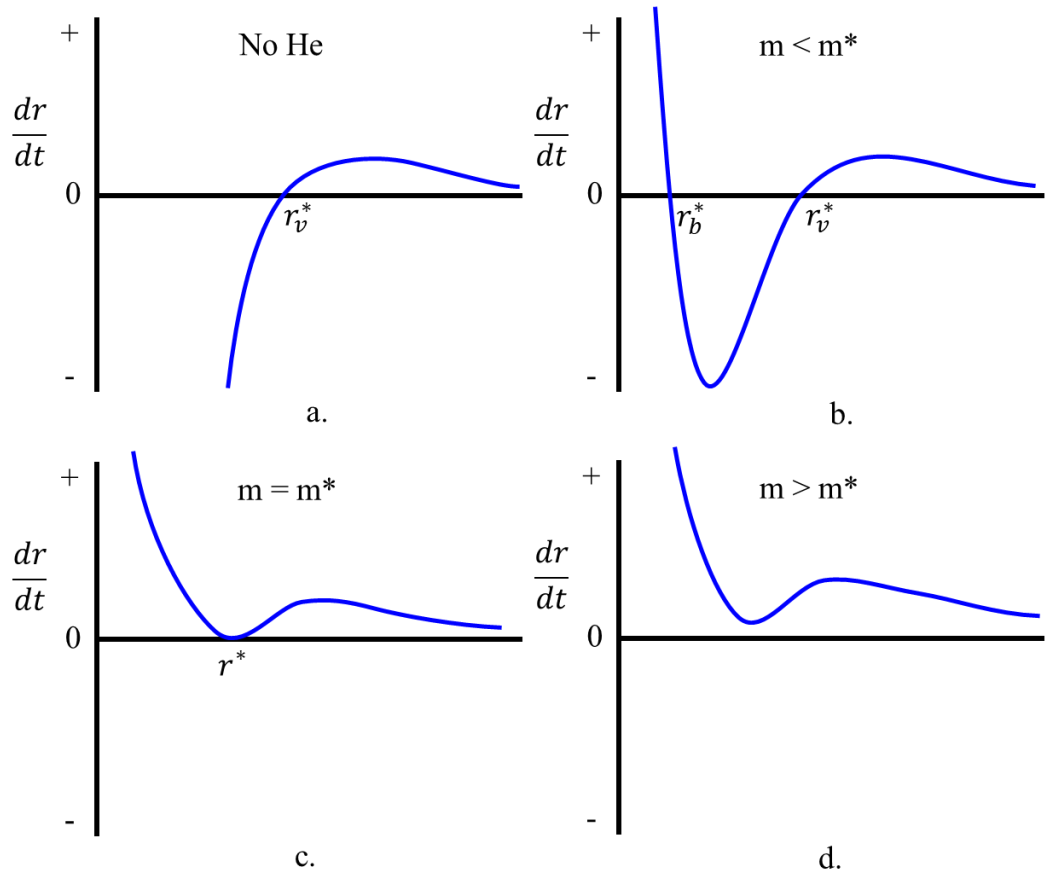

Figure 2.20: A schematic showing solutions to the cavity growth rate equation with (a) no helium, (b) less than the critical amount of helium (m < m*), (c) the critical amount of helium (m = m*) and (d) in excess of the critical amount of helium (m > m*) [90].

Chapter 3 Objective

The objective of this thesis is to understand the process by which swelling changes with helium content across a wide range of damage levels, and to use this knowledge to explain the difference in swelling behavior between pre-injected and co-injected irradiation.

The hypothesis is: *At lower damage levels before cavity growth becomes dominant, additional helium increases the rate at which cavities form which results in higher swelling. At higher damage levels during growth-dominated swelling, any amount of helium increases the bubble sink strength which reduces the cavity growth rate and suppresses swelling.* To test this hypothesis, a combination of ion irradiation experiments with careful characterization and computational modeling were used.

Two sub-objectives were identified as necessary to support the main objective. The first sub-objective required understanding how helium influences swelling at low damage levels. To answer this question, a series of experiments were performed in the laboratory with varying helium injection rates at low damage levels where swelling is still within the nucleation phase. Using the results from the experiments, bubble and void size distributions were collected to determine how they change with helium level. Specifically:

- The bubble density was used to determine the number of features that could transform into cavities.
- The cavity size distribution was collected to determine how many bubbles had transformed into cavities and the actual swelling.

- The critical radius for transition from a bubble to a cavity was collected to verify the expected effect of helium on bubble size
- The rate at which bubbles grow was estimated using the collected data to substantiate the effect of helium injection rate.

Putting all of this information together will demonstrate the effect of helium on swelling at low levels and provide an understanding of what is happening in the initial stages.

The second sub-objective was to understand how the cavities evolved and swelling changed as the damage level increased and swelling transitioned to a growth-dominated regime. A second set of well-designed experiments and modeling was used to determine this information. Of particular concern for understanding the changes in behavior as a function of helium injection rate were:

- The bubble size and density to determine the sink strength in the system
- The sink strength of other features in the microstructure to establish which features are the dominate sinks
- The rate at which cavities grow to establish differences with varying helium injection rates
- Total swelling as a function of helium level to understand establish that swelling is suppressed with increased helium

Once the full microstructure and swelling rates were known, it will be shown both experimentally and with a simple growth rate equation that increased helium retarded swelling at higher damage levels. Completion of these two sub-objectives will provide an explanation of the influence of helium on swelling across a range of damage levels, particularly during growth-dominated swelling behavior.

Chapter 4 Experimental Procedures

This chapter describes the experimental procedures used to in this work to prepare, irradiate and characterize the HT9 and T91 samples. The analysis framework for the cavity growth rate equation is also described.

4.1 Alloy and Sample Preparation

Alloys HT9, heat 84425, and T91, heat 30176 were used for this work. The compositions in weight percent are provided in Table 4.1. As discussed previously, HT9 is a nominally 12Cr ferritic-martensitic (FM) steel while T91 is a nominally 9Cr FM steel. Both are candidates for fast reactor applications because of their high resistance to cavity swelling. Each alloy had a slightly different heat treatment. HT9 was normalized at 1065°C for 30 minutes with subsequent air cooling to room temperature (RT) followed by tempering at 750°C for 30 minutes with subsequent air cooling to RT [92,93]. Several publications of data from this duct reflect different heat treatment parameters [5,26,92–96], but a proprietary certification from Carpenter verified that this was the correct heat treatment [97]. Alloy T91 was normalized at 1038°C for 30 minutes with subsequent air cooling to RT followed by tempering at 760°C for 30 minutes with subsequent air cooling to RT. These heat treatments resulted in a transformation from austenite to martensite laths with carbides forming primarily at the grain boundaries during the tempering step. Both materials exhibited traditional microstructure for tempered FM steels with prior austenite grain boundaries (PAGBs), packets, laths, coarse chromium carbides and network dislocations. HT9 have some retained δ-ferrite while T91 has fine V,Cr-nitrides.

Prior to irradiation, samples were cut from the archive duct material of HT9 into 1.5 x 1.4 x 18 mm Transmission Electron Microscope (TEM) bar specimens by electrical discharge machining (EDM). Similar bars were cut for T91 with dimensions of 1.5 x 1.5 x 20 mm bars, also using EDM. EDM is a machining process in which a voltage is applied between and electrode wire and the block of material resulting in a high frequency of sparks. These sparks typically cover a short distance of 10-100 nm and cause material removal near the wire, which is moved according to a pre-programmed path, resulting in precision on the order of 1 μm. The EDM process results in a sample without additional cold work which can be introduced through traditional machining techniques. In order to fit more samples within the irradiation area, the specimens were further cut in half for a final sample dimension of 1.5 mm x 1.4 mm x 9 mm for HT9 and 1.5 mm x 1.5 mm x 10 mm for T91.

After the samples were machined, they were polished starting with relatively coarse silicon carbide grinding paper, progressing to successively finer grits, proceeding to a diamond polish and culminating with electropolishing. The samples were mounted on a flat, aluminum disk with a thin layer of Crystalbond™ adhesive resin that melted using a hot plate. The bars for each irradiation were arranged in the center of the puck, side-by-side, as they would be on the irradiation stage. Additional bars of FM steel samples were added to either side of the irradiation samples as guide bars to both help ensure a flat sample surface and to provide weld spots for the thermocouples during irradiation. A flat surface is important to ensure good thermal contact between the samples and the stage during irradiation. After the samples were arranged, the disk was removed from the hot plate and the resin was allowed to cool. After the resin had fully cooled, the samples were wet polished by hand using Buehler® SiC paper beginning with #400 grit and working up to #4000

grit. The polishing direction was rotated 90 degrees between each grit step so that it would be easier to identify when the damage layer from the previous grit had been fully removed.

After polishing with #4000 grit on the back side (the surface that was not to be irradiated), the samples were then flipped over and the process was repeated for the opposite face. After reaching #4000 grit a second time, the samples were polished with successively finer diamond solutions starting with a 3 μm suspension, stepping down to a 1 μm suspension and finishing with a 0.25 μm suspension to produce a mirror-like finish. The samples were then removed from the disk by heating one last time. To remove any residual Crystalbond™, the samples were soaked in a beaker of acetone until all the adhesive had dissolved. The samples were then cleaned with methanol and ethanol before air drying.

The final step in sample preparation was to electropolish to remove any residual plastic deformation from the surface. Electropolishing was performed in a 1000 mL beaker containing 500 mL of a solution of 90% methanol and 10% perchloric acid. The beaker was immersed in a bath of methanol and dry ice to reduce the temperature to between -40 and -50°C. A square platinum mesh cathode was placed along the side of the beaker. Samples were electropolished for 20 seconds with an applied voltage of ~40V. A magnetic stir rod was rotated with a frequency of approximately 300 rpm to induce a circular flow with a vortex in the solution. The sample was immersed in the solution so that the face to be irradiated was facing the platinum mesh and the flow of the solution was parallel to the surface. This ensured that any oxygen bubbles would be carried away from the sample and reduce pitting of the surface. This procedure was estimated to remove approximated 2 μm of material based on the polishing curve presented in [98]. The final mechanical polishing step used 0.25 μm particles, so removal of 2 μm was considered sufficient

to remove any remaining plastic deformation. A schematic of the electropolishing setup is shown in Figure 4.1.

Because some of the irradiations of HT9 were performed before a solution to carbon uptake was identified, a coating of alumina was applied to the surface of one of the samples to prevent uptake. An atomic layer deposition (ALD) machine was used to deposit a coating with a thickness of 100 nm. ALD is a process for depositing thing films that utilizes sequential reactions of gaseous precursors to deposit thin films one atomic layer at a time.

For the deposition of alumina onto an FM steel, the steel samples on which the deposition were placed on a plate in the deposition machine. The chamber was then sealed and a series of pump and purge cycles were performed with argon. The samples were then heated to 150°C. After the temperature had stabilized, Trimethylaluminum (TMA, $Al(CH_3)_3$) was allowed into the chamber in a small burst. The TMA reacted with hydroxyl groups on the surface of the metal attaching the molecules to the substrate. The reaction for this part of the process was:

$$Al(CH_3)_3 + OH \rightarrow AlO(CH_3)_2 + CH_4, \quad \text{Eq. 4.1}$$

The TMA was then pumped out of the system before water was bubbled into the chamber. The water reacted with the methyl groups to produce more methane and new hydroxyl groups. The reaction for this step in the process was:

$$2\ H_2O + AlO(CH_3)_2 \rightarrow AlO(OH)_2 + 2\ CH_4, \quad \text{Eq. 4.2}$$

The water was then pumped out of the chamber and the process was repeated for approximated 980 cycles to achieve a film with a thickness of 100 nm.

4.2 Dual Ion Irradiations

For clarity, the ion irradiation campaigns will be divided into three different groups: the T91 irradiations in which the damage level and helium injection rate were systematically varied,

the HT9 irradiations at a single damage level with varied helium injection rates, and the HT9 irradiations at a single helium injection rate with increasing damage level. A total of twenty-three dual ion irradiation experiments were performed for this thesis: fifteen with T91 for a total of twenty different samples with varying damage levels and helium co-injection rates, and eight with HT9 for nine different samples with varying damage levels and helium co-injection rates. The T91 irradiation series was performed at damage rates of 7-8.5 × 10^{-4} dpa/s with helium injection rates of 0, 0.02, 0.2 and 4 appm He/dpa to damage levels of 17, 50 and 150 dpa for each helium condition. Additional irradiations were performed for the 0.02 appm He/dpa co-injection rate at 50, 100 and 150 dpa and for the 4 appm He/dpa co-injection rate at 50, 100 (twice), 150 and 200 dpa. The irradiations were performed incrementally, so some of the samples were on the same stage but irradiated to different damage levels. The first set of HT9 irradiations were performed at a damage rate of 6-9 × 10^{-4} dpa/s at 460°C to 188 dpa with 0, 0.06 and 4 appm He/dpa with one irradiation conducted to a total damage of 375 dpa by adding 187 dpa to the 0.06 appm He/dpa sample. For the second set of HT9 irradiations, the 4 appm He/dpa sample was taken up to 650 dpa at 460°C in increments starting at 350 dpa (162 dpa added to the 188 dpa) and increasing by 100 dpa per irradiation with a damage rate of 7-9 × 10^{-4} dpa/s. After the irradiations were performed, at least two TEM specimens were extracted for characterization of cavities. Table 4.2 summarizes the experimental details of the irradiations.

All of the irradiations were performed at the Michigan Ion Beam Laboratory (MIBL) at the University of Michigan using a dual-beam configuration [99]. Dual-beam irradiations were performed with the stage facing Beamline 4 such that the defocused 5 MeV Fe^{2+} heavy ion beam from the 3 MV NEC Pelletron accelerator was normal to the sample surface. Beamline 7 delivered a helium ion beam from the 1.7 MV General Ionex Tandem Accelerator and is 60° from BL4 in a

plane parallel to the floor. This system setup allowed for the performance of well-controlled experiments.

4.2.1 Irradiation System Setup

A multi-beam chamber (MBC) was used for all irradiations. The MBC was designed to provide a fixed intersection point for each of the three accelerators at MIBL. A schematic of the MBC is provided in Figure 4.2. A custom-built half-cylinder shape was chosen for the chamber to provide radially directed ports, allowing direct access to the irradiation stage for the accelerators and monitoring equipment and a flat back panel or easy access while minimizing chamber volume which is necessary to achieve high vacuum. Two back panels were made for the chamber with different angles for the 6" ConFlat flange for the stage port to allow the stage to face any of the beam lines. All of the irradiations for this work were performed with the stage facing beamline 4. Beamline 4 delivers an iron ion beam from the 3 MV Pelletron accelerator and is normal to the ion irradiation stage. BL7 delivers the helium ion beam from the 1.7 MV General Ionex Tandem Accelerator and it is 60 degrees from BL4 in the horizontal plane.

The MBC and the beamlines connected to it contain many diagnostic instruments to monitor the status and progress of the irradiation before, during and after the experiment. The pressure in the chamber is monitored using an InstruTech Inc. model IGM402 hot cathode ionization vacuum gauge. An Inficon Transpector® MPS Residual Gas Analyzer can be used to monitor the partial pressure of each gas species in the chamber. The chamber has also been equipped with an Evactron EP Series Plasma De-Contaminator to plasma clean the chamber. A double-walled Dewar for liquid nitrogen on top of the chamber connects to a copper frame that encircles to stage to act as a cold trap and anti-contamination device during irradiation [100]. The vacuum chamber pressure for each irradiation was maintained below 10^{-7} torr ($<1.3 \times 10^{-5}$ Pa).

The MBC also has several quartz windows to allow live viewing of the irradiation stage using a Nikon digital camera with connections through the internal laboratory network. A 2D FLIR® infrared thermal pyrometer is set up to view the stage through a germanium window. The pyrometer records the infrared emission from user-defined regions of interest on the sample at a rate of 3.125 Hz throughout the experiment. The pyrometer can cover a range of temperatures, but the most useful one for these experiments was 150 to 600°C. By using the thermocouples before the irradiation starts, the emissivity of the region can be calibrated, and the temperature can be monitored. All of these diagnostic tools provided digital outputs that were recorded and displayed using custom built LabView programs.

A slit aperture system was used on each beamline to define the irradiated area. The aperture system for each beamline consisted of four independently controlled and electrically isolated slits that could be moved into and out of the beam path (up to the middle of the beamline) via digital control. Since each slit was electrically isolated, the unsuppressed current from the slits could be measured individually throughout the irradiation. With this setup, the area of irradiation for each ion beam was defined by the geometry of the stage relative to the beamline. For the iron beam, since the plane of the stage was perpendicular to the beam direction, if 4 mm by 4 mm irradiation area was desired, both of the slits in the horizontal direction would be set to 2 mm from the center and both of the slits in the vertical direction would be set to 2 mm from the center of the beamline, resulting in the desired area. Since the helium beam was 60 degrees off from the normal to the sample surface in the horizontal direction, the calculations were slightly more complicated. The slits in the vertical direction would be set as normal, but the slits in the horizontal direction had to be corrected by the cosine of the angle between the beam and the stage normal. The results of this is that if the desired area was 10 mm by 10 mm, the horizontal slits would only be set to 2.5 mm

from the center of the beamline while the vertical slits would be set to 5 mm from the center for a total area of 10 mm by 10 mm. Furthermore, the 5 MeV Fe^{2+} beam had to be defocused such that it completely covered the area defined by the slit aperture with a maximum variation of 10%. Because scattering through the foil degrader was so significant, beam uniformity was not an issue for the helium ion beam.

The final piece of the system design is the irradiation stage which was used to hold the samples in place and provide the necessary heating and cooling to ensure a stable irradiation. A schematic of the stage is shown in Figure 4.3. The ion irradiation stage consisted of either a thermally conductive copper or nickel head attached to a stainless steel tube welded to a 6 inch ConFlat flange for use in sealing the chamber with the samples inside. The length of the stage was machined such that the sample surface would lie at the intersection of the beams traveling down the beamlines into the multi-beam chamber. The stage head had cooling air channels machined through it, a ½ inch diameter hole in the back for a resistive cartridge heater and two smaller holes for a thermocouple. A 0.25 mm thick piece of copper foil was placed on top of the stage head to enhance heat transfer between the stage and the samples. The samples and the guide bars were then aligned in the middle of the stage head on top of the copper foil with the side to be irradiated facing outward. Because the irradiation specimens were half bars instead of the typical full bars, a new hold down system was needed to ensure good thermal contact. This was achieved with a two-step process. First, a stainless steel shim was machined that covered more than half the length of the bar. This helped to exert pressure closer to the middle of the bars and make sure that they did not bow up when the hold down bars were tightened. The second step was to increase the width of the hold down bars so that more of the irradiated samples were covered, again helping to ensure that the samples stayed flat on the stage. Both the plate and the hold down bars were machined

with notches 1 mm in width and 1 mm apart to assist with alignment both while building the stage and after the stage had been mounted on the beamline. A picture of a typical irradiation stage is shown in Figure 4.4. Type J thermocouples were custom built for each irradiation using 0.05 mm diameter iron and constantan wires. The wires were threaded through ceramics to keep them from shorting, passed through the hold down bars to ensure that they would not interfere with the beam, and then spot-welded to the guide bars for temperature measurement. The other end of the wires was connected to a feedthrough which was then connected to the lab computer system for constant temperature monitoring. Once the stage was assembled, it stage was sealed to the MBC using a copper gasket and nuts and bolts. Once the stage was mounted both the resistive cartridge heater and the back thermocouple were inserted into the stage. The cartridge heater was about 4 centimeters long and 1 centimeter in diameter, with a temperature rating of up to 760°C. Cables from the computer readout were attached to the thermocouple feed through and the air lines were connected to provide cooling.

4.2.2 SRIM Damage and Helium Injection Calculations

The Stopping and Range of Ions in Matter (SRIM) [101] was used to provide depth-dependent estimations of the average damage caused by an ion, given the initial ion energy and the composition of the target material in atom percent. The SRIM damage calculations were performed using the quick Kinchin-Pease mode using the displacement energies for each element from Table 1 in ASTM Standard E591 [102]. A displacement energy of 40 eV was used for Fe, Cr, Ni, V, and Mn, a value of 60 eV was used for Nb and Mo, and a value of 90 eV was used for W. A displacement energy of 25 eV was used for all other elements. The composition presented in Table 4.1 was converted to atom percent for use in the SRIM calculation. The simulation was run for 100,000 ions to obtain smooth damage and injection curves with reasonable statistics

without excessive run times. Figure 4.5 shows the shape of both the damage profile and the injected interstitial profile as a function of depth for 5 MeV Fe^{2+} ions in HT9. (The profiles are similar in T91.) As the image clearly shows, the damage and injected interstitials vary widely across the depth. The damage level at 600 nm depth was used as the nominal damage for all irradiations in this work because this region is both far from the surface and the peak of the injected interstitial profile [103]. The damage rates calculated using SRIM for the experiments performed were 0.35 displacements / Å-ion for a 5 MeV Fe^{2+} ion beam. The damage rate from the energy degraded helium beam was determined to be orders of magnitude smaller than the damage rate for the 5 MeV Fe^{2+} ion beam, and therefore, considered negligible.

The SRIM damage rate was used to calculate the length of the irradiation for a given damage level. By making periodic beam current measurements and integrating over the time of the irradiation, an estimation of the total ion fluence was made. Using the estimated fluence, the damage level achieved in a given irradiation was calculated using the following equation:

$$dpa = \frac{(SRIM\ Damage\ Rate)\sum(ion\ beam\ current \times time)}{(Number\ Density)(Ion\ Charge)(Specimen\ Area\ Irradiated)}, \qquad \text{Eq. 4.3}$$

The helium calculations are more complicated due to scattering through the aluminum degrader foil. Using the measured thickness of the aluminum foil in the foil degrader in the multi-beam chamber, SRIM was used to calculate the energy, *E*, position vector in three dimensions, $\boldsymbol{r}$, a direction vector, $\boldsymbol{\varphi}$, in three dimensions for each ion exiting the foil and for each angle of foil rotation, $\boldsymbol{\theta}$, in one degree increments. Matlab was used to propagate each individual ion from the foil to the sample surface following the outputs from SRIM assuming no scattering occurred between the foil and the sample. This is a reasonable assumption because the multi-beam chamber was under high vacuum ($<10^{-7}$ torr). A schematic of this description is provided in Figure 4.6. The resulting "plume" of ions formed a curved distribution on the sample surface.

To ensure an even distribution of ions across the sample surface, the effects of raster scanning the beam were estimated. The plume of ions was copied and added to itself with a small change (0.5 mm) in the raster-scanned direction. This process was repeated until the entire raster-scanned distance along the x and y directions of scanning were covered. The same variation in position could be used to simulate a defocused beam passing through the foil. The position and direction of each ion were then rotated to correct for the difference between the original direction of the ion beam and the normal to the stage surface. For this setup, the helium beam was 60 degrees off from the normal to the irradiation stage. After this geometric adjustment, SRIM was used to calculate the injected distribution of the energy degraded ions for each angle of foil rotation. Although the foil can rotate to angles beyond 60 degrees, the desired ion range could be achieved within 60 degrees, and it avoided the possibility that the frame could block the beam. For the initial HT9 irradiations, there was a small error in the calculation of the losses of helium due to scattering through the foil which resulted in a non-uniform helium-to-dpa ratio as shown in Figure 4.7 with the damage rate and injected interstitial profile. This non-uniformity is not expected to impact the results in the area of interest 500-700 nm from the sample surface. As such, to limit potential artifacts from changing the helium profile, the same helium-to dpa profile was used for all HT9 irradiations. However, since the T91 irradiations will not be compared directly to the HT9 irradiations, the correct profile was used for all T91 irradiations as shown in Figure 4.8.

4.2.3 Running the Irradiation

Once the stage was mounted, the irradiation chamber was pumped down in stages, starting with an oil-free scroll pump. Once the pressure reached about 1×10^{-1} torr, the plasma cleaner was started to break down any residual hydrocarbons that might have been deposited in the chamber

or on the samples. Based on tests that had been performed previously, it was determined that running the Evactron EP Series Plasma De-Contaminator with a forward power of 15 W for 2 hours was sufficient to remove carbon from the surface of the samples. After the plasma cleaning had finished, the scroll pump continued pumping until the chamber pressure had dropped below 10^{-2} torr at which point, the scroll pump was isolated from the chamber and the gate valve to the cryopump below the chamber was opened. Once the pressure dropped below 10^{-6} torr, the gate valves to the beamlines were opened to provide additional pumping power. The chamber was then left to pump for at least 12 hours to achieve a pressure below 1×10^{-7} torr.

After confirming that the system was within the desired parameters for an irradiation, the slits were set to the desired area and the alignment of the stage was checked with a laser that was aligned down the path of beamline 4. The laser was mounted on the opposite side of a bending magnet from the chamber, near the accelerator. To diffuse the beam and simulate the effects of a defocused beam, a plastic film was placed between the laser and the quartz window on the magnet. The alignment of the stage was confirmed by ensuring that the image of the laser on the samples coincided with the desired irradiation area. Figure 4.9(a) shows an image of samples mounted on the beamline and aligned with the laser. Following laser alignment to the samples, a gridded piece of alumina was slid in front of the irradiation stage using a linear motion feedthrough. The alumina fluoresces when struck with ion beams and verified the alignment of the laser (Figure 4.9(b)) and the iron ion beam from beamline 4 (Figure 4.9(c)). The alumina piece is retracted prior to the start of the irradiation.

As the sources were started in preparation for the irradiation, the liquid nitrogen tank was opened to allow the cold trap to cool down. A series of automated valves and temperature sensors allowed the nitrogen to flow from the large Dewar into the small tank on top of the MBC. Once

the nitrogen was in the small Dewar, it would start to cool the entire copper assembly in the chamber. It took roughly two hours for the temperature to saturate, so the cold trap had to be started two hours prior to the planned start of the irradiation.

After the sources started outputting sufficient current, the iron beam was defocused to ensure uniform irradiation of the stage. The quadrupoles at the high energy end and the Einzel lenses at the low energy end were adjusted until the current variation was less than 10% across the entire irradiation area. To confirm that the beam was properly defocused, the slits were used to look at slices of the beam in both the horizontal and vertical directions. The first step was to close the slits in one direction down to 1 mm on either side and open the slits in the other direction outside of the desired irradiation area. The opened slits were then moved in 0.4 mm increments to measure the current change through the aperture. The process was repeated for both sides and both directions and the resulting differential current profile was examined to ensure that the variation was within acceptable limits.

After the beam had been defocused and the cold trap had cooled down, the stage was heated to the irradiation temperature. If the samples were fresh, they would have been outgassed previously to reduce the pressure spike as they were heated. If the samples had already been irradiated, no out-gassing was performed. In either case, the stage would be heated as quickly as possible to the irradiation temperature. For samples that could not be outgassed, this could lead to a short pressure spike to about 3-5 $\times$ 10^{-7} torr. The thermocouples and regions of interest were monitored closely during heat-up to ensure that the samples exhibited reasonably uniform heating behavior. The entire heat up process usually took about 15 minutes. As soon as the desired irradiation temperature was reached, the thermal imager was calibrated against the thermocouples for the areas of interest (AOI) by adjusting the emissivity of each AOI until the temperatures

agreed. In the thermal imaging program, a minimum of two AOIs were placed on each sample in the irradiated region and monitored for the duration of the experiment. Figure 4.10 shows a typical thermal image with AOIs on a heated irradiation stage. As soon as the pyrometer was calibrated, the Faraday cups were removed and the beams were allowed to hit the stage, starting the irradiation.

The experiment was monitored continuously while it was running to ensure that all the parameters stayed within specifications. All irradiations were conducted so as to maintain the sample temperature within 10°C of the desired irradiation temperature, and frequently, the 2σ value was less than 7°C. While the thermocouple was still monitored, the AOIs from the pyrometer were used to record accurate temperature throughout the experiment. The LabView^{TM} program interfacing with the FLIR was set to alarm if any of the AOIs deviated by more than the allowed value of 10°C from the target temperature. If fluctuations were observed, the voltage to the cartridge heater was adjusted to compensate and keep the temperature as close to the target temperature as possible. For a 5 MeV Fe^{2+} beam, only a small amount of beam heating was observed, ranging from 1-10°C depending on the ion flux. Similarly, the He^{2+} beam only added a small amount of beam heating, typically in the range of 1-2°C depending on the ion flux and the rotation of the thin foil energy degrader. The cooling lines for air flow were not typically used during the experiments since the heater cartridge could maintain a stable temperature on its own.

The pressure near the stage and in the beamlines was also monitored throughout the irradiation using the InstruTech Inc. model IGM402 hot cathode ionization vacuum gauges. A chamber pressure of 10^{-7} torr was set as the threshold for starting an experiment, but the initial heat up combined with putting the beam on the samples typically pushed the pressure into the mid-to-high 10^{-7} torr range. However, the pressure usually recovered quickly and was typically back

below 10^{-7} torr within an hour. It was important to always maintain the pressure below 10^{-6} torr during an irradiation to minimize the risk of oxidizing the samples.

The current for each ion beam was monitored continuously during the experiment by watching the current on the slits. As mentioned previously, the iron beam was defocused to have the beam fully cover the target sample area and hit the slits forming the aperture. Similarly, the helium beam was raster-scanned across the slits and aperture so that current was always visible on the slits. To get an accurate measure of the iron and He beam currents, a suppressed Faraday cup in the chamber was periodically inserted for each ion beam and the current was recorded. The time interval between measurements was typically 30-45 minutes. The Faraday cups for each beam had to be inserted simultaneously to get an accurate measurement as electrons emitted from the stage due to the beam would hit the back of the Faraday cup and cause a false reading. A continuous current measurement was not possible because the entire stage and irradiation chamber could not be isolated or suppressed. However, as mentioned previously, the current on the slits were continuously monitored to ensure the presence of beam, the alignment of the beam through the aperture and any significant changes in the current hitting the stage. If the balance on the slits changed, the bending magnet was used to realign the beam.

If at any point during the irradiation, the pressure, current or temperature were to exceed the limits of the experiment and could not be recovered within a timely manner (e.g., due to a power outage or source malfunction), the samples would be protected to ensure the integrity of the experiment. Typically, this meant that if the beam were lost for more than 5-10 minutes depending on the irradiation temperature, the heater would be turned off and the air lines would be opened. This would typically cool the samples to below 100°C within 10 minutes. Once the issue had been

resolved and the irradiation was ready to start again, the irradiation would be restarted following the same procedure as was followed to start it initially.

Once the target damage level had been achieved, the irradiation was complete. The irradiation was then terminated by blocking both of the ion beams with the respective Faraday cup, turning off the voltage to the heater and opening the air lines to rapidly cool the stage. The stage was cooled to room temperature and the chamber was left under vacuum to allow the liquid nitrogen to evaporate and the cold trap to warm up enough to avoid condensation when the MBC was vented.

4.3 Post Irradiation Characterization Methods

Following irradiation, the samples were removed from the stage for preparation for characterization. The electron transparent windows were produced using the focused ion beam (FIB) in-situ liftout method. The liftouts were then imaged using a combination of transmission electron microscopy (TEM) and scanning TEM (STEM).

4.3.1 TEM Specimen Preparation

Due to several factors, the focused ion beam (FIB) lift-out method is ideal for producing TEM samples. The shallow penetration depth of Fe^{2+} and He^{2+} ions (see Figure 4.7 and Figure 4.8) in dual ion irradiated FM steels means that there is little material that is actually damaged, and the material that is damaged lies near the surface. Additionally, FM steels are magnetic and large specimens, like a full 3 mm disc, would cause magnetic distortions in the electron beam during TEM imaging. The ability of the FIB liftout method to produce relatively small, cross-sectional slices of the material just microns into the surface addresses both of these problems.

The TEM foils were prepared using dual beam FIBs. These instruments utilize an electron beam (normal to a horizontal surface) for imaging, and a gallium ion gun (52 degrees from the

electron beam) for imaging and milling. The currents and energies of these beams can be varied according to the ideal conditions for the user. The ion beam typically operates at energies up to 30 keV and currents of up to tens of nA. Energies of 30 keV were used for most of the FIB lift-out process. The specific instruments used in this dissertation were a FEI Helios NanoLab DualBeam™ and a Nova NanoLab DualBeam™ at the Michigan Center for Materials Characterization $(MC)^2$ for all the samples.

The FIB liftout method was utilized as follows. The irradiated bar was mounted irradiated-side up using copper tape on an SEM mount and placed in the FIB chamber, which was then pumped down. The stage was tilted 52 degrees to be perpendicular to the ion beam. A random area of the sample was chosen within the irradiated region. The platinum gas injector needle was inserted, and the gallium beam was used to deposit a small layer of platinum on the targeted surface using a current of about 0.4 nA and an ion energy of 30 keV. Using a higher current of ~21 nA and the same energy of 30 keV, the gallium beam was used to create trenches using a regular cross section pattern about 4 microns deep on the long side of the platinum deposition. The long sides of the deposition were cleaned up using lower current (~7 nA followed by ~3 nA) and a cleaning cross section pattern. The stage was then tilted back to 7 degrees so that the gallium beam could make a U-shaped undercut at an angle of 45 degrees to the sample normal. The undercut was done on both sides of the samples so that the lamella was attached to the bulk of the specimen by two small pieces. A micromanipulator (called an Ominprobe™ needle) was inserted and slowly positioned such that it made contact with a corner of the platinum deposition. A small amount of platinum (approximately 1 μm^2) was used to weld the Omniprobe™ needle to the sample. The final connecting edges were then cut with the gallium beam to free the specimen from the metal bulk, and the Omniprobe™ needle was carefully lifted away with the lamella. The stage was then

carefully moved to the location of a mounted copper half grid with three posts. The needle with the attached sample was lowered into a position to either attach the lamella in the valley of a chevron post or cantilevered to the side of one of the posts. The gallium beam was used to weld the specimen to the post and then the needle was cut free from the sample and retracted from the chamber. The stage was then rotated 180 degrees to add additional platinum to the opposite side of the specimen. At this point, the specimen was still about 2 µm thick.

To achieve the target thickness of 100 nm or less, successive thinning needed to be done. The samples was tilted to 52 degrees and a current of 0.79 nA was used with the cleaning cross section pattern to create smooth surfaces. The current was then lowered to 0.43 nA and the pattern was placed within the platinum coating and using a milling depth of 0.5 µm to slowly produce two windows. The bar at the bottom of the resulting frame provided support for the liftout and reduced the chance that the liftout would fail due to twisting or bending. The sample was alternately tilted back and forth about 1.5 degrees to thin the sample in wedge shape. This method was used to minimize the amount of material milled from the top of the sample to preserve the surface while still thinning the entire specimen. The current was successively lowered as needed, while alternating the angle until the specimen was measured to be less than 200 nm thick using the SEM. The energy of the ion beam was subsequently reduced in successive steps of 5 keV and 2 keV to thin the foil to a final thickness of about 100 nm. The low energy milling was found to effectively eliminate TEM-visible damage induced by the FIB process at higher ion beam energies. The chamber was then vented and the grid with the sample was placed in a labelled membrane box for safe keeping. Figure 4.11 highlights the key steps summarizing the FIB lift-out process.

4.3.2 Cavity Imaging

Imaging of the TEM specimens in this thesis was performed using a JEOL 2100F CS-corrected Analytic Electron Microscope (AEM), a JEOL 2010F AEM and a Thermo Fisher Tecnai G2 F30 TWIN Electron Microscope at $(MC)^2$. The JEOL 2100F is a 200 keV microscope that operated mainly in STEM mode. The JEOL 2010F is a 200 keV microscope that could operate in either conventional TEM mode and STEM mode with a Gatan OneView 16-megapixel CCD camera capable of 4k resolution with 0.25 nm point to point resolution. The Tecnai G2 is a 300 keV microscope that is also able to operate in both TEM and STEM mode. All microscopes had the capability for XEDS using an EDAX® detector with EDAX® acquisition software. Additionally, a Gatan® Imaging Filter (GIF) allowed for the performance of electron energy loss spectroscopy (EELS) on the two JEOL microscopes. A software suite called DigitalMicrograph® was used to acquire the images. The TEM specimen was mounted on a Single-tilt or Double-tilt stage and inserted into the microscope.

To determine the size and density of cavities, imaging of the entire liftout was performed using STEM mode on the JEOL 2100F or the Tecnai G2, capturing high angle annular dark field (HAADF) images and a bright field (BF) image simultaneously. The contrast in the STEM HAADF images arises mainly from thickness and "Z-contrast," which is dependent on the effective atomic number of the material or spot on the liftout. Cavities, which lack both thickness and any atomic number appear as distinct, dark areas under these imaging conditions with well-defined boundaries. The HAADF images are typically free from contrast caused by dislocation networks and FIB damage allowing for accurate and convenient imaging of cavities. An example image of a typical HAADF image and its corresponding BF image is shown in Figure 4.12.

A standard procedure for consistent imaging of cavities across all samples was used for imaging cavities larger than 5 nm in diameter. Images were taken at approximately 100kx

magnification, which allowed for a field of view of around 1.4 μm × 1.4 μm. Successive images were taken along the length of the sample with minimal overlap until a complete set of HAADF and BF images covering the entire specimen were collected. In many cases, higher magnification images were taken to acquire a more detailed view of the smaller cavities and microstructural features. The point resolution for these images is about 0.68 nm [104].

Typically, conventional TEM (CTEM) images have been used to image cavities. In this work, CTEM BF images were collected to determine the size and density of cavities smaller than 5 nm in diameter using the 4k resolution of the Gatan OneView camera. A standard procedure for consistent imaging of these cavities across all samples was used. A series of underfocused and overfocused images were collected sequentially from a focus value of -2 μm to +2 μm in 0.5 μm steps. When the image is in focus, the cavities do not exhibit any noticeable contrast. In underfocused images, cavities appear as lighter features with a darker fringe around them, and in overfocused images, cavities appear as darker features with a lighter rim around them. However, the diameter of such small cavities is not reliable for focus values less than -1 μm or greater than +1 μm [105]. Therefore, the underfocused images collected closest to the focal value of +0 μm were used to estimate the size of a cavity and the remaining images were used to confirm the feature being measured was indeed a cavity. Example images of underfocused and overfocused cavities are shown in Figure 4.13. Images were taken at approximately 150kx magnification in CTEM mode, which allowed for a field of view of about 0.3 μm × 0.3 μm and a point resolution of 0.23 nm [104]. At least three areas centered at 600 nm from the surface of the TEM specimen were imaged per irradiation condition.

An attempt was made to use EELS measurements of the smaller features to estimate the concentration of helium within them. However, the small sizes of the features and the low quantity

of helium within them made it impossible to record a statistically significant signal from the helium atoms before carbon contamination overwhelmed the signal. Elastic recoil detection analysis (ERDA) and nuclear reaction analysis (NRA) with 3He ions were considered to measure the helium content in the sample. However, because the helium could not be correlated with any specific feature, the techniques were not used. Without the direct measurement of helium, a more traditional method was utilized to classify the cavities as either bubbles or voids. Cavities within the first peak of the bimodal distribution, typically less than 5 nm in diameter, were called bubbles to be consistent with existing literature. Cavities within the second peak of the bimodal distribution, typically greater than 5 nm in diameter, were called voids, again to be consistent with existing literature.

The thickness of the TEM specimen was measured using EELS (electron energy loss spectroscopy. This method estimated the thickness of the sample by measuring the amount of electron energy loss as the beam passed through the sample. The electron beam was set to a probe size of ~1 nm and the camera length was set to 2 cm (for a corresponding collection angle of about 32 mrad). A zero-loss spectrum was taken in an area of vacuum without going through the sample to calibrate the beam. Then an EELS spectrum map was taken on at least six areas of the sample (within the 500-700 nm depth region). The DigitalMicrograph® software included an algorithm to calculate the thickness by calculating the error in a logarithmic fit of the inelastic mean free path of the electrons through the sample. The error in this calculation is estimated to be around 10% [106]. The average of these thickness measurements taken from the EELS map was used as the nominal thickness of the TEM specimen.

4.3.3 Cavity Characterization

Characterization of the cavities after the images were taken was performed using a freely available image processing suit FIJI [107]. As mentioned previously, For each HAADF image, the cavities were counted and measured with the diameter and the position of the center of the cavities being recorded and stored separately from the image. During counting, the HAADF images were cross-referenced with the BF images to ensure that the cavities being counted were actually cavities and not precipitates, contrast from dislocations or other microstructural features. After the counting of an image was complete, the next sequential image was examined for any overlapping regions and marked to avoid double counting cavities in the overlapping regions. When the entire TEM specimen was counted, the resulting information was fed into a custom script written in MATLAB®. This script reads in the length of all counted regions (excluding the overlapped regions) to tally the total length of the specimen. The script also reads in the cavity diameter and position from the measurement files and sorts them into 100 nm depth bins, starting at the surface of the sample. Taking this length into account, the 100 nm depth of the bin, and the average thickness of the specimen, a total volume of the bin, V_{bin}, was calculated. The volume of each cavity was calculated assuming the cavity was a sphere. The sum of the volume of each cavity was tallied for each bin. This value was effectively the change in volume, ΔV, in the bin. Swelling was then calculated as the change in volume divided by the original volume. Therefore, the swelling of any particular depth bin could be expressed as the percentage:

$$\text{Swelling (\%)} = \frac{\Delta V}{V-\Delta V} = \frac{\sum_{j=1}^{N} \frac{4}{3}\pi r_j^3}{V-\sum_{j=1}^{N} \frac{4}{3}\pi r_j^3} \times 100\% = \frac{\sum_{j=1}^{N} \frac{4}{3}\pi r_j^3}{l*w*\delta-\sum_{j=1}^{N} \frac{4}{3}\pi r_j^3} \times 100\%, \qquad \text{Eq. 4.4}$$

where l is the length of the bin, w is the width of the bin, δ is the thickness of the TEM specimen, N is the number of cavities in the bin and d_j is the diameter of the jth cavity. For the nominal swelling value within the 500-700 nm depth region, the volume change calculation included cavities from both the 500-600 nm and the 600-700 nm depth bins. Average cavity diameter and

number densities were also determined as a function of depth. Additionally, a cavity size distribution with number density plotted as a function of size was also determined.

For the bubbles, typically smaller than 5 nm in diameter, on each underfocused BF CTEM image near the +0 μm focal point, the bubbles were counted and measured with the diameter of the bubbles being recorded and stored separately from the image. During counting, the underfocused BF images were cross-referenced with the overfocused BF images to ensure the features being counted were bubbles. After counting of an image was complete, the next sequential image was examined for any overlapping regions and marked to avoid double counting bubbles in the overlapping regions. When the entire image set for the TEM specimen was counted, the bubble sizes were collected into one file. The average bubble size from these images and number densities were also determined. The bubble size distribution with number plotted as a function of size was also determined and spliced into the cavity size distribution from the HAADF images to create size distributions for the full range of cavity sizes.

The sink strength of the total cavity size distribution was determined by summing over the size distribution with the following equation from [4]:

$$k_{cav}^2 = 2\pi \sum_{i=0}^{D} d_i N_i, \qquad \text{Eq. 4.5}$$

where N_i is the density of cavities of diameter d_i, and D is the maximum cavity size observed. Density bins in the size distribution were calculated with a resolution of 0.5 nm per bin from 0 to 5 nm and 1 nm per bin for cavities greater than 5 nm in diameter. An example of the results of depth profiling cavities from HAADF images with size, number density and swelling, along with the combined HAADF STEM and BF CTEM size distributions is shown in Figure 4.14.

4.3.4 Determination of Valid Region of Analysis

As seen in the SRIM profile in Figure 4.8, the damage rate changes as a function of depth, so the calculation of a damage level for a particular experiment is not straightforward. As mentioned previously, a depth of 600 nm in the SRIM profile was used as the nominal damage level for each experiment. This depth was chosen as it adequately avoids the effects of injected interstitials at the higher depths and avoids effects of the free surface. Zinkle and Snead [103] determined the valid depths of analysis for a Fe-10Cr system for 5 MeV iron ions which takes into account diffusion of interstitials from higher depths and the cavity-denuded surface effects. For the T91 system, which is close to the model system as a nominally Fe-9Cr alloy, at 150 dpa and 450°C, the valid depth regions remain within a range of 350 – 700 nm, which adequately avoids surface and interstitial effects. A similar depth range was determined as valid by Getto et al. [42] in HT9, and a similar process was utilized for the HT9 irradiations performed as part of this study. Thus, using a depth of 500-700 nm in the SRIM profile as the region of analysis avoids complicating artefacts from the shallow penetration depth of ion irradiation.

4.3.5 Error Analysis

For all conditions in this thesis, an effort was made to minimize the error due to counting statistics, to ensure the accuracy of the cavity size distribution measurements. The same error analysis presented in [97,98] is followed here. At least two TEM specimens for each condition were extracted, which was nominally equivalent to 2.5 μm^2 of material about 100nm thick (for the 500-700nm region). However, errors due to instrument limitations, such as TEM resolution needed to be considered. The two types of error that needed to be accounted for were error due to TEM resolution, and error due to EELS thickness measurements.

The resolution for the HAADF images taken was 0.7nm/pixel. This would mean that the error on each end of a measurement would be less than 1nm, regardless of the size of the

measurement. The error in the measurement of the size of the feature (cavity, precipitate, or dislocation), would then depend on the size of the measurement. The fractional error could then be represented for the STEM images by:

$$\mu_{res} = \frac{1nm}{L}, \quad \text{Eq. 4.6}$$

where *L* is the size of the measurement.

The resolution for CTEM BF underfocused and overfocused images was 0.07nm/pixel for the magnification used for imaging. However, the imaging resolution of the instrument for CTEM is 0.10 nm for lattice resolution and 0.25 nm for point-to-point resolution. Therefore, 0.25 nm was assumed to be the error in the CTEM BF measurements of cavities. The fractional error could then be represented for the CTEM BF images by:

$$\mu_{res} = \frac{0.25nm}{L}, \quad \text{Eq. 4.7}$$

where *L* is the size of the measurement. Figure 4.15 shows how the error due to TEM resolution changes as a function of cavity size. This measurement error would also contribute to any calculation which depends on the cavity size, such as the calculation of swelling.

As mentioned previously, the fitting of the EELS zero loss method exhibits an error of 10%. This thickness measurement affects the calculation of number density but is not dependent on any other factors. Therefore, error in number density at all times is estimated to be 10%. This is depicted as a flat line in Figure 4.15. The calculation of swelling includes both diameter and thickness measurements, therefore the contributions of error in both TEM resolution and EELS thickness measurements both contribute to the swelling error. Cavity swelling is directly proportional to the number density and proportional to the cube of the diameter, as shown below:

$$\frac{\Delta V}{V} \propto N_v \propto \left(\frac{d}{2}\right)^3. \quad \text{Eq. 4.8}$$

The propagation of error for multiplicative quantities and quantities raised to a power is shown below:

$$\mu_{mult} = \frac{\sigma_u}{u} = \sqrt{\left(\frac{\sigma_x}{x}\right)^2 + \left(\frac{\sigma_y}{y}\right)^2}, \quad \text{Eq. 4.9}$$

$$\mu_{power} = n * \left(\frac{\sigma_x}{x}\right), \quad \text{Eq. 4.10}$$

where *n* is the exponent in the original equation. For swelling, these two propagations can be combined, resulting in the following calculation for swelling error:

$$\mu_{swelling} = \sqrt{\left(\frac{\sigma_{N_d}}{N_d}\right)^2 + \left(n\frac{\sigma_d}{d}\right)^2} = \sqrt{\left(\mu_{N_d}\right)^2 + (3 * \mu_d)^2} \quad \text{Eq. 4.11}$$

where N_d is the number density, d is the cavity diameter, and μ_{N_d} and μ_d are the fractional errors in the number density and diameter respectively. The swelling error therefore depends on errors in the number density and diameter. The dependence of the error with swelling on cavity size is also shown in Figure 4.15.

It is also important to consider the high degree of inhomogeneity inherent to ferritic-martensitic steels. Grain-to-grain variation in the microstructure contributes additional uncertainty to the swelling measurements, as cavity nucleation and growth can vary extensively in adjacent grains. To minimize this uncertainty, multiple TEM specimens were extracted for each condition from different regions of the irradiated sample. At least two TEM specimens were made per condition, encompassing an area of approximately 2.5 μm^2, with foil thicknesses less than 100 nm.

4.4 Numerical Solutions to the Cavity Growth Rate Equation

Before discussing the results of the irradiation experiments, it is helpful to describe the theoretical framework to be used in the analysis. Many aspects of cavity formation and growth have been modeled approximately using the simple cavity growth rate equation and the critical bubble model (CBM) concept [88,89] as described in Section 2.4.6:

$$\frac{dr}{dt} = \frac{\Omega}{r}\left[D_v C_v - D_i C_i - D_v C_{v,T} \exp\left(\frac{2\gamma}{r} - p_g\right)\right]. \quad \text{Eq. 4.12}$$

The cavity growth rate equation depends on several parameters from the microstructure, the irradiation conditions, and the material properties. Determination of the cavity growth rate involves two principle calculations: 1) the steady state point defect concentrations, and 2) the helium gas pressure inside a cavity. To calculate the point defect concentrations a standard rate equation for the change in defect concentration of either interstitials and vacancies with time was used from [38]:

$$\frac{dC_{(i,v)}}{dt} = K_0 - K_{iv} C_i \left(C_v + C_{v,T}\right) - K_{(i,v)s} C_{(i,v)} C_s. \quad \text{Eq. 4.13}$$

The first term on the right side of the equation is the production rate of defects, K_0,. The second term, $K_{iv} C_i \left(C_v + C_{v,T}\right)$, is the loss of the point defects due to mutual recombination and includes the loss of interstitials recombining with thermally produced vacancies. The final term in the equation is the loss of point defects to sinks and is dependent on the concentration of sinks, C_s, the concentrations of point defects, and the interaction rate for either interstitials or vacancies with sinks, $K_{(i,v)s}$. To input the measured sink strengths of the microstructure, the point defect rate equations can be rewritten as:

$$\frac{dC_{(i,v)}}{dt} = K_0 - K_{iv} C_i \left(C_v + C_{v,T}\right) - k^2_{(i,v)} D_{(i,v)} C_{(i,v)}, \quad \text{Eq. 4.14}$$

where $k^2_{(i,v)}$ is the sink strength for either vacancies or interstitials and $D_{(i,v)}$ is the diffusion coefficient for the respective point defect.

The recombination parameter for defects was taken from [38]:

$$K_{iv} = \frac{z_{iv} \Omega (D_i + D_v)}{a^2},\ z_{iv} \sim 500, \quad \text{Eq. 4.15}$$

where z_{iv} is the combinatorial factor, Ω is the atomic volume, and a is the lattice parameter.

The sink strengths for interstitials and vacancies will be calculated for each irradiation condition using the microstructure measured in Chapter 5 . For each specie, the total sink strength is the sum of the sink strengths of the individual measured sinks:

$$k_v^2 = k_{dis}^2 + k_{cav}^2 + k_{gb}^2, \quad \text{Eq. 4.16}$$

$$k_i^2 = k_{dis}^2(1 + bias) + k_{cav}^2 + k_{gb}^2, \quad \text{Eq. 4.17}$$

where the sink strengths are calculated by:

$$k_{cav}^2 = 4\pi r_{cav}\rho_{cav} = \sum_j 4\pi r_{cav,i}\rho_{cav,i}, \quad \text{Eq. 4.18}$$

$$k_{dis}^2 = 2\pi r_{dis}\rho_{dis} = \sum_j 4\pi r_{dis,i}\rho_{dis,i}, \quad \text{Eq. 4.19}$$

$$k_{gb}^2 = \frac{24}{d_{gb}^2}, \quad \text{Eq. 4.20}$$

where r is the radius of the respective feature, ρ is the density of the respective feature and d_{gb} is the effective diameter of a grain.

The diffusion of interstitials and vacancies was assumed to have an Arrhenius dependence:

$$D_{i,v} = \alpha_{i,v}\omega_{i,v} exp\left(\frac{-E_m^{i,v}}{kT}\right), \quad \text{Eq. 4.21}$$

where α is 1/6 for interstitials and 1 for vacancies, ω is the jump frequency for either vacancies or interstitials, k is the Boltzmann constant, T is the temperature, and E_m is the migration energy for the point defect specie.

Finally, the thermal vacancy concentration was estimated using:

$$C_{v,T} = \frac{1}{\Omega} exp\left(\frac{S_f}{k}\right) exp\left(\frac{-E_f^v}{kT}\right), \quad \text{Eq. 4.22}$$

where S_f is the entropy of formation, and E_f^v is the vacancy formation energy. The thermal interstitial concentration was assumed to be negligible.

All of the previously described equations were used with the time derivative in Eq. 4.14 set to zero to solve for the steady state concentration of interstitials and vacancies using a numerical

solver in MATLAB®. The dislocation bias for interstitials has been reported in literature in the range of 1% to 25% using analytic solutions [108–111] and 1 to 5% using rate theory approaches [94,112–115]. A value of 5% was chosen for this analysis to include the largest effect in the range of both approaches.

Table 4.1: Chemical Composition (wt%) of HT9, heat 84425, and T91, heat 30176 [94,116].

	Fe	Cr	Mn	Nb	Mo	Ni	Si	V	C	N	Al	S	P	Ti	Cu	W
HT9	Bal.	11.8	0.50		1.03	0.51	0.21	0.33	0.21	0.006	0.03	0.003	0.008	<0.01		0.24
T91	Bal.	8.76	0.44	0.086	0.86	0.10	0.25	0.23	0.091	0.052	0.0004	0.002	0.007	0.003	0.062	0.004

Table 4.2: Experimental details for ion irradiations conducted as part of this thesis.

Date of Completion	Material	Damage Level (Quick Kinchin-Pease dpa)	Temperature (°C)	Damage Rate (dpa/s)	Helium Co-injection Rate (appm He/dpa)	He Injected (appm He)
May 13, 2017	T91	17	445	7.0×10^{-4}	0	0
May 15, 2019	T91	50 (17 + 33)	445	7.1×10^{-4}	0	0
Aug. 15, 2019	T91	150 (50 + 100)	445	8.0×10^{-4}	0	0
Oct. 21, 2019	T91	17	445	7.6×10^{-4}	0.02	0.34
Nov. 14, 2019	T91	50 (17 + 33)	445	7.8×10^{-4}	0.02	1
Dec. 20, 2019	T91	150 (50 + 100)	445	8.0×10^{-4}	0.02	3
		100				2
Feb. 24, 2020	T91	150 (100 + 50)	445	7.7×10^{-4}	0.02	3
		50				1
Dec. 7, 2018	T91	17	445	7.2×10^{-4}	0.2	3.4
May 23, 2019	T91	50 (17 + 33)	445	7.8×10^{-4}	0.2	10
Aug. 6, 2019	T91	150 (50 + 100)	445	8.0×10^{-4}	0.2	30
Sep. 9, 2019	T91	17	445	8.0×10^{-4}	4	68
Sep. 19, 2019	T91	50 (17 + 33)	445	8.0×10^{-4}	4	200
Dec. 14, 2019	T91	150 (50 + 100)	445	8.2×10^{-4}	4	600
		100				400
Jan. 17, 2020	T91	150 (100 + 50)	445	7.8×10^{-4}	4	600
		50				200
Feb. 28, 2020	T91	200 (150 + 50)	445	8.3×10^{-4}	4	800
		100 (50 + 50)				400
Oct. 21, 2016	HT9	188	460	8.4×10^{-4}	0.06	11.28
May 17, 2017	HT9	188	460	7.5×10^{-4}	0	0
Dec. 19, 2016	HT9	188	460	6.4×10^{-4}	0.06	11.28
		375				22.5
Apr. 3, 2017	HT9	188	460	8.6×10^{-4}	4	752
Jan. 15, 2018	HT9	350	460	7.7×10^{-4}	4	1400
Apr. 16, 2018	HT9	450	460	8.2×10^{-4}	4	1800
Jul. 27, 2018	HT9	550	460	7.2×10^{-4}	4	2200
Mar. 5, 2019	HT9	650	460	8.5×10^{-4}	4	2600

Table 4.3: Table of input parameters for calculating the cavity growth rate equation.

Parameter	**Value**	**Reference**
Temperature, T	Input parameter	This work
Damage Rate, K_0	Input parameter	This work
Helium Co-Injection Rate	Input parameter	This work
N	8.34×10^{22} at/cm^3	[10]
Lattice parameter (a)	0.288 nm	[10,97]
Sink strength	From microstructure	This work and [90]
ω_i	2.9×10^{12} s^{-1}	[10]
ω_v	1.6×10^{13} s^{-1}	[10]
Γ	1.75 J/m^2	[97]
E_{vm}	0.63 eV	[97]
E_{vf}	1.6 eV	[10]
E_{im}	0.35 eV	[10]
S_f	2.17k	[38]
Dislocation Bias	5%	See text.

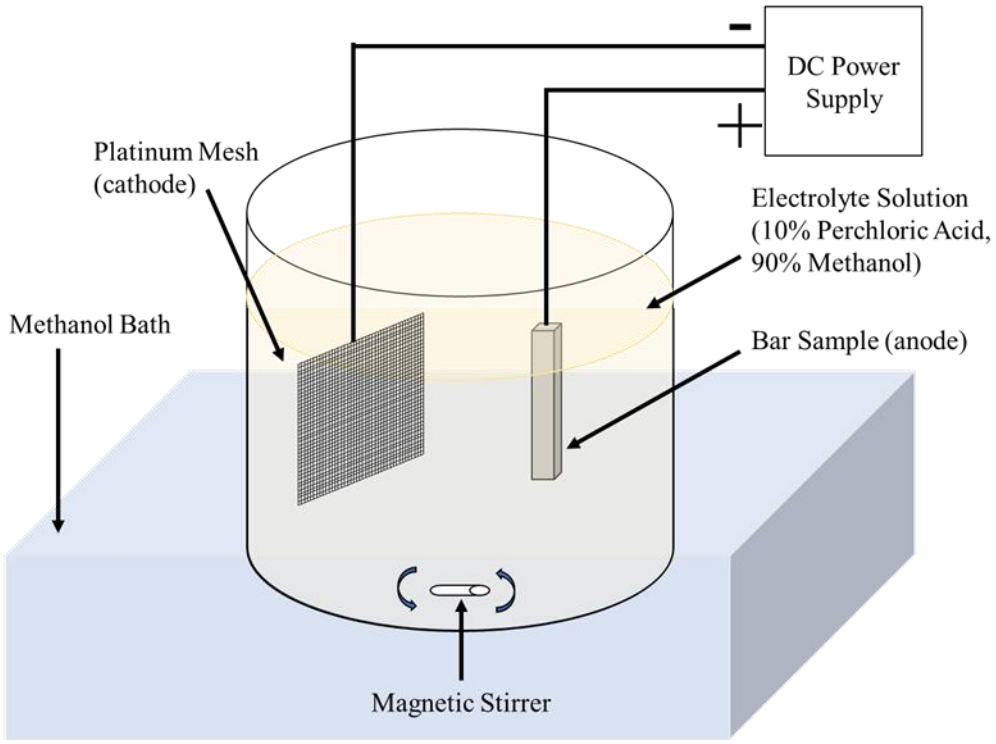

Figure 4.1: A schematic of the electropolishing setup [90].

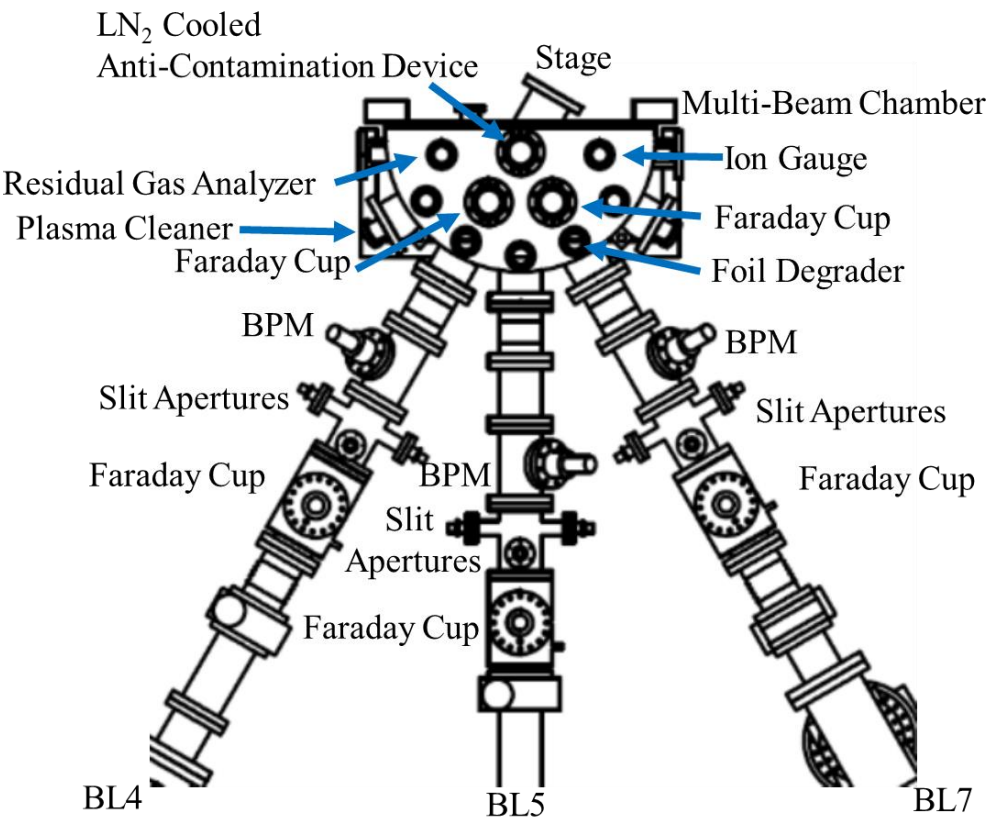

Figure 4.2: Multi-beam chamber with connecting beamlines. Each beamline is equipped with Faraday cups to record the ion beam current, slit apertures to define the irradiation area and a beam profile monitor (BPM) to assess the beam shape [99].

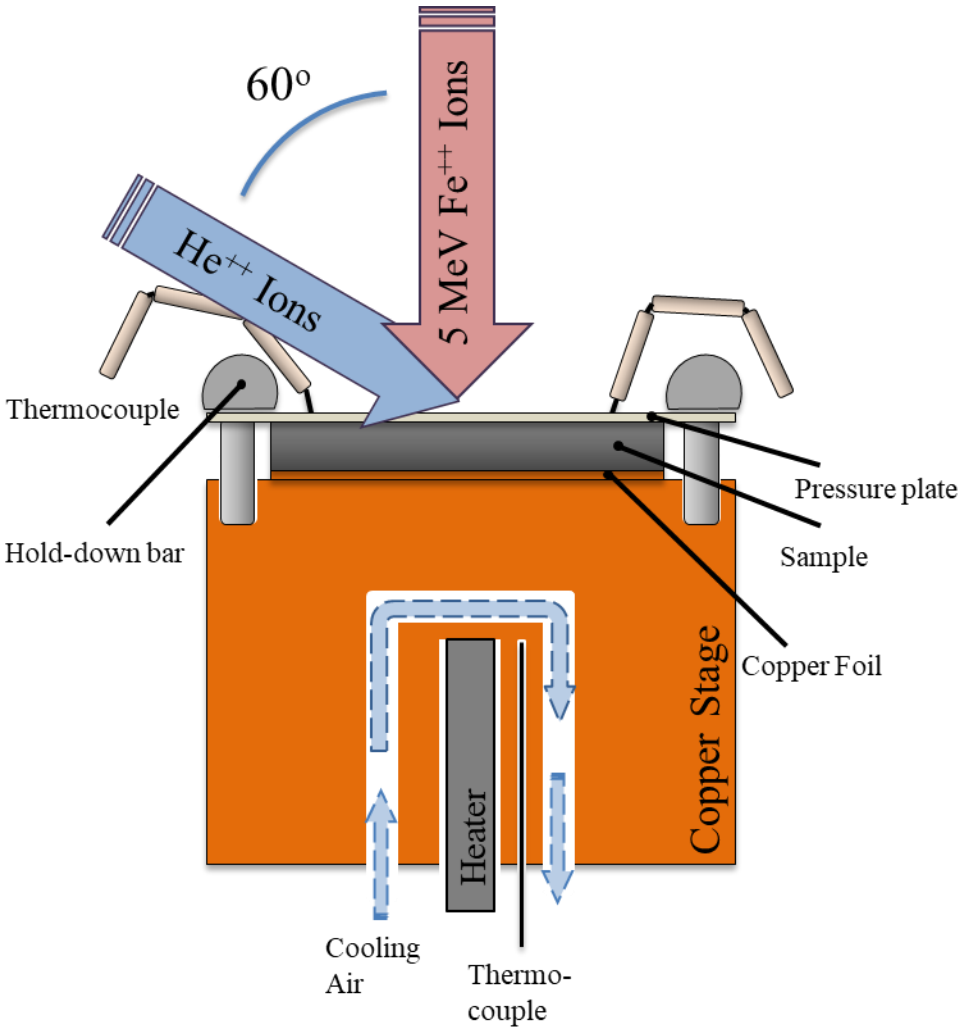

Figure 4.3: Schematic drawing of the stage used for dual ion irradiation in this work.

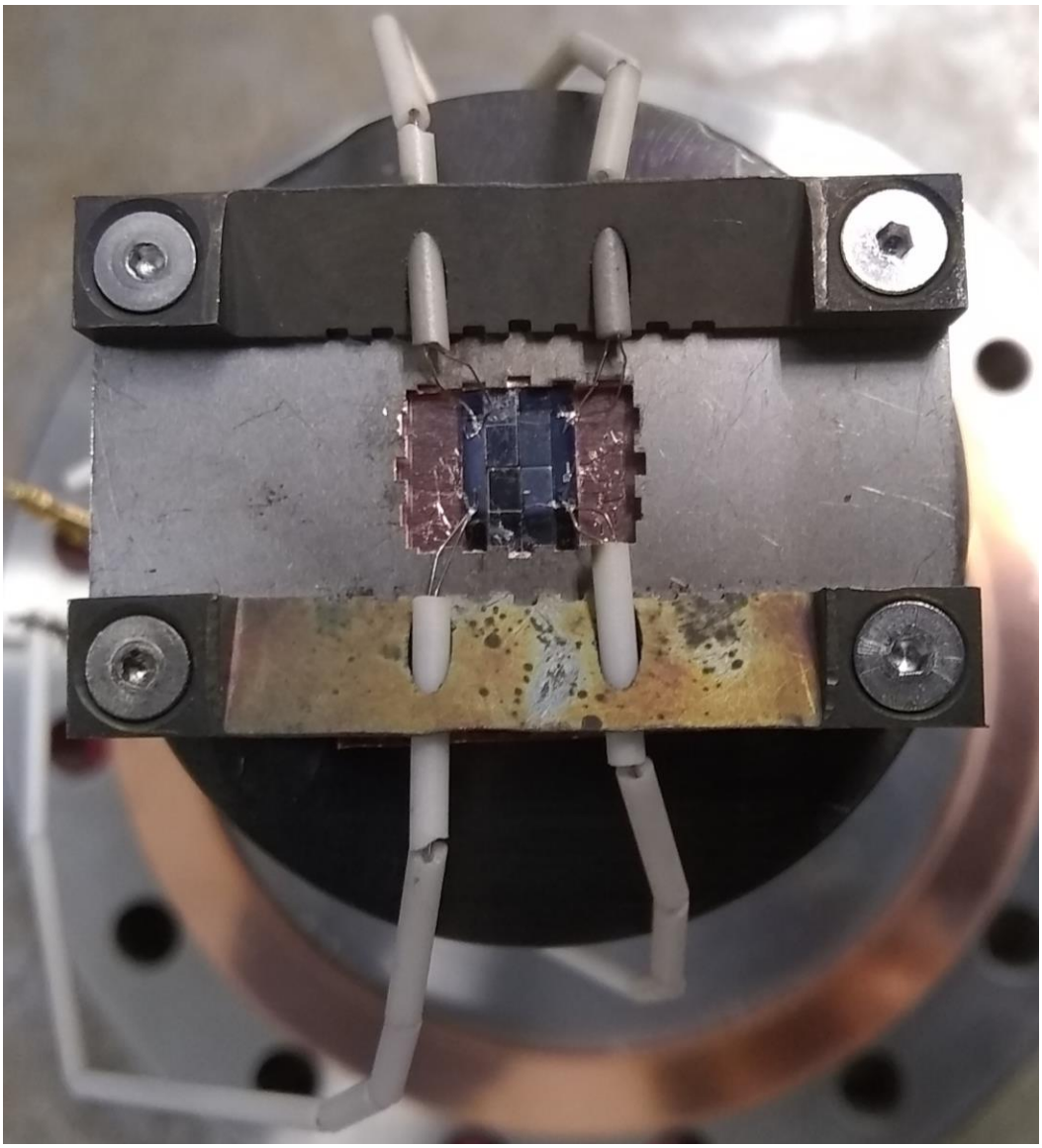

Figure 4.4: A picture of a fully assembled dual-ion irradiation stage.

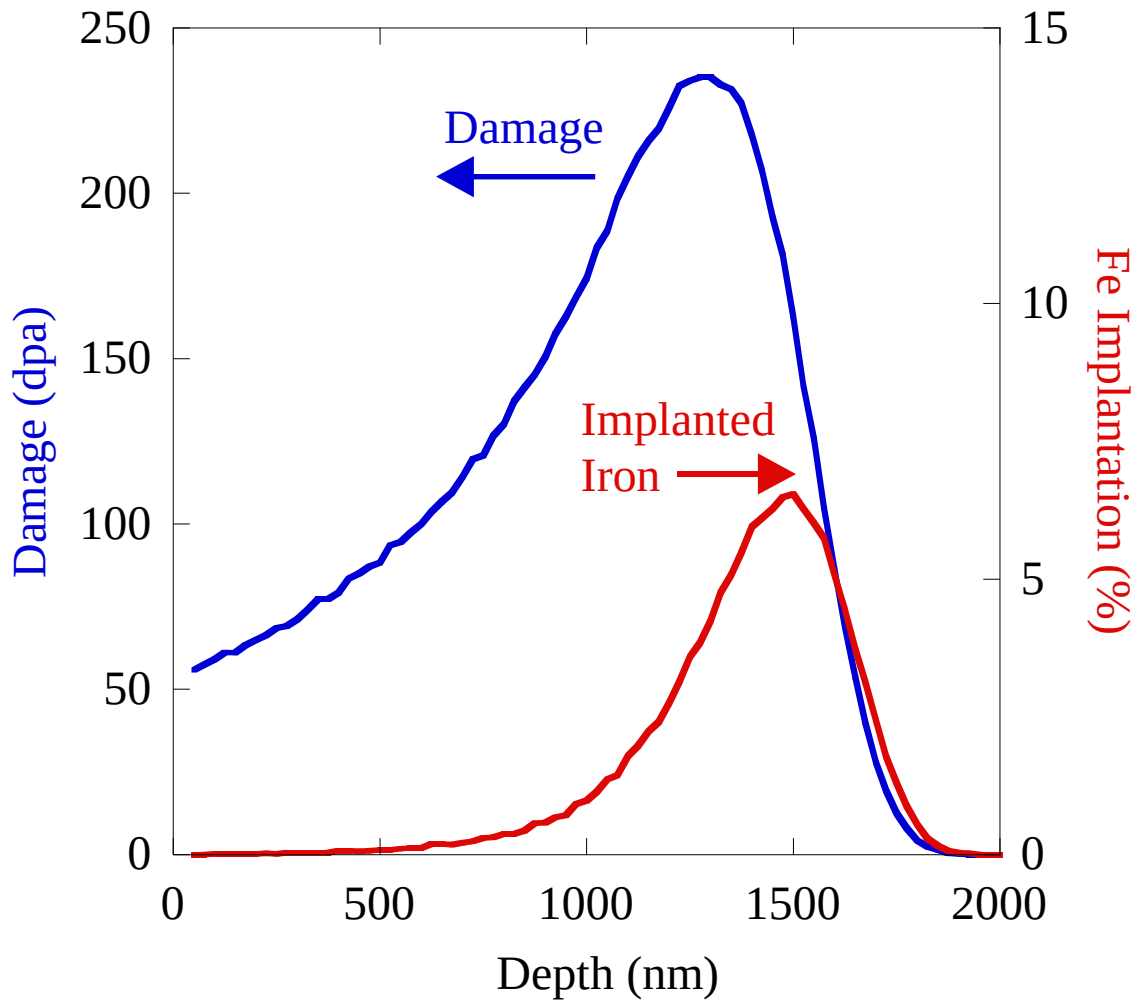

Figure 4.5: The damage profile and injected ion concentration as a function of depth for 5 MeV Fe^{2+} in HT9 as calculated by SRIM for a damage level of 100 dpa at 600 nm from the surface.

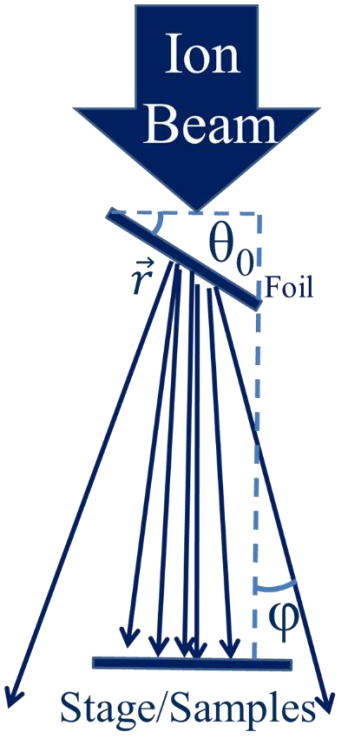

Figure 4.6: A schematic of the foil degrader geometry considered for SRIM based calculations based on the foil rotation angle, $\boldsymbol{\theta}$, position of the ions after degradation, $\boldsymbol{r}$, and direction of the ions relative to the original trajectory, $\boldsymbol{\varphi}$ [90].

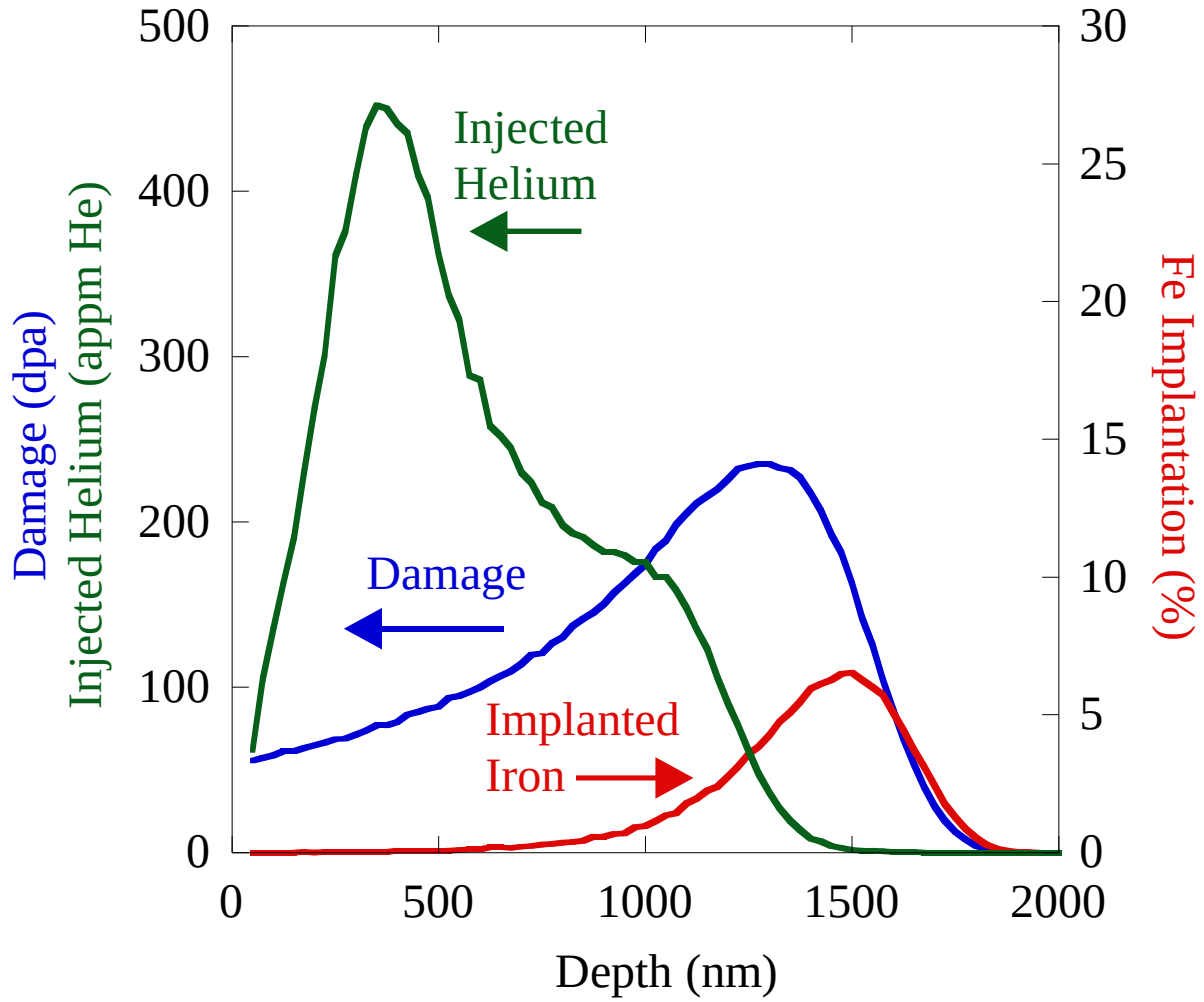

Figure 4.7: The helium injection profile, damage profile and injected ion concentration as a function of depth for 5 MeV Fe^{2+} in HT9 as calculated by SRIM for a damage level of 100 dpa at 600 nm from the surface for 4 appm He/dpa with a non-uniform helium-to-dpa profile.

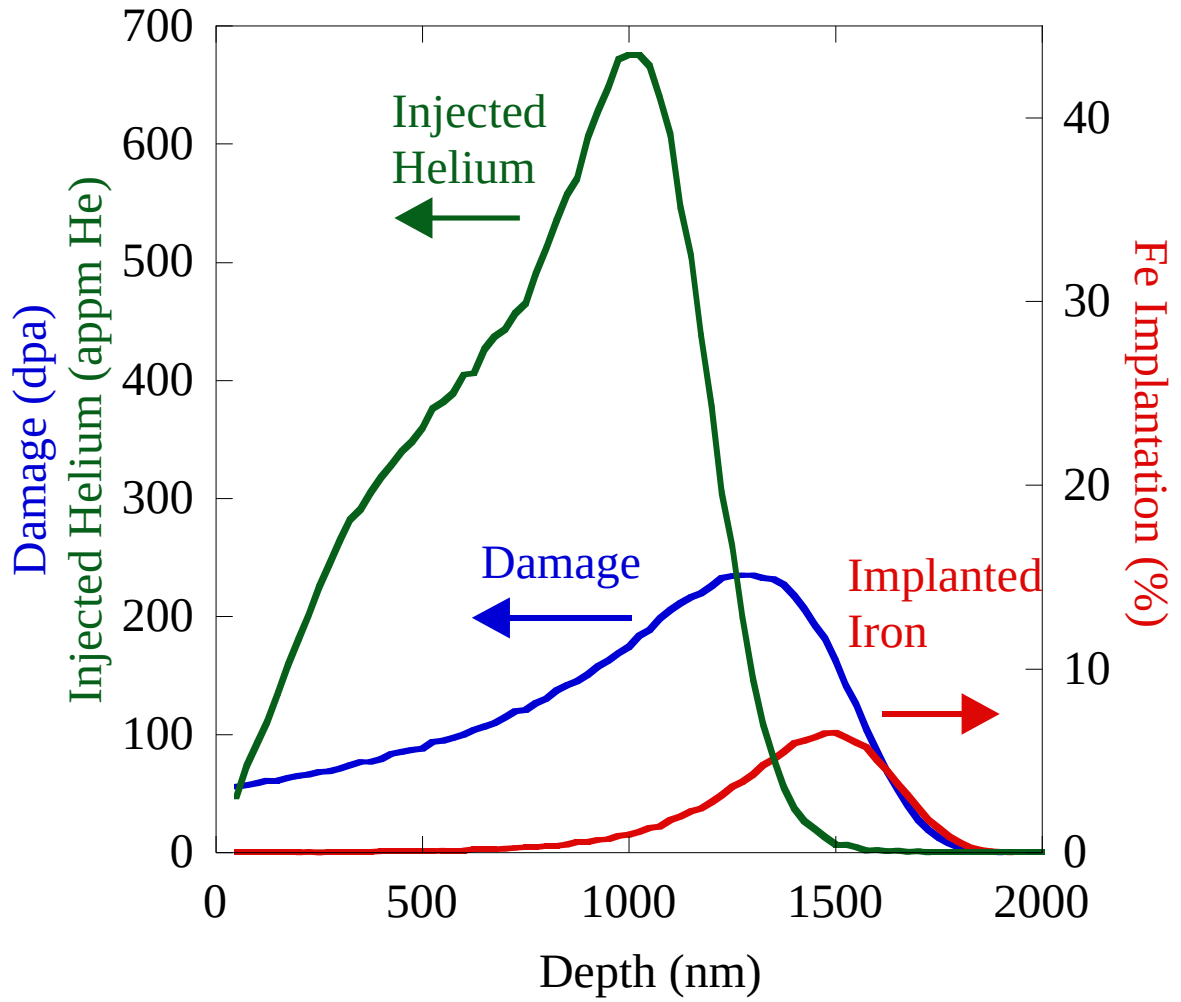

Figure 4.8: The helium injection profile, damage profile and injected ion concentration as a function of depth for 5 MeV Fe^{2+} in T91 as calculated by SRIM for a damage level of 100 dpa at 600 nm from the surface for 4 appm He/dpa with a flat helium-to-dpa profile.

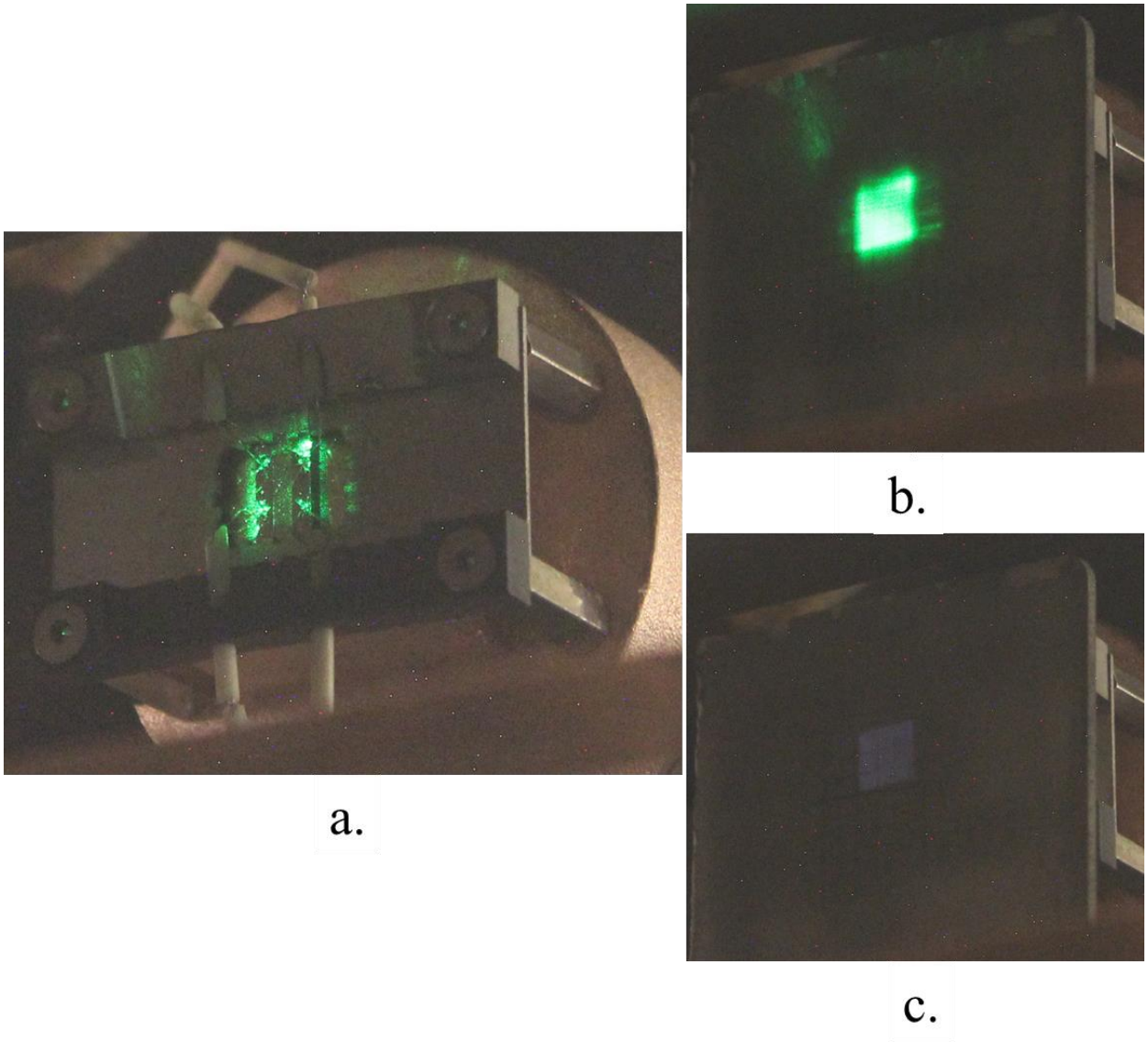

Figure 4.9: Pictures of the alignment verification process showing (a) the diffuse laser on the irradiation stage, (b) the same diffuse laser on an alumina piece in front of the irradiation stage and (c) fluorescence of the alumina piece from the 5 MeV Fe^{2+} ions [90].

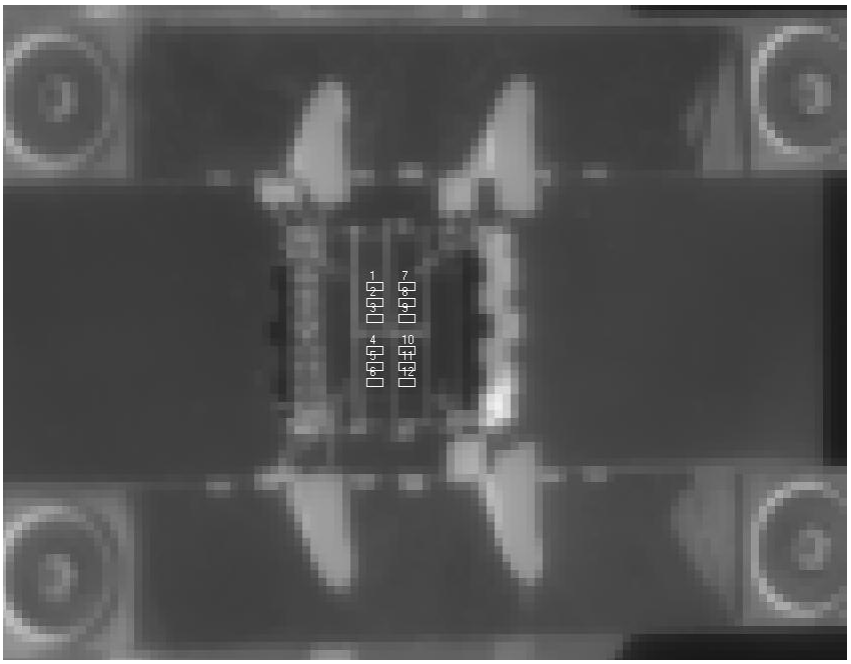

Figure 4.10: A typical thermal image with AOIs on a heated irradiation stage. The middle AOIs are in the ion irradiated area struck by both the 5 MeV Fe^{2+} beam and the energy degraded He^{2+} beam. The outer four AOIs are present to ensure the beam does not shift during irradiation.

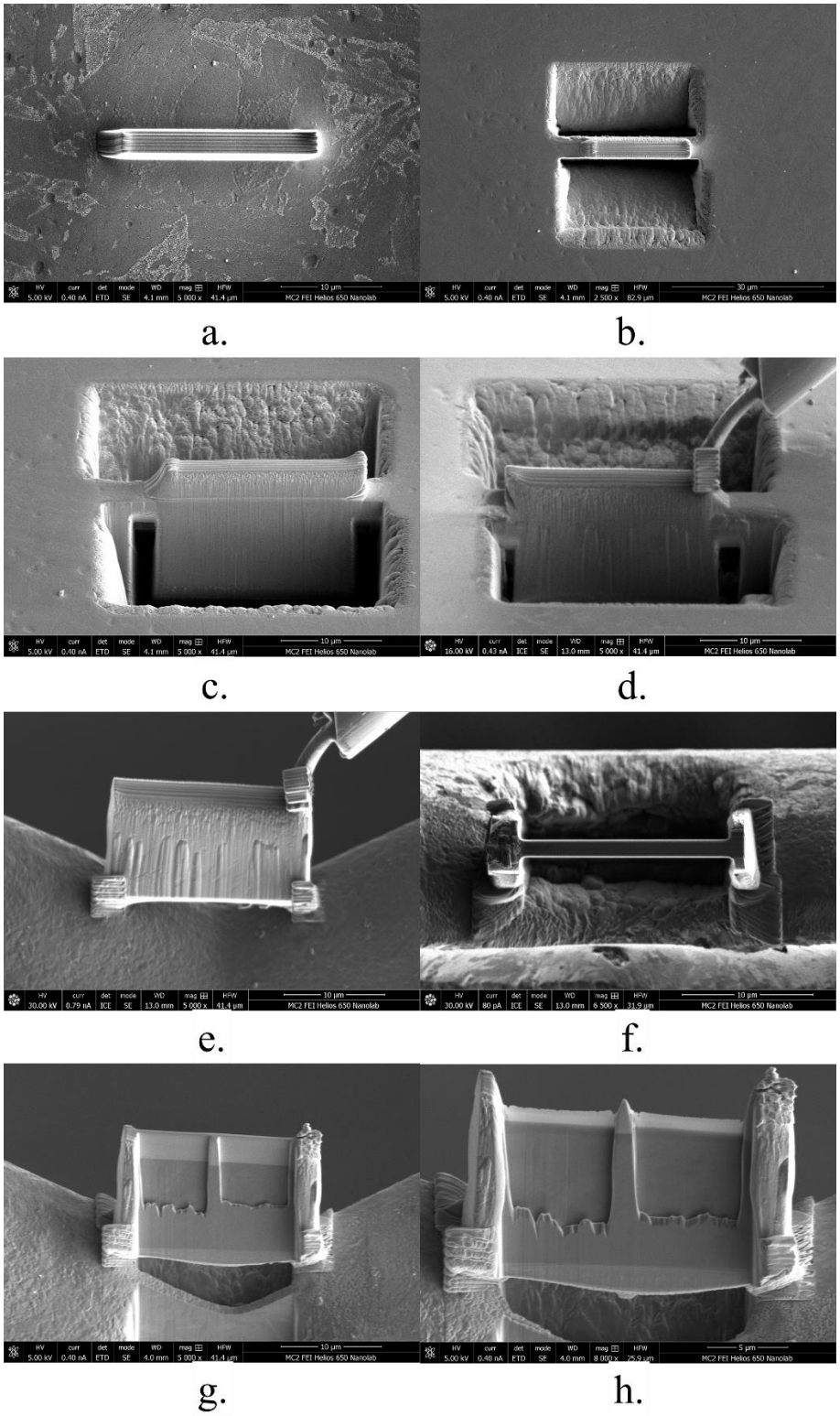

Figure 4.11: A schematic of the FIB process, showing a) platinum deposition on the surface, b) trenching around the platinum deposition, c) undercut of the sample at 52°, d) attaching of the Omniprobe to the sample, e) attaching of the sample to the copper grid, f) thinning the specimen prior to window formation, g) after window formation, and h) after final thinning [90].

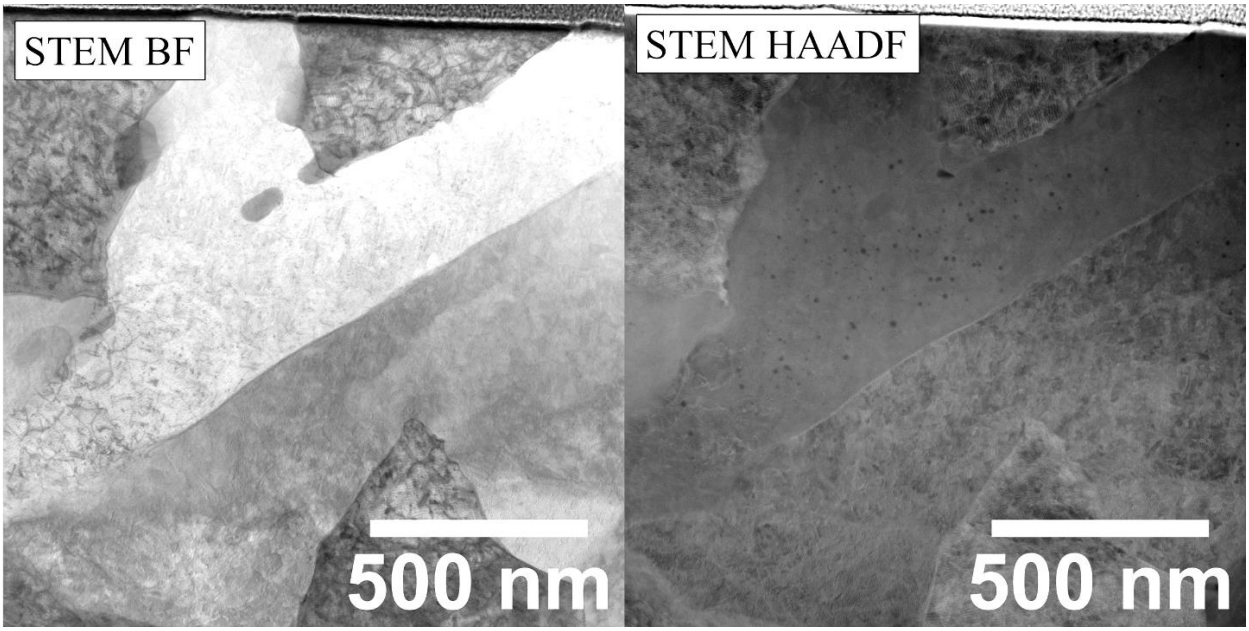

Figure 4.12: STEM BF (left) and STEM HAADF (right) micrographs of the same area on a T91 specimen irradiated to 16.6 dpa at 445°C with 4 appm He/dpa and 7.1×10^{-4} dpa/s .

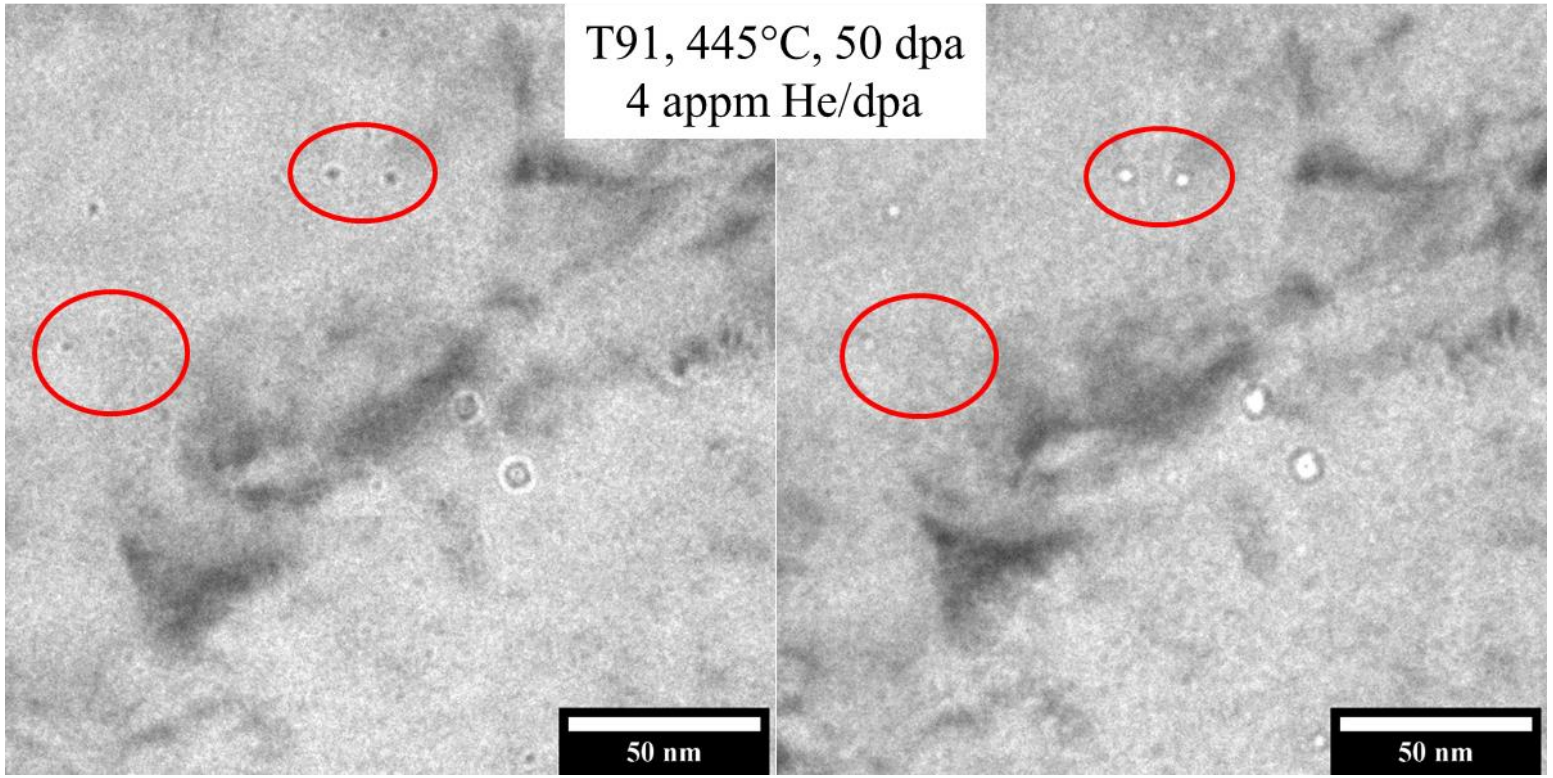

Figure 4.13: CTEM BF overfocused (left) and CTEM BF underfocused (right) micrographs of the same area on a T91 specimen irradiated to 50 dpa at 445°C with 4 appm He/dpa and 7.1×10^{-4} dpa/s. The circled areas highlight some of the small cavities observed with CTEM.

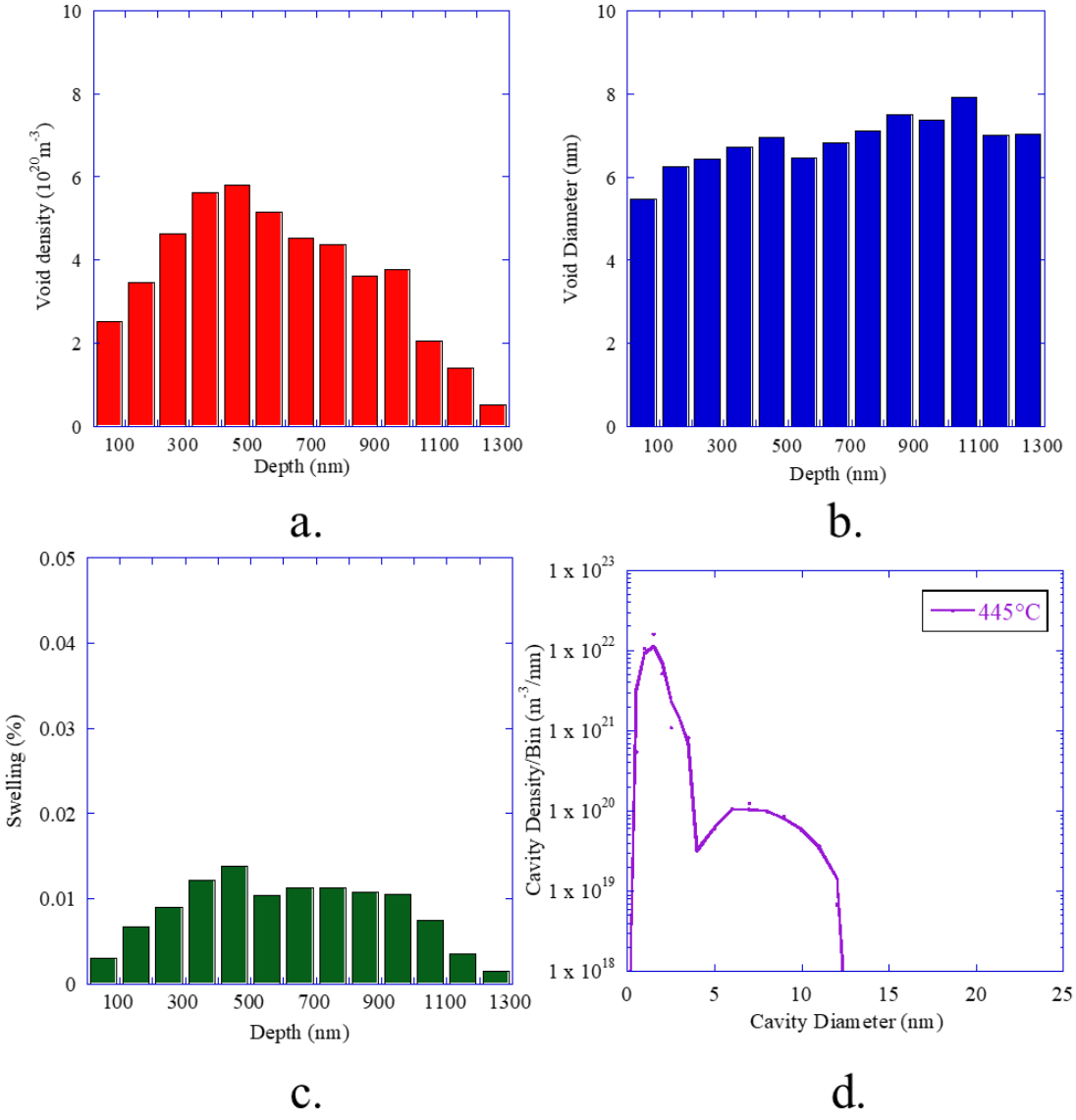

Figure 4.14: An example of profiling cavities through depth in T91 irradiated to 16.6 dpa at 445°C with 4 appm He/dpa at 7.1 × 10^{-4} dpa/s for (a) number density, (b) average diameter and (c) swelling from STEM imaging. The resulting combined STEM and CTEM cavity size distribution from the 500-700 nm region is shown in (d) [90].

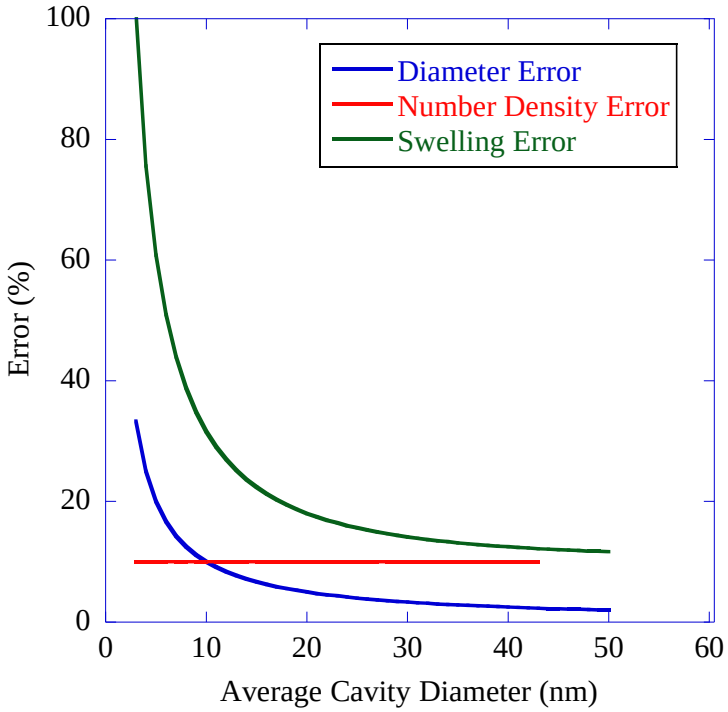

Figure 4.15: The error in diameter, number density and welling is plotted as a function of cavity diameter.

Chapter 5 Results

This chapter presents the results from the characterization of the ion irradiation experiments detailed in Chapter 4 The results are divided into two sections based on both the alloy and the irradiation campaign undertaken. The first section focuses on the results of the T91 irradiations conducted across a wide range of damage levels and helium injection rates. The second section features the characterization of the irradiations of alloy HT9 at a single damage level with varied helium injection rates, and at two helium levels across a significant range of damage levels. As mentioned in Chapter 4 the nomenclature adopted to break the cavities into groups is based on the size distribution of the cavities with "bubbles" referring to features in the first peak of the bimodal distribution, typically smaller than 5 nm in diameter, and "voids" referring to features in the second peak of the bimodal distribution, typically larger than 5 nm in diameter. While the cutoff between the two is arbitrary, it simplifies the discussion without affecting the results or the conclusions drawn.

5.1 Microstructural Evolution in T91 Across a Range of Helium Co-injection Rates and Damage Levels

This section of the results will be further broken up into three subsections: non-irradiated microstructure, swelling and cavity evolution, and dislocation loop evoluation.

5.1.1 Non-irradiated Microstructure Characterization of T91

Prior to irradiation, FIB liftouts of the as-tempered samples were prepared and characterized to establish the baseline microstructure. Measurements of grain size, precipitates ($M_{23}C_6$ carbides and V,Cr-nitrides) size and density and dislocation line length were measured and

presented in this section. The effective lath diameter and dislocation line length were measured from STEM bright field images while the precipitate diameters and densities were measured using EDS-based spectrum images. The $M_{23}C_6$ carbides were typically observed on grain boundaries while the V,Cr-nitrides were more uniformly distributed within the grains.

As reported in [116], the effective grain diameter was 800 nm for a sink strength of 4 x 10^{13} m^{-2}. The average size of $M_{23}C_6$ was ~100 nm with an estimated number density between 10^{18} and 10^{19} m^{-3} yielding a sink strength of ~1 x 10^{12} m^{-3}. The average size of V,Cr-nitrides was ~40 nm, again with an estimated number density of 10^{18} and 10^{19} m^{-3} yielding a sink strength of ~1 x 10^{12} m^{-3}. Finally, the network dislocation density varied slightly from area-to-area, but was estimated to be ~10^{15} m^{-2}. Overall, the dislocations were the dominant sink strength in the non-irradiated microstructure.

5.1.2 Swelling and Cavity Evolution in T91

At least a few voids were observed at all damage levels and helium co-injection rates. The damage level dependence of the void diameter, number density and swelling are tabulated in Table 5.1 and plotted in Figure 5.1. The average void diameter started out at a similar value of 6-8 ± 1 nm for all helium injection levels at 17 dpa, but then became dependent on He level as the damage increased with a final average diameter of 30 ± 1 nm without any injected helium to 18 ± 1 nm with 4 appm He/dpa at 150 dpa. The void number density exhibited two different trends with the lower helium levels of 0 and 0.02 appm He/dpa exhibiting monotonic growth in the density with increasing damage level, and the higher helium levels of 0.2 and 4 appm He/dpa showing a peaked behavior with the maximum occurring at an intermediate damage level. Cavity swelling started out low for all helium conditions at the lowest damage level ranging from 0.00014 ± 0.00002 % with 0 appm He/dpa to 0.0073 ± 0.001 % with 4 appm He/dpa at 17 dpa. All the conditions

exhibited growth with increasing damage level. However, the condition without helium exhibited the largest increase reaching 0.60 ± 0.09 % at 150 dpa while the condition with the most helium, 4 appm He/dpa, exhibited the least growth only reaching 0.082 ± 0.01 % at 150 dpa. The size distributions are plotted for each damage level in Figure 5.2-Figure 5.6. Bimodal size distributions are observed for all conditions in which helium was injected for all damage levels. In addition, consistent with the observed increase in average void diameter, the width of the size distribution increases with increasing damage level.

The void evolution dependence can be seen more clearly when the data is plotted as a function of helium co-injection rate for each of the damage levels for which all conditions have data (17, 50 and 150 dpa). Figure 5.7 shows the replotted data. Since the exact numbers have already been mentioned, only the trends will be examined here. As shown in Figure 5.7(a), the average void diameter is relatively constant with helium co-injection rate at 17 dpa. At 50 dpa, a slight negative slope is observed with a higher average at 0 appm He/dpa and a slow drop off to 4 appm He/dpa. Finally, at the highest damage level, the difference becomes more extreme, particularly with the transition from no helium to some helium. As seen in Figure 5.7(b), the void density for the first two damage levels of 17 and 50 dpa increases monotonically with increasing damage level. At 150 dpa, the trend changes slightly as the density at the highest helium co-injection rate of 4 appm He/dpa decreases below the density of the second highest helium co-injection rate. This relates to another trend that was touched upon in previous paragraph in that, with the exception of 100 dpa (not shown in Figure 5.7(b)), the void density at 4 appm He/dpa decreased with increasing helium level. Finally, swelling is plotted in Figure 5.7(c). The trend in the data shows the maximum swelling occurring at the highest helium co-injection rates at 17 dpa.

The trend then starts to become more uniform across helium co-injection rates at 50 dpa. Finally, the trend reverses with the highest swelling observed without helium at 150 dpa.

The bubble evolution with damage level for each helium co-injection rate is plotted in Figure 5.8 (a similar plot of bubble behavior with helium co-injection rate is plotted in Figure 5.9, but the trends are obvious enough that it will not be broken out in the same way that voids were above). To begin with, no bubbles were observed for the case without any injected helium. While bubble diameter has been plotted in Figure 5.8(a), the trends are not consistent with a monotonic decrease in diameter observed at 0.02 appm He/dpa and 4 appm He/dpa, but a u-shaped profile for 0.2 appm He/dpa. The bubble density in Figure 5.8(b) shows more consistent trends. All of the helium co-injection rates that had bubbles showed a monotonic increase in density with increasing damage level. The increase was more pronounced in the 17-50 dpa region than at higher damage levels. Of particular interest is the change in the relative bubble density. At 17 dpa, the bubble density increases monotonically with increasing helium co-injection rate. At 50 and 150 dpa, the swelling is minimized for 0.2 appm He/dpa with 0.02 appm He/dpa and 4 appm He/dpa both exhibiting a higher bubble density.

5.1.3 Dislocation Loop Evolution in T91

Dislocations loops were observed to form under all irradiation conditions in T91. STEM-BF images of dislocation loops were collected for each helium co-injection rate irradiated at 445°C to 17 dpa and for all damage levels at 0.2 appm He/dpa. The summary of the average dislocation loops diameter and number density tabulated in Table 5.2 and plotted in Figure 5.10. The primary dislocation loops observed at each helium co-injection rate were **a**<100> dislocation loops with very few **a**/2<111> dislocation loops observed. The average dislocation loop diameter did not change significantly with helium co-injection rate at 17 dpa from 18 ± 3 nm to 25 ± 3 nm or with

damage level at 0.2 appm He/dpa from 18 ± 3 nm to 22 ± 3 nm. The dislocation loop density did not significantly change with helium co-injection rate at 17 dpa in the range of $3.1 \pm 0.5 \times 10^{21}$ m^{-3} to $3.9 \pm 0.5 \times 10^{21}$ m^{-3} or with damage level at 0.2 appm He/dpa in the range of $2.9 \pm 0.5 \times 10^{21}$ m^{-3} to $3.9 \pm 0.5 \times 10^{21}$ m^{-3}. Because the dislocation loop microstructure was not observed to change significantly with damage level at 0.2 appm He/dpa, it was not measured at any other helium level. Dislocation lines were observed at all helium co-injection rates and no significant alteration of the existing network dislocation density was noted compared to the as-tempered condition.

5.2 Microstructure Evolution Behavior in HT9

This section of the results will be further broken up into three subsections: non-irradiated microstructure, swelling and cavity evolution, and dislocation loop evoluation.

5.2.1 Non-irradiated Microstructure Characterization of HT9

Prior to irradiation, FIB liftouts of the as-received samples were prepared and characterized to establish the baseline microstructure. Measurements of grain size, precipitates ($M_{23}C_6$ carbides) size and density and dislocation line length were measured and presented in this section. The effective lath diameter, precipitate diameter and density, and dislocation line length were measured from STEM bright field images. The $M_{23}C_6$ carbides were typically observed on grain boundaries while the V,Cr-nitrides were more uniformly distributed within the grains.

As reported in [97], the effective grain diameter was ~530 nm for a sink strength of 8.6 x 10^{13} m^{-2}. The average size of $M_{23}C_6$ was ~50 nm with a number density of 1.7 x 10^{19} m^{-3} yielding a sink strength of 5 x 10^{12} m^{-2}. Finally, the network dislocation density varied slightly from area-to-area but was estimated to be ~2 x 10^{14} m^{-2}. Overall, the grain boundaries and dislocations dominated the sink strength for a combined strength of ~3 x 10^{14} m^{-2}. It should be noted that there was ~10% retained δ-ferrite in the microstructure.

5.2.2 Cavity and Swelling Evolution in HT9

Because of the limited number of irradiations performed with HT9, the results will be presented in two sections. In the first, the behavior will be shown at a single damage level with three different helium co-injection rates. In the second, the behavior will be shown with increasing damage at a single helium co-injection rate.

5.2.2.1 Constant Damage Level with Varied Helium Co-injection Rate

Voids were observed to form under all three helium implantation modes in HT9 at 188 dpa and 460°C while bubbles were only observed for the two conditions under which helium was injected: 0.06 appm He/dpa and 4 appm He/dpa. The average behavior for voids is plotted in Figure 5.11 with the swelling and recorded in Table 5.3. The average void diameter was highest at 0 appm He/dpa with a value of 44 ± 1 nm. It dropped to 31 ± 1 nm at 0.06 appm He/dpa and reached a minimum of 24 ± 1 nm with 4 appm He/dpa. Void density exhibited the opposite trend with helium co-injection rate with a value of 6.9 x 10^{20} m^{-3} at 0 appm He/dpa, increasing to 13 x 10^{20} m^{-3} at 0.06 appm He/dpa and reaching a maximum of 17 x 10^{20} m^{-3} at 4 appm He/dpa. Swelling followed a similar trend to void diameter with a maximum of 4.7% with 0 appm He/dpa, decreasing to 3.7% at 0.06 appm He/dpa and reaching a minimum of 1.8% at 4 appm He/dpa. As shown in Table 5.3, even with the differences in void evolution, the void sink strength was relatively constant varying between 1.9-2.6 x 10^{14} m^{-2}.

The average behavior for bubbles is plotted in Figure 5.12 and also tabulated in Table 5.3. No bubbles were observed without the injection of helium. With increasing helium co-injection rate, both the average bubble diameter and the bubble density increased from 0.5 nm and 130 x 10^{20} m^{-3} at 0.06 appm He/dpa to 3 nm and 440 x 10^{20} m^{-3} at 4 appm He/dpa. In contrast to the void sink strength, these differences in bubble evolution significantly changed the bubble sink strength,

starting with no sink strength without the bubbles at 0 appm He/dpa, increasing to a small value of 0.39 x 10^{14} m^{-2} at 0.06 appm He/dpa and then surpassing the void sink strength with a value of 8.3 x 10^{14} m^{-2} at 4 appm He/dpa.

The size distributions for these irradiations are plotted in Figure 5.13. Without the addition of helium, a unimodal distribution develops. With the addition of a small amount of helium (0.06 appm He/dpa), a narrow lower peak develops producing a bimodal distribution. With the addition of helium at higher rates (4 appm He/dpa), the peak both increases in height and broadens. The trends for the second peak of the distribution (or the single mode of the 0 appm He/dpa condition) follow a slightly different trend. With the addition of helium, the second mode shrinks in width, spanning a range of ~60 nm without any helium, but only ~40 nm at the highest helium injection rate. Conversely, the height of the distribution increases with increasing helium co-injection rate.

5.2.2.2 Varied Damage Level with Constant Helium Co-injection Rate

The evolution of the cavities and swelling was tracked as a function of damage level for the highest helium level of 4 appm He/dpa in HT9. The results are plotted in Figure 5.14-Figure 5.16 and tabulated in Table 5.3. As seen in Figure 5.14, the voids grew with increasing damage level starting at 24 nm at 188 dpa and increasing to 34 nm at 650 dpa. The void density followed the opposite trend with a slight decrease in density as the damage level increased, starting at 17 x 10^{20} m^{-3} at 188 dpa and dropping to 11 x 10^{20} m^{-3} at 650 dpa. Swelling increase mostly linearly from 1.8% at 188 dpa to 6.5% at 650 dpa.

The average behavior of the bubbles is plotted in Figure 5.15. In general, the average bubble diameter decreased with increasing damage level. The one exception was 350 dpa where there was a significant drop in the average diameter, but everything else follows a consistent trend.

Similarly, the higher damage levels showed a consistent decrease in bubble density, but 188 dpa was lower than the other observed densities and 350 dpa showed a higher density.

The size distributions are plotted in Figure 5.16 with the full distribution shown in (a) and the bubble region expanded in (b). All of the distributions show a clear bimodal distribution with a high density of bubbles at low sizes (<~7 nm). The second peak of the distribution follows consistent trends with increasing damage level, the height of the peak drops as the tail at higher sizes extends slowly. The swelling is driven by an increase in the length of the tail to higher sizes. Looking at the enhanced view of the bubble end of the distribution, the peak does not change much. The main difference occurs for 350 dpa where there is a significantly higher density of bubbles in the 0-2 nm size range than in any other distribution.

5.2.3 Dislocation Loop Evolution in HT9

Dislocations loops were observed to form under all irradiation conditions in HT9. STEM-BF images of dislocation loops were collected for each irradiation condition. The summary of the average dislocation loops diameter and number density tabulated in Table 5.4 and plotted in Figure 5.17. The primary dislocation loops observed at each helium co-injection rate were **a**<100> dislocation loops with very few **a**/2<111> dislocation loops observed. The average dislocation loop diameter did not change significantly with helium co-injection rate at 188 dpa from 34 ± 4 nm to 37 ± 5 nm or with damage level at 4 appm He/dpa from 32 ± 4 nm to 38 ± 4 nm. The dislocation loop density changed a little bit more with helium co-injection rate at 188 dpa in the range of $0.31 \pm 0.1 \times 10^{21}$ m^{-3} to $1.6 \pm 0.5 \times 10^{21}$ m^{-3} and with damage level at 4 appm He/dpa in the range of $0.43 \pm 0.1 \times 10^{21}$ m^{-3} to $1.3 \pm 0.5 \times 10^{21}$ m^{-3}, but it was likely due to local variation and the relatively limited number of counted loops. Dislocation lines were observed at all helium

co-injection rates and no significant alteration of the existing network dislocation density was noted compared to the as-tempered condition.

Table 5.1: Summary of characterization results for cavities in dual ion irradiated T91 at 445°C with a damage rate of 7-8 x 10-4 dpa/s. N.O. indicates that the feature was not observed. N.M. indicates that the condition was not characterized for this feature.

Damage (dpa)	Helium Co-Injection Rate (appm He/dpa)	Sample #	Number Of Bubbles Examined	Average Bubble Diameter (nm)	Bubble Density (10^{20} m^{-3})	Bubble Sink Strength (10^{14} m^{-2})	Number of Voids Examined	Average Void Diameter (nm)	Void Density (10^{20} m^{-3})	Swelling (%)	Void Sink Strength (10^{14} m^{-2})
17	0	1	0	N.O.	N.O.	N.O.	4	6.9 ± 1	0.082	0.00014	0.0036
50	0	1	0	N.O.	N.O.	N.O.	15	11 ± 1	0.53	0.016	0.037
150	0	1	0	N.O.	N.O.	N.O.	117	30 ± 1	2.7	0.6	0.51
17	0.02	1	27	3.1	3.0	0.058	47	5.8 ± 1	1.1	0.0044	0.057
50	0.02	1	25	1.6	190	1.9	12	8.6 ± 1	0.82	0.0035	0.044
50	0.02	3	152	N.M.	N.M.	N.M.	65	7.5 ± 1	2.4	0.01	0.11
100	0.02	2	93	1	3000	19	114	14 ± 1	3.3	0.084	0.29
150	0.02	1	152	0.73	4000	18	54	16 ± 1	2.6	0.1	0.26
150	0.02	2	25	N.M.	N.M.	N.M.	40	18 ± 1	3.1	0.18	0.36
17	0.2	1	32	2.5	7.0	0.11	238	5.9 ± 1	3.4	0.0051	0.13
50	0.2	1	6	1.8	26	0.29	425	9.9 ± 1	8.0	0.078	0.50
150	0.2	1	27	3.2	97	2.0	237	21 ± 1	4.6	0.38	0.61
17	4	1	85	2.6	320	5.2	167	5.6 ± 1	4.9	0.0073	0.17
50	4	1	103	2.1	270	3.6	166	7.5 ± 1	4.5	0.021	0.21
50	4	3	200	1.6	2700	27	147	8.5 ± 1	6.4	0.043	0.34
100	4	2	180	1.6	2800	28	766	12 ± 1	10	0.17	0.75
100	4	3	211	1	10000	63	81	9.6 ± 1	11	0.16	0.66
150	4	1	102	1.2	6100	46	232	12 ± 1	2.5	0.066	0.18
150	4	2	229	1.2	9790	74	77	18 ± 1	2.2	0.098	0.25
200	4	2	229	0.86	27000	150	227	17 ± 1	3.5	0.14	0.37

Table 5.2: Summary of characterization results for dislocation loops in dual ion irradiated T91 at 445°C. N.O. indicates that the feature was not observed. N.M. indicates the condition was not characterized for this feature. Negl. indicates the feature was observed but not in a large enough quantity to characterize for a representative value. 17 dpa data from [117].

Helium Co-Injection Rate (appm /dpa)	Damage Level (dpa)	Number of Dislocation Loops Examined	Dislocation Loop Density (10^{21} m^{-3})	Average Dislocation Loop Diameter (nm)	Dislocation Loop Line Density (10^{13} m^{-2})	Total Dislocation Loop Sink Strength (10^{14} m^{-2})
0	17	156	3.8	19 ± 2	2.3	2.8
0.02	17	141	3.1	19 ± 2	1.8	2.3
0.22	17	104	3.9	18 ± 2	2.1	2.7
0.22	50	113	2.9	22 ± 3	2.1	2.6
0.22	150	107	3.3	22 ± 3	2.3	2.8
4.3	17	103	3.5	25 ± 3	2.8	2.5

Table 5.3: Summary of characterization results for cavities in dual ion irradiated HT9 at 460°C. N.O. indicates that the feature was not observed. N.M. indicates that the condition was not characterized for this feature.

Damage (dpa)	Helium Co-Injection Rate (appm He/dpa)	Number Of Bubbles Examined	Average Bubble Diameter (nm)	Bubble Density (10^{20} m^{-3})	Bubble Sink Strength (10^{14} m^{-2})	Number of Voids Examined	Average Void Diameter (nm)	Void Density (10^{20} m^{-3})	Swelling (%)	Void Sink Strength (10^{14} m^{-2})
188	0	0	N.O.	N.O.	N.O.	308	44 ± 1	6.9	4.7	1.9
188	0.06	134	0.5	130	0.39	1343	31 ± 1	13	3.7	2.4
188	4	264	3	440	8.3	1774	24 ± 1	17	1.8	2.6
350	4	892	1.6	2000	20	573	27 ± 1	16	3	2.7
450	4	771	2.5	1290	20	724	30 ± 1	12	3.5	2.3
550	4	507	2.4	1100	17	604	33 ± 1	18	5.4	3.7
650	4	237	2.1	870	11	679	34 ± 1	11	6.5	2.3

Table 5.4: Summary of characterization results for dislocation loops in dual ion irradiated HT9 at 460°C. N.O. indicates that the feature was not observed. N.M. indicates the condition was not characterized for this feature. Negl. indicates the feature was observed but not in a large enough quantity to characterize for a representative value.

Helium Co-Injection Rate (appm /dpa)	Damage Level (dpa)	Number of Dislocation Loops Examined	Dislocation Loop Density (10^{21} m^{-3})	Average Dislocation Loop Diameter (nm)	Dislocation Loop Line Density (10^{14} m^{-2})	Total Dislocation Loop Sink Strength (10^{14} m^{-2})
0	188	31	1.6	34 ± 4	1.7	2.2
0.06	188	47	0.31	37 ± 5	0.36	0.46
4	188	29	0.73	35 ± 5	0.80	1.0
4	350	36	1.2	36 ± 5	1.4	1.7
4	450	47	0.83	32 ± 4	0.83	1.1
4	550	56	0.43	35 ± 5	0.47	0.60
4	650	38	1.3	38 ± 5	1.6	2.0

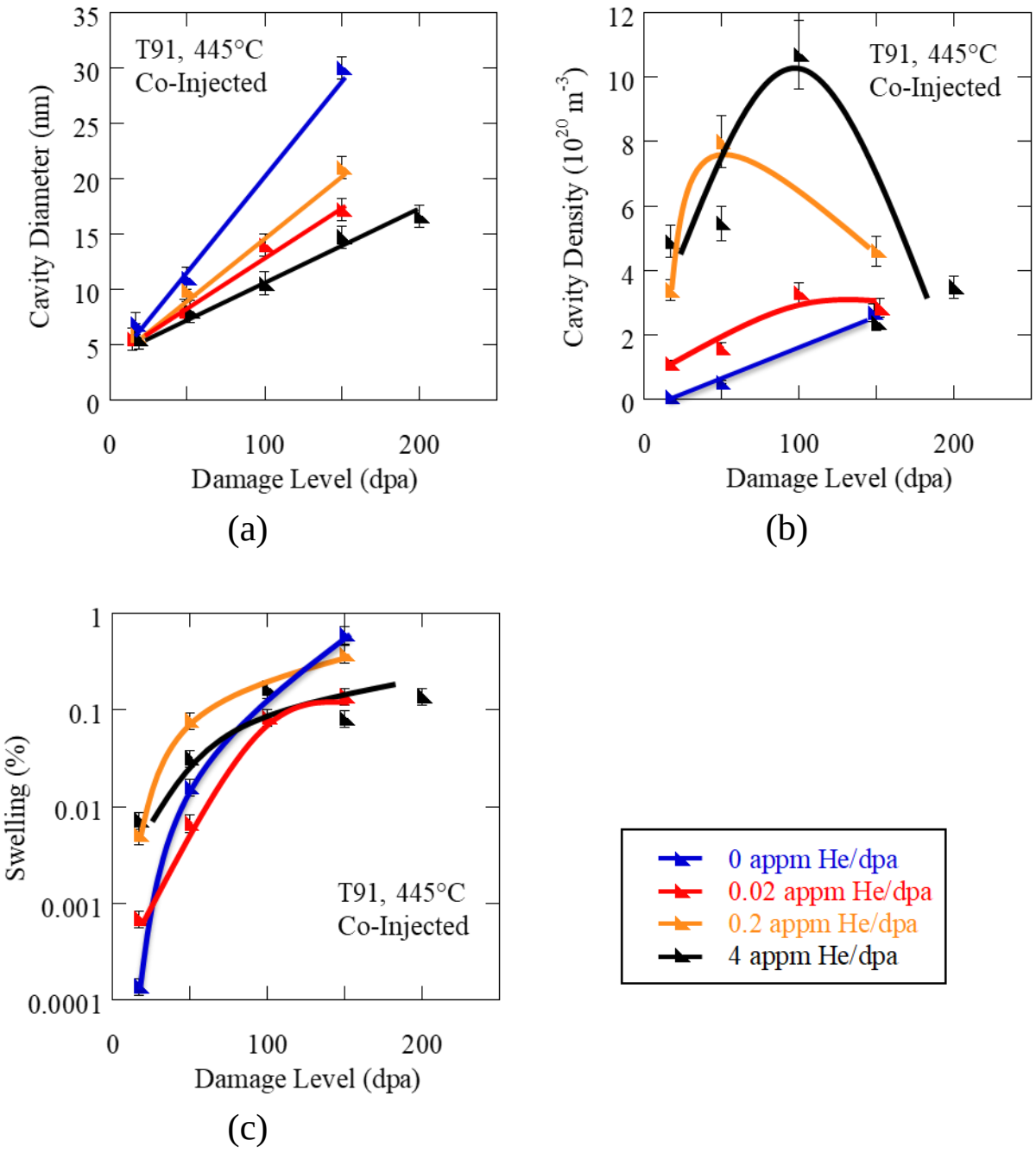

Figure 5.1: Void Diameter (a), Void Density (b) and Swelling (c) in T91 as a function of damage level for 0 Helium/dpa (blue), 0.02 Helium/dpa (red), 0.2 Helium/dpa (orange) and 4 Helium per dpa (black) at 445°C with 7-8 x 10^{-4} dpa/s.

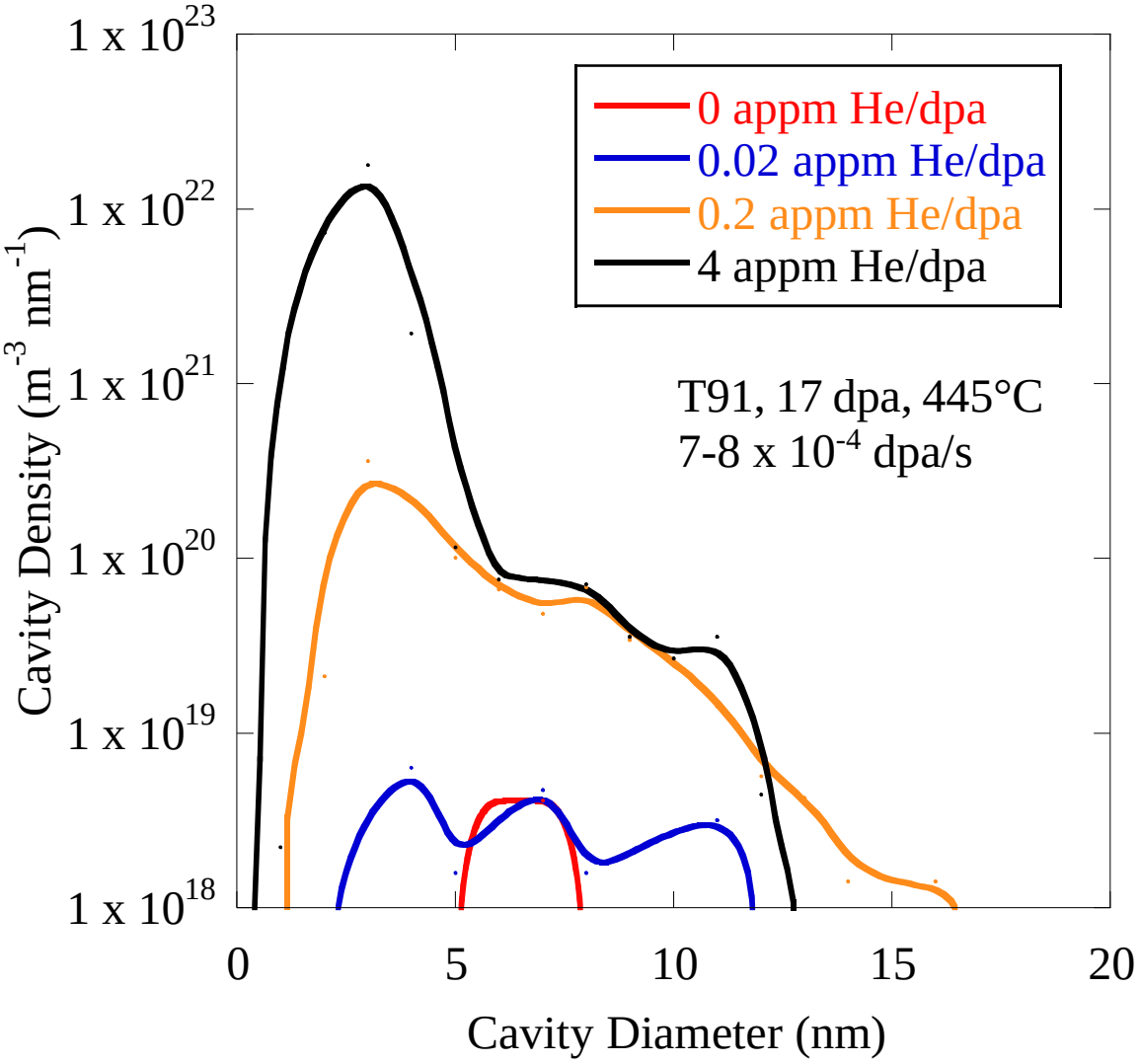

Figure 5.2: Cavity size distributions for dual ion irradiated T91 to 17 dpa at 445°C as a function of helium co-injection rate: 0 appm He/dpa (red), 0.02 appm He/dpa (blue), 0.2 appm He/dpa (orange) and 4 appm He/dpa (black).

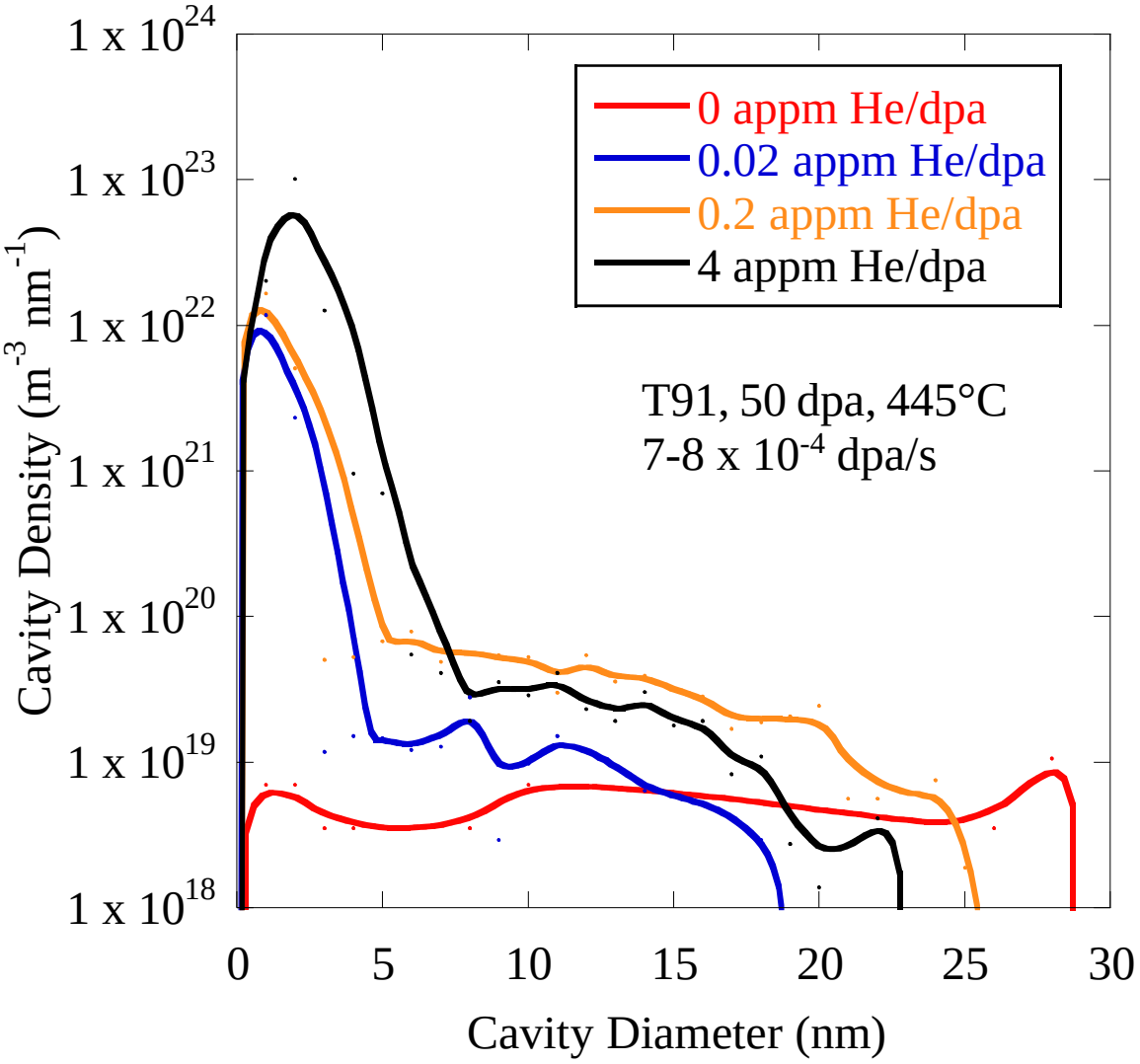

Figure 5.3: Cavity size distributions for dual ion irradiated T91 to 50 dpa at 445°C as a function of helium co-injection rate: 0 appm He/dpa (red), 0.02 appm He/dpa (blue), 0.2 appm He/dpa (orange) and 4 appm He/dpa (black).

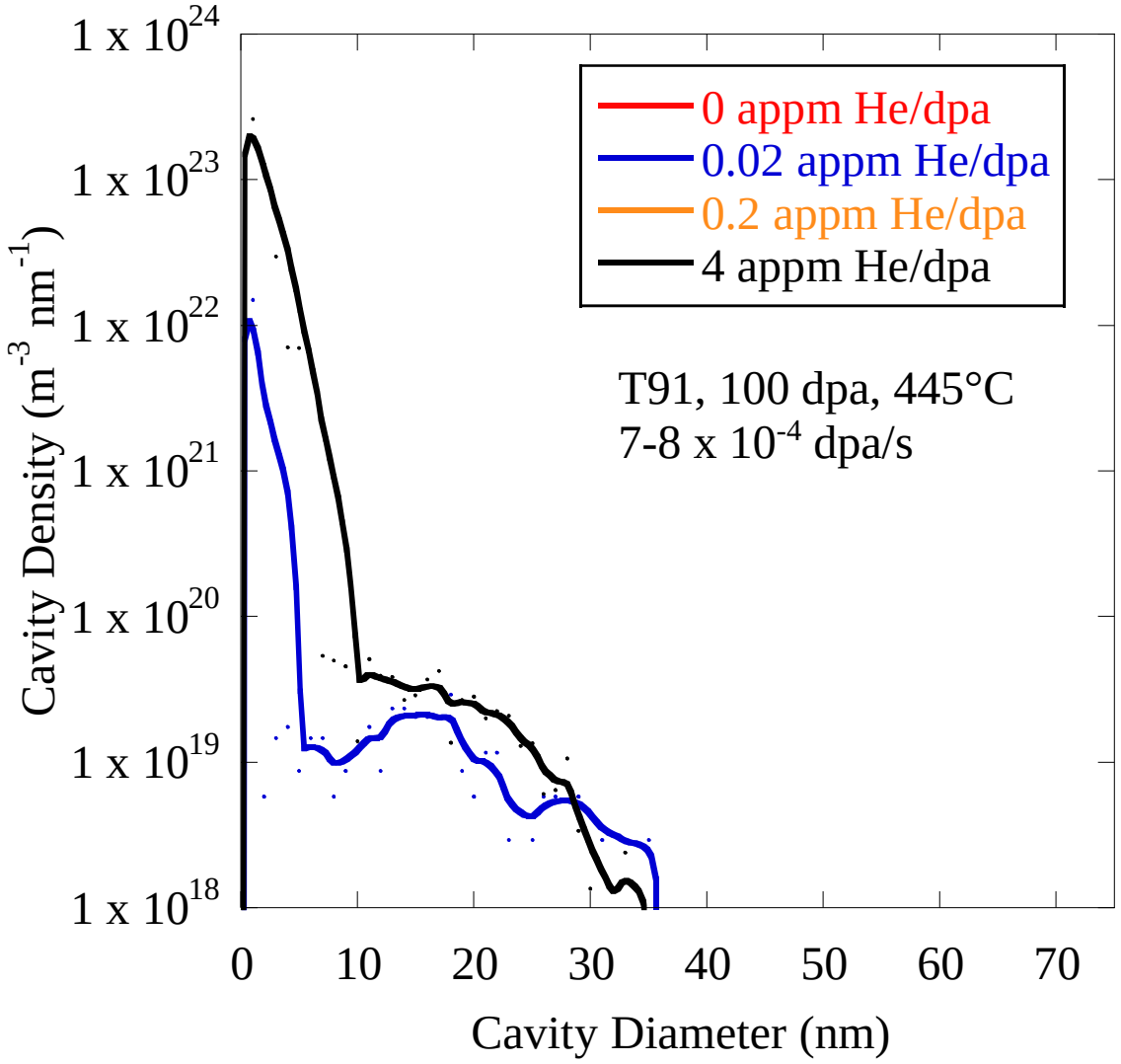

Figure 5.4: Cavity size distributions for dual ion irradiated T91 to 100 dpa at 445°C as a function of helium co-injection rate: 0.02 appm He/dpa (blue), and 4 appm He/dpa (black).

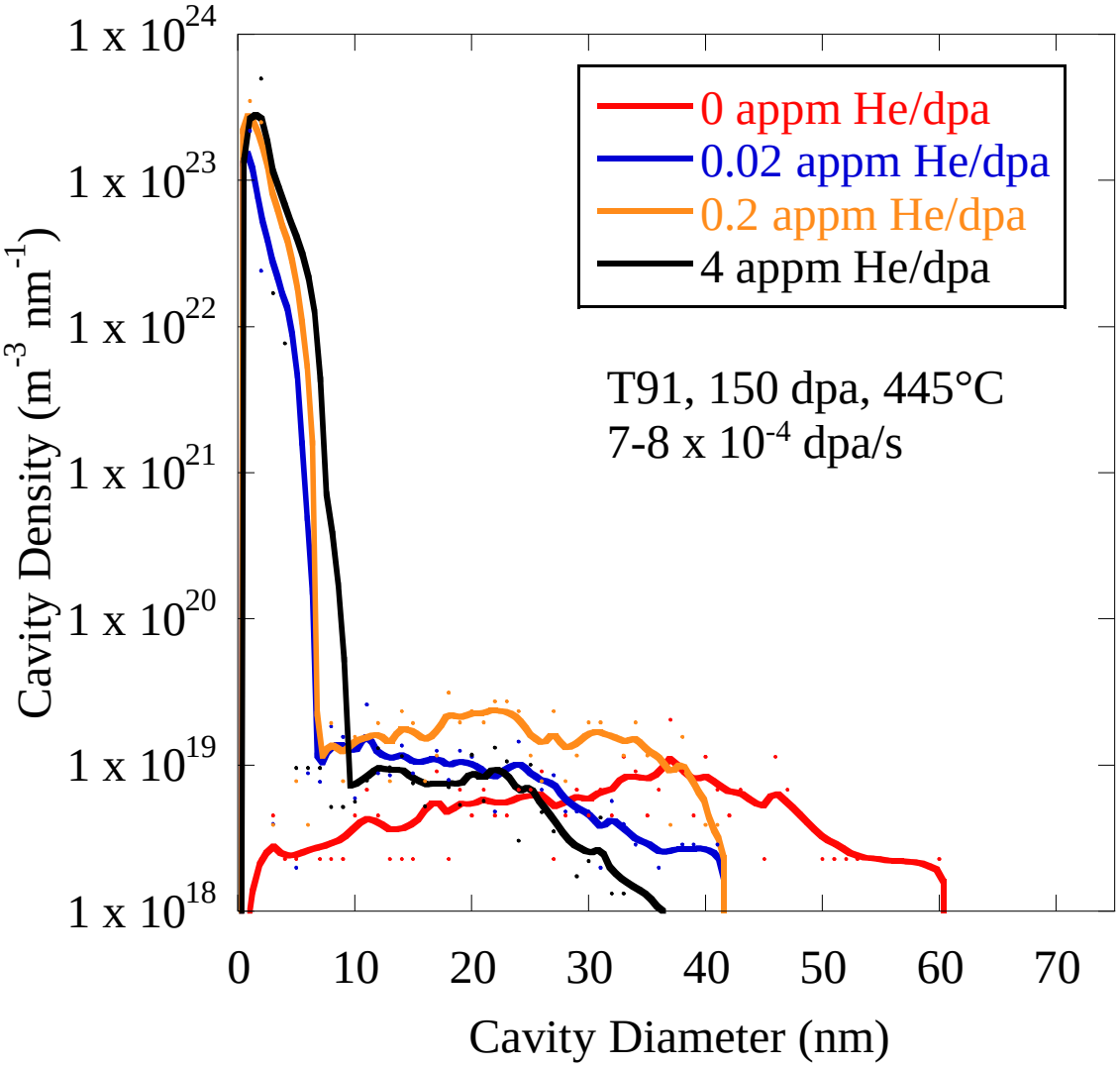

Figure 5.5: Cavity size distributions for dual ion irradiated T91 to 150 dpa at 445°C as a function of helium co-injection rate: 0 appm He/dpa (red), 0.02 appm He/dpa (blue), 0.2 appm He/dpa (orange) and 4 appm He/dpa (black).

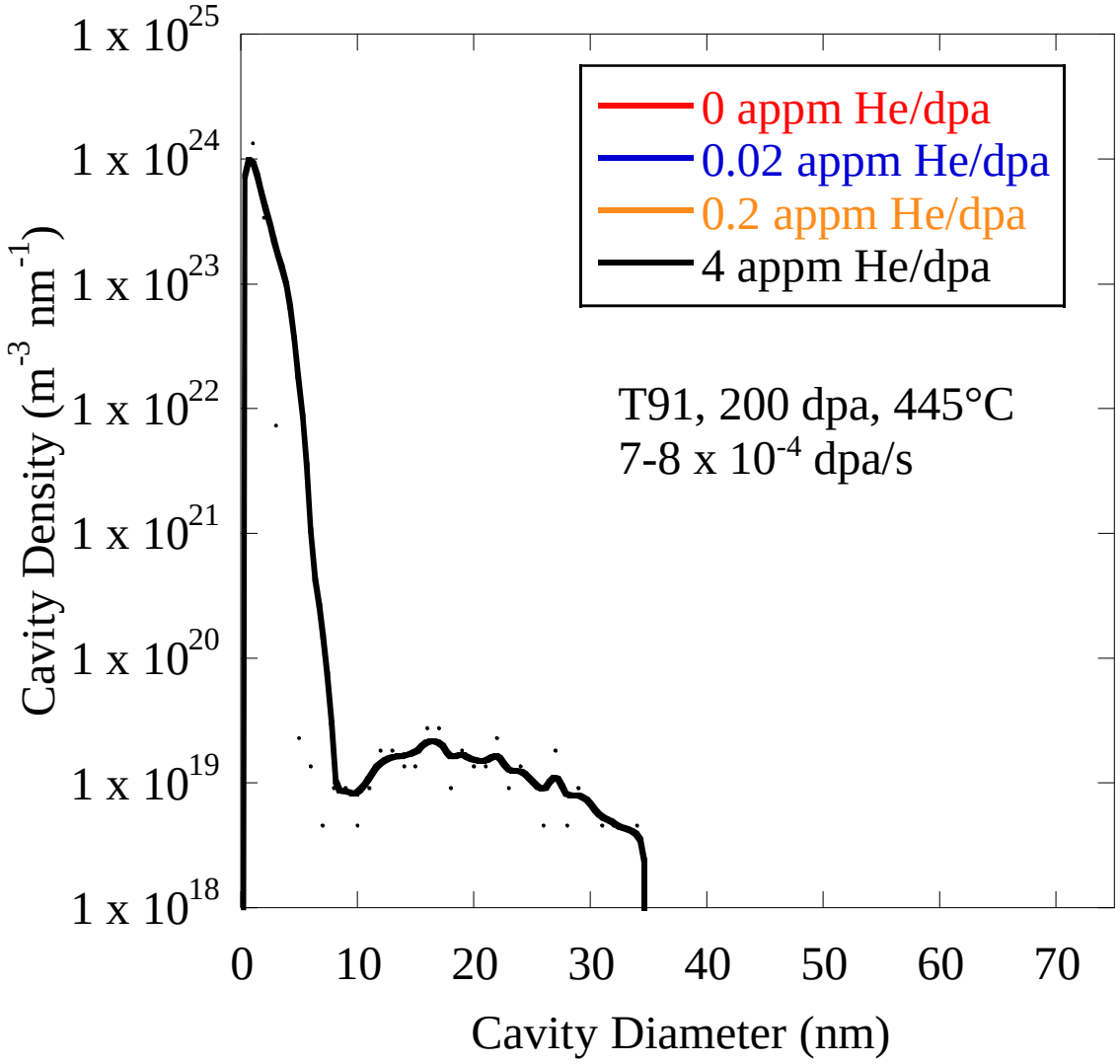

Figure 5.6: Cavity size distributions for dual ion irradiated T91 to 200 dpa at 445°C as a function of helium co-injection rate: 4 appm He/dpa (black).

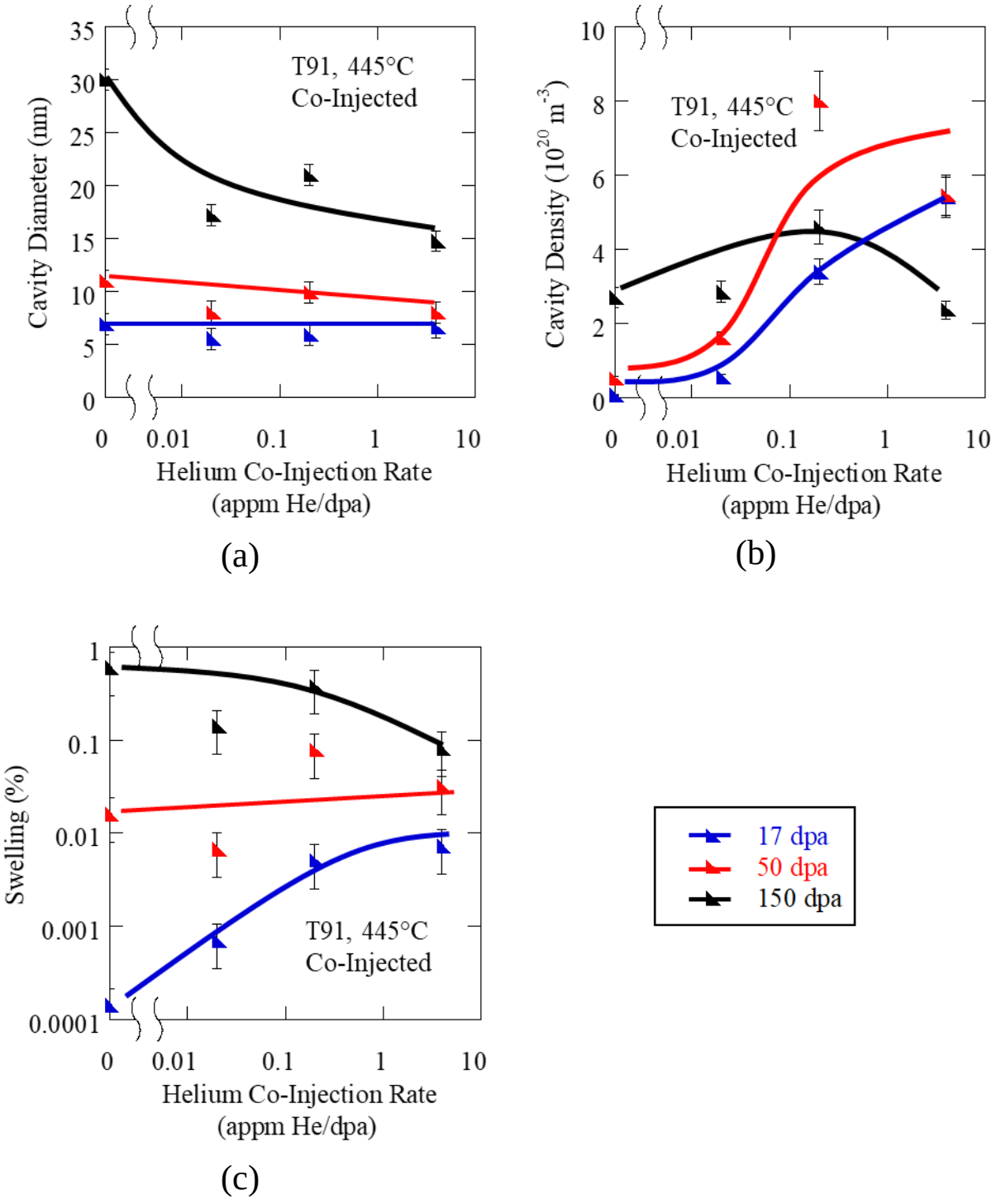

Figure 5.7: Void Diameter (a), Void Density (b) and Swelling (c) in T91 as a function of helium co-injection rate (appm He/dpa) for 17 dpa (blue), 50 dpa (red) and 150 dpa (black) at 445°C with 7-8 x 10-4 dpa/s.

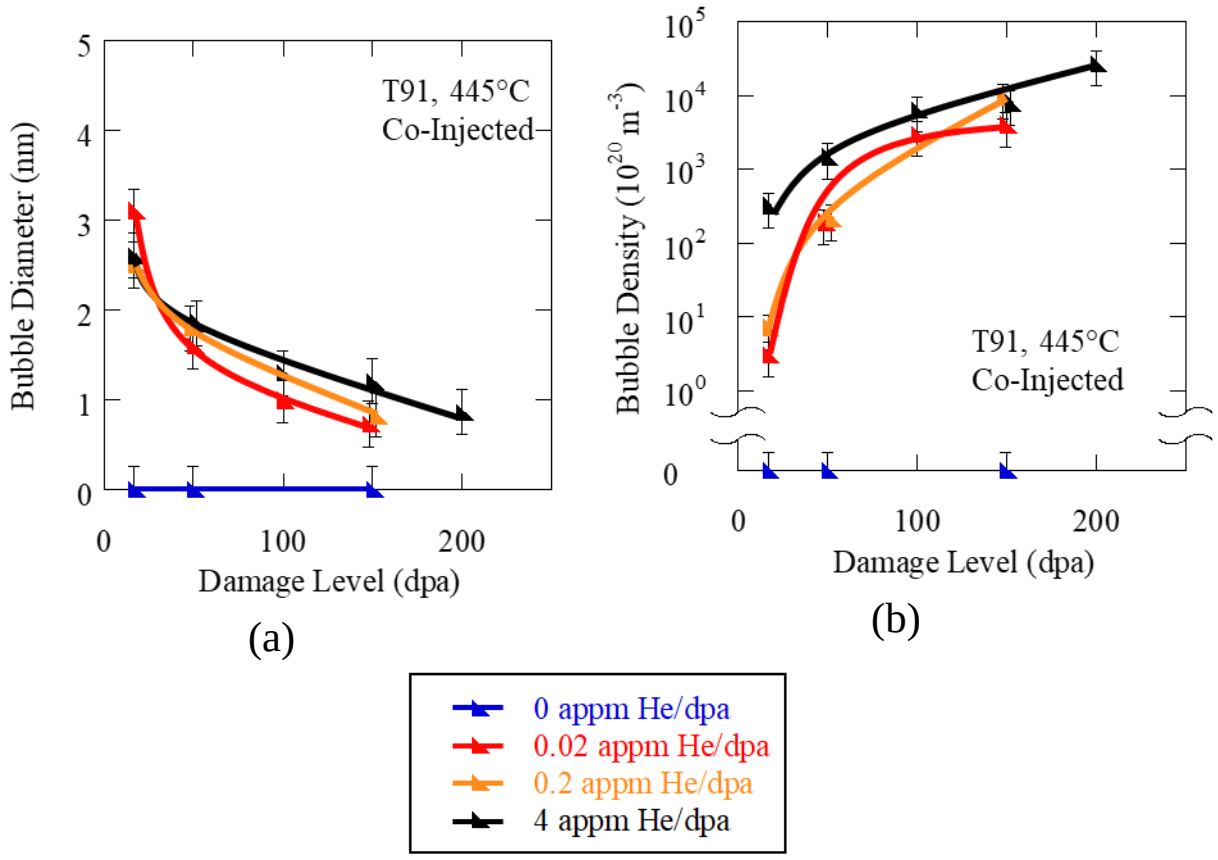

Figure 5.8: Bubble Diameter (a) and Bubble Density (b) in T91 as a function of damage level for 0 Helium/dpa (blue), 0.02 Helium/dpa (red), 0.2 Helium/dpa (orange) and 4 Helium per dpa (black) at 445°C with 7-8 x 10^{-4} dpa/s.

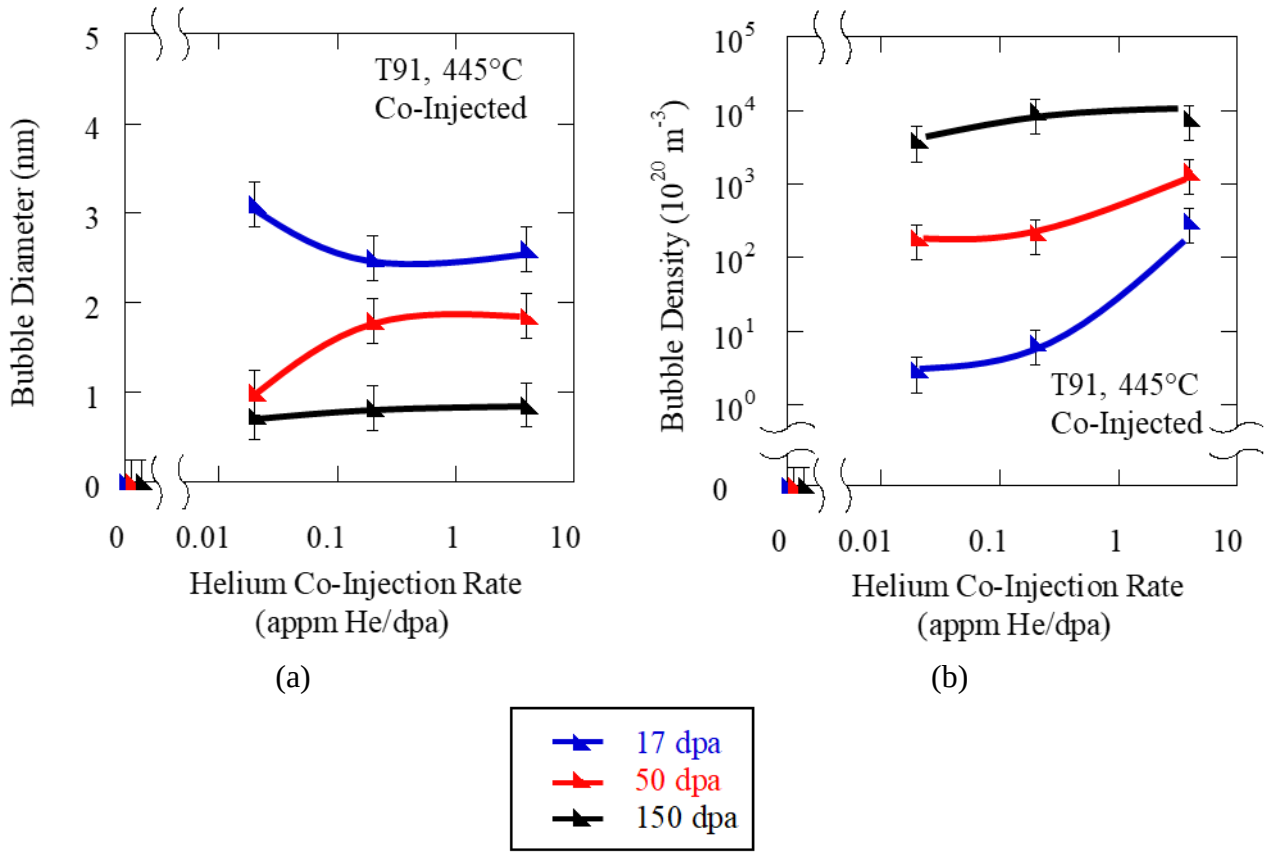

Figure 5.9: Bubble Diameter (a) and Bubble Density (b) in T91 as a function of helium co-injection rate for 17 dpa (blue), 50 dpa (red) and 150 dpa (black) at 445°C with 7-8 x 10^{-4} dpa/s.

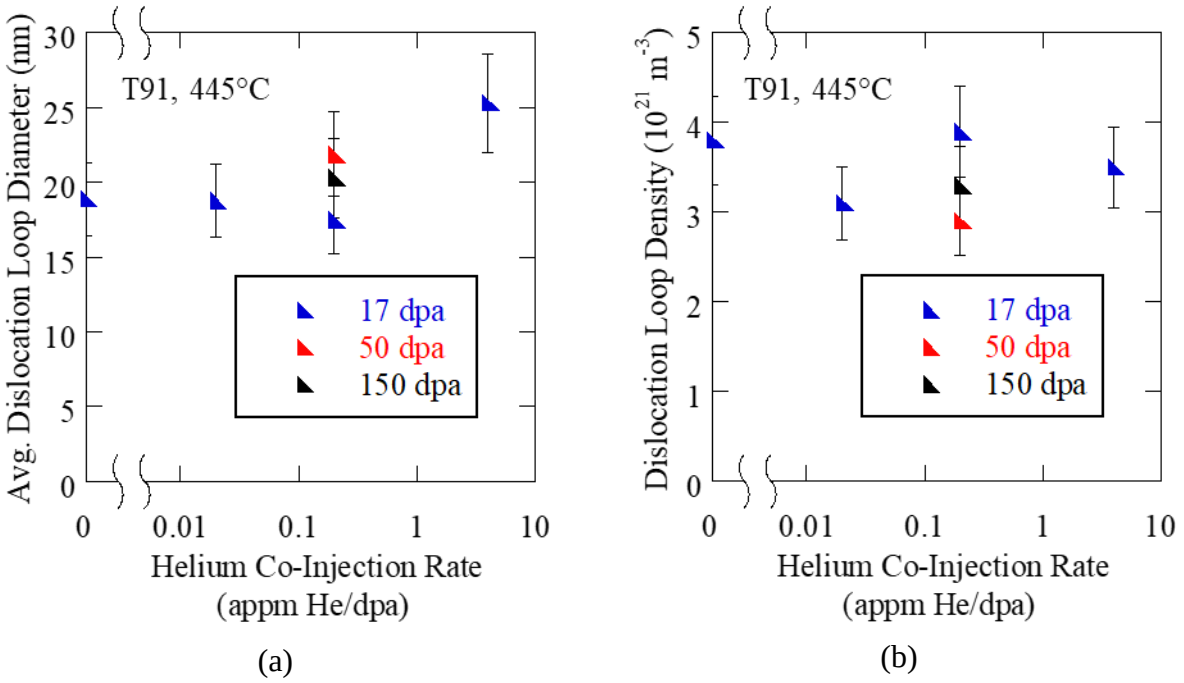

(a) (b)

Figure 5.10: Average dislocation loop diameter (a) and dislocation loop density (b) as a function of helium-to-dpa ratio for 17 dpa (blue), 50 dpa (red) and 150 dpa (black) for dual ion irradiated T91 at 445°C. Multiple damage levels were only examined for 0.2 appm He/dpa because little change was observed in the dislocation loop microstructure after 17 dpa.

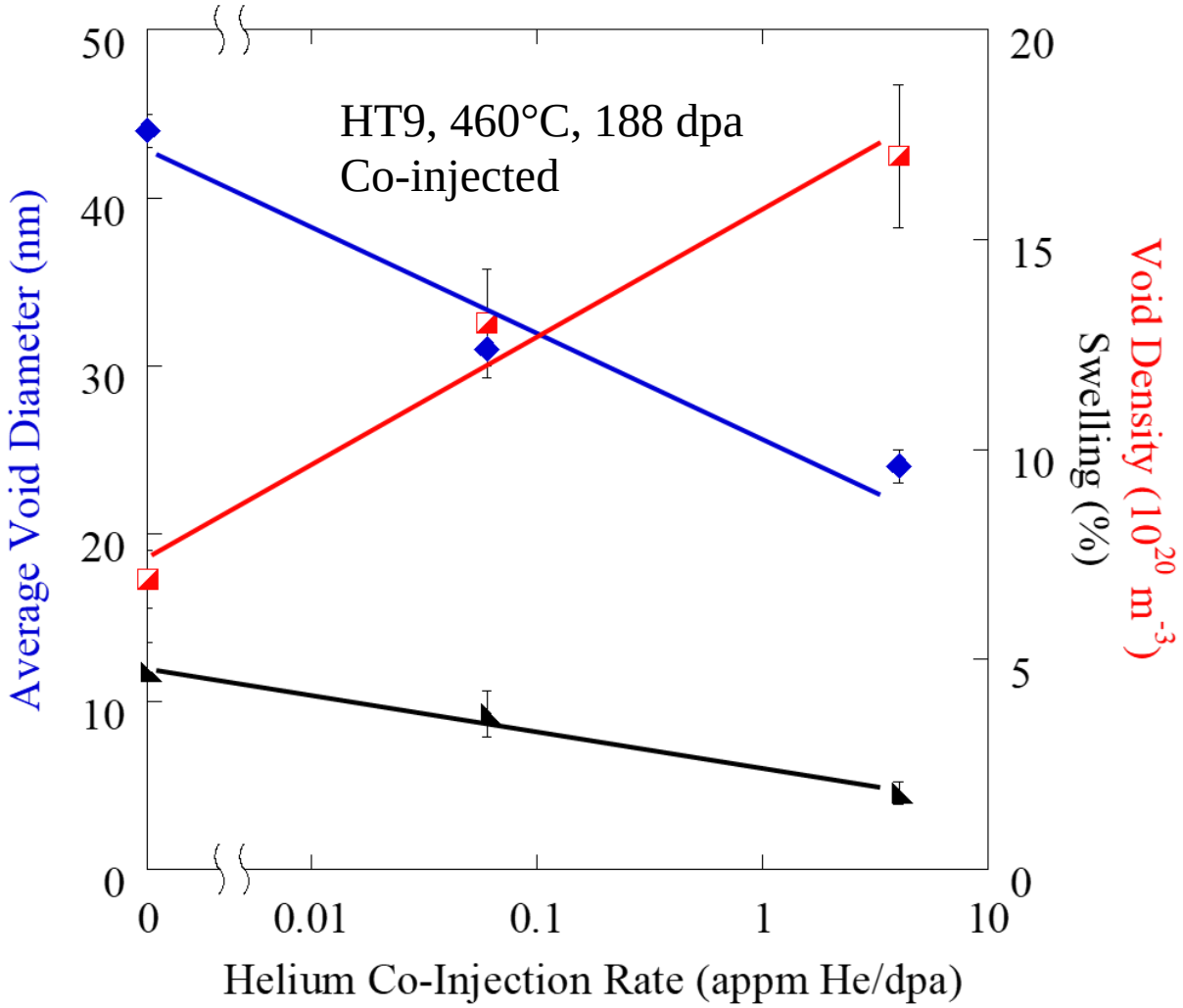

Figure 5.11: Average void diameter (blue, left axis), void density (red, right axis) and swelling (black, right axis) for dual ion irradiated HT9 at 460°C to 188 dpa with helium co-injection rates of 0 appm He/dpa, 0.06 appm He/dpa and 4 appm He/dpa.

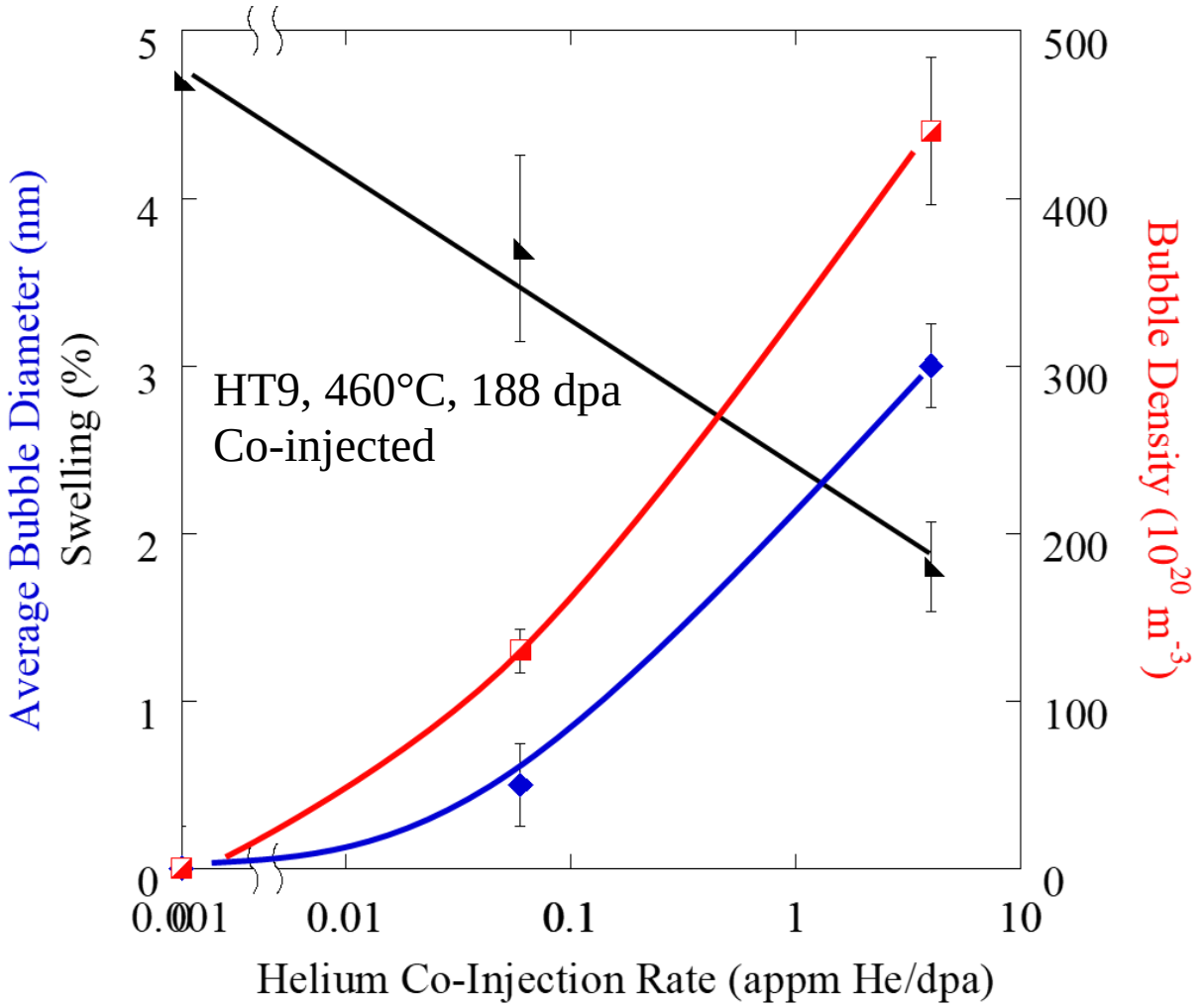

Figure 5.12: Average bubble diameter (blue diamonds, left axis), bubble density (red squares, right axis) and swelling (black triangles, left axis) for dual ion irradiated HT9 at 460°C to 188 dpa with helium co-injection rates of 0 appm He/dpa, 0.06 appm He/dpa and 4 appm He/dpa. Note that no bubbles were observed for the 0 appm He/dpa case, so the two points lie on top of each other at 0.

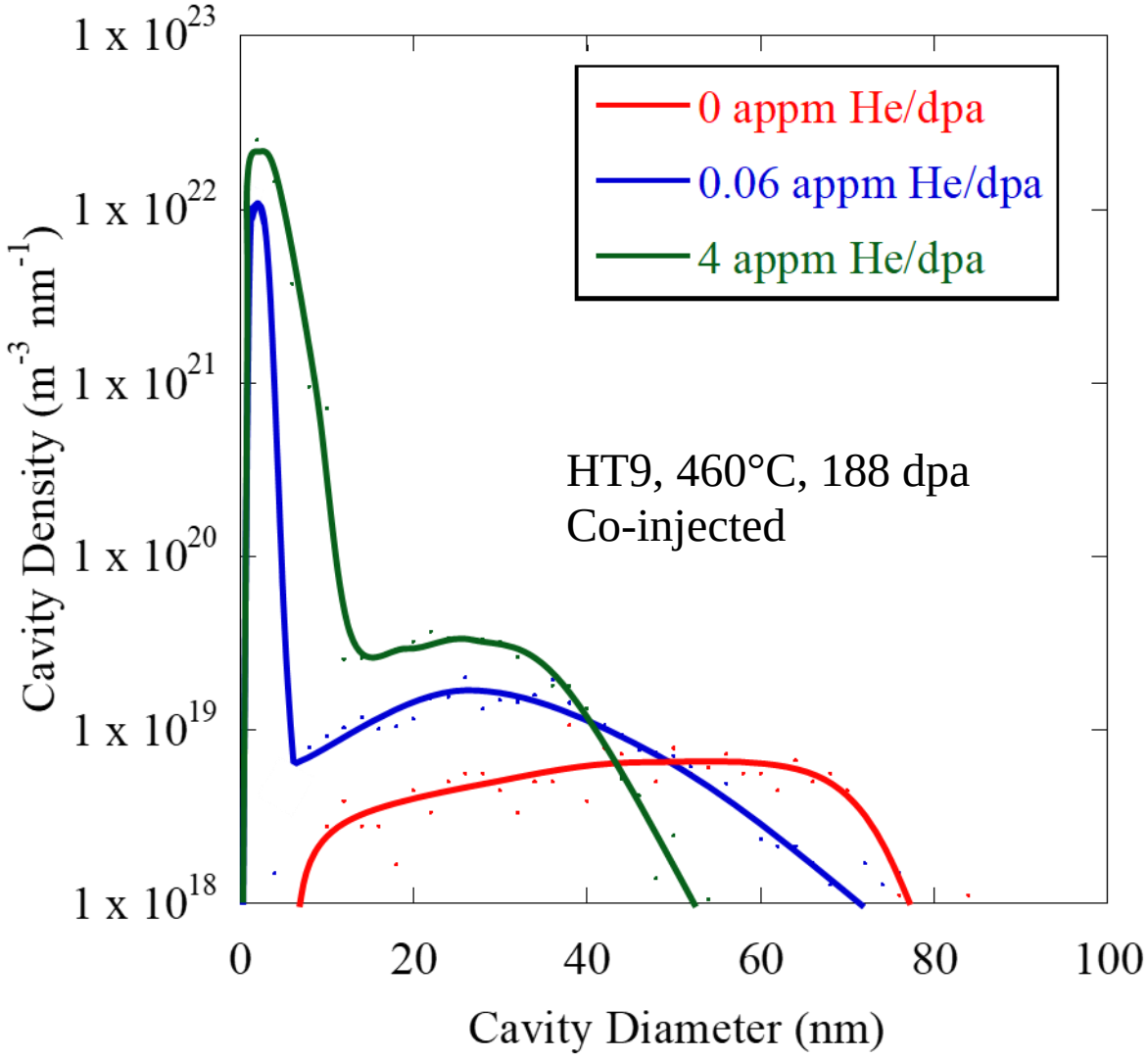

Figure 5.13: Size distributions for dual ion irradiated HT9 at 445°C to 188 dpa with helium co-injection rates of 0 appm He/dpa (red), 0.06 appm He/dpa (blue) and 4 appm He/dpa (green).

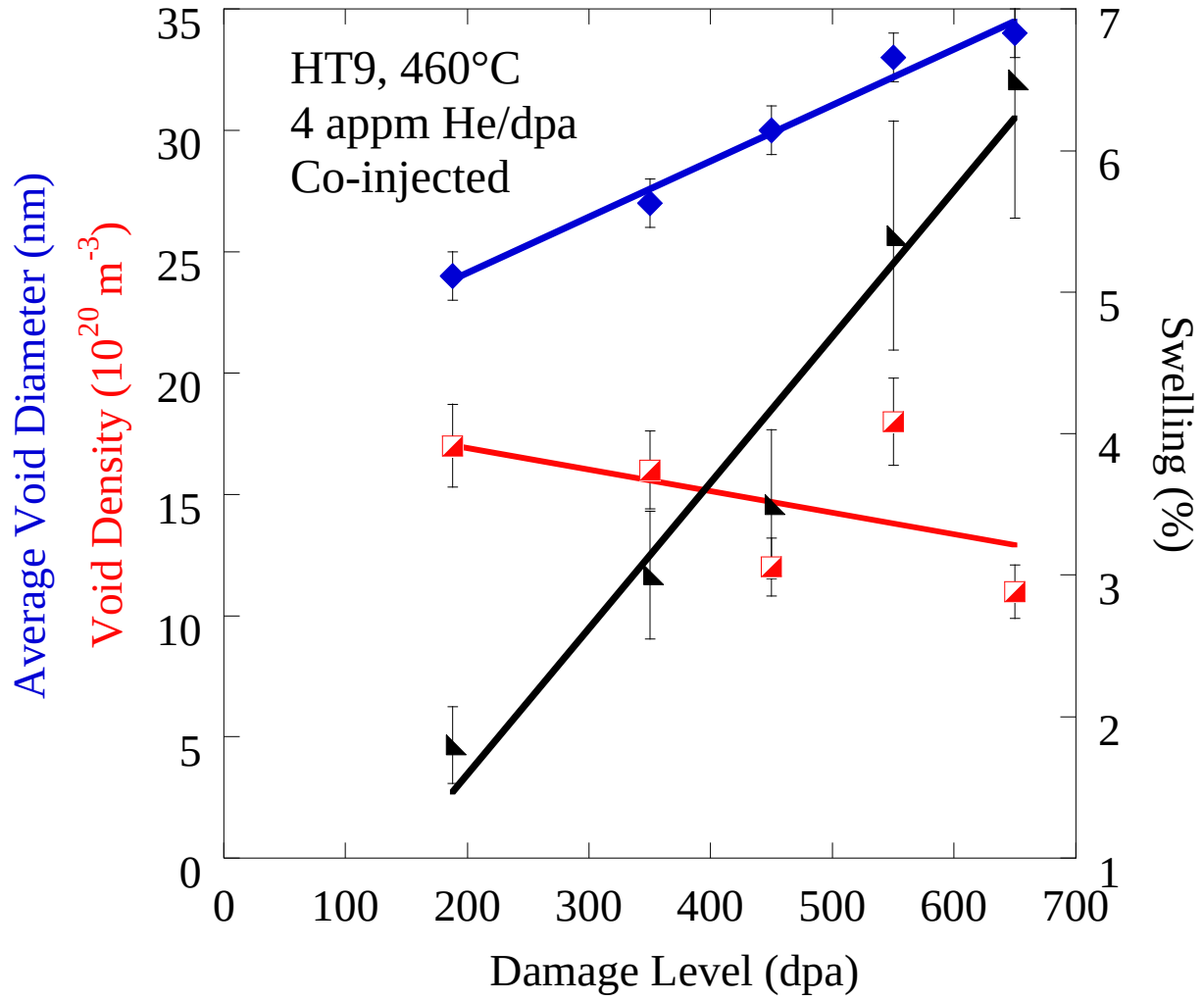

Figure 5.14: Average void diameter (blue, left axis), void density (red, left axis) and swelling (black, right axis) for dual ion irradiated HT9 at 460°C and 4 appm He/dpa.

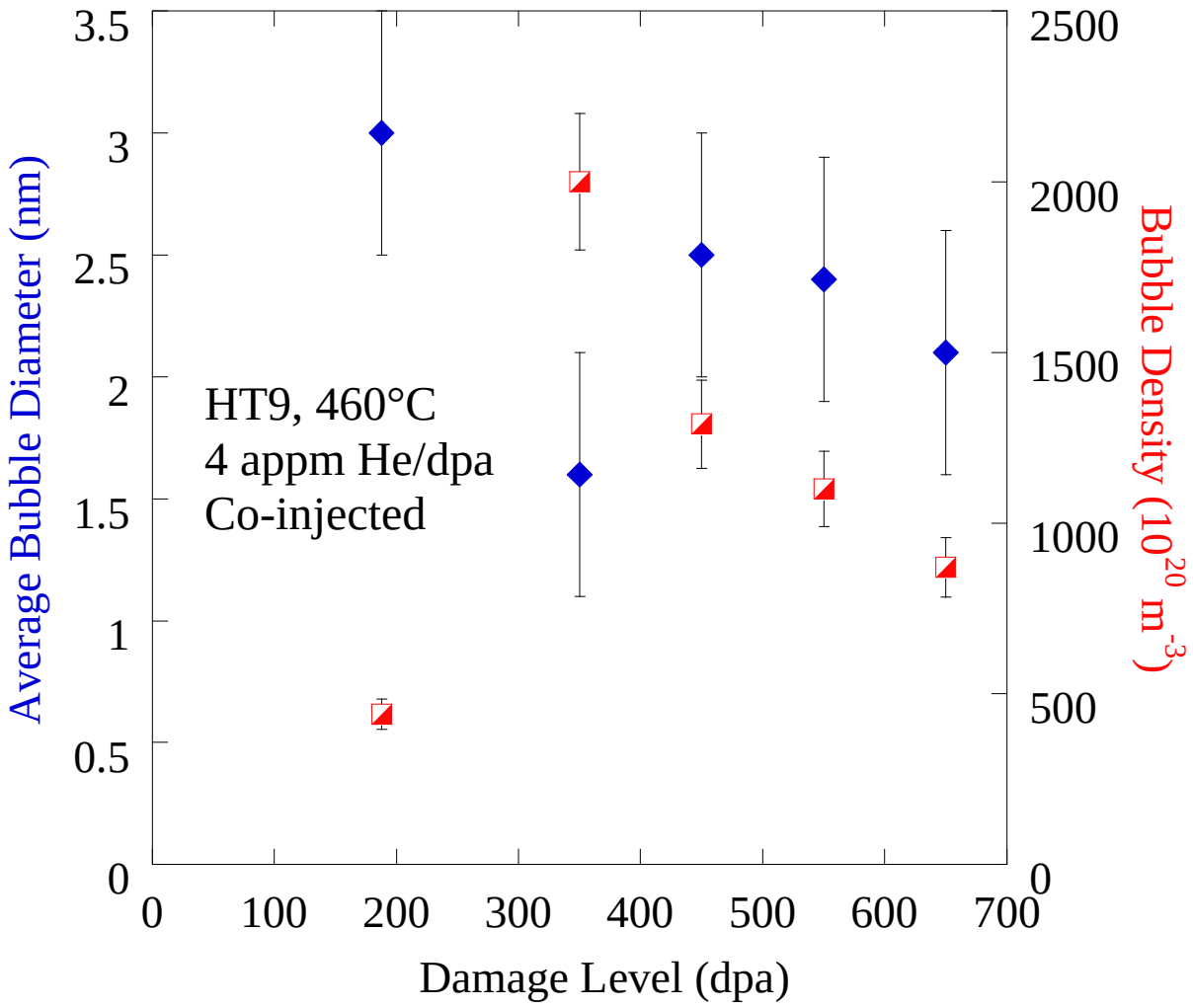

Figure 5.15: Average bubble diameter (blue, left axis) and bubble density (red, right axis) for dual ion irradiated HT9 at 460°C and 4 appm He/dpa.

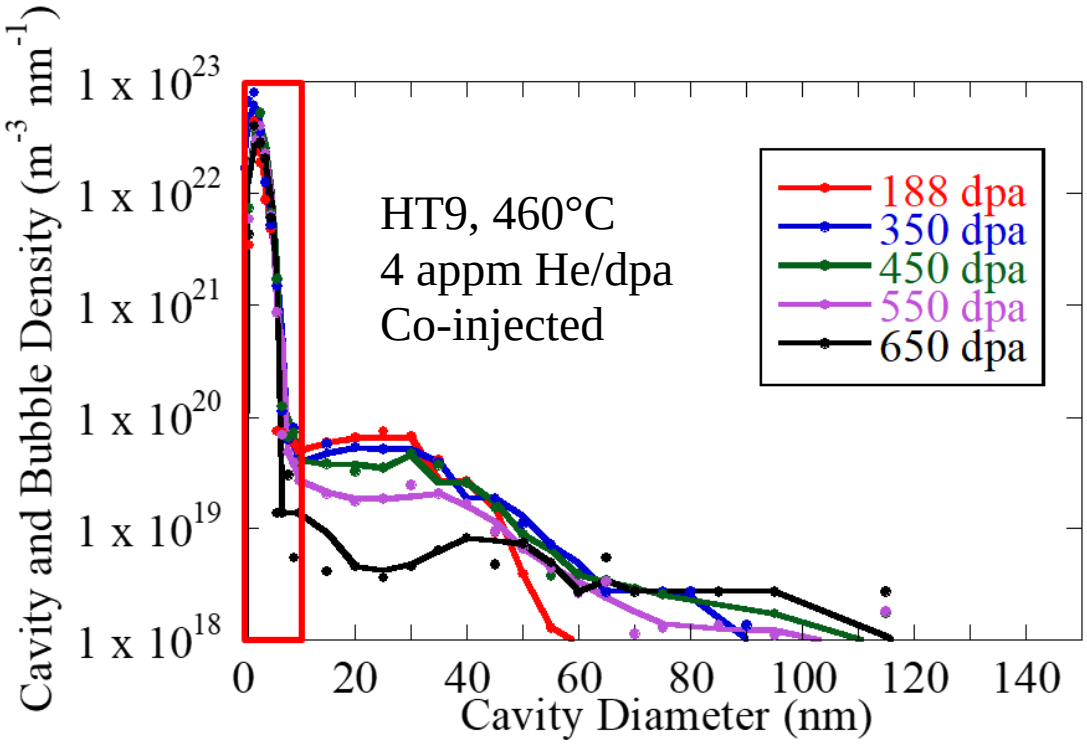

(a)

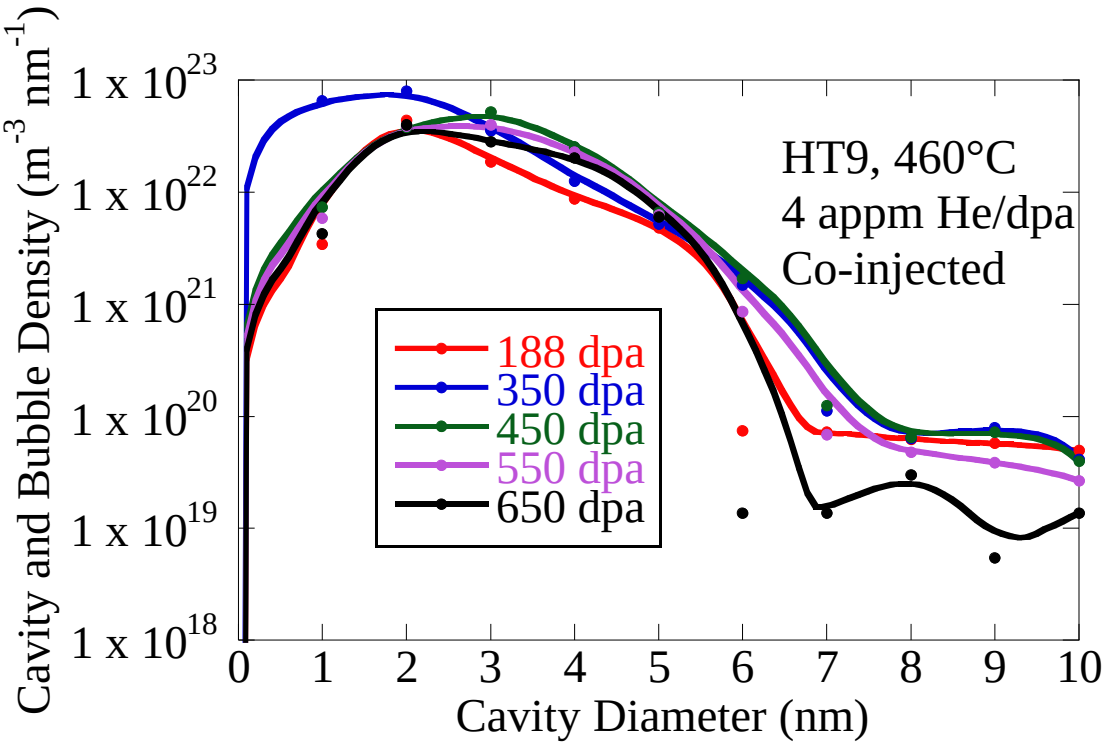

(b)

Figure 5.16: (a) Size distributions for dual ion irradiated HT9 at 460°C with 4 appm He/dpa at multiple damage levels. (b) An enhanced plot of the red region in (a) showing the fine details in the bubble region.

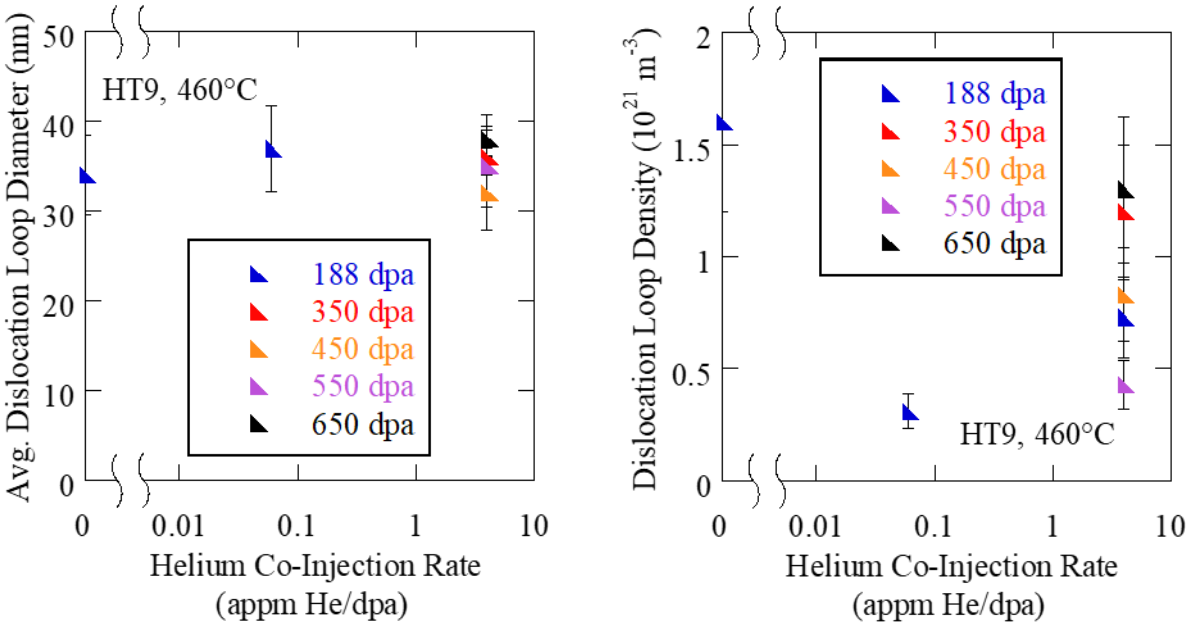

Figure 5.17: Average dislocation loop diameter (a) and dislocation loop density (b) as a function of helium-to-dpa ratio for 188 dpa (blue), 350 dpa (red), 450 dpa (orange), 550 dpa (purple) and 650 dpa (black) for dual ion irradiated HT9 at 460°C.

Chapter 6 Discussion

The results from Chapter 5 will be discussed in light of the existing understanding of the effect of helium on swelling. As mentioned in section 2.3, swelling can be broken into three damage level regimes [4,29]. At low damage levels, swelling is in the nucleation regime in which the increase in cavity density drives the swelling. At high damage levels, swelling is in the growth-dominated regime in which cavity growth drives swelling. At intermediate damage levels, both effects are active in the so-called transition regime. Helium is known to increase cavity nucleation, but its effect on cavity growth has not been studied in depth, particularly in ferritic-martensitic steels [90]. The primary conclusion of this thesis was that the relative swelling between different helium co-injection rates changes with increasing damage until the maximum swelling is observed without any helium co-injection as seen in Figure 6.1. While the data is sparse and spans a fairly broad temperature range for dual ion irradiated ferritic-martensitic steels, the data follows a consistent trend. In contrast, pre-injected irradiations show more complicated behavior. As seen in Figure 6.2, the maximum swelling still shifts to lower helium values as the damage level increases in both T91 and HT9 at 460°C. However, swelling is not maximized at 0 He even at the highest damage levels in HT9, but the maximum swelling does occur at lower He levels as the damage level increases. Both the co-implanted and pre-implanted data contrast with the behavior seen in other alloys such as copper and austenitic stainless steels (Figure 6.3). The swelling process was examined at each damage level to understand why the swelling behaves differently in FM alloys than in austenitics. The simple cavity growth rate equation based on point defect accumulation at a cavity was then used to demonstrate that the bubble sink strength due to stabilization from helium

is sufficient to capture the shift in the helium-to-dpa ratio at which maximum swelling is observed. To maintain consistency with the results section, cavities in the second peak of the bimodal size distribution, typically with diameters greater than 5 nm, will be referred to as voids and cavities in the first peak of the bimodal size distribution, typically with diameters less than 5 nm, will be referred to as bubbles.

6.1 Swelling and Cavity Evolution in Ferritic-Martensitic Steels under Helium Co-Injection

This section will examine the effects of helium co-injection rate on swelling in ferritic-martensitic steels. Helium will be shown to have a direct effect on swelling at low damage levels by enhancing the nucleation of cavities. The effect of helium then transitions to an indirect effect at high damage levels when cavity growth begins to drive swelling. Specifically, helium stabilizes bubbles and accelerates the transition from bubble to void. At low damage levels, this results the highest swelling levels at the highest helium level because the cavity (both bubble and void) density is higher. As the damage level increases, the stable bubble density increases which increases the sink density and results in a reduction in the swelling rate, such that at high enough damage levels, the swelling without helium overtakes that with any helium.

6.1.1 Effect of Helium Co-Injection Rate at a Low Damage Level

Helium stabilizes bubbles and promotes the transition of bubbles to voids. This process has been analyzed extensively in the T91 samples at 17 dpa [90]. At this damage level the maximum swelling was observed at the highest helium co-injection rate of 4 appm He/dpa and decreased monotonically with decreasing helium co-injection rate as seen in Figure 6.4. The trends in bubble density, void diameter and void density shown in Figures 5.7 and 5.9 illustrate the different swelling rates. The density of both bubbles and voids increased with increasing helium-to-dpa ratio

which is expected as helium has been shown to increase cavity nucleation. In contrast, the bubble and void diameter is relatively constant with increasing helium-to-dpa ratio.

The resulting swelling distributions for each helium level at 17 dpa are shown in Figure 6.5. To produce this plot, the swelling was calculated for each size bin using Eq. 4.4. Because the bins had different widths, the swelling was then normalized to the bin width to allow for direct comparison of the swelling between the bins. To calculate the total swelling, multiply the height of each bin by its width and then sum over all bins. One important note to interpreting this plot is that the difference in height (or lack thereof) within a bin is strictly due to density differences within the bin. Looking at the plot, two trends become obvious. First, as the helium co-injection rate increases, both the width and the height of the cavity sizes increase. The broadening distribution is important because it shows that the density is driving the swelling because of the increase in the number of cavities in every size class. The second important feature is the first hump in the distribution for the highest helium co-injection rate of 4 appm He/dpa. The hump is important because it shows that the bubbles are also contributing to the swelling at this helium level in a way that is not seen for the other helium levels. Taking these two features (the first peak in the 4 appm He/dpa case and the broadening and rising distributions) together, the trend of increasing swelling at higher helium co-injection rates is clearly the result of nucleation of a high density of cavities at the highest helium-to-dpa ratios. For the highest helium co-injection rates, the bubbles contribute significantly to the swelling while at the other helium levels, the voids dominate the swelling. Considering that 4 appm He/dpa was the highest co-injection rate examined in this study, maximizing swelling at the highest co-injection rate does not conflict with the existing experimental data for F82H. Figure 2.19(a) shows a direct comparison between this work and the results from Yamamoto in which he examined swelling in F82H at helium-to-dpa ratios

between 15 and 55 appm He/dpa at both 10 and 26 dpa at 500°C [49]. The data from this work continues to increase as it approaches the helium levels used by Yamamoto. However, there is no overlap between the helium co-injection rates. Figure 2.19(b) shows a zoomed in view of Yamamoto's data for clarity, the maximum swelling was observed at an intermediate helium co-injection rate of 40 appm He/dpa.

The swelling dependence on the cavity density at a damage level of 17 dpa is consistent with the work of Getto, Monterrosa, and others who have examined swelling in ferritic-martensitic steels and observed an incubation regime that lasts for tens of dpa [29,118,119] and suggests that the lowest damage level observed here is still in the incubation regime. While the critical bubble model is a rough approximation in that it only considers motion of single defects or a single helium atom, it still captures the basic trends observed during swelling as they relate to helium [90]. Under the critical bubble model, some helium is assumed to be required to stabilize bubbles and promote bubbles to voids. At low damage levels, this means that the highest swelling is observed at higher helium levels where more cavities are nucleated [90]. These predictions match the behavior observed in this thesis as described in the previous paragraph.

Taken together, the evidence shows that at low damage levels, the effect of helium is to stabilizes bubbles and accelerate the transition from bubble to void. These two effects result in the highest swelling at the highest helium injection rates because the cavity density is highest.

6.1.2 Effect of Helium Co-Injection Rate at an Intermediate Damage Level

As the damage level is increased, the swelling transitions from a nucleation-dominated regime in which cavity density drives the increase in swelling to a growth-dominated regime in which cavity growth and maximum size drive the increase in swelling. Thus, it would be expected that the effect of helium on swelling would change as well. The shift in maximum swelling from

4 appm He/dpa at 17 dpa to 0.2 appm He/dpa at 50 dpa as seen in Figure 6.7 demonstrates that this is in fact true. The purpose of this section is to examine how the microstructure evolved and determine the influence of helium on the swelling process.

The first step for the intermediate damage level of 50 dpa is to determine whether the swelling has transitioned to a regime in which cavity growth drives swelling. A few different parameters give an indication about whether this is the case or not. The first indication would be if the cavity density, and more importantly, the void density was constant while increasing from 17 to 50 dpa. The void densities were plotted in Figure 5.7b and the bubble densities were plotted in Figure 5.9b. Looking at both of these figures, it is clear that the density of all cavities at all helium co-injection rates increased with the increase from 17 to 50 dpa. Specifically, the void density increased by about a factor of 2 while the bubble density increased by 1-2 orders of magnitude. The increase in density indicates that nucleation is still occurring at a measurable level, so the cavity growth must be examined to determine whether swelling is still nucleation-dominated or in transition. Figure 5.7a shows the average void diameter for each helium level. In contrast to the 17 dpa case, the void diameters at 50 dpa damage level start to show some variation as the helium co-injection rate changes. The change in average diameter is also apparent in the size distributions plotted in Figure 5.3. With both the diameter and density changing, it can be difficult to determine which, if either, is driving swelling more. To try to establish which is more important, the size distribution was converted to a swelling distribution in Figure 6.8.

A comparison between Figure 6.5 and Figure 6.8 shows that the swelling due to bubbles has not changed significantly between these two damage levels even though the bubble density has increased. Thus, the increase in swelling is due to changes in the void microstructure. Comparing the swelling contribution at the larger sizes, it is apparent that both nucleation and

growth are contributing to the increase in swelling. As discussed in the previous section, an increase in the amount of swelling within a given bin is due to an increase in density. Since the swelling contribution of each of the bins in the void range increased, nucleation is still clearly having an effect on the swelling. Growth is also playing a role however as demonstrated by the fact that the swelling distribution is extending to larger sizes. The fact that nucleation and growth are both influencing swelling will be critical for understanding why the maximum swelling shifted to only slightly lower helium co-injection rates.

Having established that both nucleation and growth are occurring, it is reasonable to ask why growth is occurring more slowly for the higher helium co-injection rates as compared to the lower helium co-injection rates. The simple cavity growth rate equation and the critical bubble model provide a framework that can be used to explore which parameters or microstructural features are most likely to explain the change in swelling rate. As a reminder, the cavity growth rate equation is

$$\frac{dr}{dt} = \frac{\Omega}{r}\left[D_v C_v - D_i C_i - D_v C_{v,T} \exp\left(\frac{2\gamma}{r} - p_g\right)\right], \quad \text{Eq. 6.1}$$

where r is the radius of a cavity, t is time (and can be converted to dpa using the damage rate), Ω is the atomic volume of the alloy, D_x is the diffusion rate for vacancies (v) or interstitials (i), C_x is the concentration of vacancies (v) or interstitials (i), $C_{v,T}$ is the thermal concentration of vacancies, γ is the surface energy of the alloy and p_g is the gas pressure (assumed to be 0 for voids). The point defect concentrations can be calculated using the steady-state point defect equations

$$0 = K_0 - K_{iv} C_i \left(C_v + C_{v,T}\right) - k^2_{(i,v)} D_{(i,v)} C_{(i,v)}, \quad \text{Eq. 6.2}$$

where K_0 is the damage rate, K_{iv} is the recombination coefficient and k_x^2 is the sink strength for vacancies (v) or interstitials (i). The inputs for these equations are provided in Table 4.3. The sink strengths for dislocations can be calculated from the size distributions using

$$k_{dis}^2 = \sum_j 2\pi r_j \rho_j, \quad \text{Eq. 6.3}$$

where r_j is the average radius of and ρ_j is the dislocation density in bin j. Similarly, the cavity sink strength can be calculated from the size distribution using

$$k_{cav}^2 = \sum_j 4\pi r_j \rho_j, \quad \text{Eq. 6.4}$$

where r_j is the average radius of and ρ_j is the cavity density in bin j. The sink strengths for the microstructure in each irradiation were calculated and tabulated in Table 6.2. Finally, the swelling rate can be calculated from the growth rate using the equation

$$\frac{dS}{dt} = 4\pi r^2 \rho \frac{dr}{dt} = \sum_j 4\pi r_j^2 \rho_j \frac{dr_j}{dt}, \quad \text{Eq. 6.5}$$

where the summation has been added to allow for calculation using the size distribution. An example of the calculated growth rate overlaid with the size distribution is shown in Figure 6.9. After calculating the swelling rate for each bin, the results were summed to calculate the overall swelling rate.

The 50 dpa, 0.2 appm He/dpa irradiation of T91 was chosen as a reference case to test the significance the change in the cavity and dislocation sink strengths on the cavity growth rate because this irradiation condition was close to median in terms of helium co-injection rate and overall sink strength. The cavity and dislocation sink strengths were perturbed by 1% to determine their effect on the overall cavity growth rate because these were the primary variables that varied between irradiations. Because the cavity growth rate changes as a function of the cavity size, the swelling rate is not linearly proportional to the change in cavity growth rate and instead must be weighted by the cavity size distribution. Since the cavity size distribution varies between irradiation conditions, the significance of the cavity and dislocation sink strengths will be calculated on the cavity growth rate as a function of cavity size rather than on the swelling rate as a function of damage level or helium co-injection rate and the results were plotted in Figure 6.10.

Sizes that had negative growth rates in the reference case were ignored. A 1% increase in the cavity sink strength resulted in a drop in the cavity growth rate of ~0.37% at the larger cavity sizes. Similarly, a 1% increase in the dislocation sink strength resulted in a drop of ~0.30% in the cavity growth rate at larger cavity sizes. Both of the sink strengths had a significance approaching ~1% for cavities less than 10 nm in diameter. The changing significance of cavity and dislocation sink strengths on the cavity growth rate with cavity diameter is the reason that the significance cannot easily be converted to a significance in the swelling rate because the cavity size distribution starts to play an important role. The cavity and dislocation sink strengths can clearly play a significant role if the change is sufficiently larger, so the next questions are whether the model accurately captures the swelling rate or not, and if so, which parameter explains the difference between irradiation conditions.

Clearly, as seen in Figure 6.7, the maximum swelling shifts from 4 appm He/dpa to 0.2 appm He/dpa as the damage level is increased from 17 to 50 dpa, so a difference in swelling rate must exist. To determine whether the differences in the cavity and dislocation sink strengths were sufficient to explain the different swelling rates, the swelling rates were calculated for each of the irradiation conditions at 50 dpa and plotted alongside the measured swelling rates in Figure 6.11. Immediately, it is apparent that the model follows the measured swelling rate reasonably well although it does tend to overestimate the swelling rate slightly. With this knowledge, the variation in the temperature, damage rate, cavity sink strength and dislocation sink strength can all be examined to determine which of these four factors have the largest impact on the swelling rate. Figure 6.12 shows the cavity and dislocation sink strengths for these irradiation conditions. The dislocation sink strength had a maximum variation of 6.5×10^{14} m^{-2} to 7.7×10^{14} m^{-2} or 19%. This is much smaller than the difference in cavity sink strength which varied from 3.66×10^{12} m^{-2}

without helium to 1.56 x 10^{15} m^{-2} with 4 appm He/dpa. These sink strengths represent a change of three orders of magnitude which is significantly higher than the change for any other factor. Thus, since the calculated swelling rates match well with the measured swelling rates and the cavity sink strength is the most significant difference between each of the irradiation conditions, the shift in the maximum swelling from 4 appm He/dpa to 0.2 appm He/dpa can be explained by the difference in cavity sink strength.

One point that has not been addressed explicitly yet is how helium affected swelling in this regime besides the enhanced nucleation observed at 17 dpa. To determine that, the cavity sink strength must be broken down into the bubble contribution and the void contribution. Without helium, the cavity sink strength is due exclusively to voids and is 3.66 x 10^{12} m^{-2}. At 0.02 appm He/dpa, some bubbles are observed and the bubble sink strength at 1.91 x 10^{14} m^{-2} starts to dominate the overall cavity sink strength of 1.95 x 10^{14} m^{-2}. The bubbles also dominate the sink strength at 0.2 appm He/dpa (bubble sink strength of 2.47 x 10^{14} m^{-2} out of a total cavity sink strength of 2.96 x 10^{14} m^{-2}) and 4 appm He/dpa (bubble sink strength of 1.54 x 10^{15} m^{-2} out of a total cavity sink strength of 1.56 x 10^{15} m^{-2}). So, in addition to continuing to nucleate cavities, the stable bubble density increases which increases the sink density and results in a reduction in the swelling rate. The combined effects of the two processes results in a shift in maximum swelling toward a lower helium co-injection rate at intermediate damage levels.

6.1.3 Effect of Helium Co-Injection Rate at High Damage Level

The influence of helium on cavity growth is expected to continue as the damage level continues to increase while the impact of increased nucleation is expected to drop off. As seen in Figure 6.13, the maximum swelling has shifted fully from 4 appm He/dpa at 17 dpa to 0 appm He/dpa at 150 dpa. A similar analysis of cavity nucleation and growth that was performed at the

beginning of the previous section can be performed here to determine whether nucleation still plays a large role at 150 dpa. First, the bubble density increased slightly as seen in Figure 5.9b. In contrast, the cavity density in Figure 5.7b has either decreased or remained the same between 50 and 150 dpa for all helium co-injection rates except 0 appm He/dpa (which does not have any helium). On the other hand, the average void diameter as seen in Figure 5.7a shows that the voids have grown even more at the lower helium co-injection rates relative to the 50 dpa irradiations. The increase in void diameter is also obvious when comparing the size distributions at 50 dpa (Figure 5.3) and at 150 dpa (Figure 5.5). Finally, the swelling contribution as a function of cavity size was plotted for 150 dpa in Figure 6.14. As compared to the other swelling contribution plots (17 dpa in Figure 6.5 and 50 dpa in Figure 6.8), the obvious difference is the extension of the swelling contribution to larger sizes as opposed to an increase in the height for any given bin. This is a strong indication that cavity growth has become the driving factor for swelling.

Having established that the swelling is in the growth-dominated regime, the cavity growth equation and critical bubble model can be used again to determine which factors are most important for influencing swelling. The measured and calculated swelling rates were plotted in Figure 6.15. While the swelling rate is overestimated for most helium-to-dpa ratios, the trend still follows the data reasonably well indicating that the model is capturing the swelling behavior.

Following a similar process to what was done for the intermediate damage level, the most important factor between the cavity and dislocation sink strengths that drive the change in swelling rate as a function of helium co-injection rate can be examined. Figure 6.16 shows the cavity and dislocation sink strengths for these irradiation conditions. The dislocation sink strength had a maximum variation of 6.5×10^{14} m^{-2} to 7.7×10^{14} m^{-2} or 19%. This is decent, but it is much smaller than the difference in cavity sink strength which varied from 5.09×10^{13} m^{-2} without helium to

6.01 x 10^{15} m^{-2} with 4 appm He/dpa. These sink strengths represent a change of two orders of magnitude which is significantly higher than the change for any other factor that changed in the calculation. Thus, the difference in swelling can be explained almost exclusively by the difference in cavity sink strength.

Using a similar comparison to the intermediate damage level, the cavity sink strength can be shown to be comprised almost exclusively by the bubble sink strength. Without helium, the cavity sink strength is exclusively to voids and is 5.09 x 10^{13} m^{-2}. At 0.02 appm He/dpa, some bubbles are observed and the bubble sink strength at 1.83 x 10^{15} m^{-2} dominates the overall cavity sink strength of 1.87 x 10^{15} m^{-2}. The bubbles also dominate the sink strength at 0.2 appm He/dpa (bubble sink strength of 5.03 x 10^{15} m^{-2} out of a total cavity sink strength of 5.09 x 10^{15} m^{-2}) and 4 appm He/dpa (bubble sink strength of 5.99 x 10^{15} m^{-2} out of a total cavity sink strength of 6.01 x 10^{15} m^{-2}).

One final piece of supporting evidence that the helium-stabilized bubble density shifts the maximum swelling to a condition without helium comes from the irradiations of HT9 to 188 dpa. Figure 6.17 shows that the maximum swelling for HT9 irradiated at 460°C to 188 dpa is observed for the case without helium. The swelling rate for each of these conditions can be calculated using the cavity and dislocation sink strengths tabulated in Table 6.2 and plotted in Figure 6.19. Unfortunately, a direct comparison cannot be made between the measured and calculated swelling rates because only one damage level exists for the HT9 irradiations, so any measured swelling rate would inherently under-estimate the swelling rate at 188 dpa because it includes the nucleation regime. However, the calculated swelling rate can still be used to determine whether the high cavity sink strength at 4 appm He/dpa does in fact explain the lower swelling rate. Although the calculated swelling rate at 0.06 appm He/dpa is slightly higher than the calculated swelling rate at

0 appm He/dpa, the two values are well within error of each other. In contrast, the calculated swelling rate at 4 appm He/dpa is well below the two other helium co-injection rates. So while the equation does not completely capture the real swelling rates, the difference is likely due to error in the input parameters rather than an issue with the model. The maximum swelling at 0 appm He/dpa combined with the results of the cavity growth rate equation in HT9 provide one more piece of evidence that the helium-stabilized bubble microstructure reduces the swelling rate at high damage levels pushing the maximum swelling to the irradiation condition without any injected helium.

At this point, it is also worthwhile to step back, look at the difference in swelling and swelling rate between the two alloys, and determine whether the initial microsctructure provides any insight into the behavior of helium. As mentioned in sections 5.1.1 and 5.2.1, the non-irradiated sink strengths of T91 and HT9 were 1×10^{15} m^{-2} and 3×10^{14} m^{-2}, respectively. Breaking it down further, network dislocations were the largest contributor for both systems (1×10^{15} m^{-2} for T91 and 2×10^{14} m^{-2} for HT9), grain boundaries were significant for HT9, but not T91 (4×10^{13} m^{-2} for T91 and 9×10^{13} m^{-2} for HT9), and precipitates were negligible for both (on the order of 10^{12} m^{-2}). Of note, the precipitates in HT9 were almost exclusively on the grain boundaries while T91 had small V,Cr-nitrides distributed throughout the matrix. The swelling of T91 at 150 dpa and 445°C and HT9 at 188 dpa and 445°C is plotted as a function of helium-to-dpa ratio in Figure 6.20(a). It is immediately clear that the HT9 swells to a much higher level that cannot be explained by just the difference in damage which indicates that the starting microstructure, specifically the large difference in dislocation sink strength, is playing a large role. Another question that can be asked is whether the starting microstructure influences the behavior of helium. Figure 6.20(b) shows the bubble density as a function of helium-to-dpa ratio for the same conditions in T91 and HT9. The bubble density in T91 is about an order of magnitude higher than

that observed in HT9 for all conditions in which bubbles nucleated. Dislocations and precipitates are known to be traps for helium, and T91 had almost an order of magnitude higher dislocation density as compared to HT9. While the factor being exactly the same is likely a coincidence, the fact that the bubble density is correlated well with the sinks, and dislocations specifically, indicates that the dislocations do serve as a trap for helium. This would also help to explain why bubbles continued to nucleate as the damage level increased because the dislocations continued to absorb helium.

In conclusion, as the damage level increases, the stable bubble density increases due to the continued addition of helium which increases the sink density and results in a reduction in the swelling rate, such that at high enough damage levels, the swelling without helium overtakes that with any helium as seen in Figure 6.13.

6.2 Application of the Effects of Helium to the Difference Between Co-Injection and Pre-Injection of Helium

In this section, the effects of helium at high damage will be applied to the analyze the differences between pre-injected and co-injected helium irradiations. The most direct comparison that can be made is between the T91 using co-injected helium from this work and the T91 irradiated using pre-injected helium by Monterrosa in [119]. There are a few minor differences, specifically, this work used heat 30176 while Monterrosa used heat C2269. The compositions of heat 30176 and heat C2269 are provided in Table 4.1. Because both alloys are T91, they have similar compositions. The primary differences are higher nickel and copper concentrations in C2269 as compared to 30176. Both elements are expected to precipitate, nickel as g-phase and copper as small copper precipitates. However, the compositional differences are not expected to be high enough to lead to a significant difference in precipitation or an effect on swelling. The other

important difference is the heat treatment which determines the average lath diameter and the network dislocation density. Heat C2269 was normalized at 1066°C for 46 minutes followed by tempering at 790°C for 42 minutes. Heat 30176 was normalized at 1038°C for 30 minutes followed by tempering at 760°C for 30 minutes. Both heats were air cooled both between the normalizing and tempering steps and after tempering. These heat treatments lead to slightly different starting microstructures. Heat 30176 had an average effective lath diameter of 0.8 μm with a dislocation density of ~5 x 10^{14} m^{-2} while heat C2269 had an average effective lath diameter of 1.6 μm with a dislocation density of ~3 x 10^{14} m^{-2}. From these numbers, it is clear that heat 30176 had a slightly higher initial sink strength although this is not expected to change the effects of helium. Another difference between the irradiations was the temperature. The irradiations performed for this work were at 445°C used in this work while Monterrosa used a temperature of 460°C. The swelling from both sets of data are plotted in Figure 6.21(a) as a function of helium-to-dpa ratio (appm He/dpa) and Figure 6.21(b) as a function of helium concentration (appm He). In both cases, it is clear that swelling follows a similar trend with helium as the damage level increases. As established by this work under co-injection, the maximum swelling shifts to lower helium co-injection rates as the damage level is increased. Similar behavior is seen under pre-injection. The maximum swelling is observed in the sample that was pre-implanted with 10 appm He at the lowest damage level of 50 dpa (for a helium-to-dpa ratio of 0.2 appm He/dpa). As the damage level was increased to 150 and 300 dpa, the maximum swelling shifted to the condition without any helium pre-injected. Even though the trends with helium are consistent, more information can be determined by examining the two different irradiation types in more detail.

To explore whether these behaviors are consistent independent of helium injection mode, the cavity growth equation can be applied to the work by Monterrosa. The sink strengths and

microstructural values were taken from the work by Monterrosa and input into the model with the appropriate irradiation parameters (for exact details, see [90]). The measured and calculated swelling rates from both this work and Monterrosa's work have been plotted for multiple damage levels as a function of helium-to-dpa ratio in Figure 6.22(a) and Figure 6.22(b). Note that the helium content in the pre-injected samples did not change with damage level, so the data points for a given single ion condition gradually shift toward lower helium-to-dpa ratios. As discussed previously, the measured and calculated swelling rates were in reasonable agreement in both magnitude and trend for the co-injected samples. The maximum swelling was to be at the intermediate helium co-injection rate of 0.2 appm He/dpa at 50 dpa with a shift to 0 appm He/dpa as the damage level increased to 150 dpa. The swelling rate for the pre-injected samples followed similar trends, but the magnitudes did not match as well. Both the measured and calculated swelling rates were maximized 10 appm He (0.2 appm He/dpa) at 50 dpa. However, the value differed by about two orders of magnitude. As the damage level was increased, the maximum swelling rate (both measured and calculated) shifted down to 0 appm He (0 appm He/dpa) at 150 and 300 dpa. Overall, both systems show similar trends in both the measured and calculated swelling rates.

The two order of magnitude discrepancy between measured and calculated swelling rates in the pre-injected samples as seen in Figure 6.22(b) is worth more examination since the model captures the behavior with co-injected helium well in Figure 6.22(a). Part of the observed difference can be attributed to the method used to image cavities for the pre-injected helium conditions. Only traditional STEM imaging was performed on those samples which has the potential to miss the smaller cavities that through-focus BFTEM or Integrated Differential Phase Contrast STEM (iDPC-STEM) can capture. So, it is possible that some of the smaller features

were missed resulting in a lower calculated sink strength that actually existed in the samples. Rerunning the calculations using a higher sink strength indicates that a sink strength of 1-2 x 10^{15} m^{-2} would be required to match the swelling rate observed in the samples. Assuming an average diameter of 1 nm, this corresponds to a bubble or feature density of ~2 x 10^{23} m^{-3}. As a point of comparison, the co-injected helium irradiation at 150 dpa and 0.02 appm He/dpa had a helium concentration was 3 appm He. The sink strength measured in that sample was 1.87 x 10^{15} m^{-2} from a bubble density of 4 x 10^{23} m^{-3}. Since more of the helium would be expected to go to bubbles under pre-implantation (since radiation induced microstructural changes have not produced other sinks for the helium), it is reasonable to conclude that the discrepancy in swelling rate is due to small features that were missed due to the imaging technique.

One final piece of evidence can be extracted by comparing the evolution of swelling in HT9, heat 84425, under co-injection at 4 appm He/dpa and pre-injection of 10 appm He. Figure 6.23 shows both (a) the swelling and (b) the sink strengths for single-ion irradiations with pre-injected helium (PI) and dual-ion irradiations with co-injected helium (CI) as a function of damage level. Before jumping into a discussion of the data and the implications of the observed swelling, it is important to acknowledge that the helium concentration between the two irradiations varied by almost two orders of magnitude (at 188 dpa, the total helium concentration with 4 appm He/dpa is ~750 appm He, by 650 dpa, this jumps to ~2600 appm He). Starting with the swelling depicted in Figure 6.23(a), both irradiation methods display a similar amount of swelling at 188 dpa, but the pre-injected samples swell more quickly (~0.03 %/dpa) as compared to the co-injected samples (~0.01 %/dpa). Furthermore, the incubation damage (or the damage level at which the linear fit to the data intersects the x-axis which has traditionally been defined to be the onset of growth-dominated swelling), is ~120 dpa for the pre-injected samples and only ~50 dpa for the co-injected

samples indicating that the samples with co-injected helium entered the growth-dominated swelling regime earlier, but did not grow as quickly afterwards.

Moving to the sink strengths, an examination of the sink strength in Figure 6.23(b) was performed to determine whether it fit the trends observed in the T91 samples. The total sink strength of the microstructure is ~2.5 times larger in the co-injected helium case as compared to the pre-injected helium case. So the condition with the higher sink strength exhibits a lower swelling rate consistent with the behavior observed in T91. Breaking the sink strength into components (ignoring the grain boundaries and splitting up cavities into bubbles and voids), the dislocation sink strength and void sink strength is similar magnitude between the two. On the other hand, the pre-injected condition has a much higher precipitate sink strength (driven primarily by M_2X precipitates) while the co-injected condition has a much higher bubble sink strength. By using these sink strengths in the cavity growth rate equation (and treating precipitates as unbiased sinks), a swelling rate of 0.31 %/dpa was calculated for the single-ion irradiated samples as compared to a measured swelling rate of 0.03 %/dpa for about a factor of ten difference. For the dual-ion irradiated samples, the calculated swelling rate was 0.05 %/dpa as compared to a measured swelling rate of 0.01 %/dpa for a factor of 5 difference. There are a few possible explanations for this discrepancy. The most obvious one would be the existence of bubbles that were below the resolution of the microscope used to image the samples. A higher bubble density would increase the sink strength and correspondingly reduce the amount of swelling. Further simulations indicate that a difference in sink strength of about a factor of two results in a change in swelling rate of about a factor of five. That would require a very high density of additional bubbles, so there are likely other underlying factors. While the exact numbers did not match, they were off by similar

amounts in the same direction. This provides confidence that the microstructure changes explain the difference in swelling rather than an effect of the helium content.

The final, and perhaps most important question from the of HT9 analysis is whether the difference in cavities, and specifically bubbles, is due to the helium injection method or the significant difference in helium concentration. Unfortunately, this study does not have enough data to draw a conclusion to that regard, but Packan et Al. looked at the effects of helium implantation method in an Fe-17Ni-17Cr-2.5Mo austenitic stainless steel [73]. In this work, irradiations were with helium co-injected at a rate of 20 appm He/dpa and with helium pre-injected at room temperature to a level equivalent to 20 appm He/dpa (20 appm He at 1 dpa, 200 appm He at 10 dpa and 1400 appm He at 70 dpa) at three different damage levels. (No injection, hot pre-injection and triple beam irradiation were also performed, but are irrelevant to this discussion.) At all damage levels, the swelling was lower, the cavity diameter was lower, and the density was higher in the cold pre-injected condition relative to the co-injected condition. At the highest damage level of 70 dpa, Packan was able to see the formation of a bimodal size distribution in the pre-injected condition, but not the co-injected condition. These results indicate that, for the same final helium concentration, helium pre-injection should produce a cavity microstructure with a higher sink strength and lower swelling overall. Applying Packan's results to the swelling behavior observed in HT9 in Figure 6.23(a), it becomes clear that the difference in the bubble microstructure is due to the difference in helium concentration rather than the helium injection method. If the irradiations were performed with the same helium concentration at each damage level, it would be expected that the pre-injected samples would exhibit a larger bubble microstructure and lower swelling rate.

To wrap everything up, plots of the helium-to-dpa ratio and total helium concentration at which the maximum swelling was observed are shown in Figure 6.24. Across three different alloys

(F82H, HT9 and T91), four different heats and two modes of helium injection the effect of helium with increasing damage level shows a very clear trend. At low damage levels during nucleation dominated swelling, the maximum swelling is observed at a relatively high helium-to-dpa ratios and concentrations. As the damage level is increased and swelling entered the transition and then growth-dominated regimes, the maximum swelling shifted toward lower and lower helium-to-dpa ratios and concentrations. Ultimately, the maximum swelling was observed to occur without any helium at all. Furthermore, for the damage levels at which the two irradiation types overlapped (50 and 150 dpa), the maximum swelling was observed to occur at the same helium-to-dpa ratio/total helium concentration (0.2 appm He/dpa and 10 appm He at 50 dpa and 0 appm He/dpa and 0 appm He at 150 dpa). This also extends to the HT9 with co-injected helium at 188 dpa which is similar in damage level to 150 dpa and had the maximum swelling at 0 appm He/dpa as well. The fact that the shift in maximum swelling toward lower helium-to-dpa ratios and concentrations occurs across multiple ferritic-martensitic alloys and under both pre-injection and co-injection provides strong evidence that this process occurs for all ferritic-martensitic steels and is not just an artifact of a single alloy, heat or irradiation method.

Table 6.1: Table of input parameters for calculating the cavity growth rate equation.

Parameter	**Value**	**Reference**
Temperature, T	Input parameter	This work
Damage Rate, K_0	Input parameter	This work
Helium Co-Injection Rate	Input parameter	This work
N	8.34×10^{22} at/cm^3	[10]
Lattice parameter (a)	0.288 nm	[10,97]
Sink strength	From microstructure	This work and [117]
ω_i	2.9×10^{12} s^{-1}	[10]
ω_v	1.6×10^{13} s^{-1}	[10]
γ	1.75 J/m^2	[97]
E_{vm}	0.63 eV	[97]
E_{vf}	1.6 eV	[10]
E_{im}	0.35 eV	[10]
S_f	2.17k	[38]
Dislocation Bias	5%	See text.

Table 6.2: Sink strengths, measured and calculated swelling rates, and the ratio of the two for ferritic-martensitic steels irradiated in MIBL under the listed conditions. Dislocations sink strengths marked with an * were not measured directly, but instead used the sink strength measured at the same damage level but different helium content.

Material	Helium Injection Method	Damage Level (dpa)	Helium-to-dpa Ratio (appm He/dpa)	Helium Concentration (appm He)	Temperature (°C)	Cavity Sink Strength (m^{-2})	Dislocation Sink Strength (10^{14} m^{-2})	Measured Swelling Rate (%/dpa)	Calculated Swelling Rate (%/dpa)	Ratio of Calculated To Measured Swelling
HT9	Co-Injected	188	0.000	0.00	460	1.91×10^{14}	3.5×10^{14}	0.025	0.510	20.4
HT9	Co-Injected	188	0.060	11.28	460	3.14×10^{14}	3.7×10^{14}	0.568	0.568	28.9
HT9	Co-Injected	188	4.000	752.00	460	1.09×10^{15}	3.2×10^{14}	0.010	0.119	12.4
HT9	Co-Injected	350	4.000	1400.00	460	2.28×10^{15}	3.3×10^{14}	0.007	0.046	6.2
HT9	Co-Injected	450	4.000	1800.00	460	2.25×10^{15}	3.2×10^{14}	0.005	0.038	7.6
HT9	Co-Injected	550	4.000	2200.00	460	2.03×10^{15}	3.5×10^{14}	0.019	0.028	1.5
HT9	Co-Injected	650	4.000	2600.00	460	1.38×10^{15}	3.7×10^{14}	0.011	0.018	1.7
HT9	Pre-Injected	188	0.053	10.00	460	2.25×10^{14}	3.2×10^{14}	0.015	0.349	22.6
HT9	Pre-Injected	350	0.029	10.00	460	2.67×10^{14}	3.2×10^{14}	0.019	0.303	15.8
HT9	Pre-Injected	450	0.022	10.00	460	3.37×10^{14}	3.5×10^{14}	0.028	0.258	9.2
HT9	Pre-Injected	550	0.018	10.00	460	2.97×10^{14}	4.6×10^{14}	0.045	0.313	7.0
HT9	Pre-Injected	650	0.015	10.00	460	2.67×10^{14}	4.5×10^{14}	0.027	0.318	11.8
T91	Co-Injected	17	0.000	0.00	445	3.55×10^{11}	7.3×10^{14}	0.0008	0.0033	392.0
T91	Co-Injected	50	0.000	0.00	445	3.66×10^{12}	$*6.5 \times 10^{14}$	0.0318	0.0415	0.9
T91	Co-Injected	150	0.000	0.00	445	5.09×10^{13}	$*7.0 \times 10^{14}$	0.4067	0.6197	1.0
T91	Co-Injected	17	0.020	0.34	445	1.16×10^{13}	6.8×10^{14}	0.0012	0.0599	49.5
T91	Co-Injected	50	0.020	1.00	445	1.95×10^{14}	$*6.5 \times 10^{14}$	0.0150	0.0220	1.5
T91	Co-Injected	150	0.020	3.00	445	1.87×10^{15}	$*7.0 \times 10^{14}$	0.1448	0.2028	1.5
T91	Co-Injected	17	0.200	3.40	445	2.36×10^{13}	7.1×10^{14}	0.0300	0.1818	6.1
T91	Co-Injected	50	0.200	10.00	445	2.96×10^{14}	6.5×10^{14}	0.2218	0.5240	2.4
T91	Co-Injected	150	0.200	30.00	445	5.09×10^{15}	7.0×10^{14}	0.3034	0.8980	3.0
T91	Co-Injected	17	4.000	68.00	445	5.40×10^{14}	7.7×10^{14}	0.0647	0.0756	1.2
T91	Co-Injected	50	4.000	200.00	445	1.56×10^{15}	$*6.5 \times 10^{14}$	0.0581	0.1200	2.1
T91	Co-Injected	150	4.000	600.00	445	6.01×10^{15}	$*7.0 \times 10^{14}$	0.0596	0.0107	0.2
T91	Pre-Injected	50	0.000	0.00	460	7.40×10^{13}	$*1.1 \times 10^{15}$	0.0018	0.2024	111.0
T91	Pre-Injected	150	0.000	0.00	460	2.12×10^{14}	9.9×10^{14}	0.0083	0.5531	66.7
T91	Pre-Injected	300	0.000	0.00	460	3.70×10^{14}	$*5.7 \times 10^{14}$	0.0199	0.8978	45.2
T91	Pre-Injected	50	0.020	1.00	460	1.10×10^{14}	$*1.1 \times 10^{15}$	0.0021	0.2559	120.0
T91	Pre-Injected	150	0.007	1.00	460	1.99×10^{14}	6.0×10^{14}	0.0047	0.6433	136.0
T91	Pre-Injected	300	0.003	1.00	460	3.83×10^{14}	$*5.7 \times 10^{14}$	0.0221	0.8996	40.6
T91	Pre-Injected	50	0.200	10.00	460	1.29×10^{14}	1.1×10^{15}	0.0024	0.2880	116.0
T91	Pre-Injected	150	0.067	10.00	460	2.16×10^{14}	6.9×10^{14}	0.0044	0.6327	145.0
T91	Pre-Injected	300	0.033	10.00	460	3.14×10^{14}	5.7×10^{14}	0.0143	0.8473	59.0
T91	Pre-Injected	50	2.000	100.00	460	1.82×10^{14}	$*1.1 \times 10^{15}$	0.0010	0.0000	0.0
T91	Pre-Injected	150	0.667	100.00	460	2.31×10^{14}	6.5×10^{14}	0.0015	0.2270	153.0
T91	Pre-Injected	300	0.333	100.00	460	2.07×10^{14}	$*5.7 \times 10^{14}$	0.0027	0.2762	101.0
T91	Pre-Injected	50	20.000	1000.00	460	8.89×10^{14}	$*1.1 \times 10^{15}$	0.0012	0.0000	0.0
T91	Pre-Injected	150	6.667	1000.00	460	8.69×10^{14}	5.5×10^{14}	0.0005	0.0000	0.0
T91	Pre-Injected	300	3.333	1000.00	460	8.51×10^{14}	$*6.5 \times 10^{14}$	0.0001	0.0000	0.0

Table 6.3: Chemical Composition (wt%) of HT9, heat 84425, and T91, heat 30176 [9,127].

Heat	Fe	Cr	Mn	Nb	Mo	Ni	Si	V	C	N	Al	S	P	Ti	Cu	W
30176	Bal.	8.76	0.44	0.086	0.86	0.10	0.25	0.23	0.091	0.052	0.0004	0.002	0.007	0.003	0.062	0.004
C2269	Bal.	8.37	0.45	-	0.90	0.21	0.28	0.22	0.10	-	-	-	-	-	0.17	-

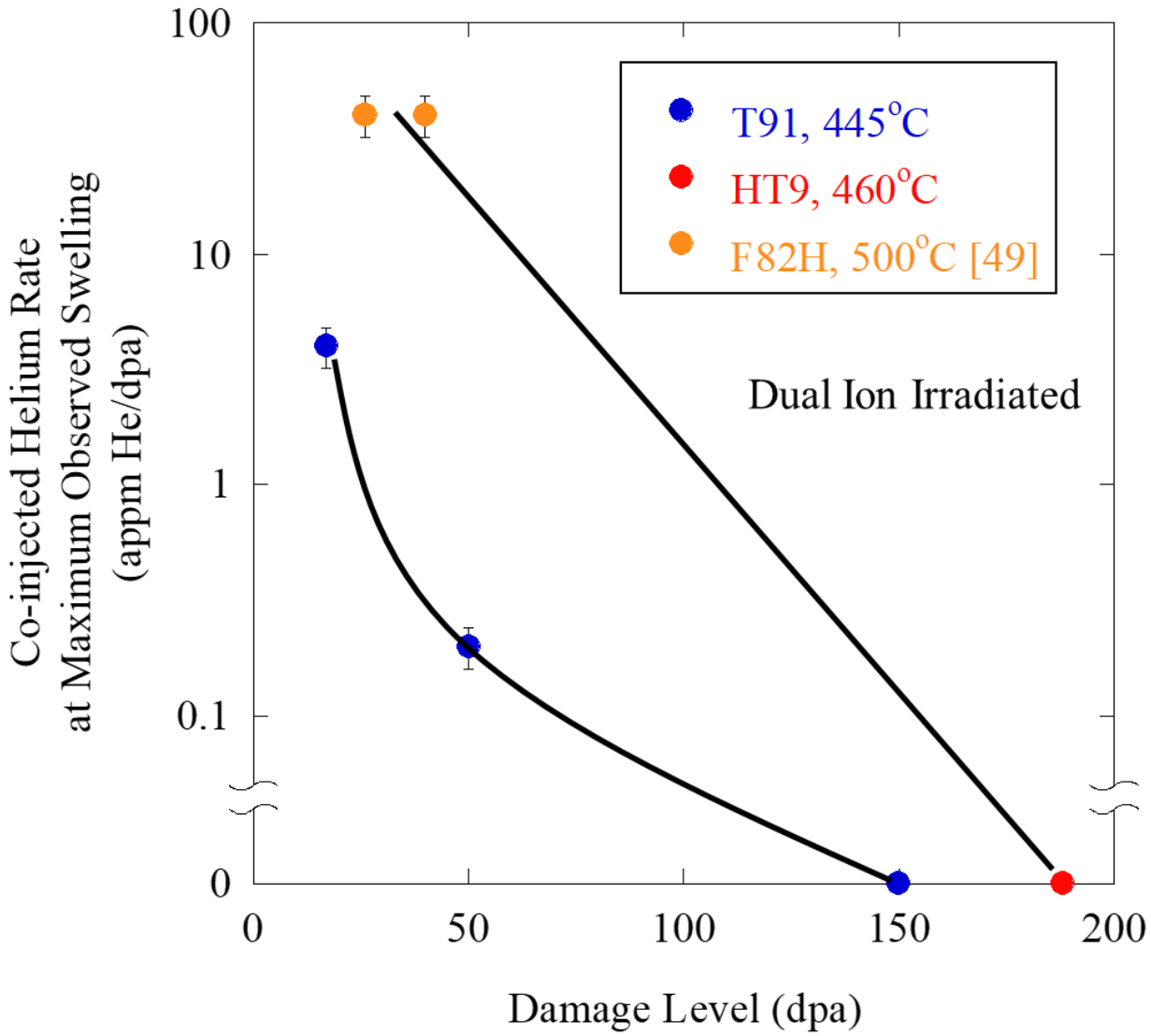

Figure 6.1: Helium-to-dpa ratio at which the maximum swelling was recorded for dual-ion irradiated T91 at 445°C (blue), HT9 at 460°C (red) and F82H at 500°C (black, [49]) as a function of damage level. The lines have been added to guide the eyes and represent rough bounding curves based on the available data.

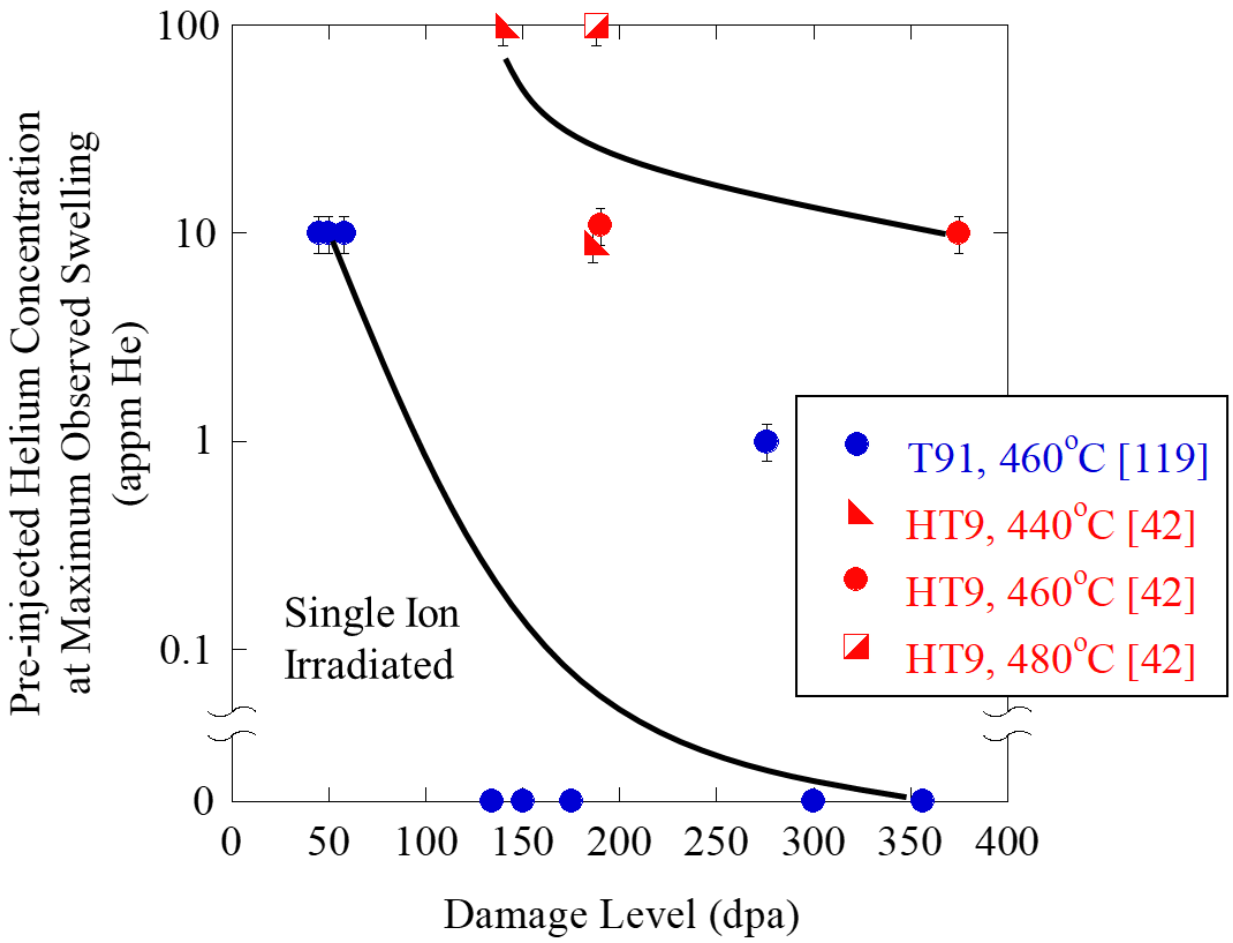

Figure 6.2: Pre-injected helium level at which the maximum swelling was recorded for single-ion irradiated ferritic-martensitic steels as a function of damage level. The lines have been added to guide the eyes and represent rough bounding curves based on the available data.

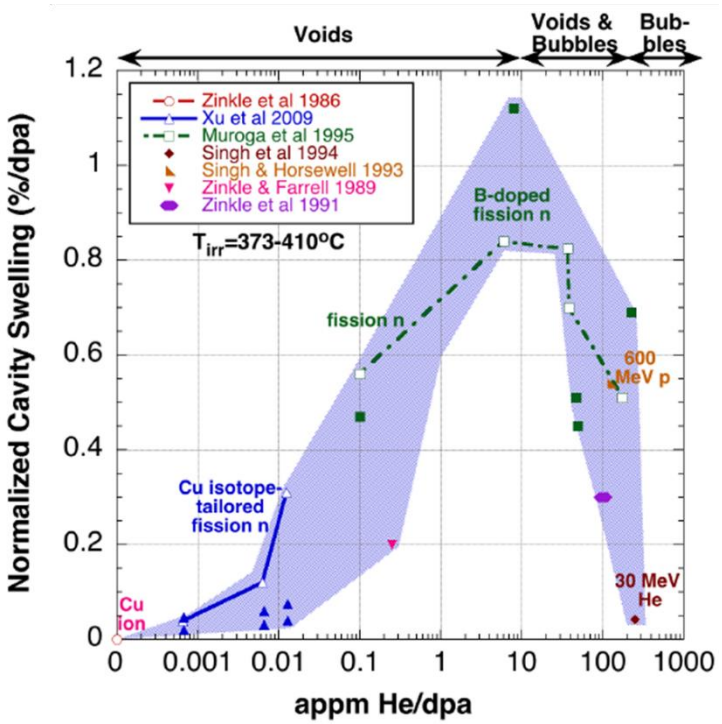

Figure 6.3: Normalized cavity swelling as a function of He/dpa ratio for copper irradiated between 373 and 410C. Figure produced by S. Zinkle from [63,67–72].

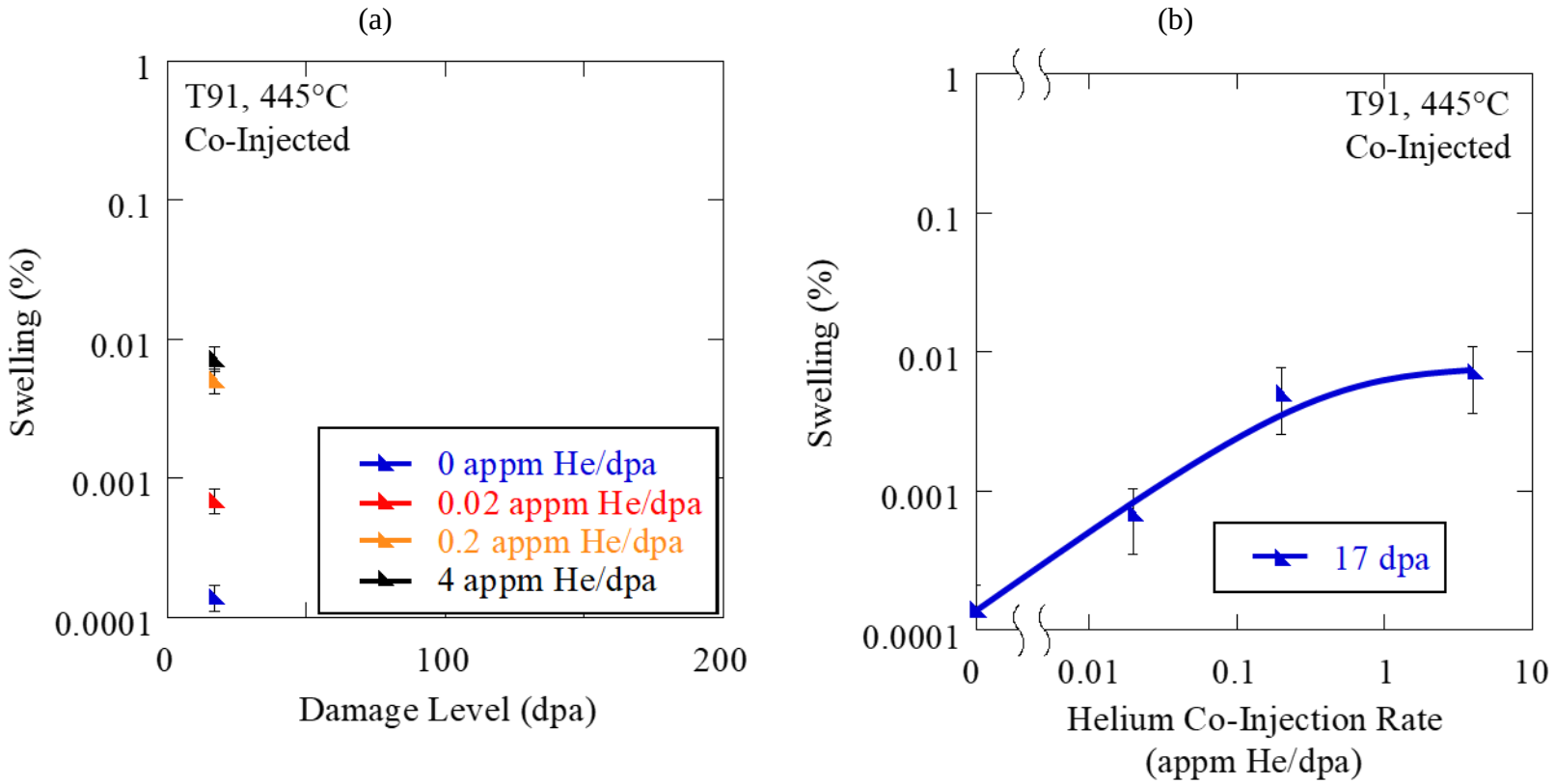

Figure 6.4: Swelling as a function of damage level (a) and helium co-injection rate (b) for T91 dual ion irradiated at 445°C. Lines have been added to guide the eyes.

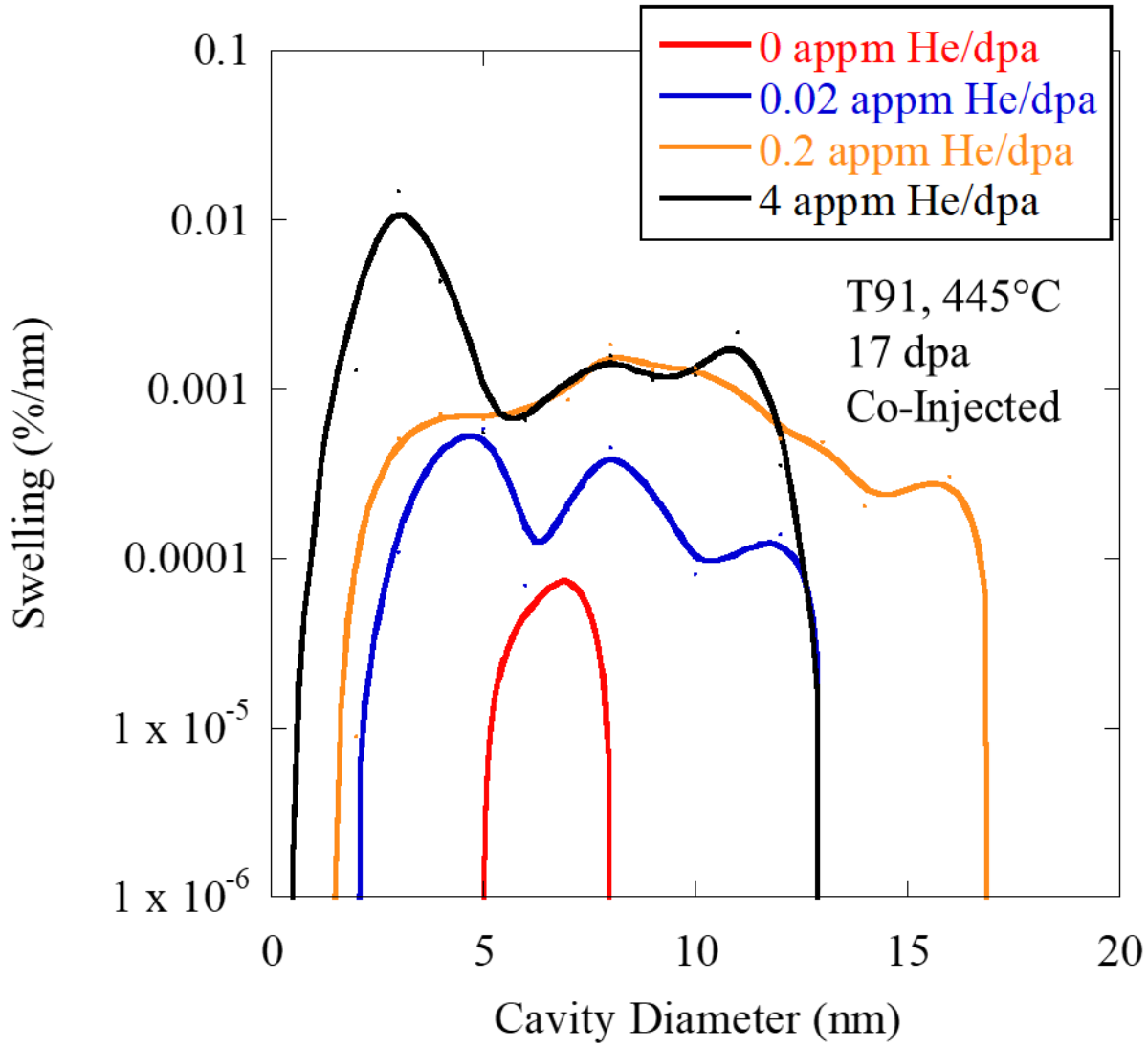

Figure 6.5: Swelling contribution as a function of cavity diameter in T91, heat 30176, irradiated at 445°C to 17 dpa with co-injected helium. Of note, only the highest helium co-injection rate had a higher contribution to swelling by bubbles as opposed to voids. For the other helium co-injection rates, the bubbles contributed a similar amount of swelling per size bin. Note that height differences at a specific size are due solely to differences in densities at those sizes.

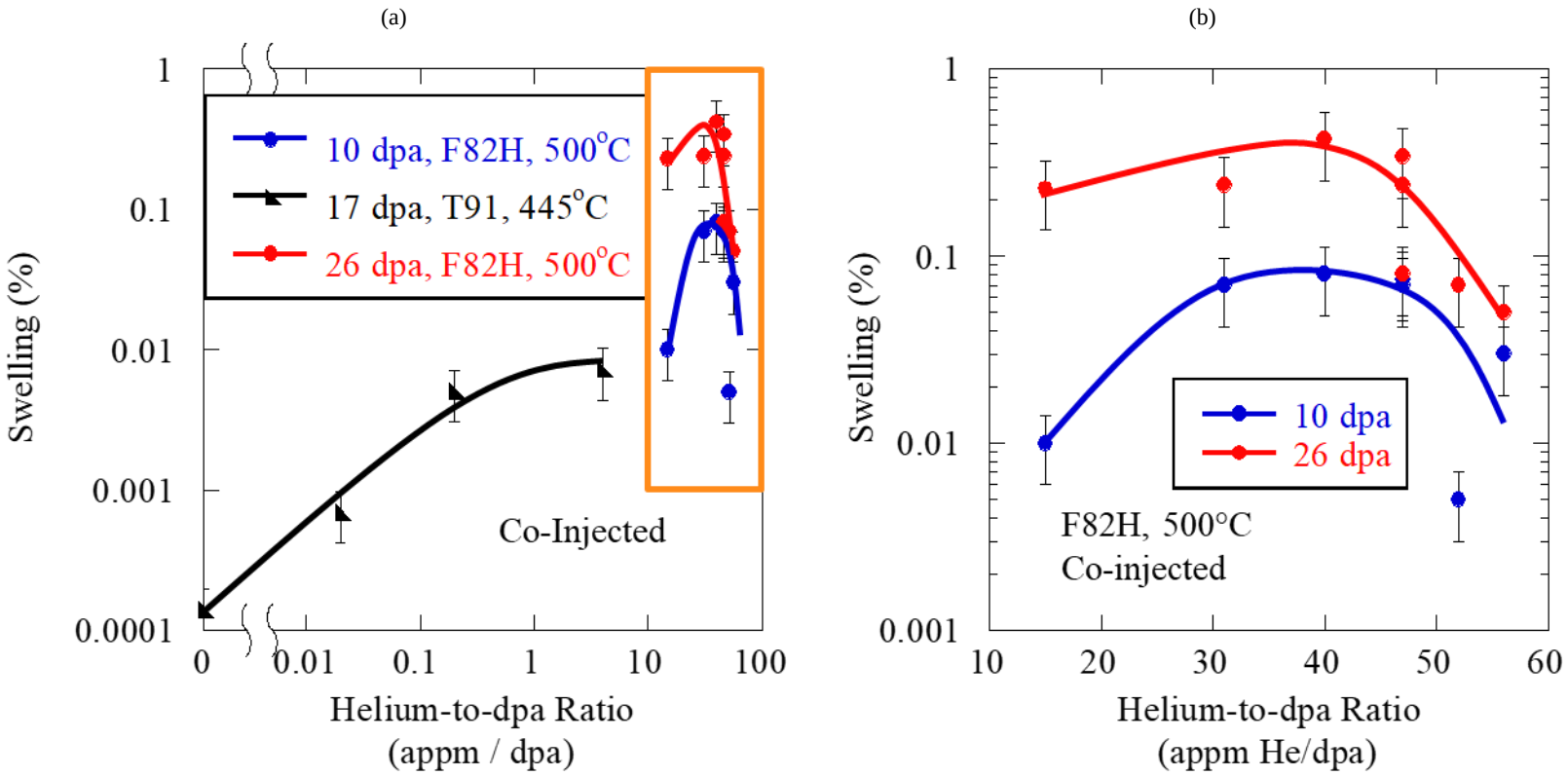

Figure 6.6: Swelling as a function of helium-to-dpa ratio for (a) T91 at 445°C at 17 dpa and F82H at 500°C at 10 and 26 dpa, both under dual-ion irradiation [49]. (b) shows a zoomed in image of the orange box from (a) to illustrate the influence of helium-to-dpa ratio in F82H.

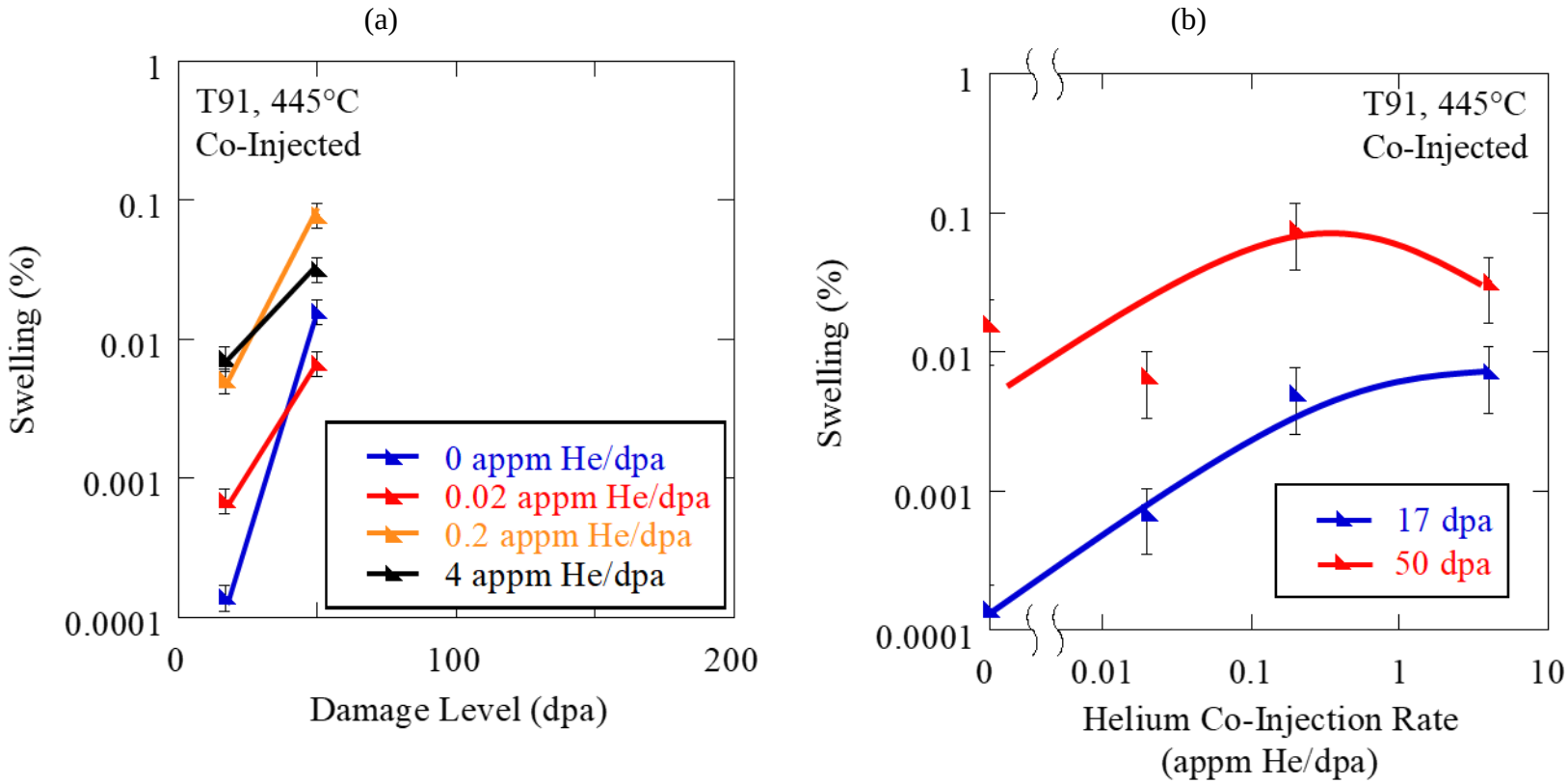

Figure 6.7: Swelling as a function of damage level (a) and helium co-injection rate (b) for T91 dual ion irradiated at 445°C. Lines have been added to guide the eyes.

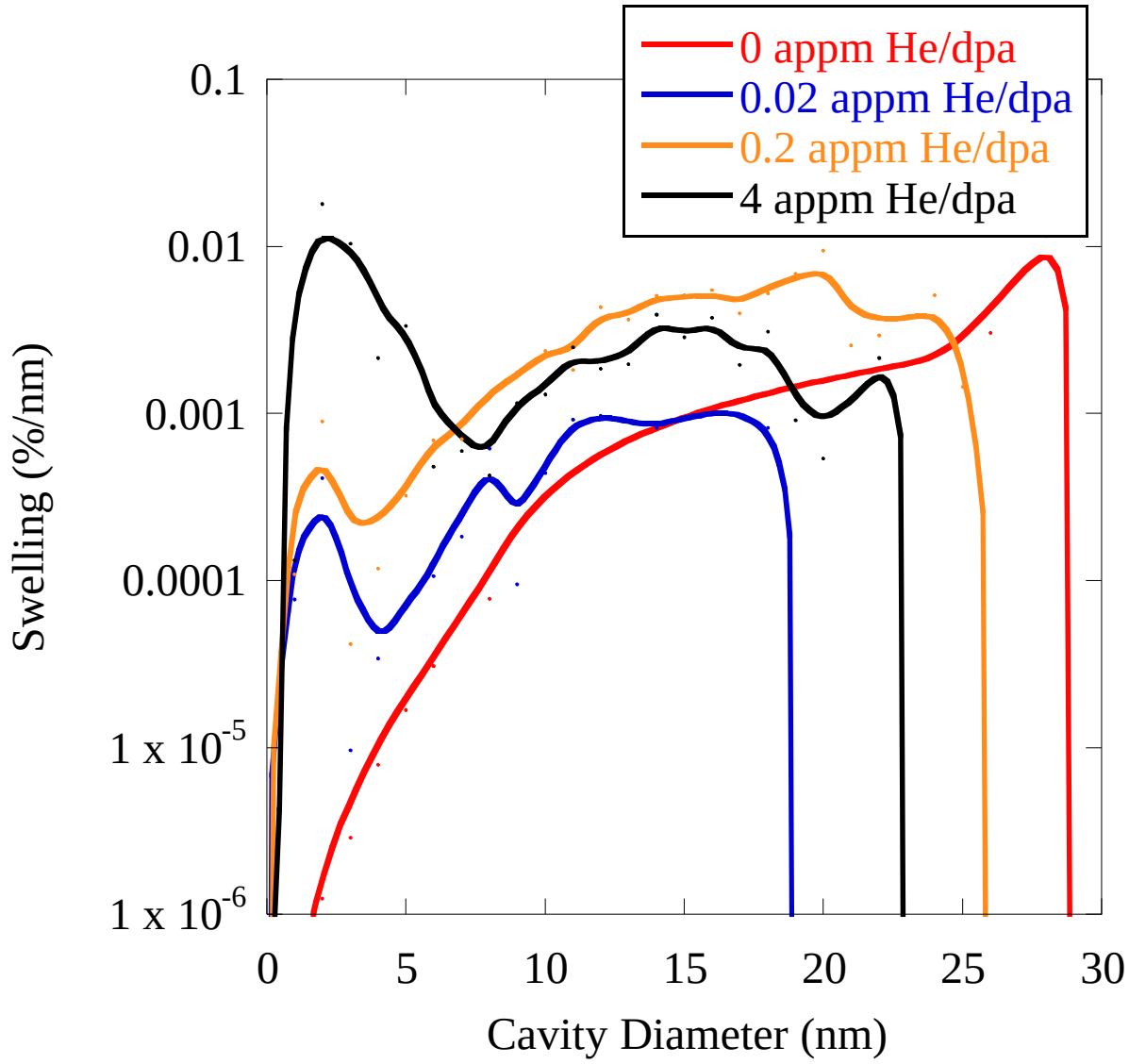

Figure 6.8: Swelling contribution as a function of cavity diameter in T91, heat 30176, irradiated at 445°C to 50 dpa with co-injected helium. Of note, only the highest helium co-injection rate had a higher contribution to swelling by bubbles as opposed to voids. For the other helium co-injection rates, the bubbles contributed a similar amount of swelling per size bin. Note that height differences at a specific size are due solely to differences in densities at those sizes.

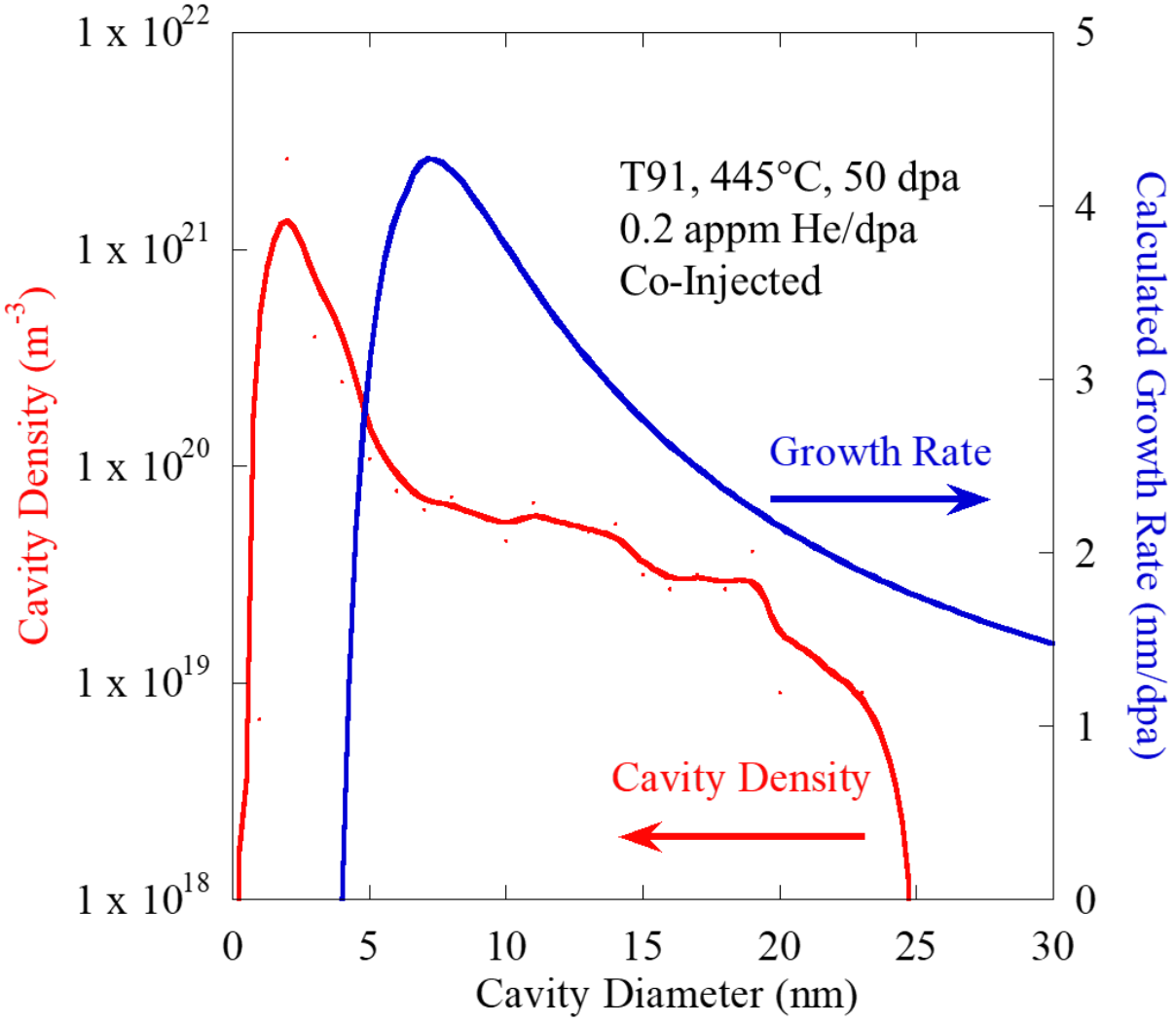

Figure 6.9: Cavity size distribution and calculated cavity growth rate for dual ion irradiation T91 at 445C with 0.2 appm He/dpa at 50 dpa. The swelling rate was calculated by applying Eq. 6.5 to the size distributions and then summing the results.

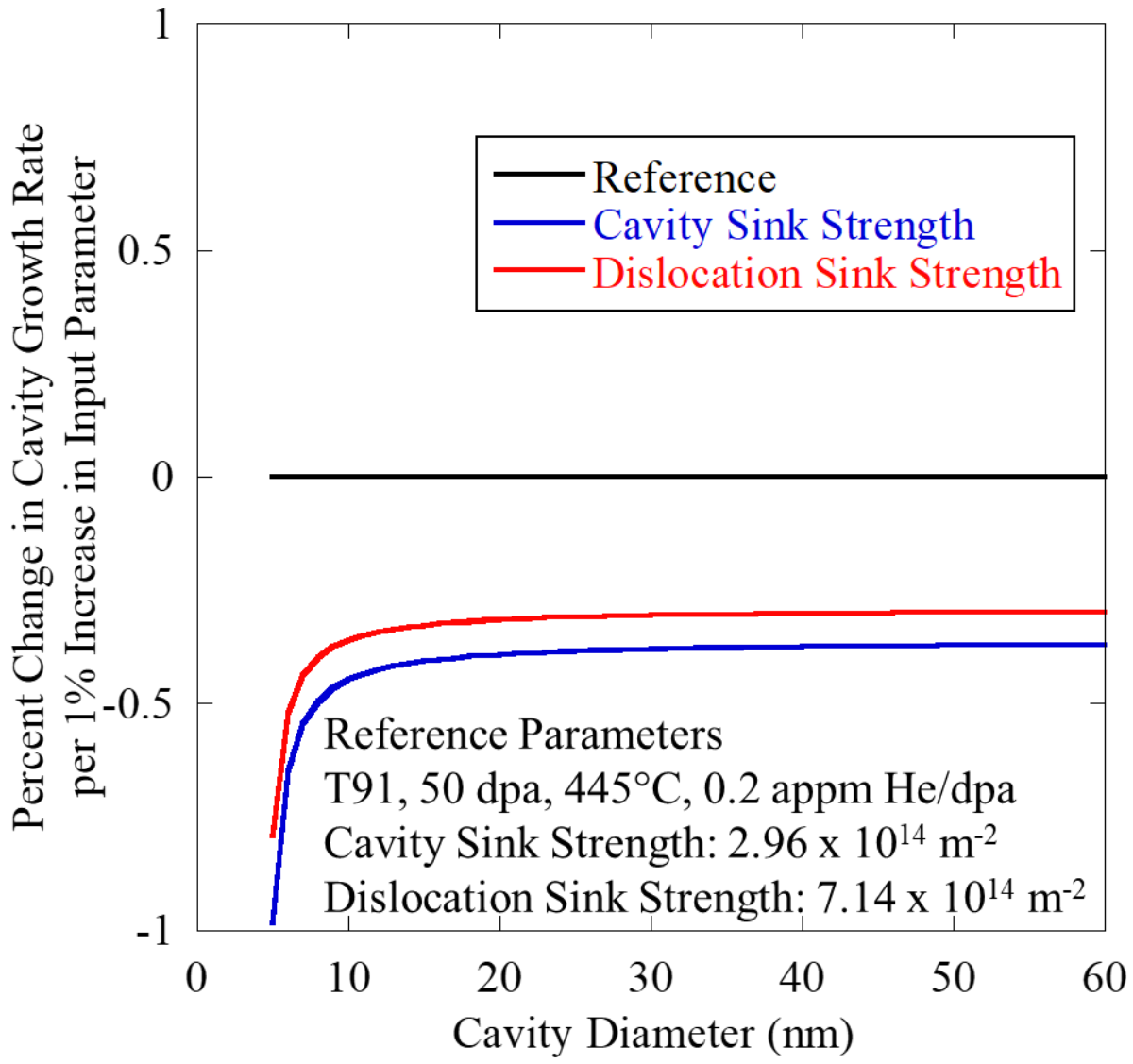

Figure 6.10: Significance of cavity (blue) and dislocation (red) sink strengths on the cavity growth rate for the cavity growth rate equation with a reference case of dual ion irradiated T91 at 445°C with 0.2 appm He/dpa at 50 dpa. The reference cavity sink strength was 2.96 x 10^{14} m^{-2}. The reference dislocation sink strength was 7.14 x 10^{14} m^{-2}. One at a time, these values were perturbed by 1% and the calculation was performed again (for values of cavity sink strength = 2.99 x 10^{14} m^{-2} and dislocation sink strength = 7.21 x 10^{14} m^{-2}). The percent change in the calculated growth rate was then plotted as a function of cavity size. The reference case is included as a black line at 0.

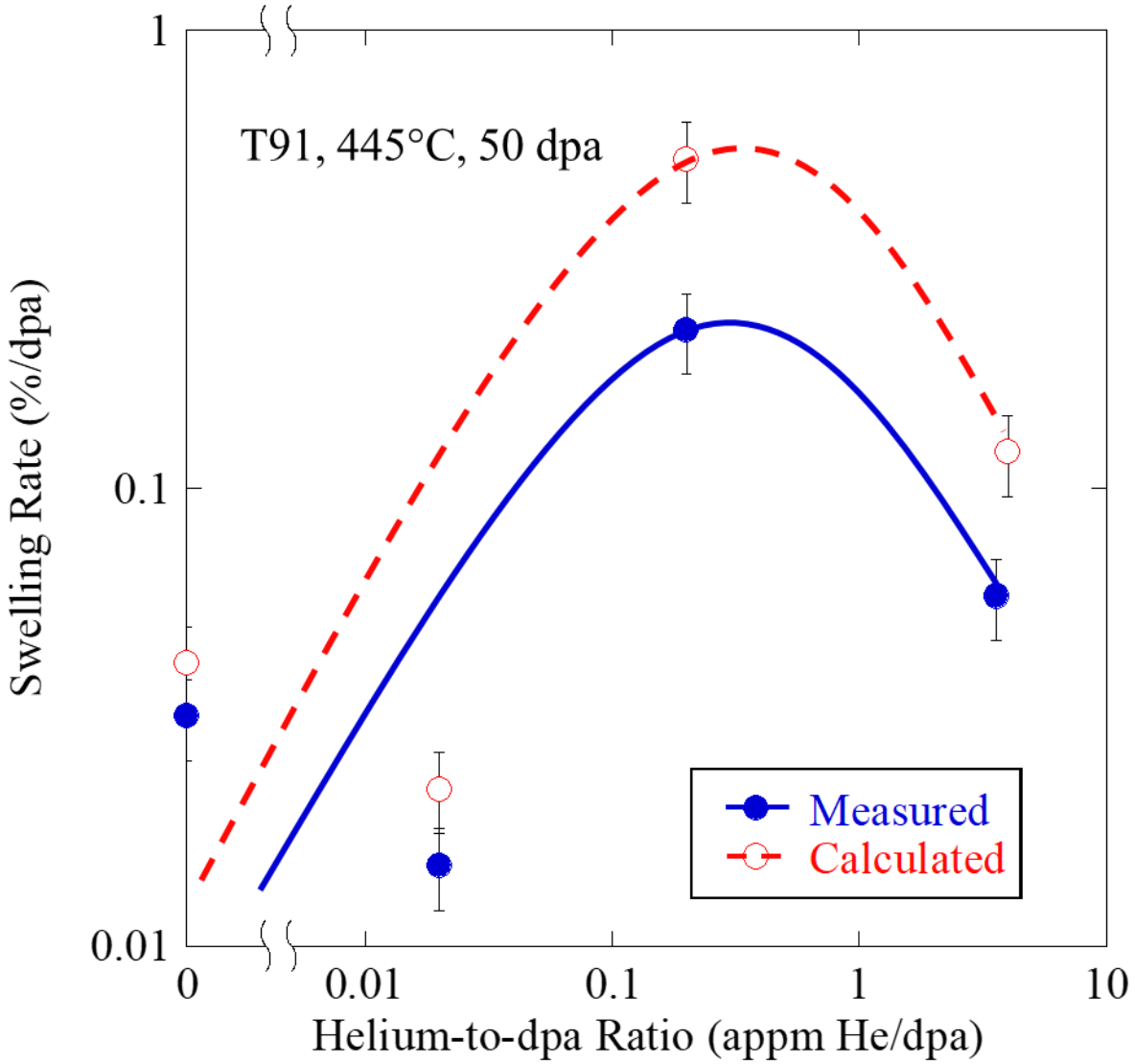

Figure 6.11: Measured (blue, filled circles, solid line) and calculated (red open circles, dashed line) swelling rates for T91 dual ion irradiated at 445°C at 50 dpa. The lines have been added to guide the eyes.

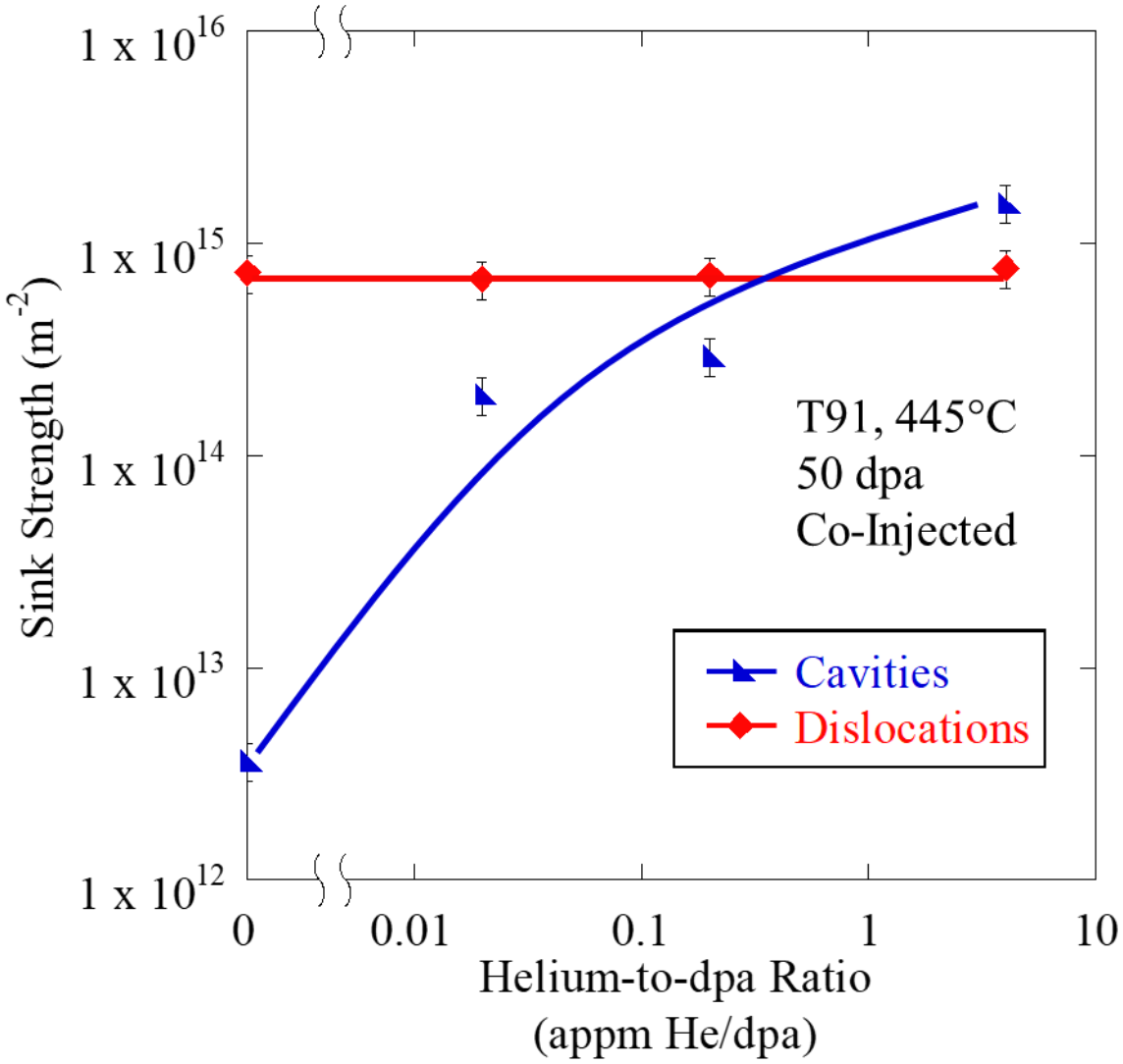

Figure 6.12: Cavity (blue triangles) and dislocation (red diamonds) sink strengths for dual-ion irradiated T91 at 445°C at 50 dpa The dislocation microstructure was measured at a single damage level for all helium-to-dpa ratios and then at multiple damage levels for a single helium-to-dpa ratio because helium was not observed to change the microstructure significantly. Lines are not trendlines and have only been added to guide the eyes.

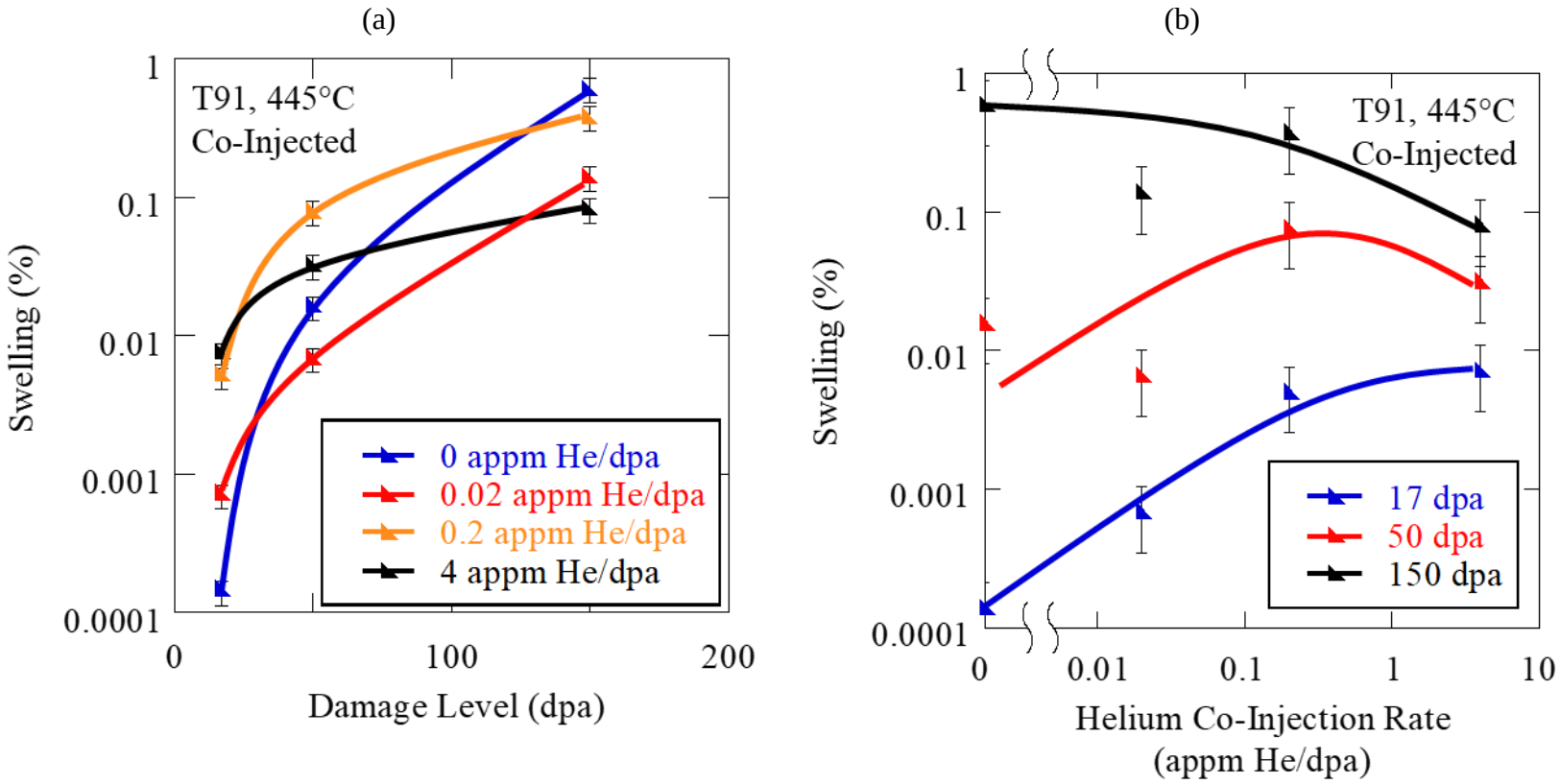

Figure 6.13: Swelling as a function of damage level (a) and helium co-injection rate (b) for T91 dual ion irradiated at 445°C. Lines have been added to guide the eyes.

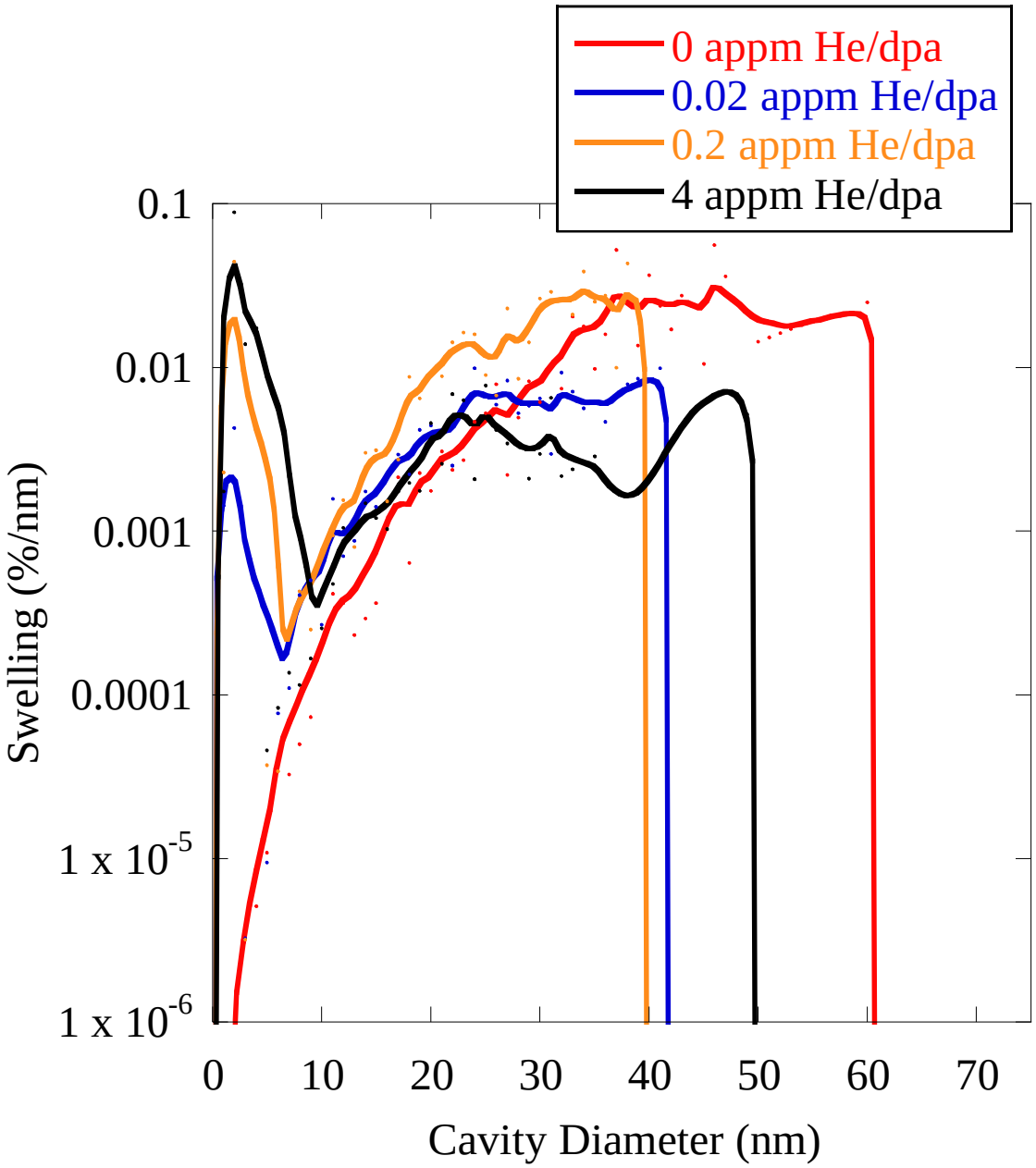

Figure 6.14: Swelling contribution as a function of cavity diameter in T91, heat 30176, irradiated at 445°C to 150 dpa with co-injected helium. Of note, only the highest helium co-injection rate had a higher contribution to swelling by bubbles as opposed to voids. For the other helium co-injection rates, the bubbles contributed a similar amount of swelling per size bin. Note that height differences at a specific size are due solely to differences in densities at those sizes.

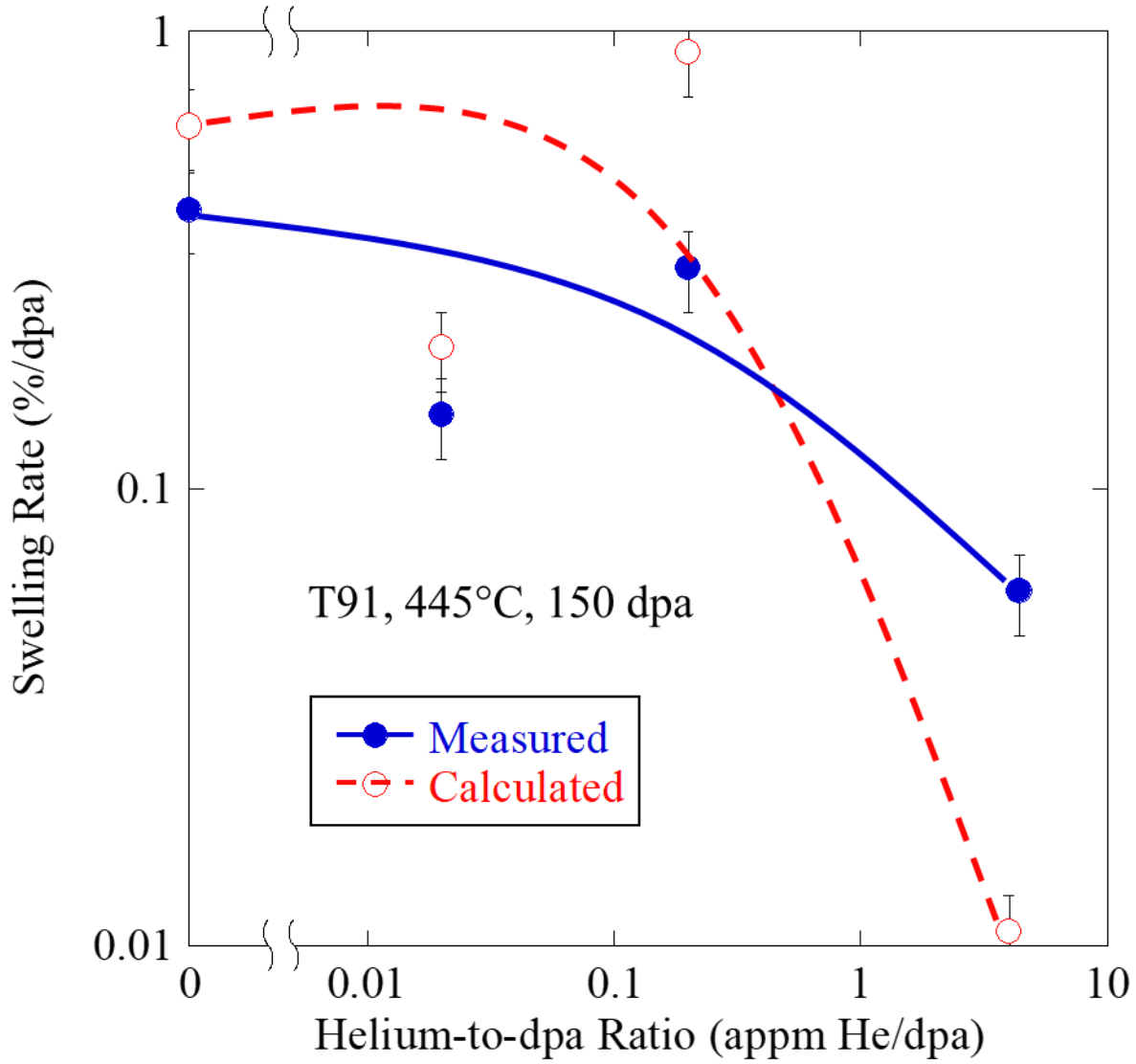

Figure 6.15: Measured (blue, filled circles, solid line) and calculated (red open circles, dashed line) swelling rates for T91 dual ion irradiated at 445°C at 150 dpa. The lines have been added to guide the eyes.

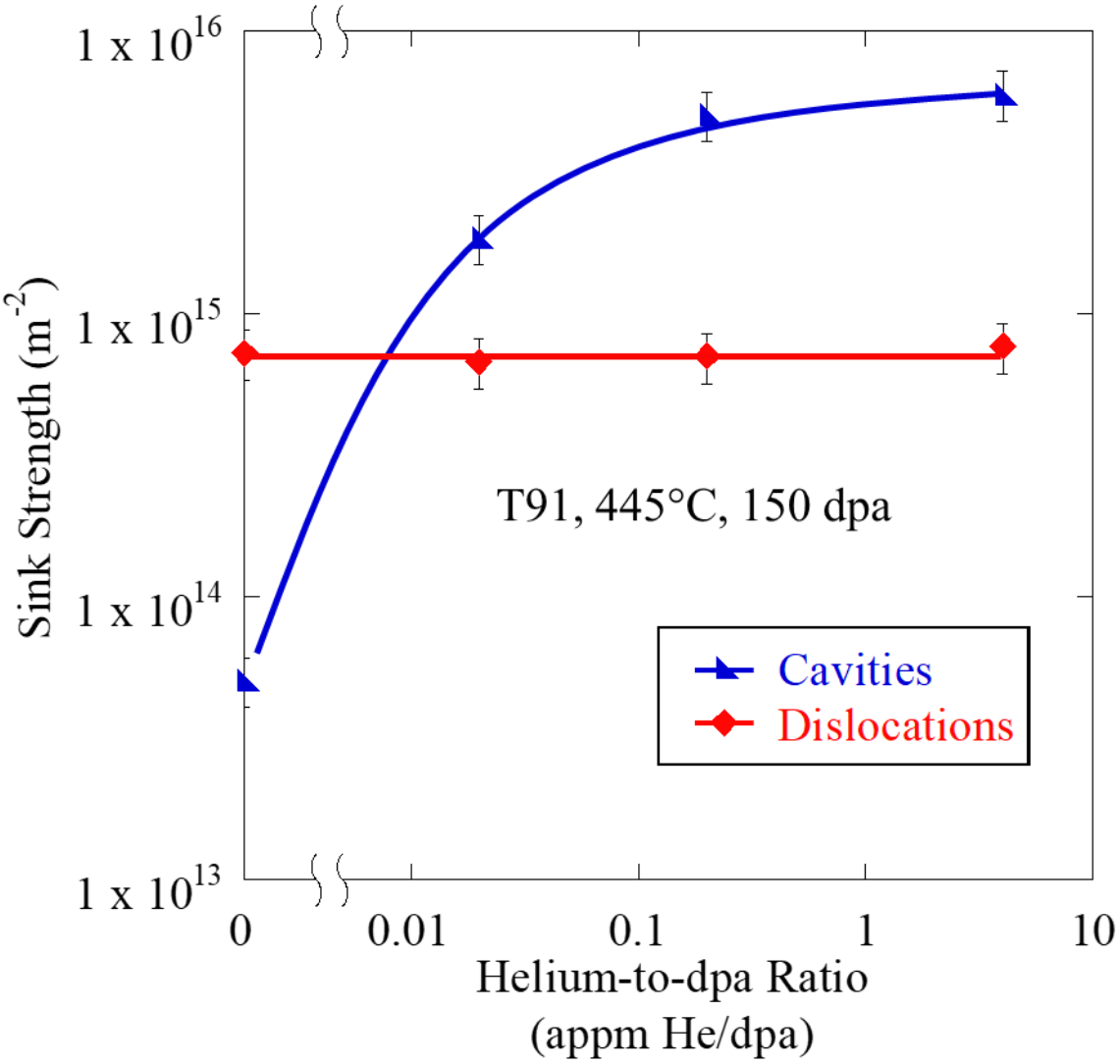

Figure 6.16: Cavity (blue triangles) and dislocation (red diamonds) sink strengths for dual-ion irradiated T91 at 445°C at 150 dpa The dislocation microstructure was measured at a single damage level for all helium-to-dpa ratios and then at multiple damage levels for a single helium-to-dpa ratio because helium was not observed to change the microstructure significantly. Lines are not trendlines and have only been added to guide the eyes.

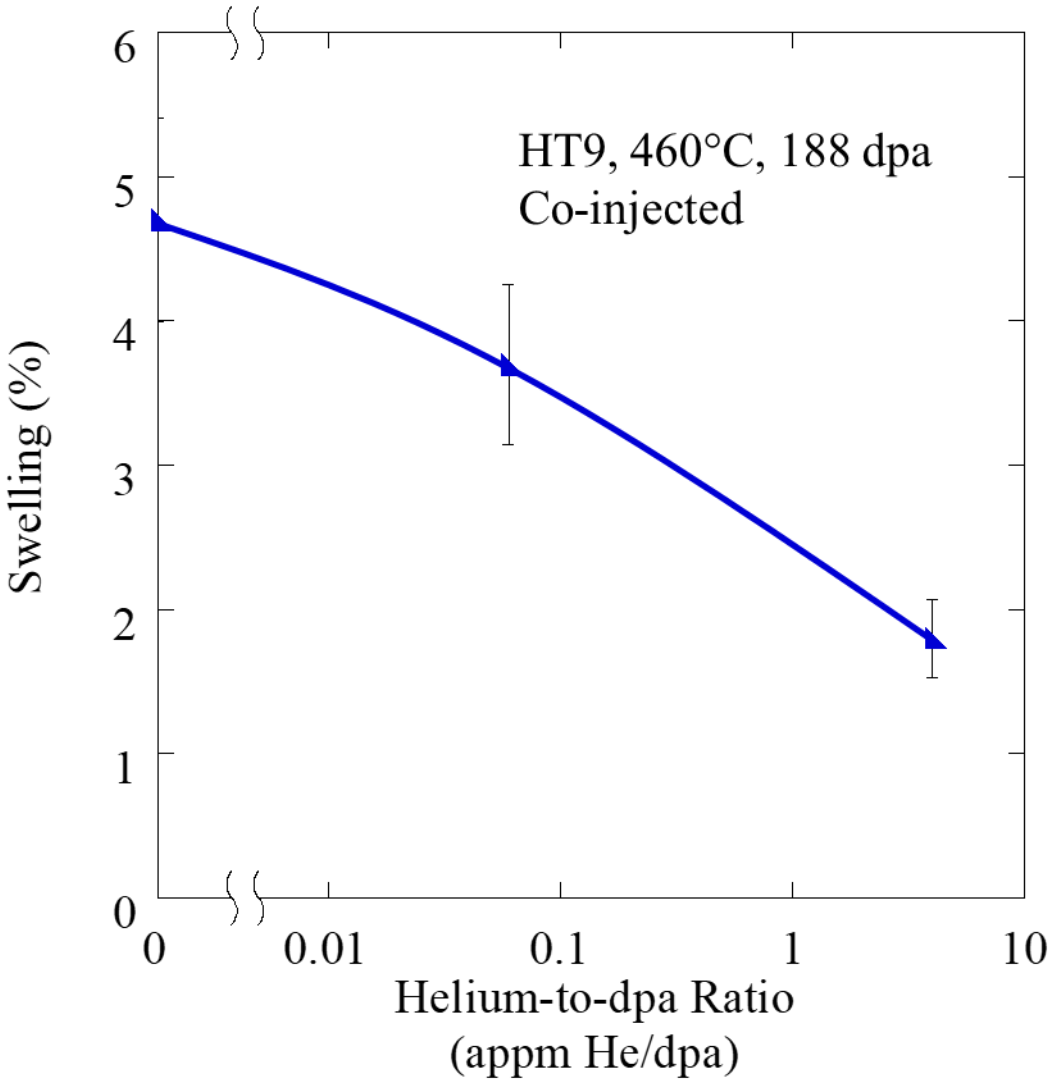

Figure 6.17: Swelling as a function of helium-to-dpa ratio for HT9 dual ion irradiated at 460°C to 188 dpa. Lines have been added to guide the eyes.

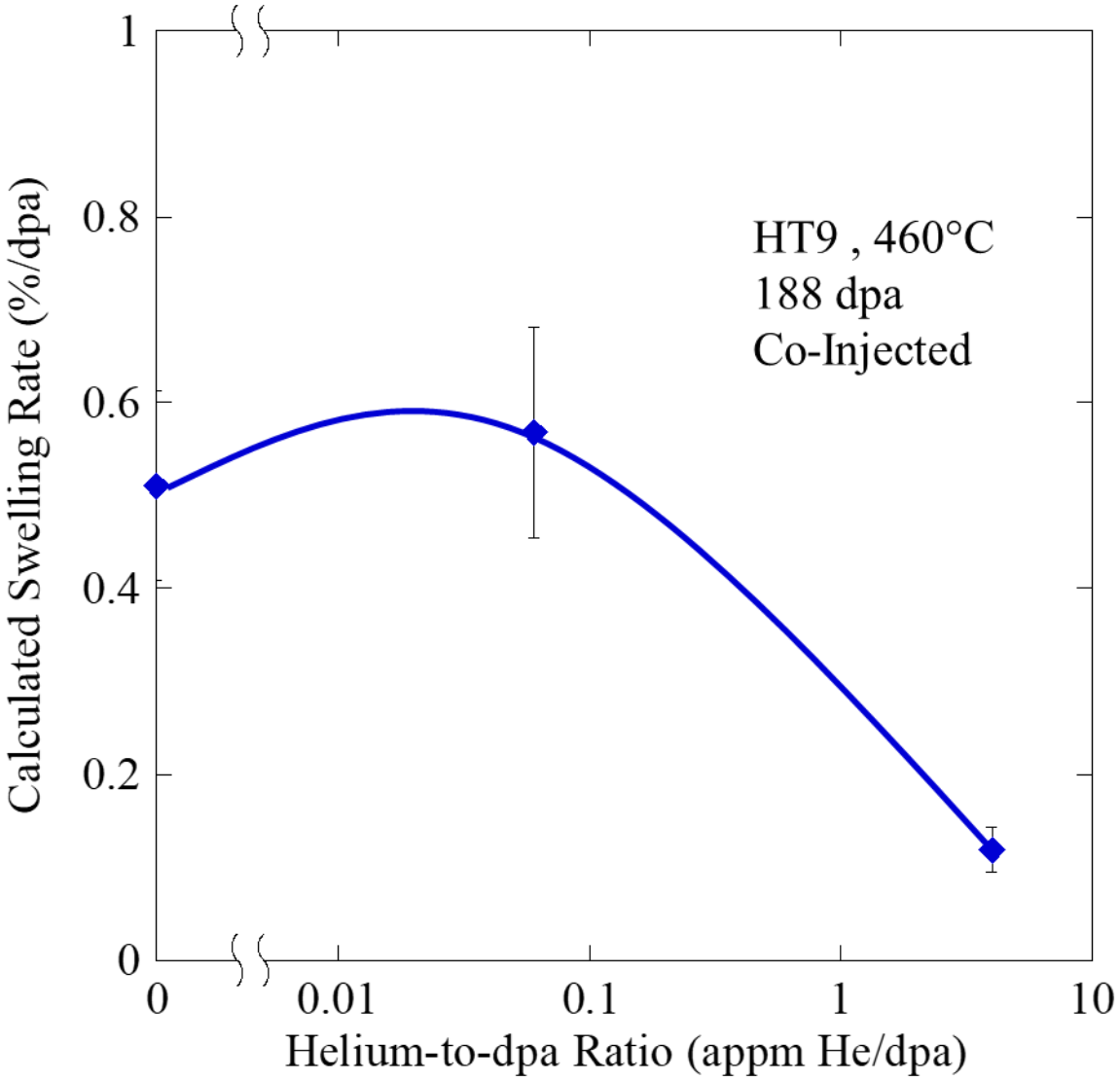

Figure 6.18: Calculated swelling rates for HT9 dual ion irradiated at 460°C to 188 dpa. The lines have been added to guide the eyes.

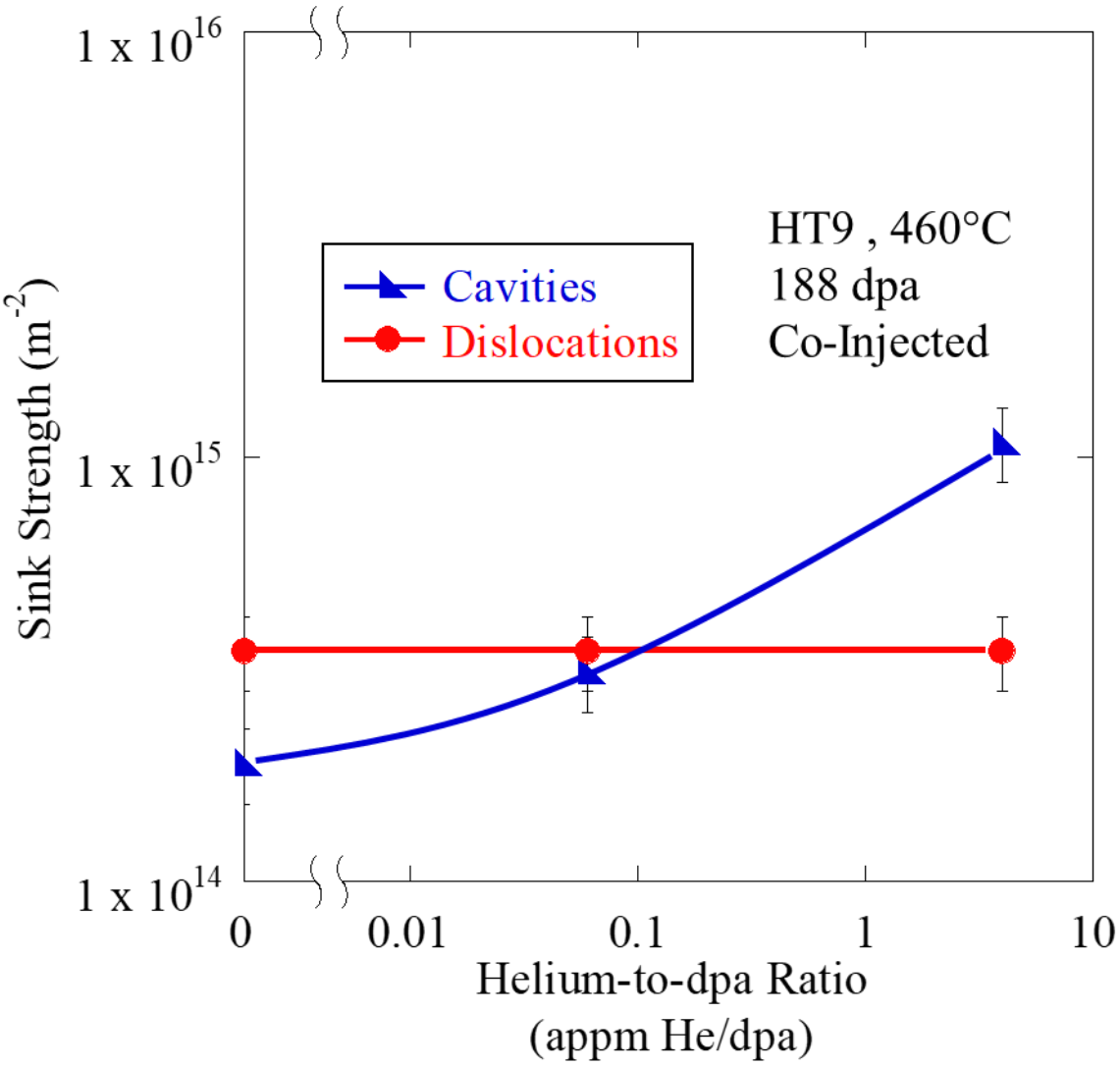

Figure 6.19: Cavity (blue triangles) and dislocation (red circles) sink strengths for dual-ion irradiated T91 at 445°C at 150 dpa The dislocation microstructure was measured at a single damage level for all helium-to-dpa ratios and then at multiple damage levels for a single helium-to-dpa ratio because helium was not observed to change the microstructure significantly. Lines are not trendlines and have only been added to guide the eyes.

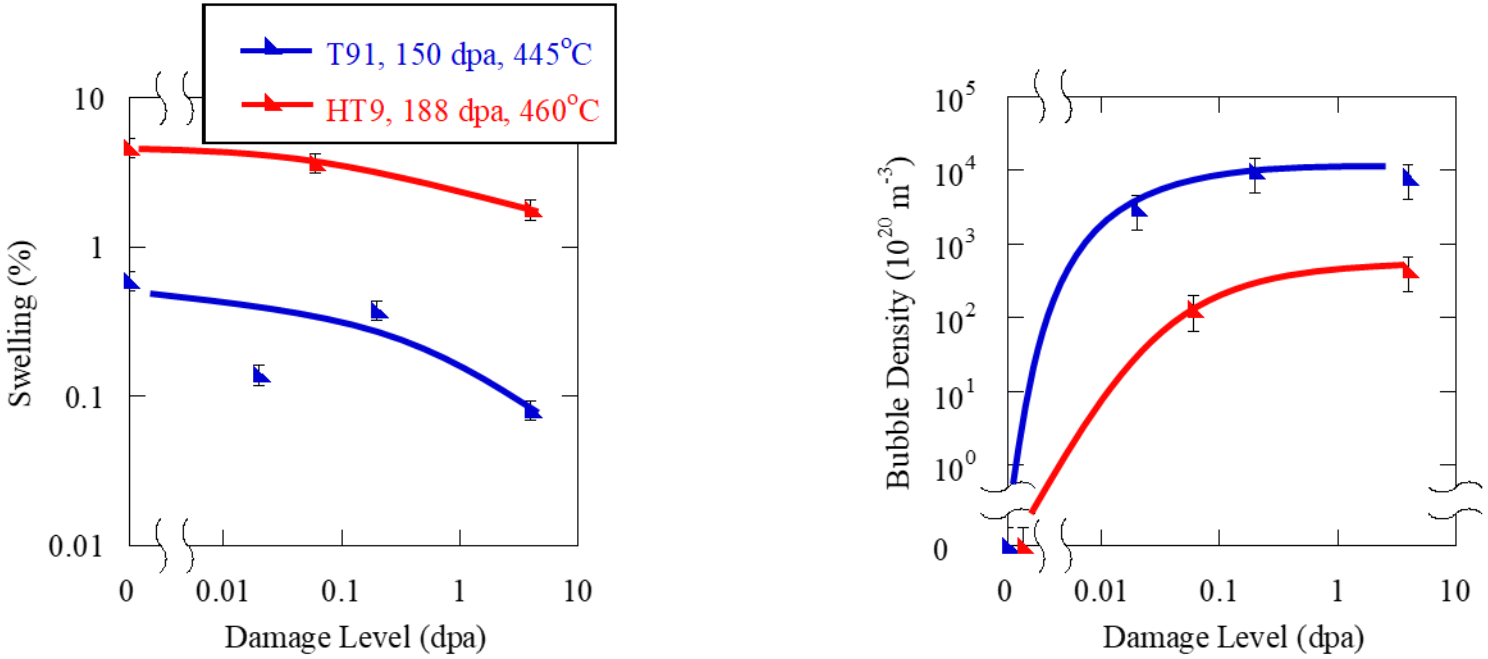

Figure 6.20: Comparison of swelling (a) and bubble density (b) for dual ion irradiated T91 at 150 dpa and 445C (blue) and HT9 at 188 dpa and 460C (red). Lines have been added to guide the eyes.

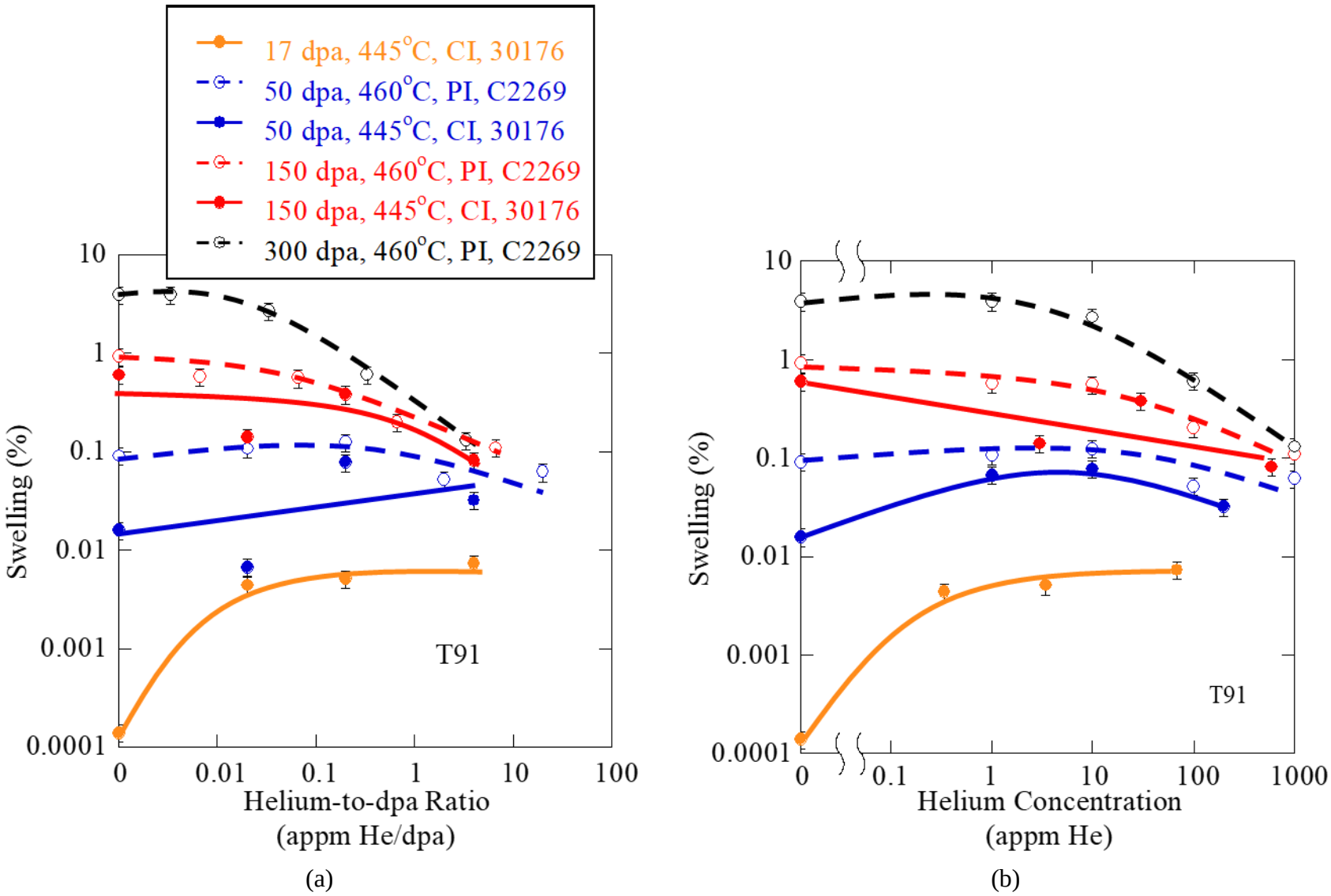

Figure 6.21: Swelling as a function of helium-to-dpa ratio, appm He/dpa, (a) and helium concentration, appm He, (b) for pre-injected (PI), single ion irradiated T91, heat C2269, at 460°C (circles, solid lines) and co-injected (CI), dual ion irradiated T91, heat 30176, at 445°C (triangles, dashed lines) at multiple damage levels [119]. Lines have been added to guide the eyes.

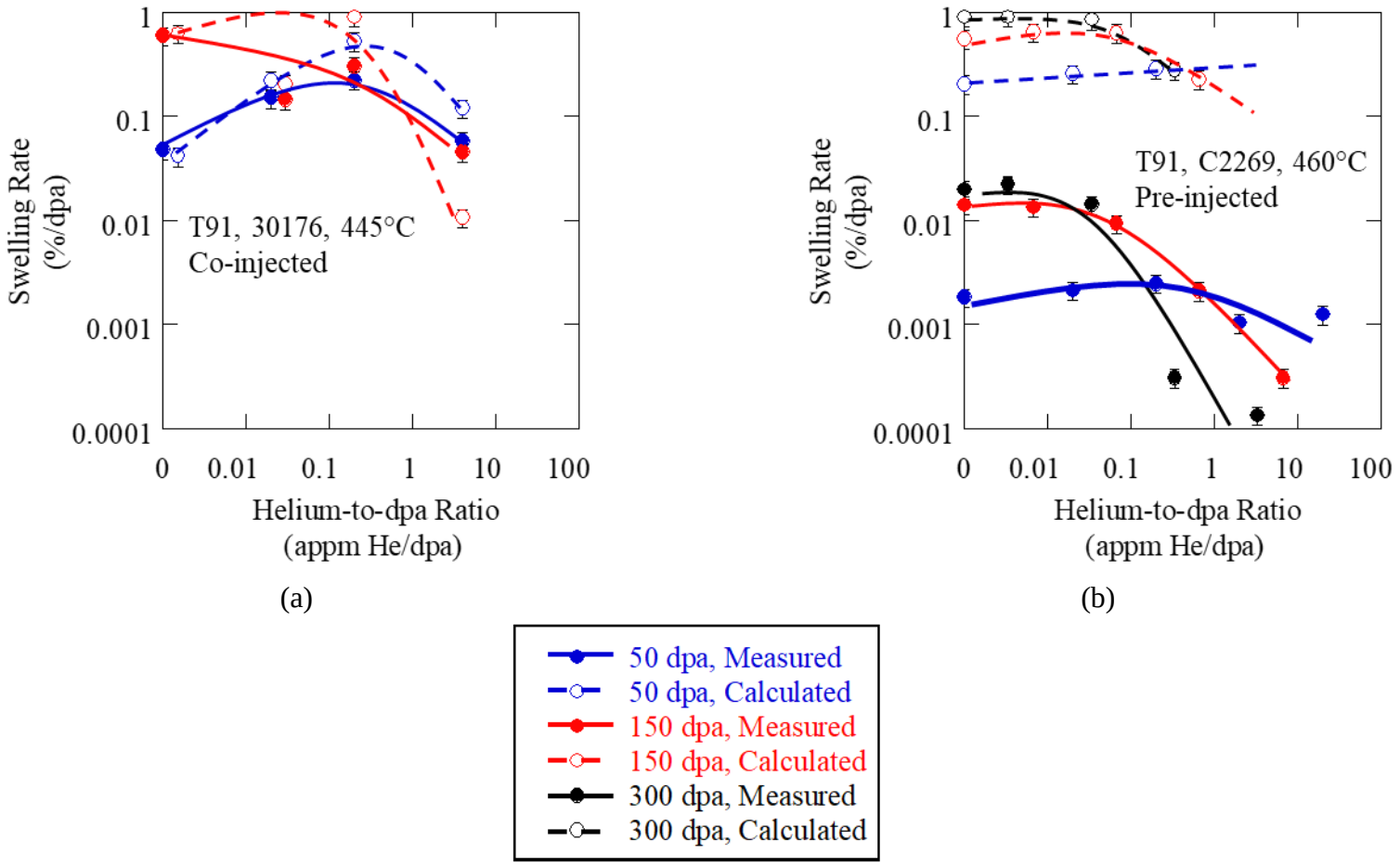

Figure 6.22: Measured (filled circles, solid lines) and calculated (open circles, dashed lines) swelling rates for (a) T91, heat 30176, dual-ion irradiated with co-injected helium at 445°C and (b) T91, heat C2269, single-ion irradiated with pre-injected helium at 460°C. The lines are added to guide the eye and are not fits to the data. SI refers to the single-ion pre-injected irradiations, DI refers to the dual-ion co-injected irradiations. The 17 dpa case has not been included because the system is still in the nucleation regime of swelling.

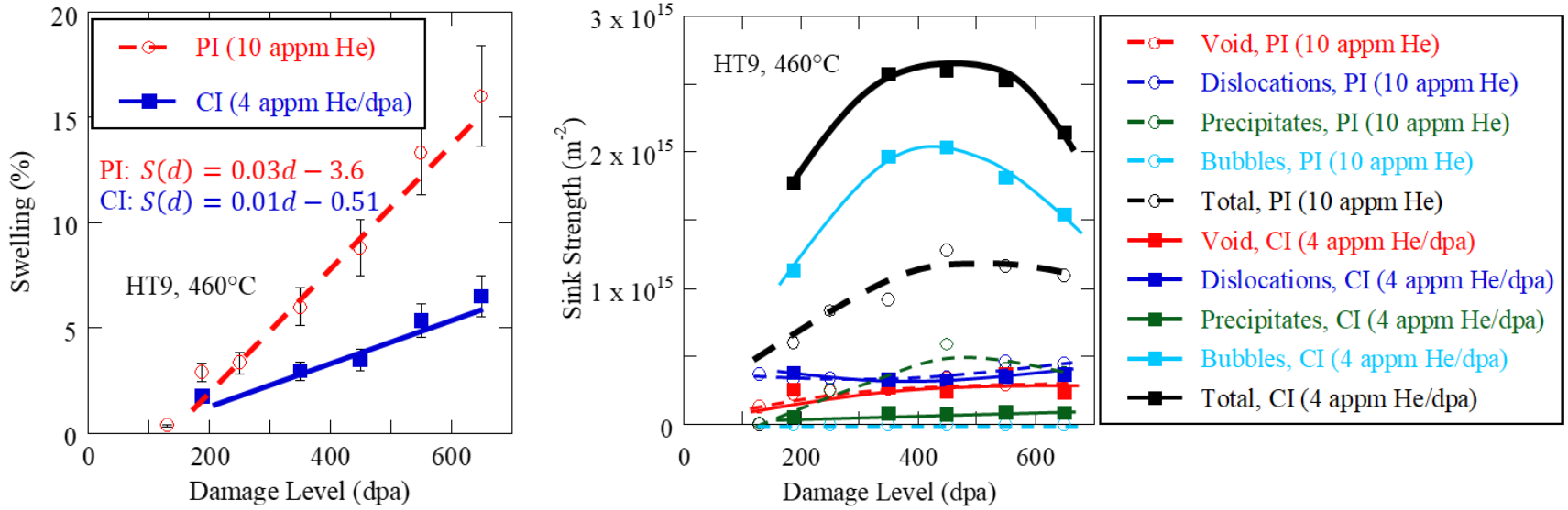

Figure 6.23: Swelling (a) and sink strengths (b) for HT9 at 460°C under both single-ion irradiation with 10 appm He pre-injected helium (PI, open symbols, dashed lines, [29]) and dual-ion irradiation with 4 appm He/dpa co-injected helium (CI, filled symbols, solid lines). The linear fit to the swelling is shown in (a) for both irradiation conditions. The sink strengths in (b) are broken out by void (red), dislocation (blue), precipitates (green), bubbles (sky blue) and total (black).

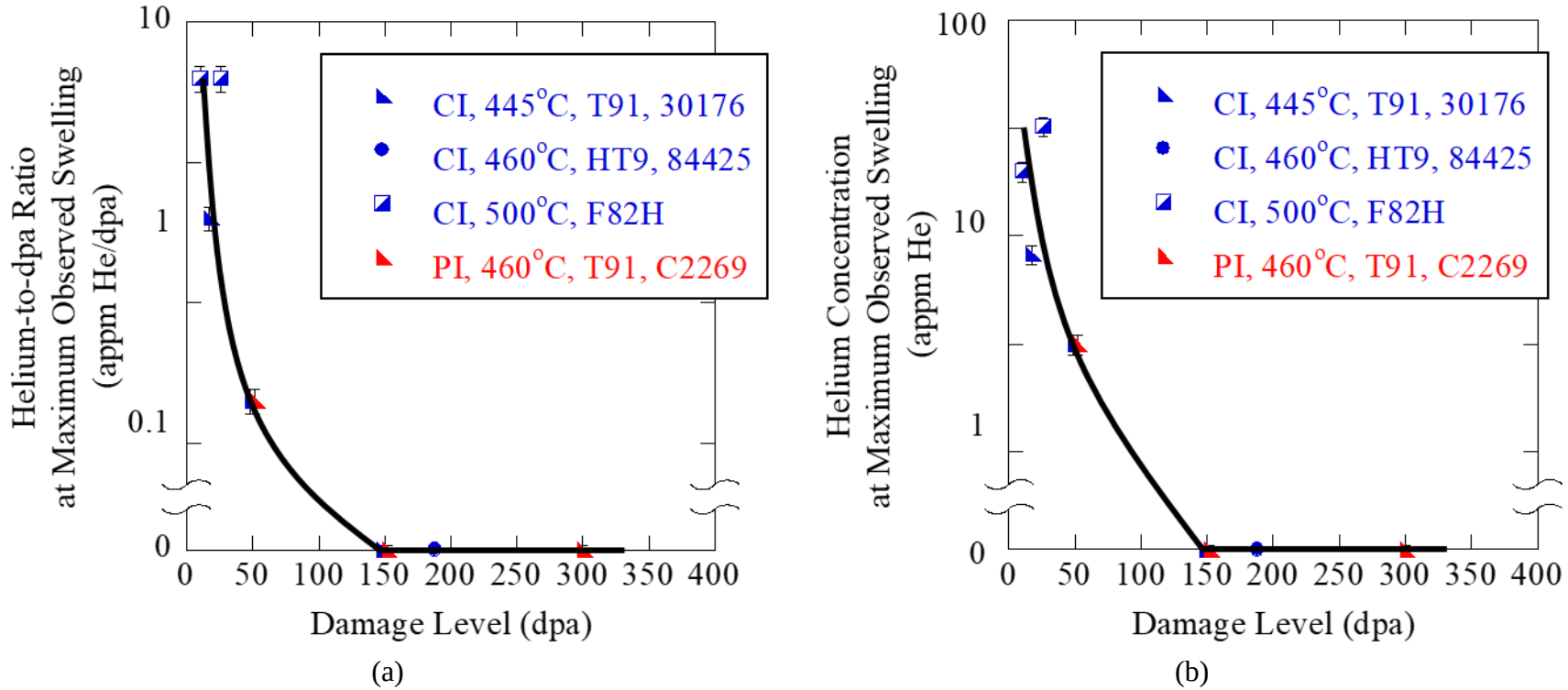

Figure 6.24: Helium-to-dpa ratio (a) and total helium concentration (b) at which the maximum swelling was recorded for helium co-injected (CI), dual-ion irradiated T91 at 445°C (blue triangles), HT9 at 460°C (blue circles), F82H at 500°C (blue half-squares, [49]) and helium pre-injected (PI) single-ion irradiated T91 at 460°C (red triangles, [119]) as a function of damage level. The lines have been added to guide the eyes. Pre-injected, single-ion irradiated HT9 has been omitted from this plot since most conditions were only irradiated at two helium concentrations.

Chapter 7 Conclusions

The following conclusions have been reached regarding the influence of helium on swelling in ion irradiated ferritic-martensitic steels T91 and HT9.

Helium stabilizes bubbles and accelerates the transition from bubble to void. At low damage levels, this results in the highest swelling levels at the highest helium level because the cavity (both bubble and void) density is highest and in the nucleation regime swelling is dominated by the cavity density rather than cavity size.

As the damage level increases, the stable bubble density increases which increases the sink density that causes a reduction in the swelling rate. Thus, the maximum swelling shifts to a lower helium co-injection rate.

As the damage level increases, the stable bubble density increases which increases the sink density and results in a reduction in the swelling rate, such that at high damage levels, the swelling without helium overtakes that with any helium, resulting in the maximum swelling occurring with no helium co-injection.

Irradiations with pre-injected helium show the same effect of helium on swelling as seen during irradiations with co-injected helium. For the same amount of helium, pre-injection results in a larger bubble sink strength early in the irradiation. This sink strength reduces the vacancy

supersaturation which in turn reduces the cavity growth rate and, consequently, swelling. Nevertheless, in both pre-injected and co-injected cases, the peak in swelling shifts to lower helium levels with increasing damage level in both T91 and HT9.

Chapter 8 Future Work

The results and findings of this dissertation provided insight into the role helium co-injection rate on cavity growth. However, there are many unanswered questions and areas which merit further study.

The role of heterogeneous nucleation on cavity nucleation. In this work, the mechanism of nucleation was ignored due to the complex underlying processes. However, to better understand the effects of helium on swelling at all stages, early nucleation must be examined. Much work has been performed using a homogeneous critical bubble model. However, that does not allow for precise modeling of the early stages of nucleation. Early in an irradiation, the roles of precipitate-matrix interfaces, dislocations, and solute impurities are likely to play a larger role in cavity nucleation. The heterogenous nucleation sites are expected to lower the barrier for bubbles to transition to unstably growing voids and will be relevant at lower vacancy supersaturation values, such as those for reactor irradiation. Additional studies on other possible nucleation sites for cavities and the spatial heterogeneity of the microstructure need to be performed.

The effects of hydrogen implantation on cavity growth. In this work, helium was the only gas responsible for the nucleation and growth of cavities. In reactor, other gases are produced, including hydrogen through (n,p) reactions. The hydrogen can also serve to nucleate and stabilize cavities through the formation of H_2 gas inside a vacancy cluster [120,121][120,121][120,121][120,121][120,121][120,121][120,121]or through chemical bonding between the alloying elements and hydrogen. Additional dual ion irradiations using iron ions and hydrogen co-implantation can isolate the role of hydrogen on cavity nucleation. Furthermore,

hydrogen gas accumulation with helium gas accumulation appears to have a synergistic effect on cavity growth that is poorly understood. Triple ion beam irradiations with iron ions, helium co-injection, and hydrogen co-injection simultaneously will assess the roles of these gases on cavity nucleation in an environment closer to reactor irradiation.

Utilize advanced STEM techniques to improve microstructure characterization results. In this work, basic HAADF STEM imaging was used to characterize the larger cavities while through-focus BF TEM was used to characterize the smaller features. HAADF STEM depends on z-contrast imaging, so smaller features are hard to observe while BF TEM can result in enlargement of features. Recent advancements such as 4D-STEM and integrated differential phase contrast STEM allow for a hybrid of the two methods allowing for the imaging of smaller features in focus, preventing any enlargement. EELS measurement of helium in bubbles was a technique that was attempted unsuccessfully in this work that could also be used to further our understanding of the effect of helium on cavity development and subsequent swelling.

Appendices

Appendix A : **IRRADIATION PARAMETERS**

The iron current, helium current, temperature and pressure for each irradiation performed as part of this thesis are presented in this appendix.

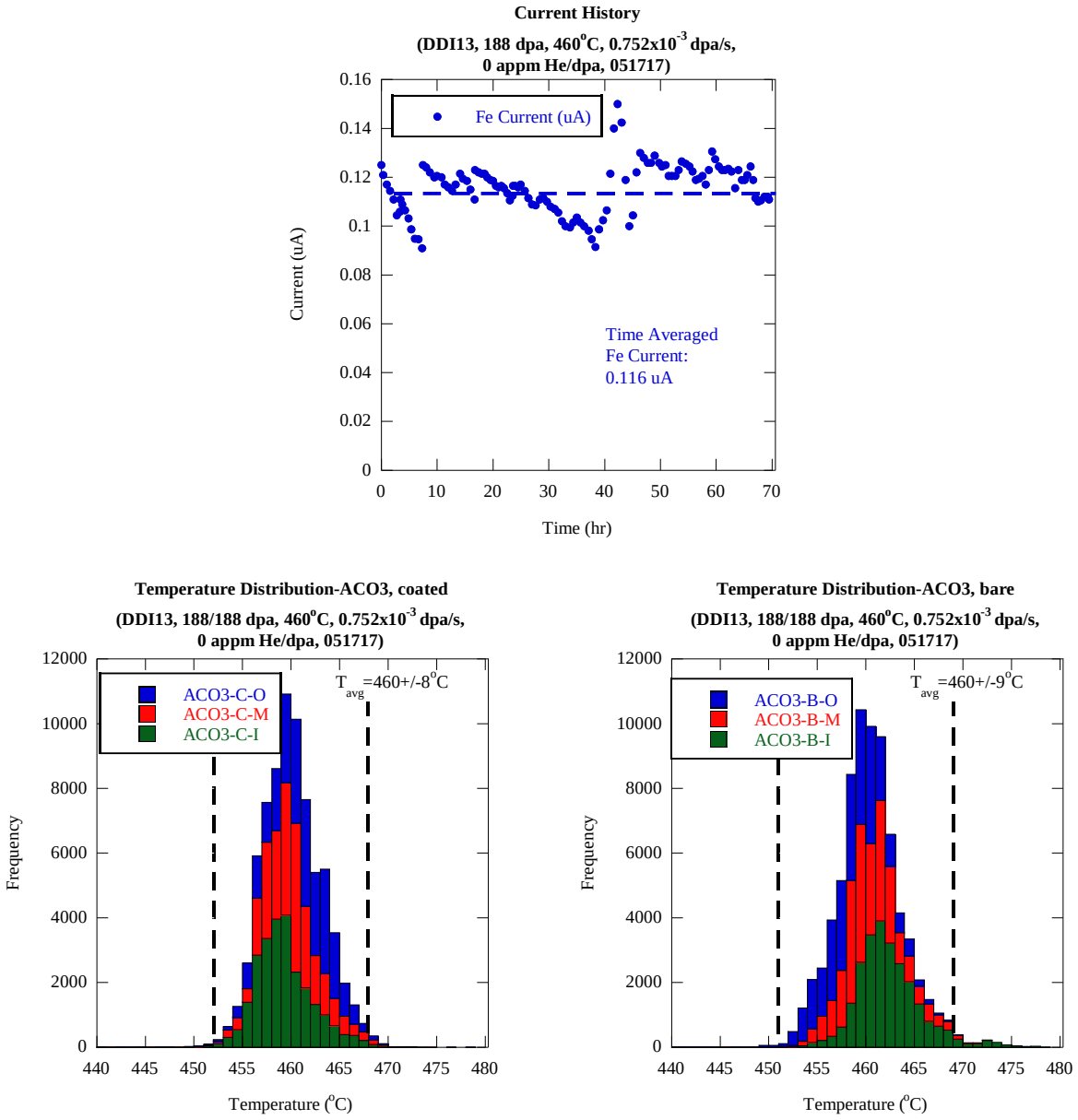

Figure A.1: Current and temperature for the dual ion irradiation of HT9 to 188 dpa at 460°C with 0 appm He/dpa co-injected helium.

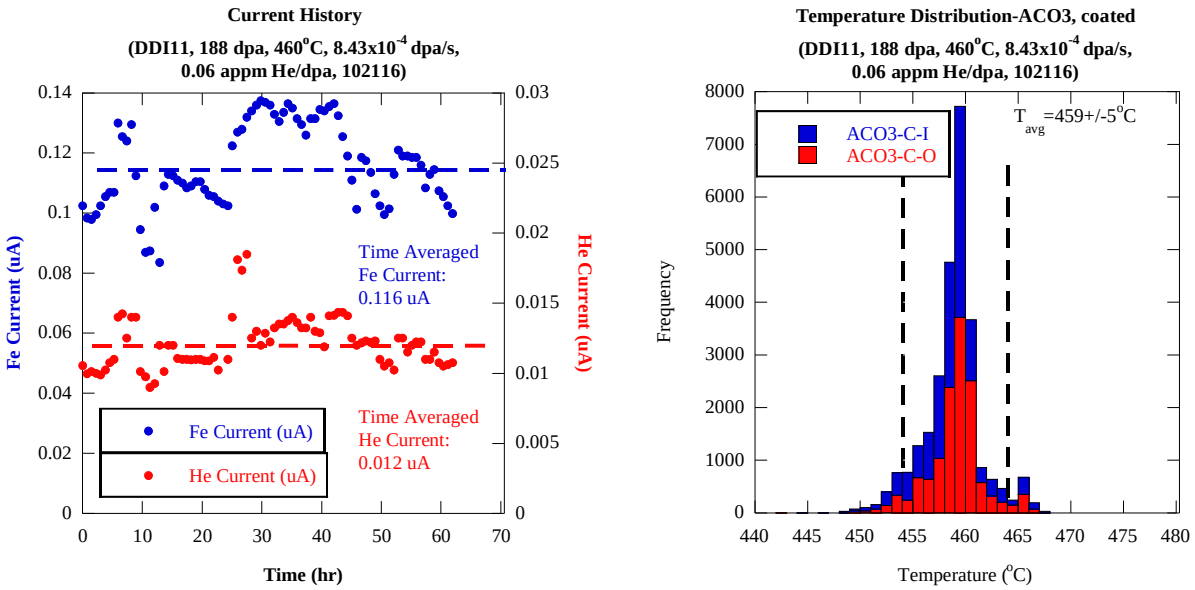

Figure A.2: Current and temperature for the dual ion irradiation of HT9 to 188 dpa at 460°C with 0.06 appm He/dpa co-injected helium.

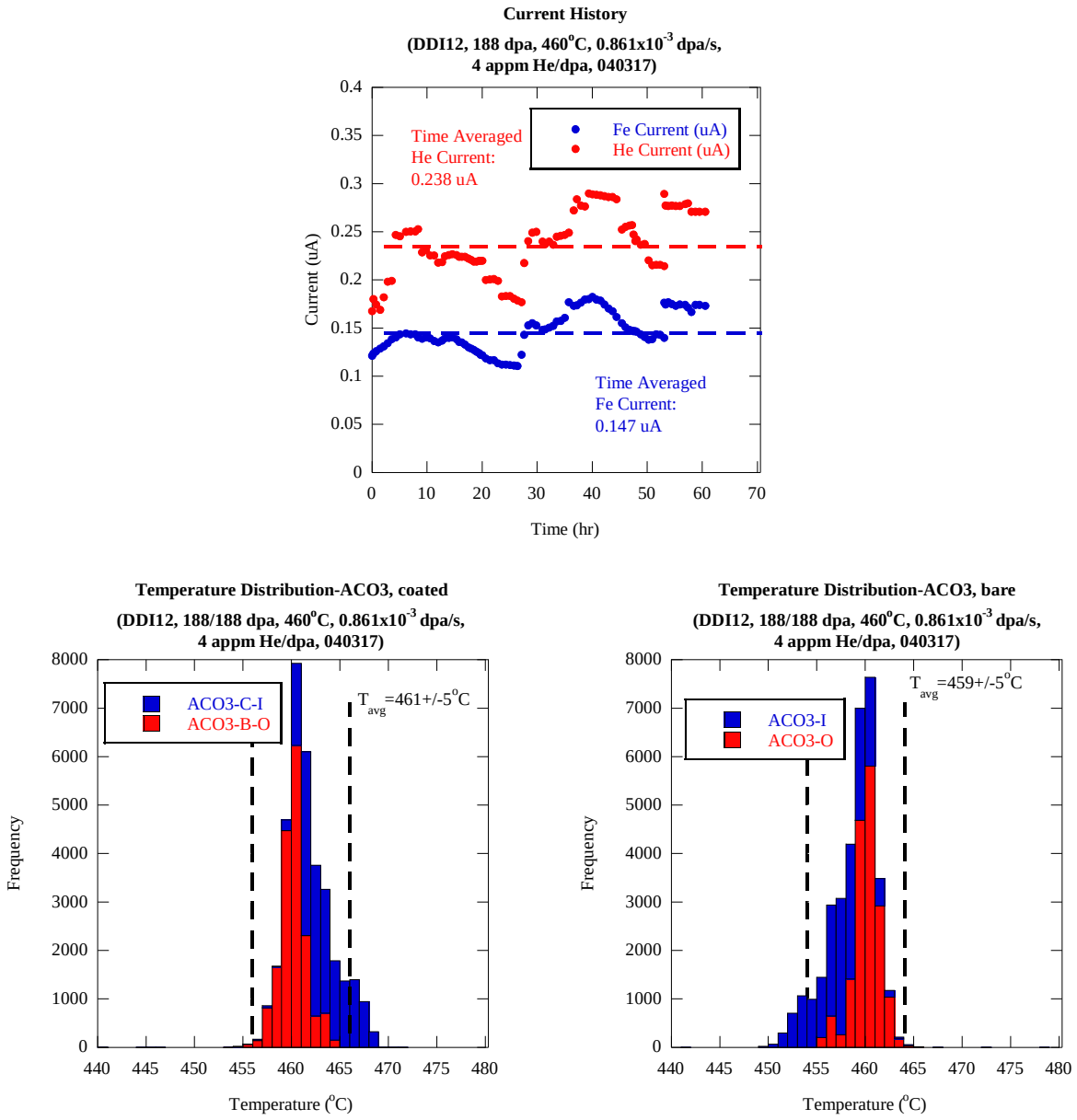

Figure A.3: Current and temperature for the dual ion irradiation of HT9 to 188 dpa at 460°C with 4 appm He/dpa co-injected helium.

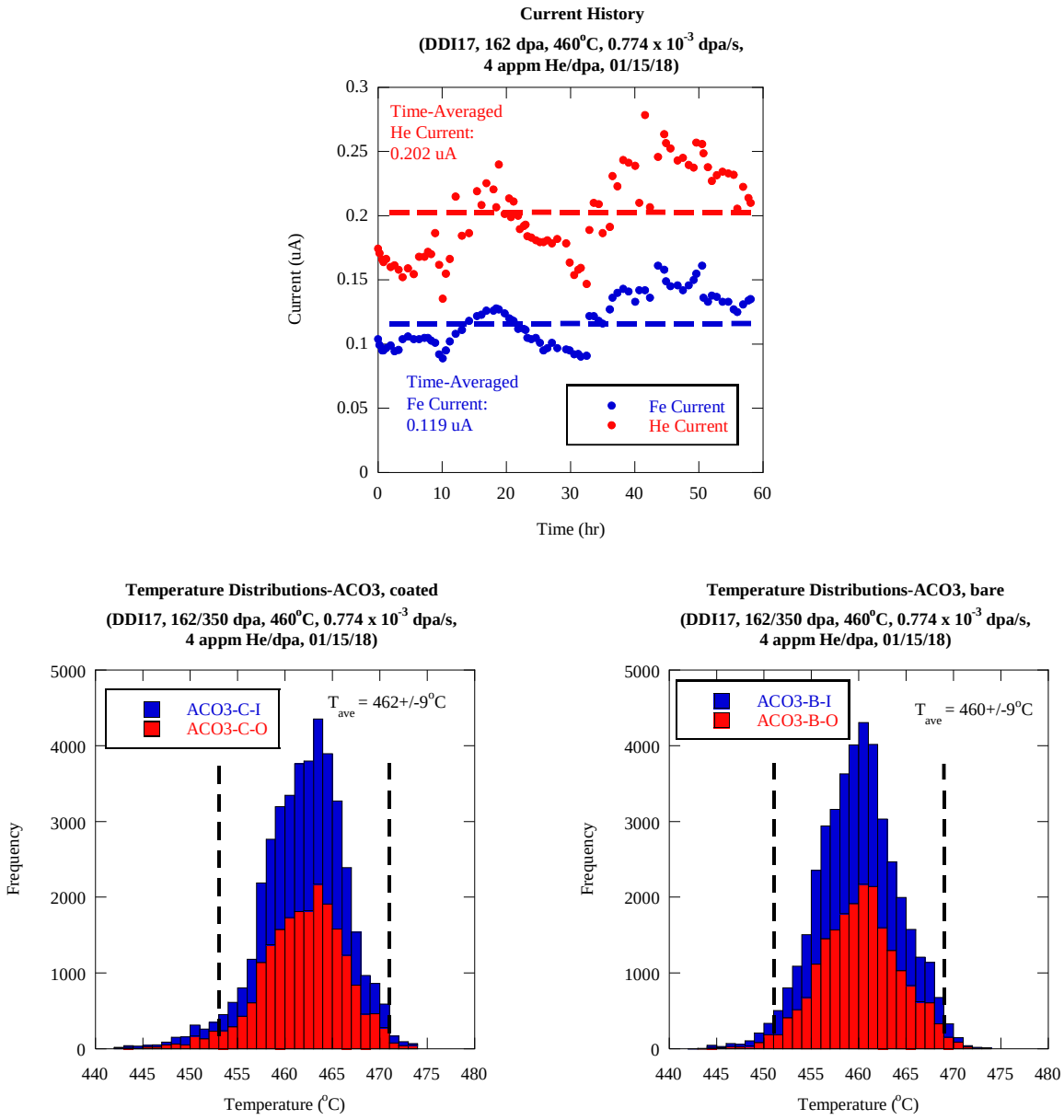

Figure A.4: Current and temperature for the dual ion irradiation of HT9 to 350 dpa at 460°C with 4 appm He/dpa co-injected helium.

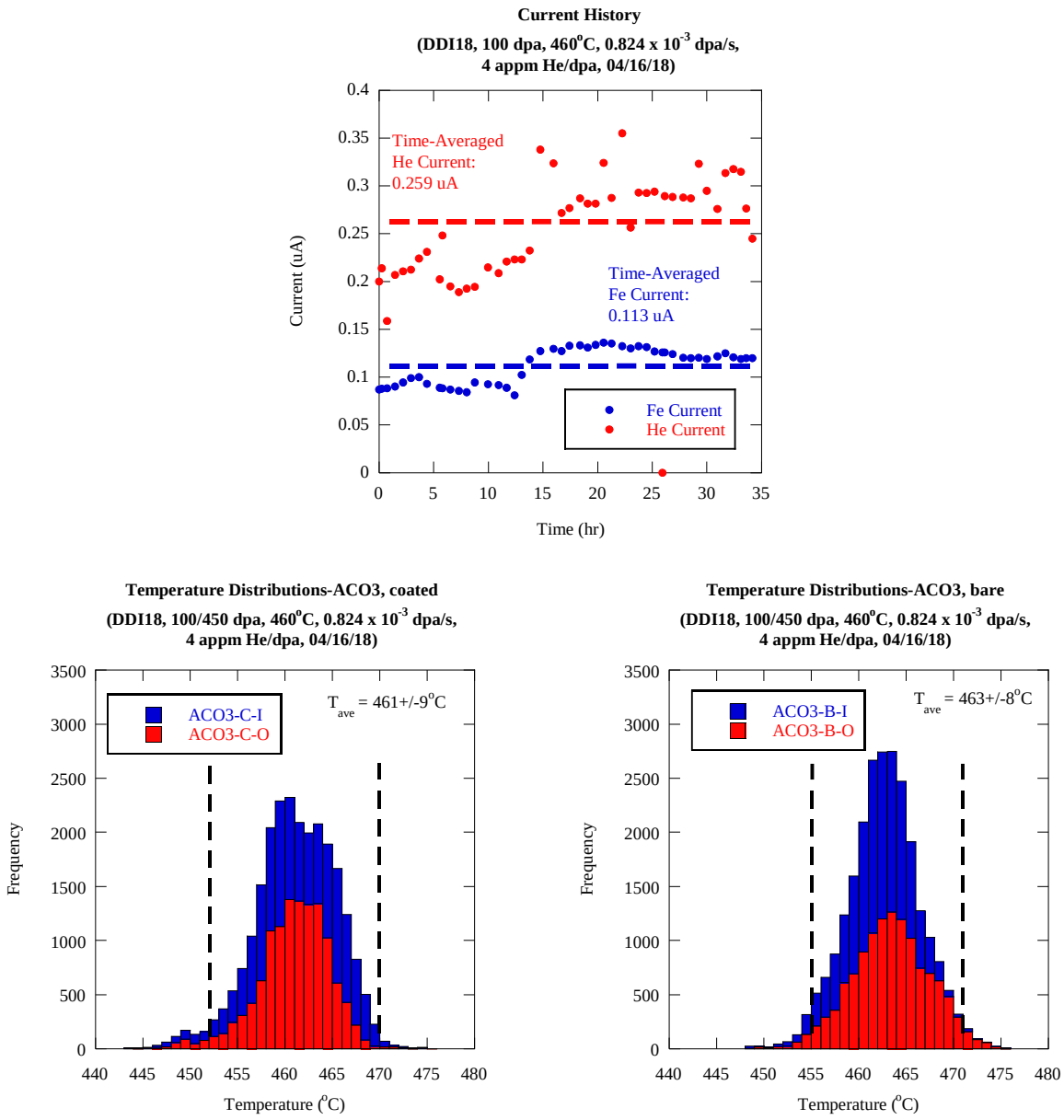

Figure A.5: Current and temperature for the dual ion irradiation of HT9 to 450 dpa at 460°C with 4 appm He/dpa co-injected helium.

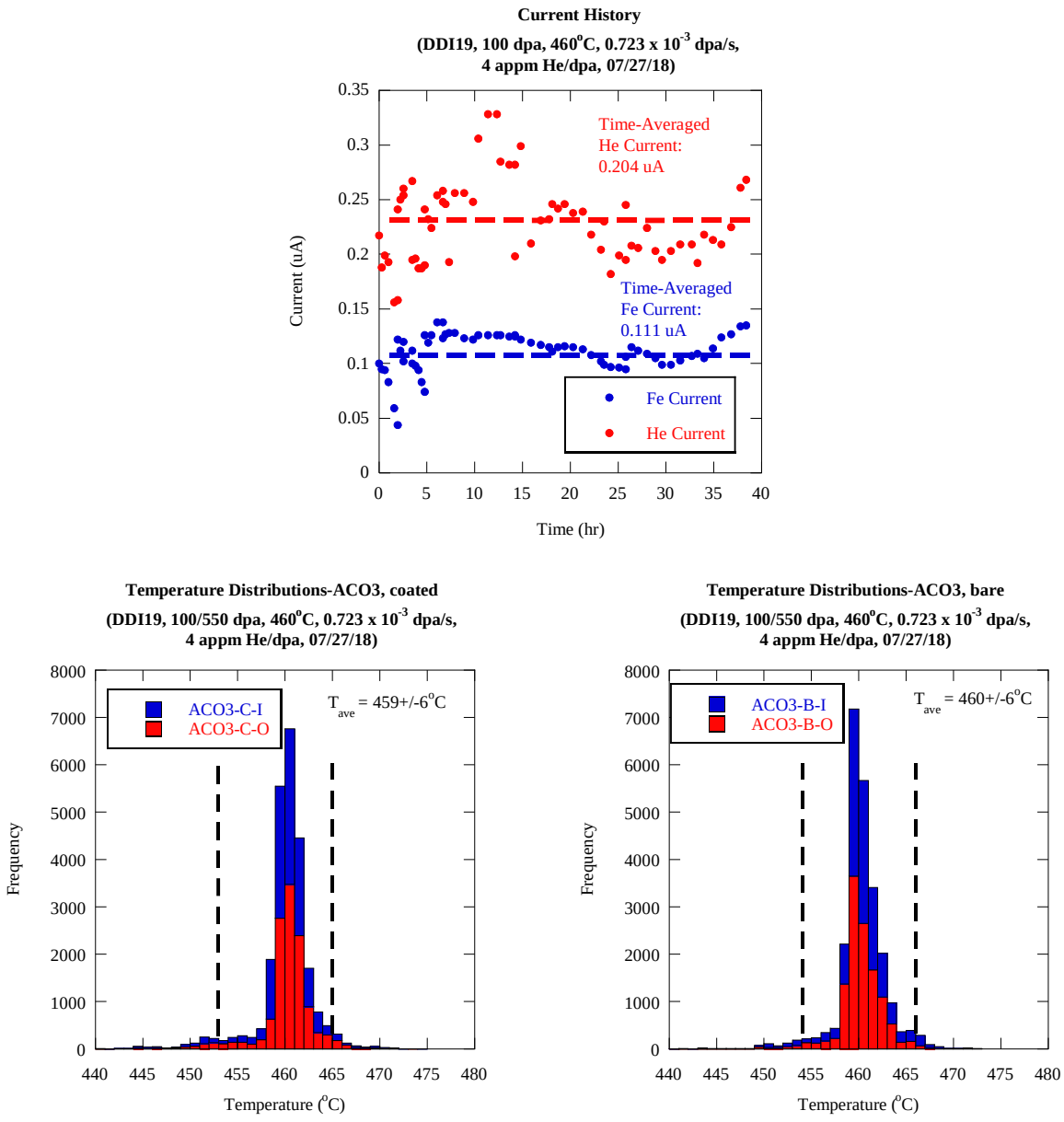

Figure A.6: Current and temperature for the dual ion irradiation of HT9 to 550 dpa at 460°C with 4 appm He/dpa co-injected helium.

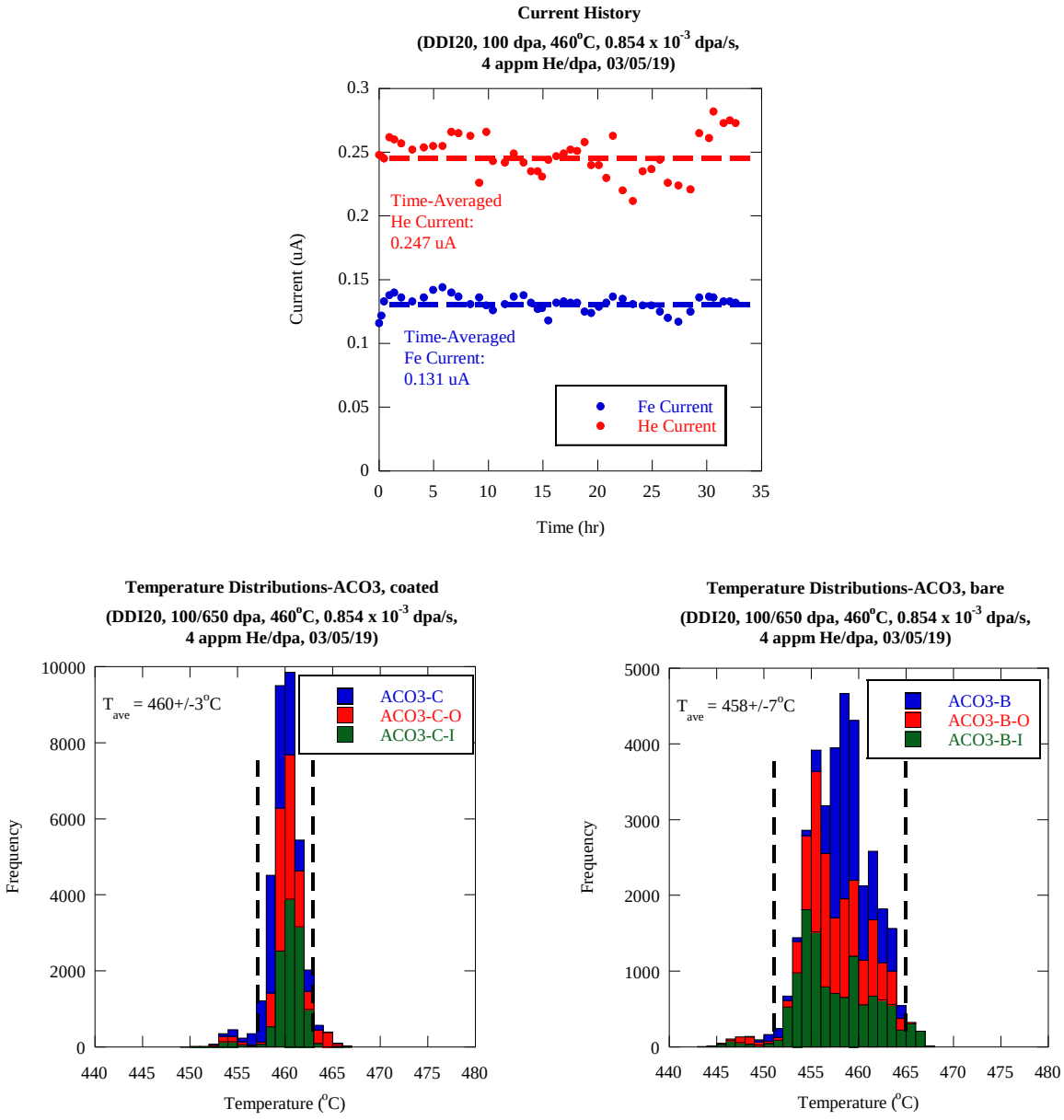

Figure A.7: Current and temperature for the dual ion irradiation of HT9 to 650 dpa at 460°C with 4 appm He/dpa co-injected helium.

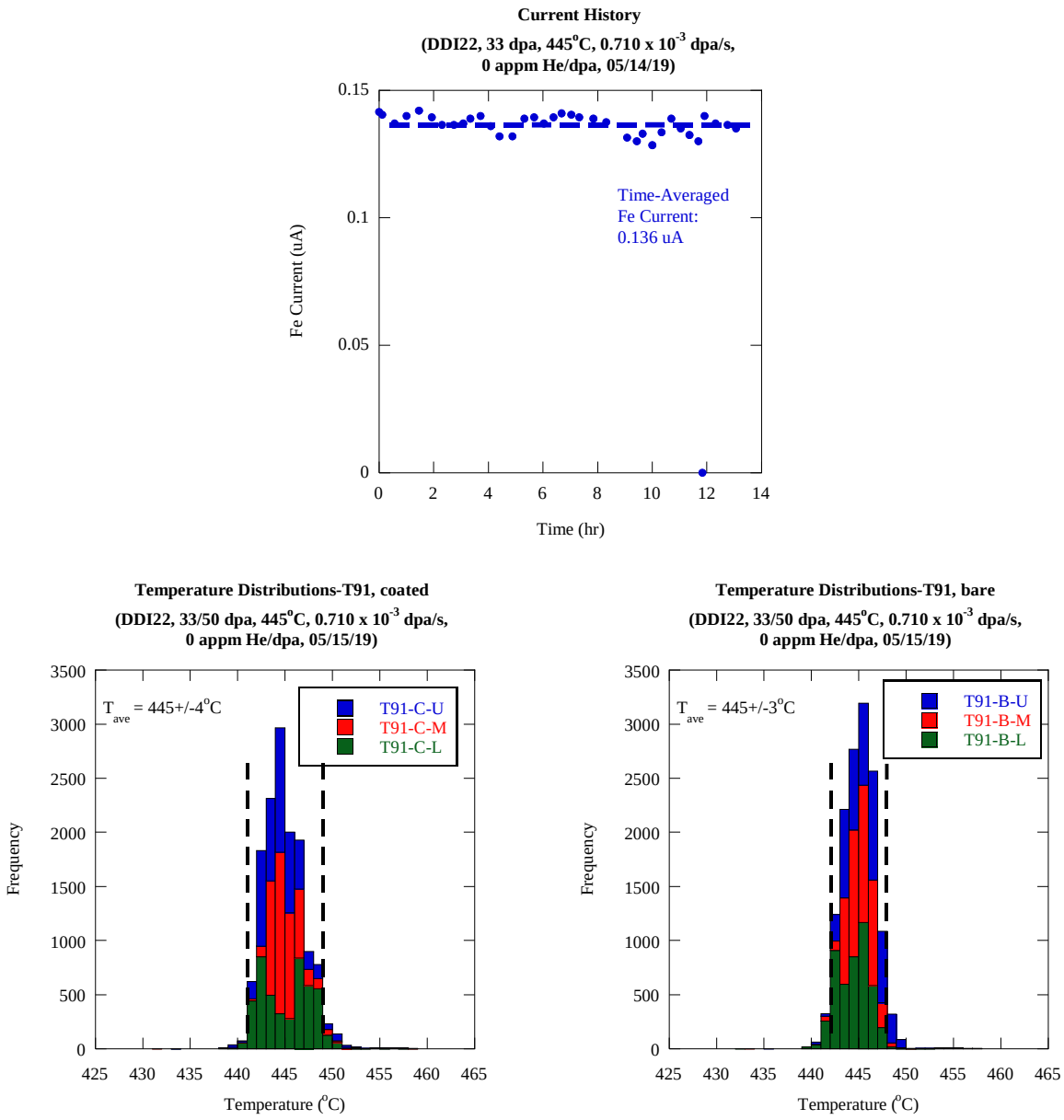

Figure A.8: Current and temperature for the dual ion irradiation of T91 to 17 dpa at 445°C with 0 appm He/dpa co-injected helium.

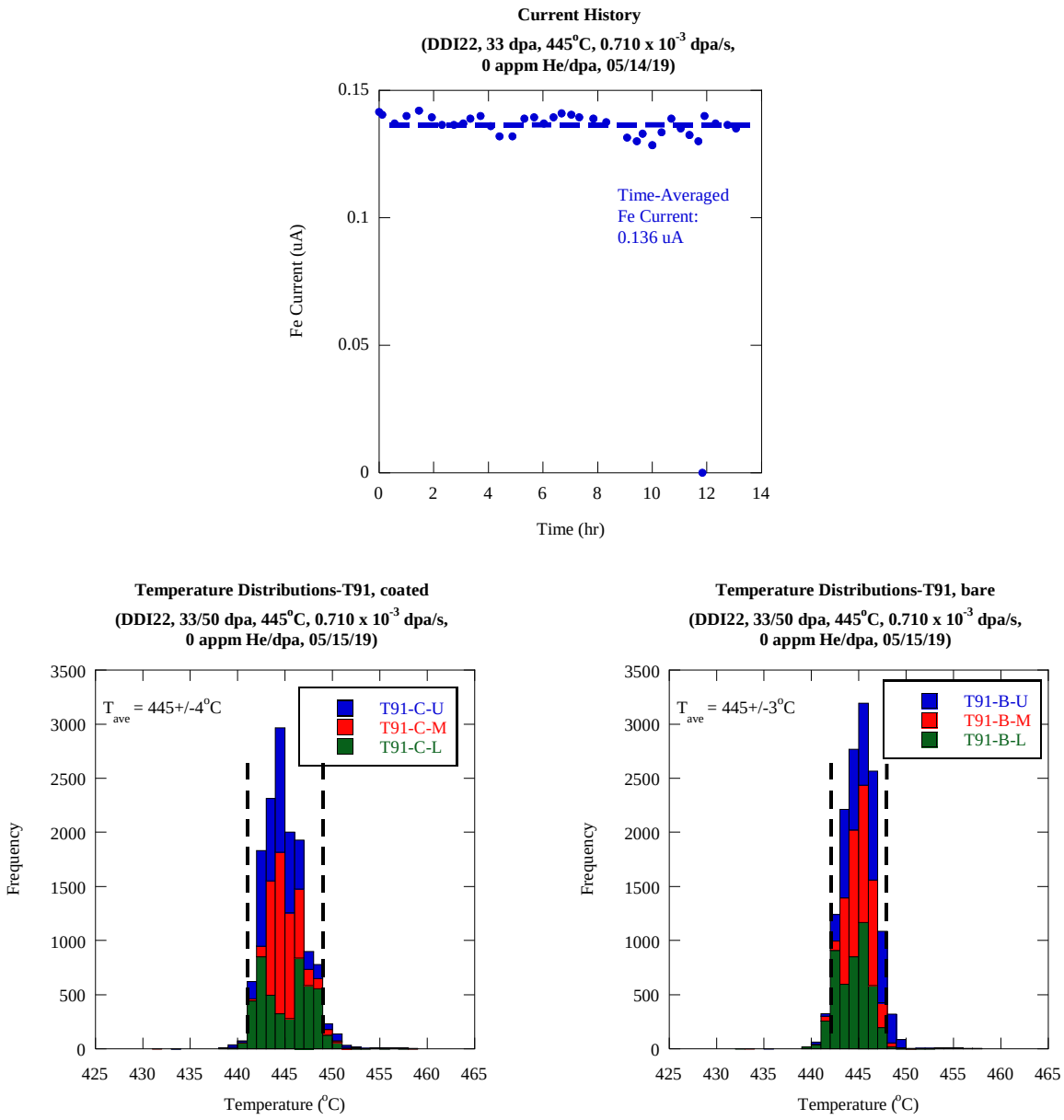

Figure A.9: Current and temperature for the dual ion irradiation of T91 to 17 dpa at 445°C with 0 appm He/dpa co-injected helium.

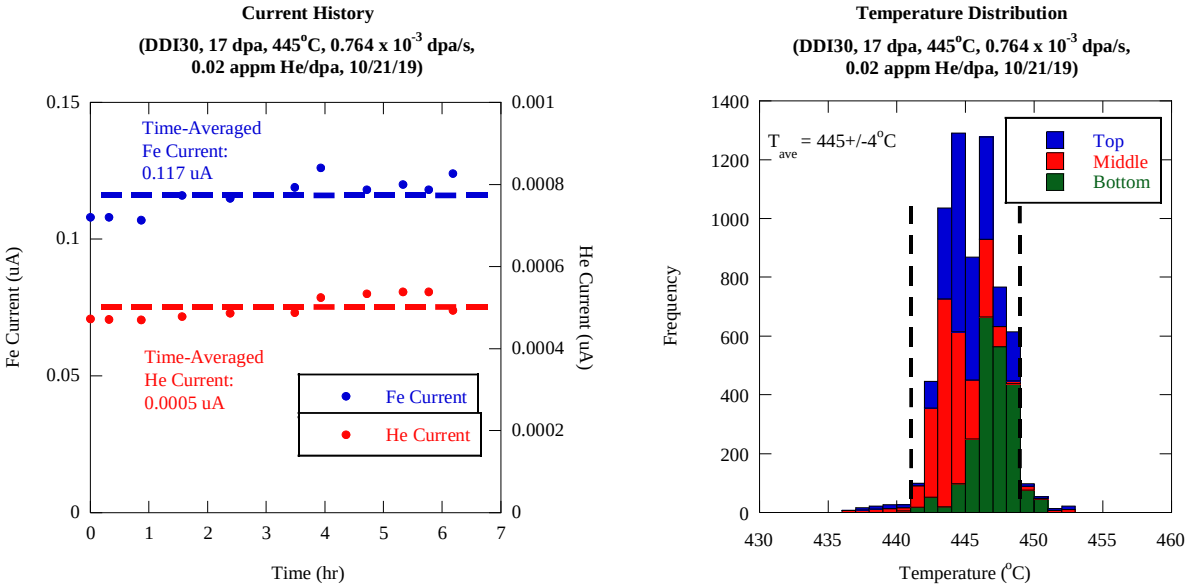

Figure A.10: Current and temperature for the dual ion irradiation of T91 to 17 dpa at 445°C with 0.02 appm He/dpa co-injected helium.

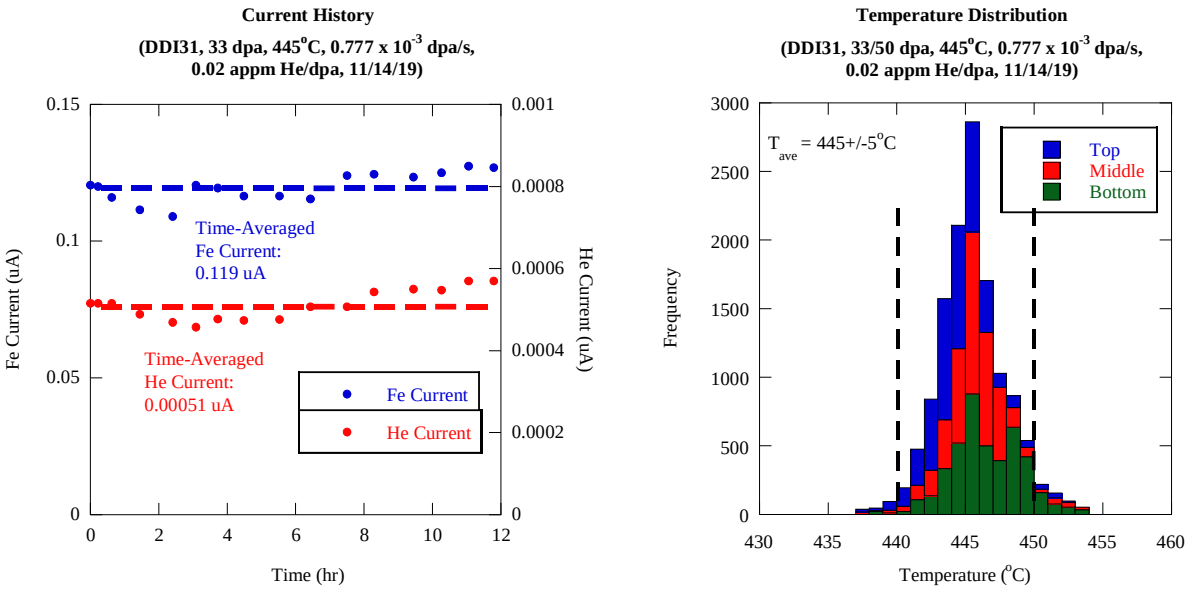

Figure A.11: Current and temperature for the dual ion irradiation of T91 to 17 dpa at 445°C with 0 appm He/dpa co-injected helium.

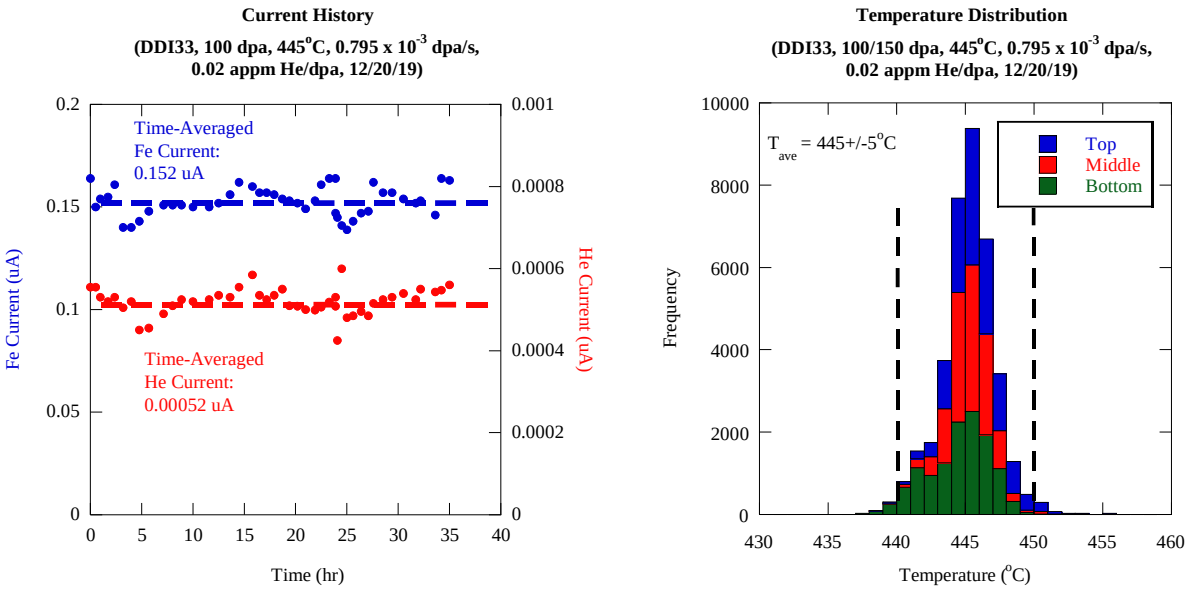

Figure A.12: Current and temperature for the dual ion irradiation of T91 to 100 dpa at 445°C with 0.02 appm He/dpa co-injected helium.

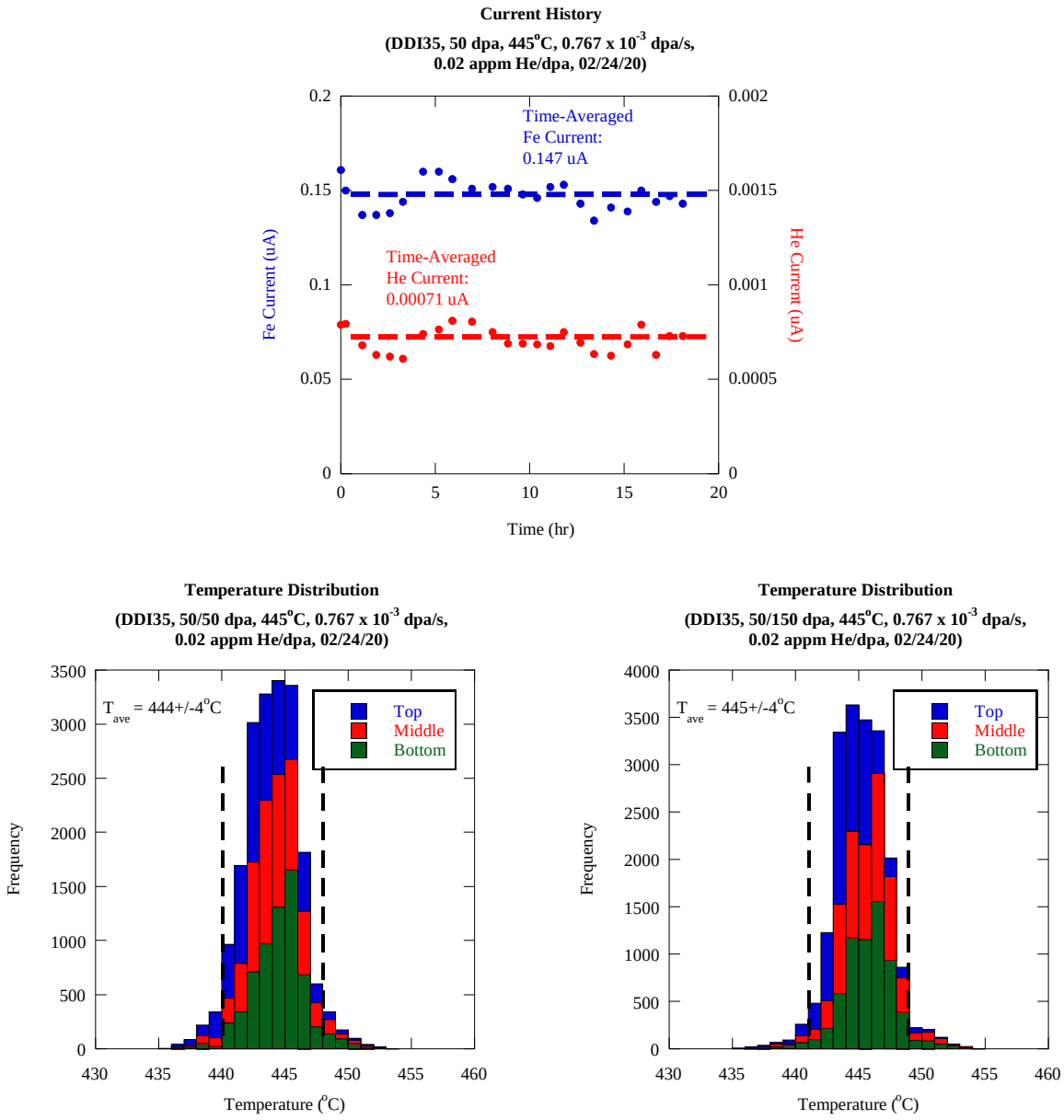

Figure A.13: Current and temperature for the dual ion irradiation of T91 to 50 dpa at 445°C with 0.02 appm He/dpa co-injected helium.

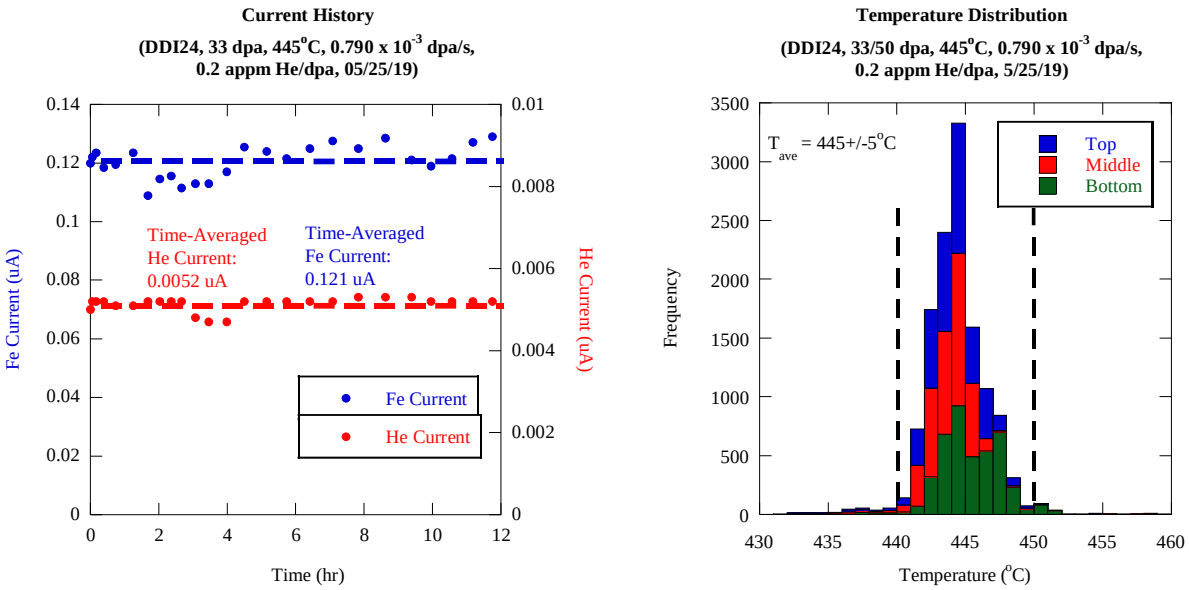

Figure A.14: Current and temperature for the dual ion irradiation of T91 to 33 dpa at 445°C with 0.2 appm He/dpa co-injected helium.

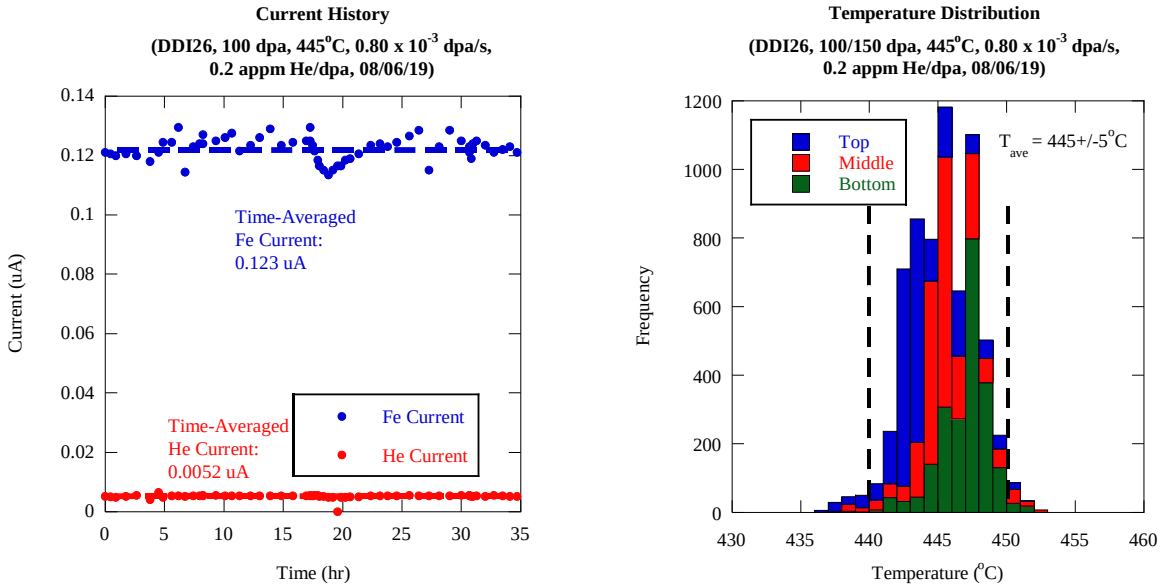

Figure A.15: Current and temperature for the dual ion irradiation of T91 to 100 dpa at 445°C with 0.2 appm He/dpa co-injected helium.

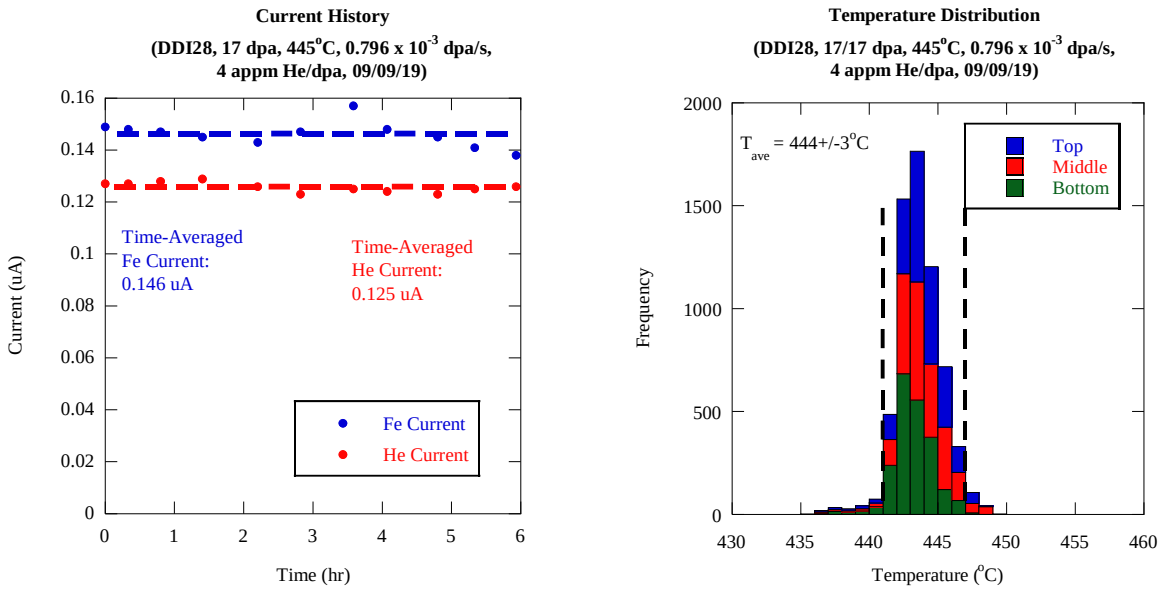

Figure A.16: Current and temperature for the dual ion irradiation of T91 to 17 dpa at 445°C with 4 appm He/dpa co-injected helium.

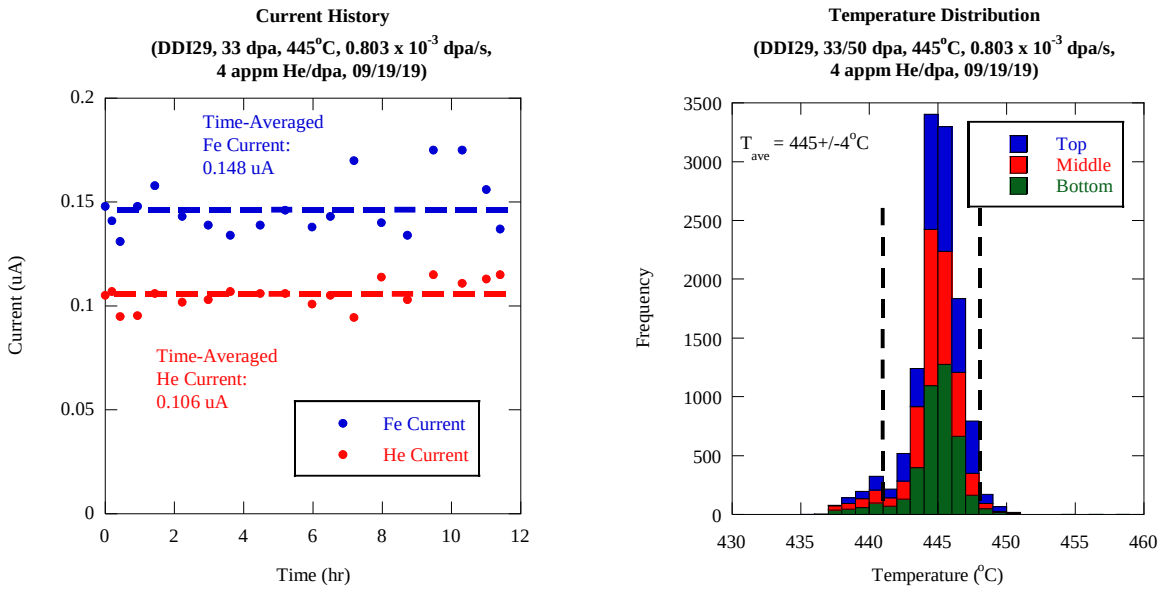

Figure A.17: Current and temperature for the dual ion irradiation of T91 to 33 dpa at 445°C with 4 appm He/dpa co-injected helium.

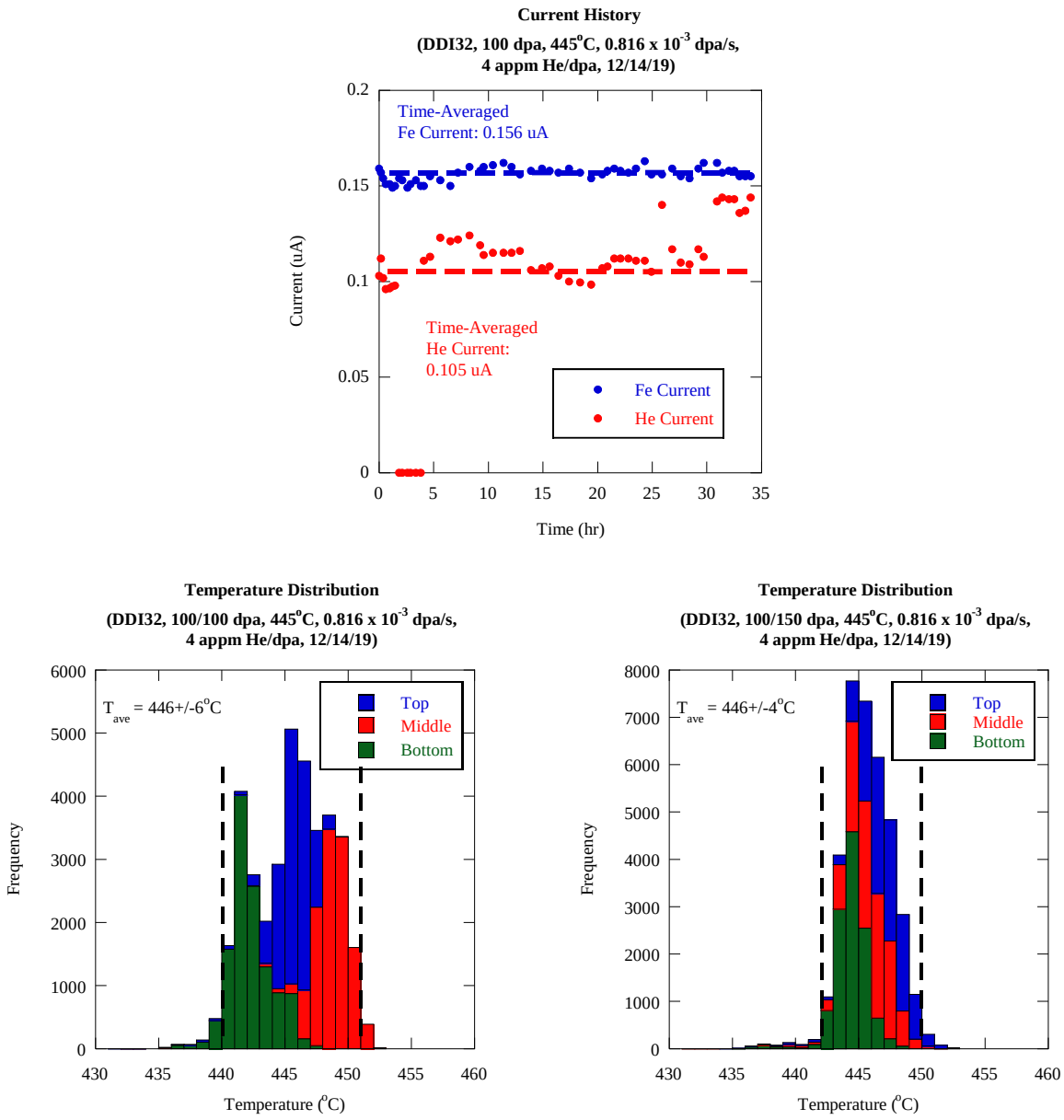

Figure A.18: Current and temperature for the dual ion irradiation of T91 to 100 dpa at 445°C with 4 appm He/dpa co-injected helium.

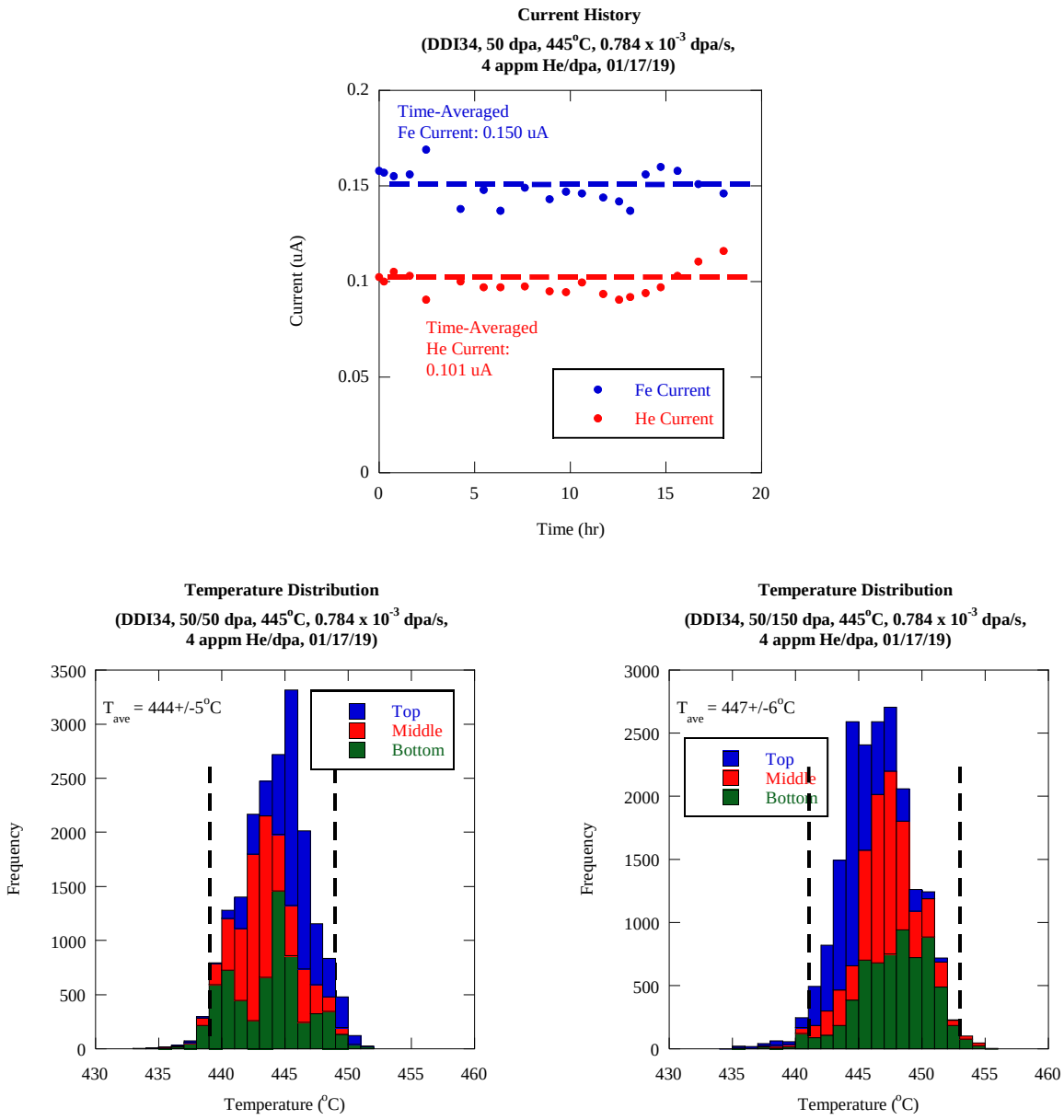

Figure A.19: Current and temperature for the first dual ion irradiation of T91 to 50 dpa at 445°C with 4 appm He/dpa co-injected helium.

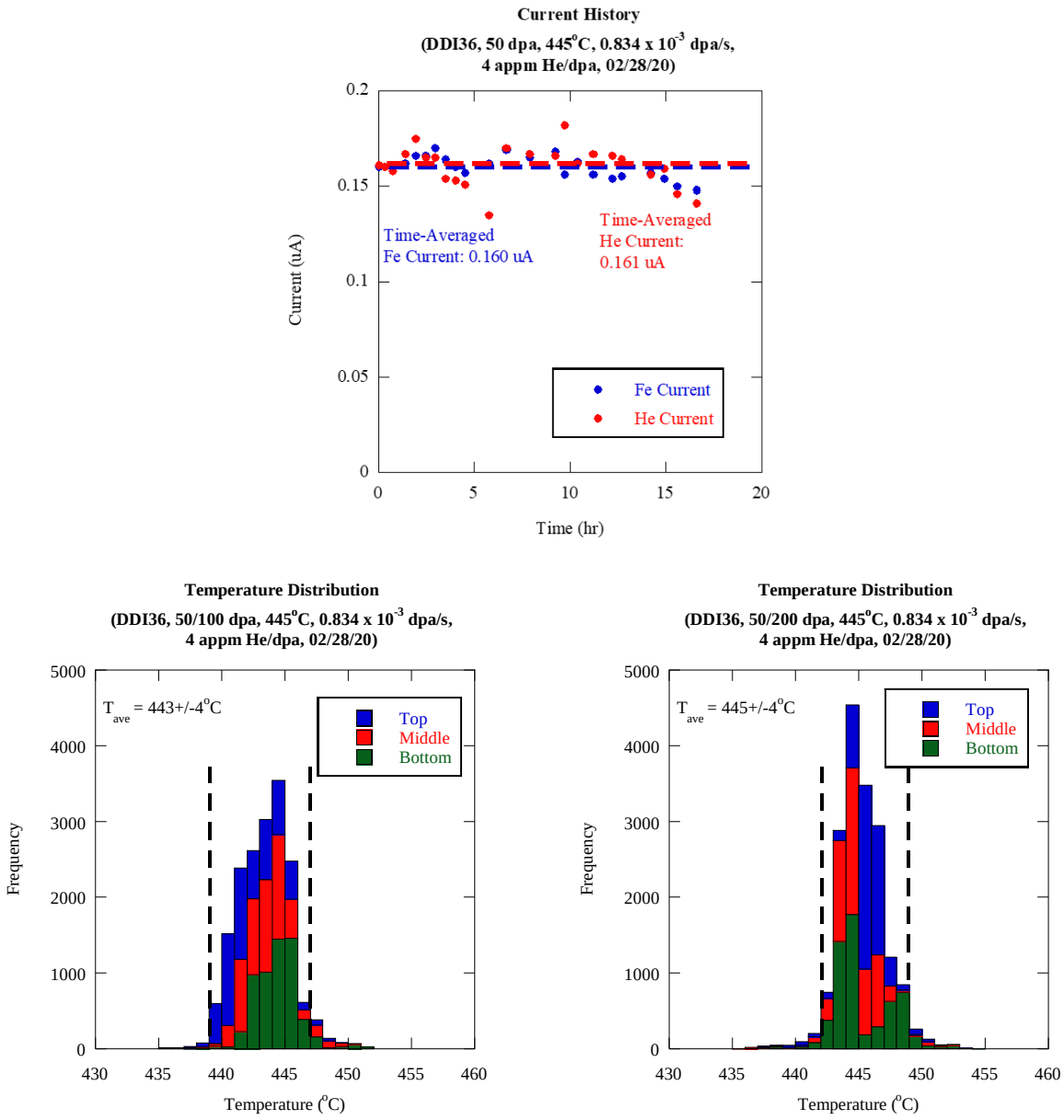

Figure A.20: Current and temperature for the second dual ion irradiation of T91 to 50 dpa at 445°C with 4 appm He/dpa co-injected helium.

Appendix B : **LIFTOUT IMAGES**

High angle annular dark field images (HAADF) STEM images for each irradiated condition are presented in this appendix.

Figure B.1: STEM HAADF Images for liftouts from the irradiation of HT9 at 460°C with 0 appm He/dpa to 188 dpa.

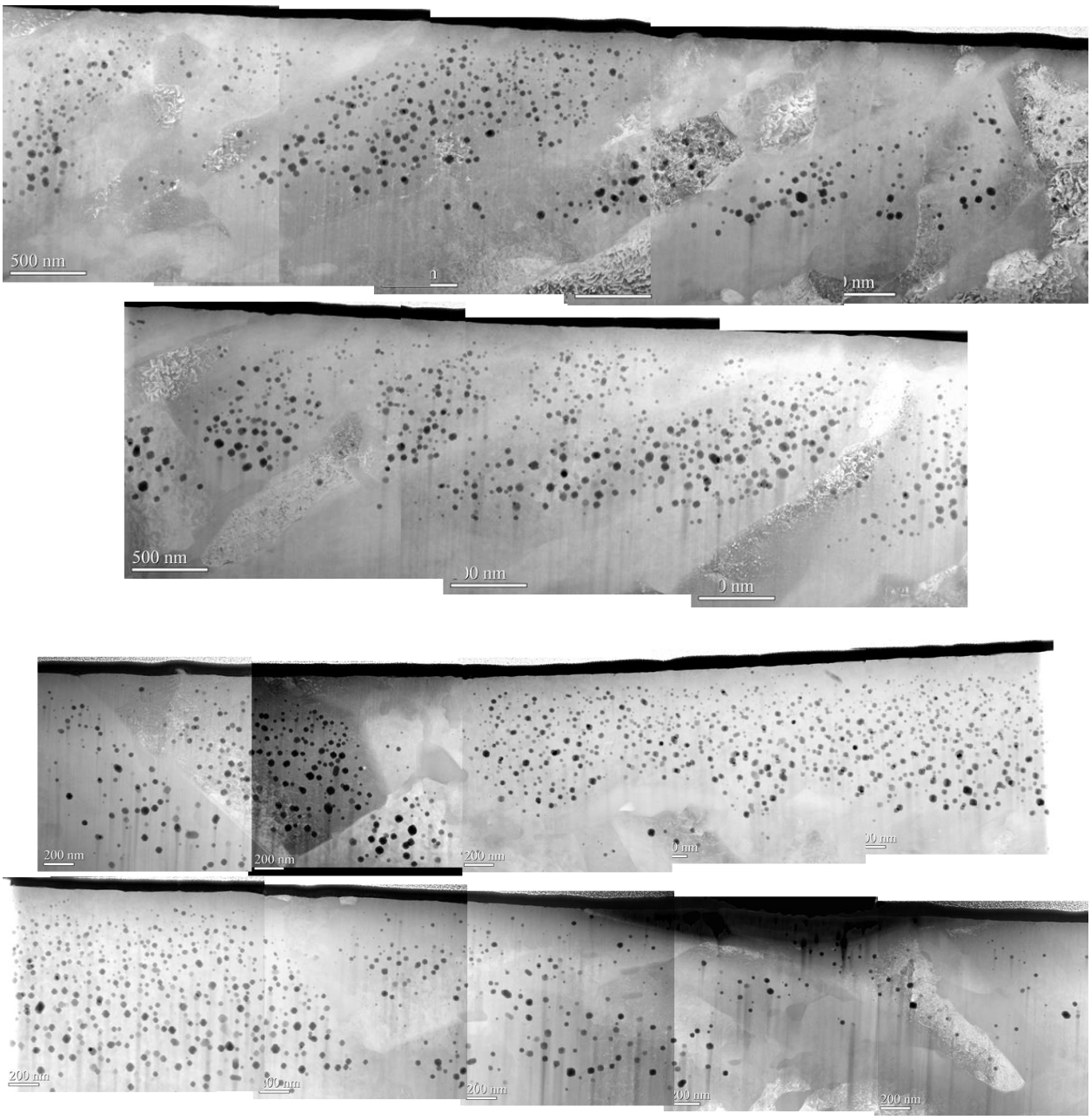

Figure B.2: STEM HAADF Images for liftouts from the first irradiation of HT9 at 460°C with 0.06 appm He/dpa to 188 dpa.

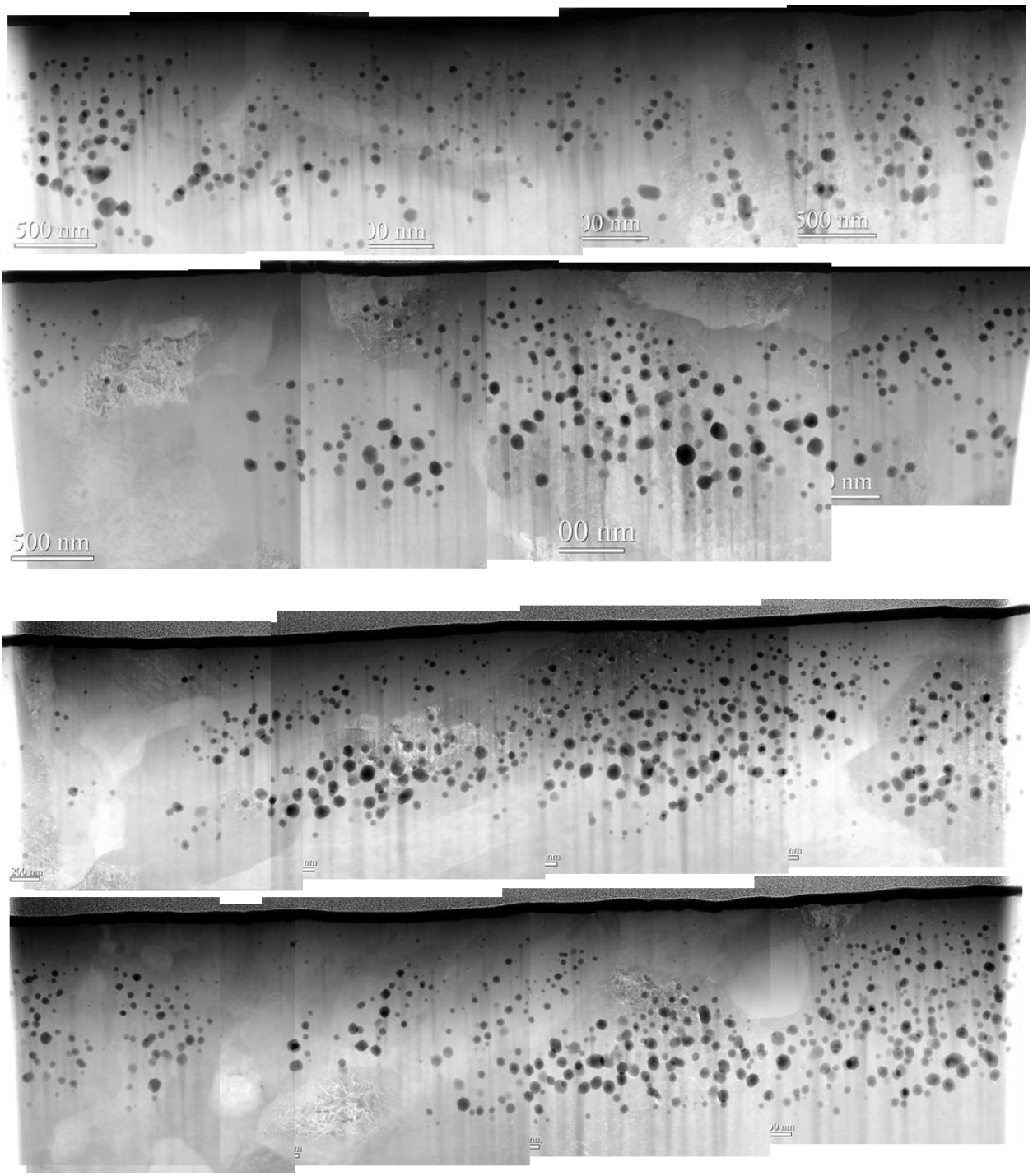

Figure B.3: STEM HAADF Images for liftouts from the second irradiation of HT9 at 460°C with 0.06 appm He/dpa to 188 dpa.

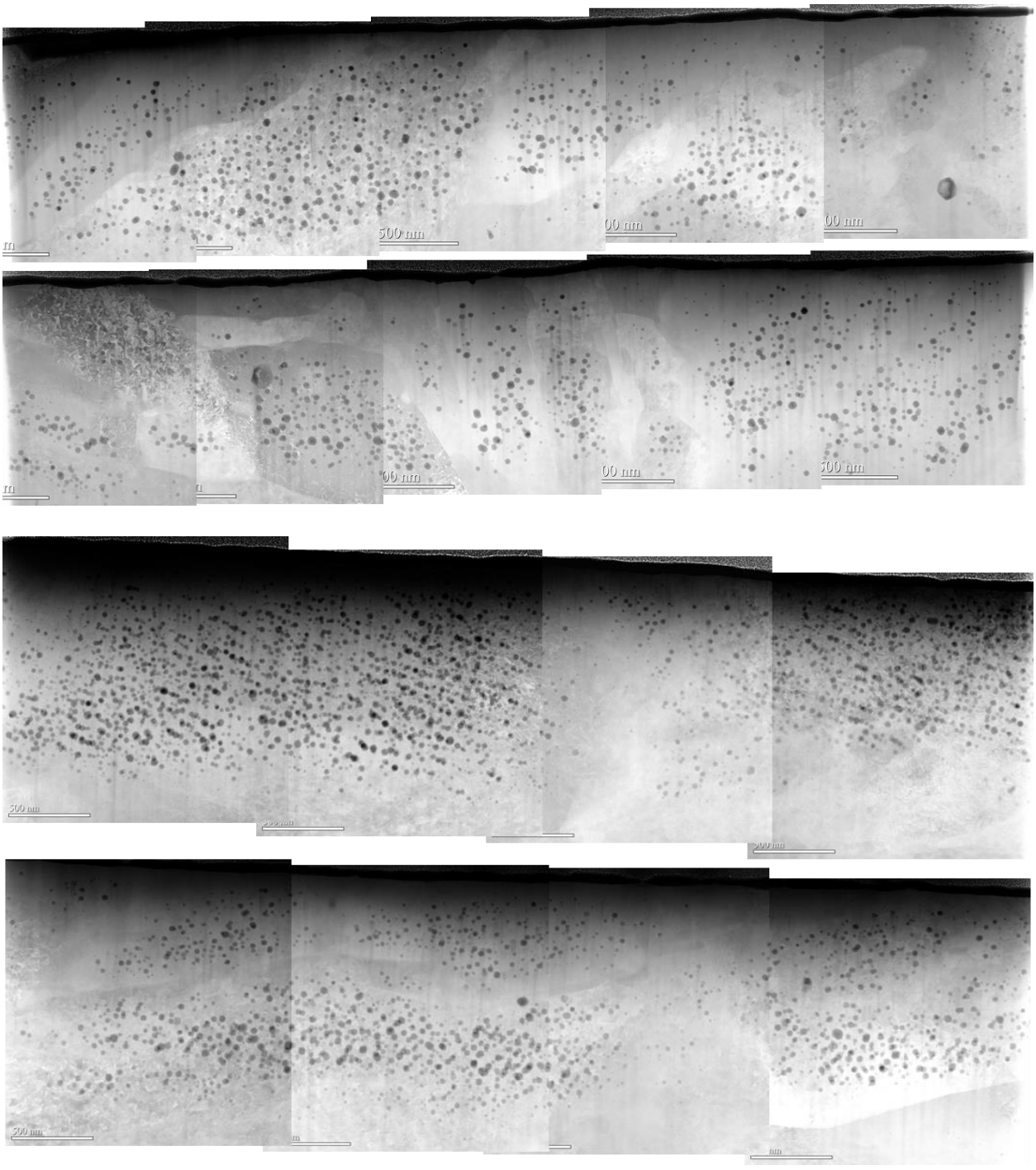

Figure B.4: STEM HAADF Images for liftouts from the irradiation of HT9 at 460°C with 4 appm He/dpa to 188 dpa.

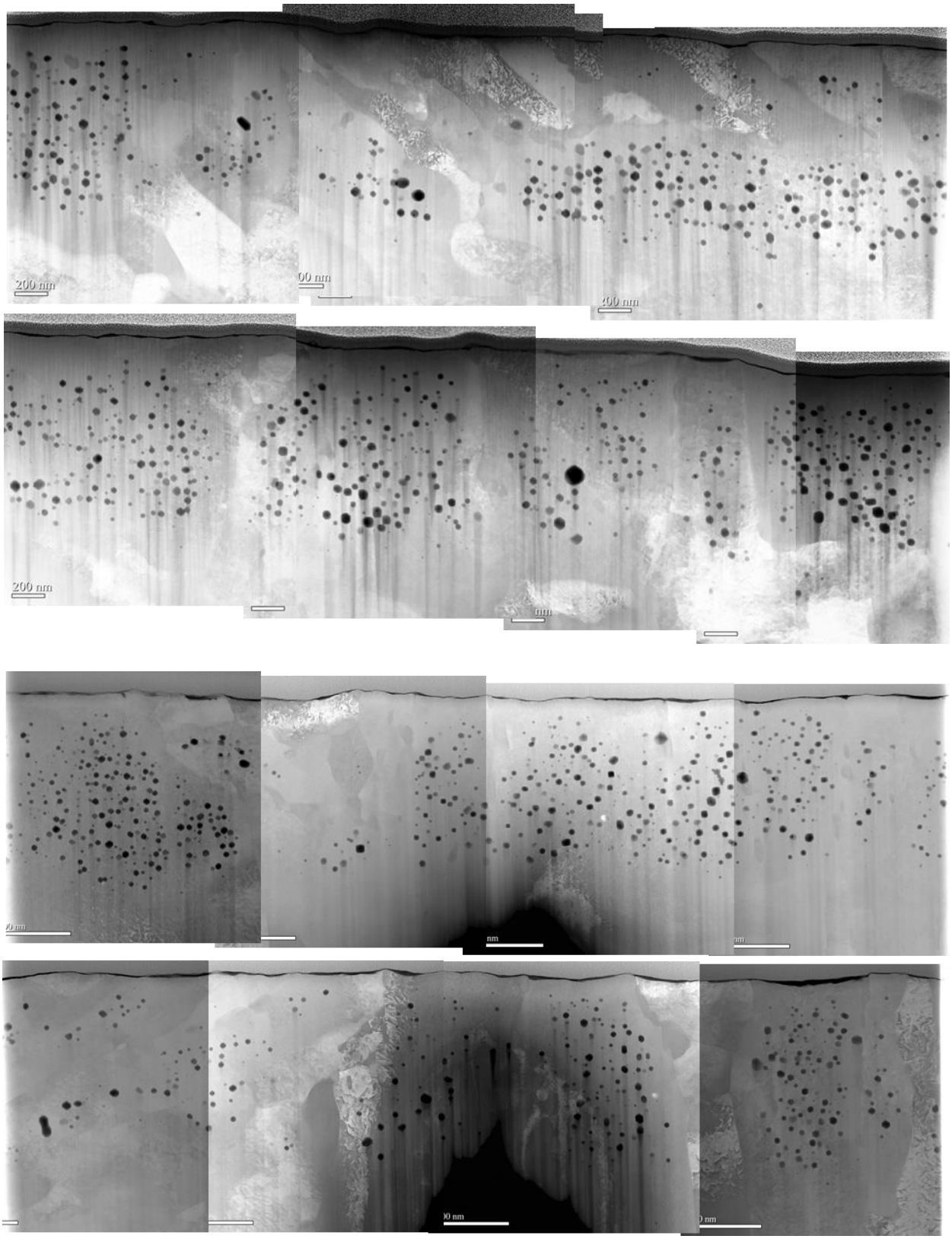

Figure B.5: STEM HAADF Images for liftouts from the irradiation of HT9 at 460°C with 4 appm He/dpa to 350 dpa.

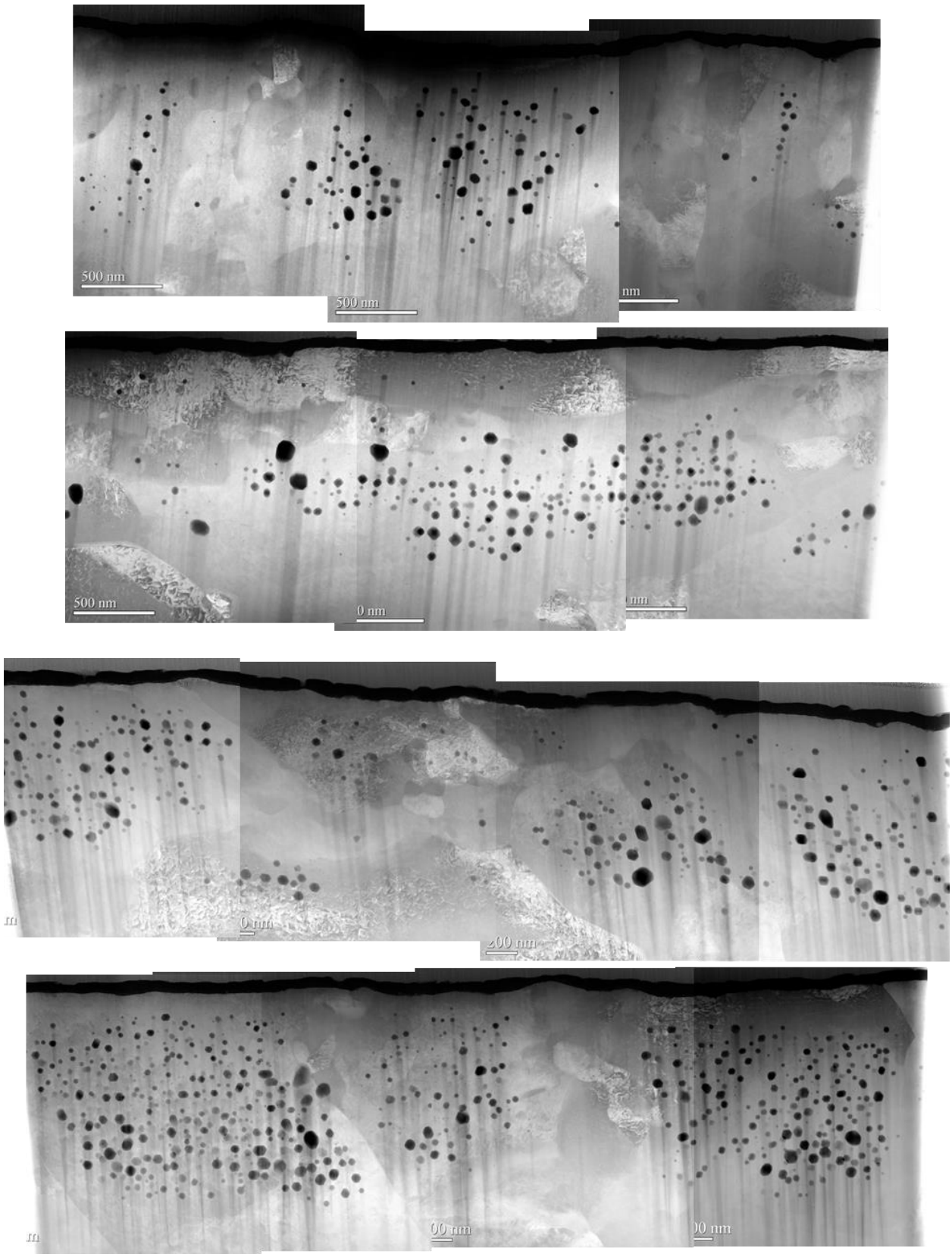

Figure B.6: STEM HAADF Images for liftouts from the irradiation of HT9 at 460°C with 4 appm He/dpa to 450 dpa.

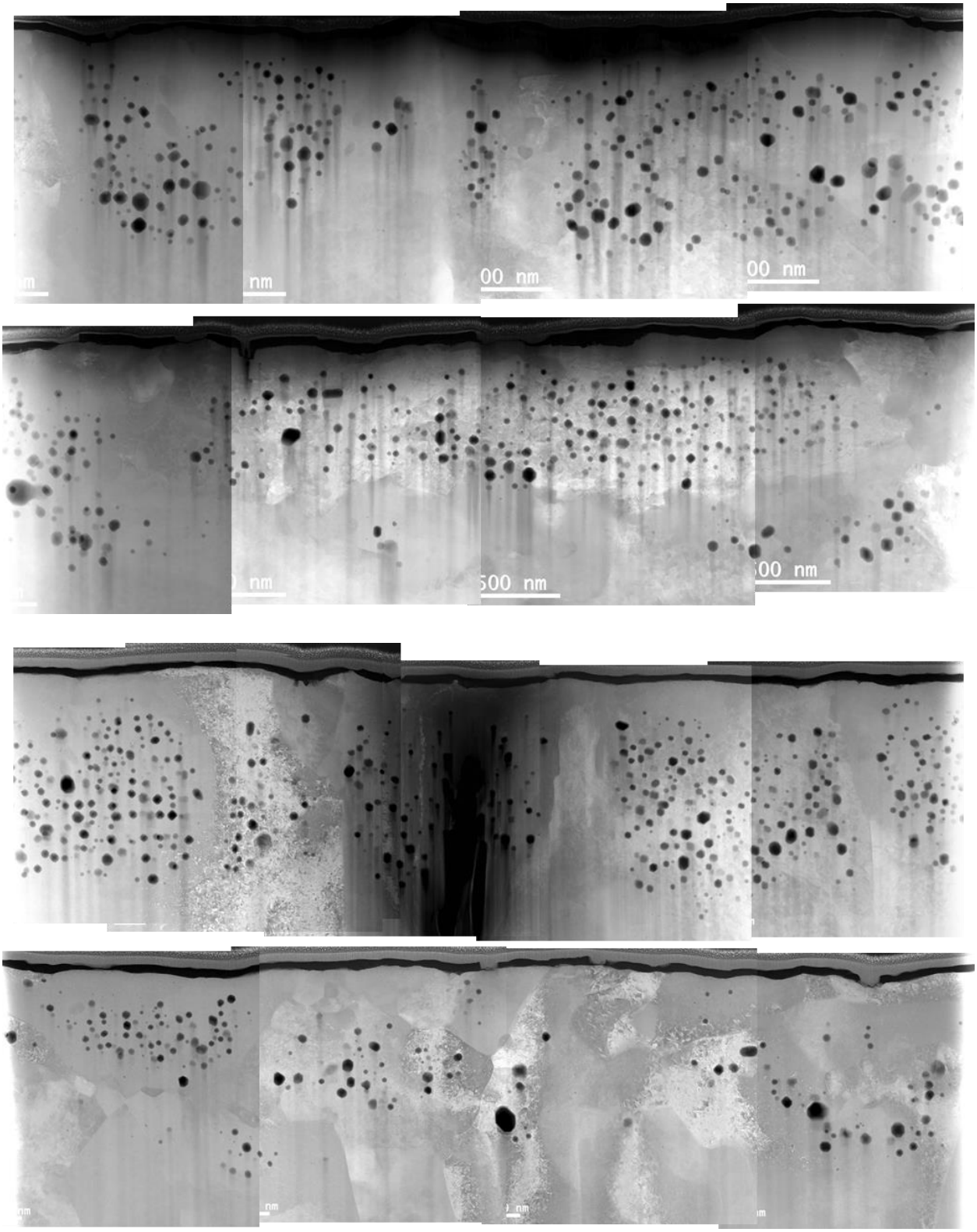

Figure B.7: STEM HAADF Images for liftouts from the irradiation of HT9 at 460°C with 4 appm He/dpa to 550 dpa.

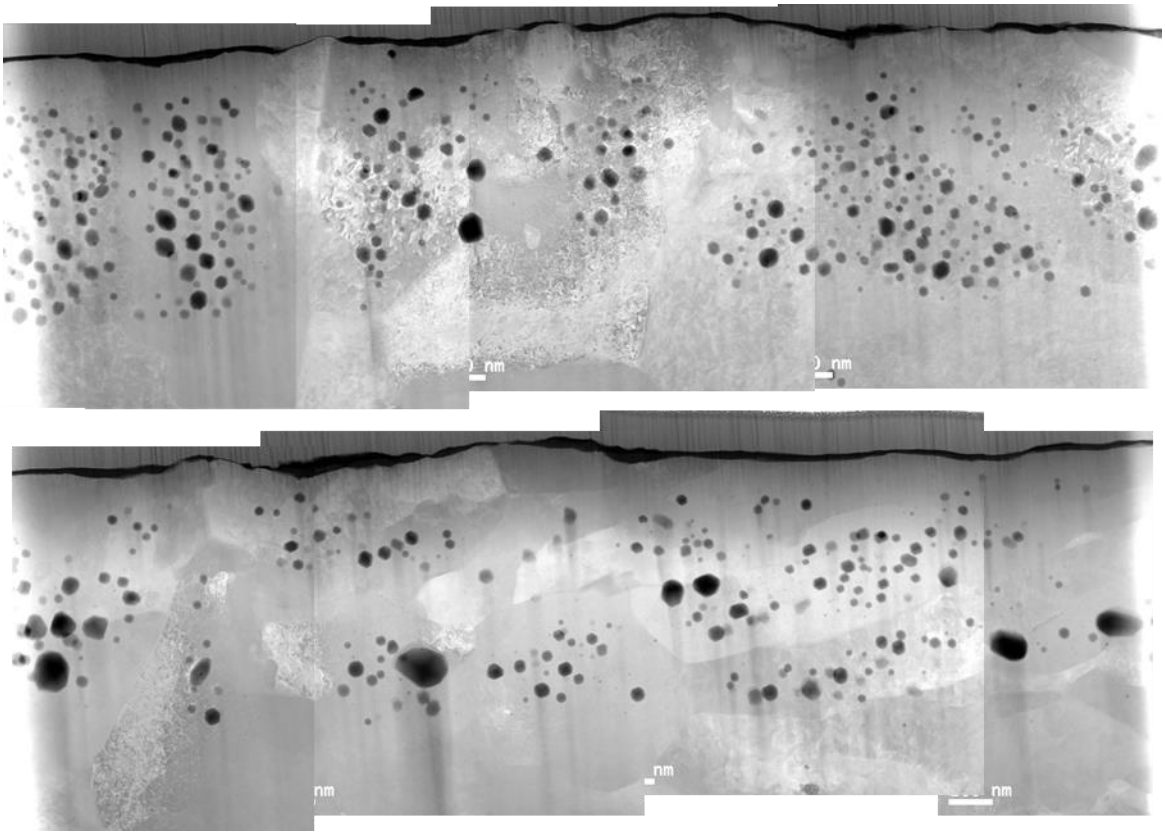

Figure B.8: STEM HAADF Images for liftouts from the irradiation of HT9 at 460°C with 4 appm He/dpa to 650 dpa.

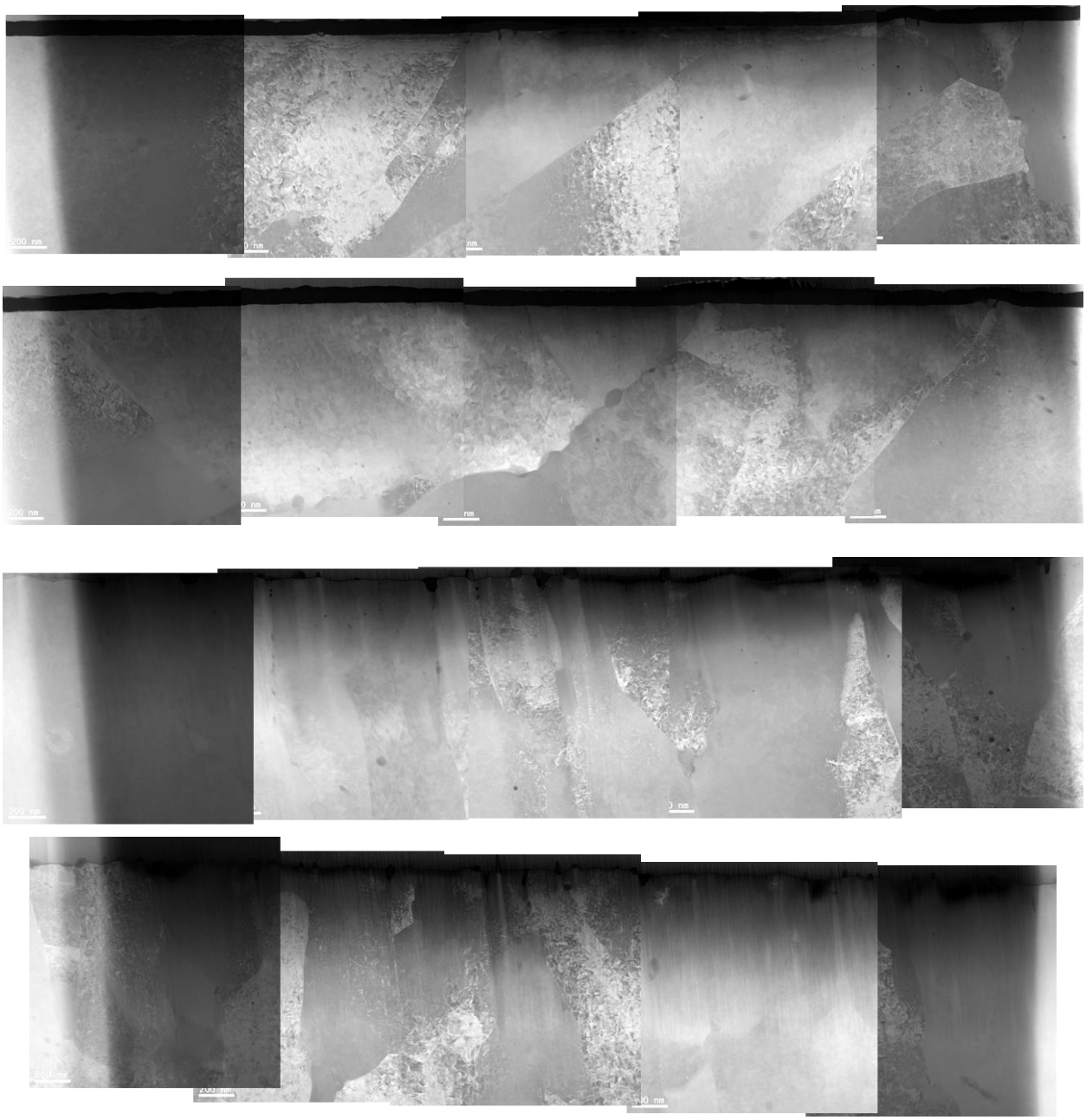

Figure B.9: STEM HAADF Images for liftouts from the irradiation of T91 at 445°C with 0 appm He/dpa to 50 dpa.

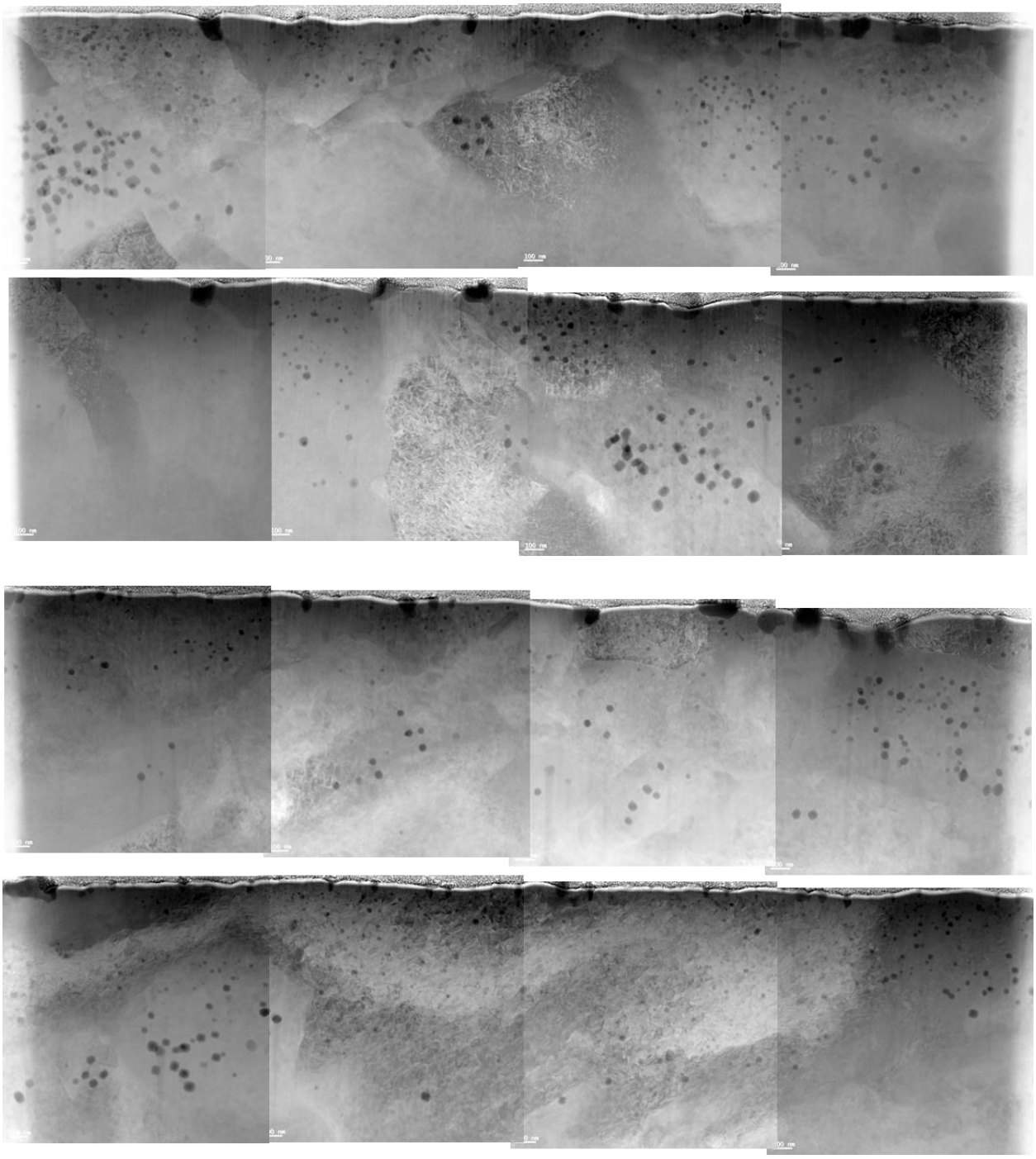

Figure B.10: STEM HAADF Images for liftouts from the irradiation of T91 at 445°C with 0 appm He/dpa to 150 dpa.

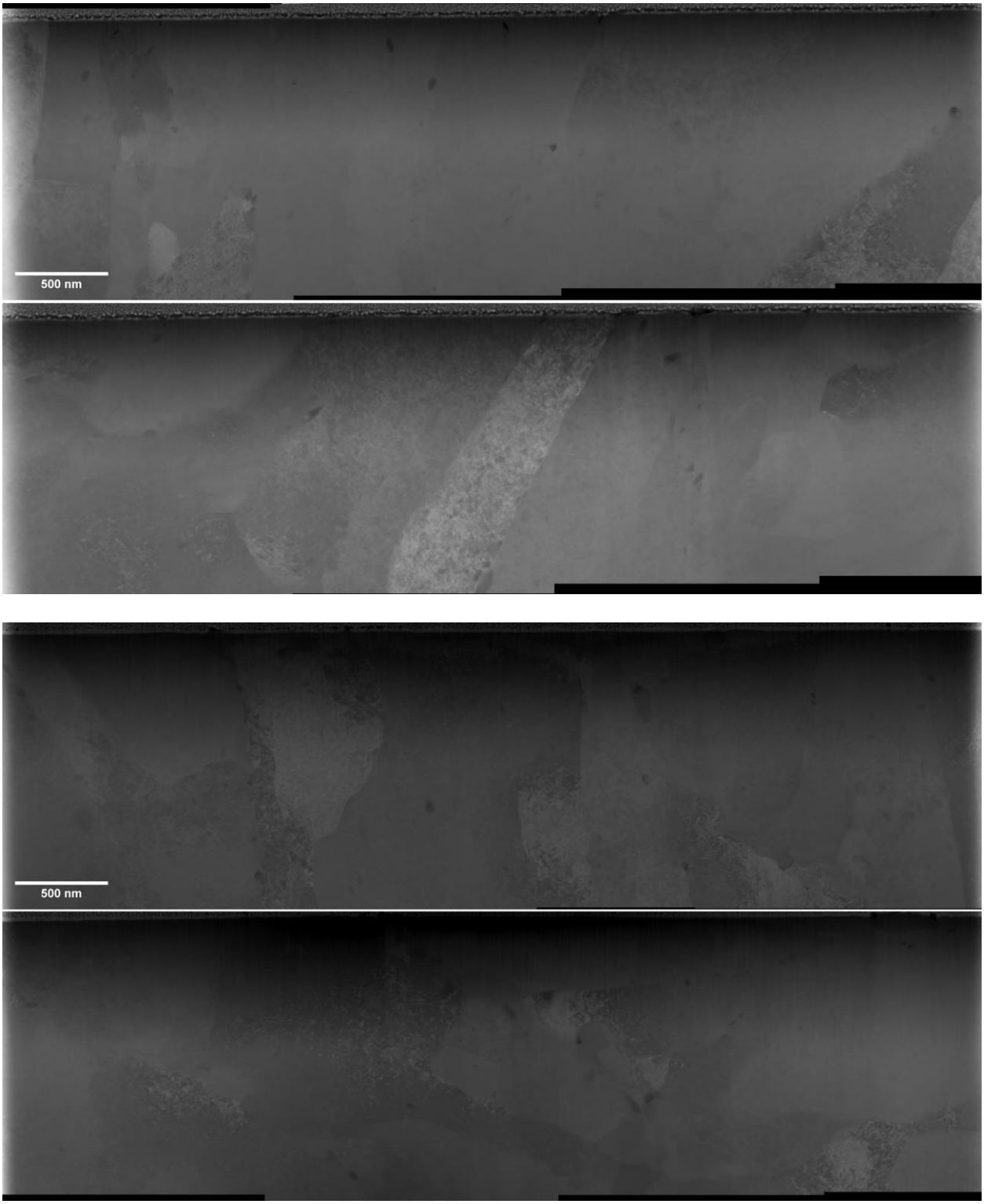

Figure B.11: STEM HAADF Images for liftouts from the irradiation of T91 at 445°C with 0.02 appm He/dpa to 17 dpa.

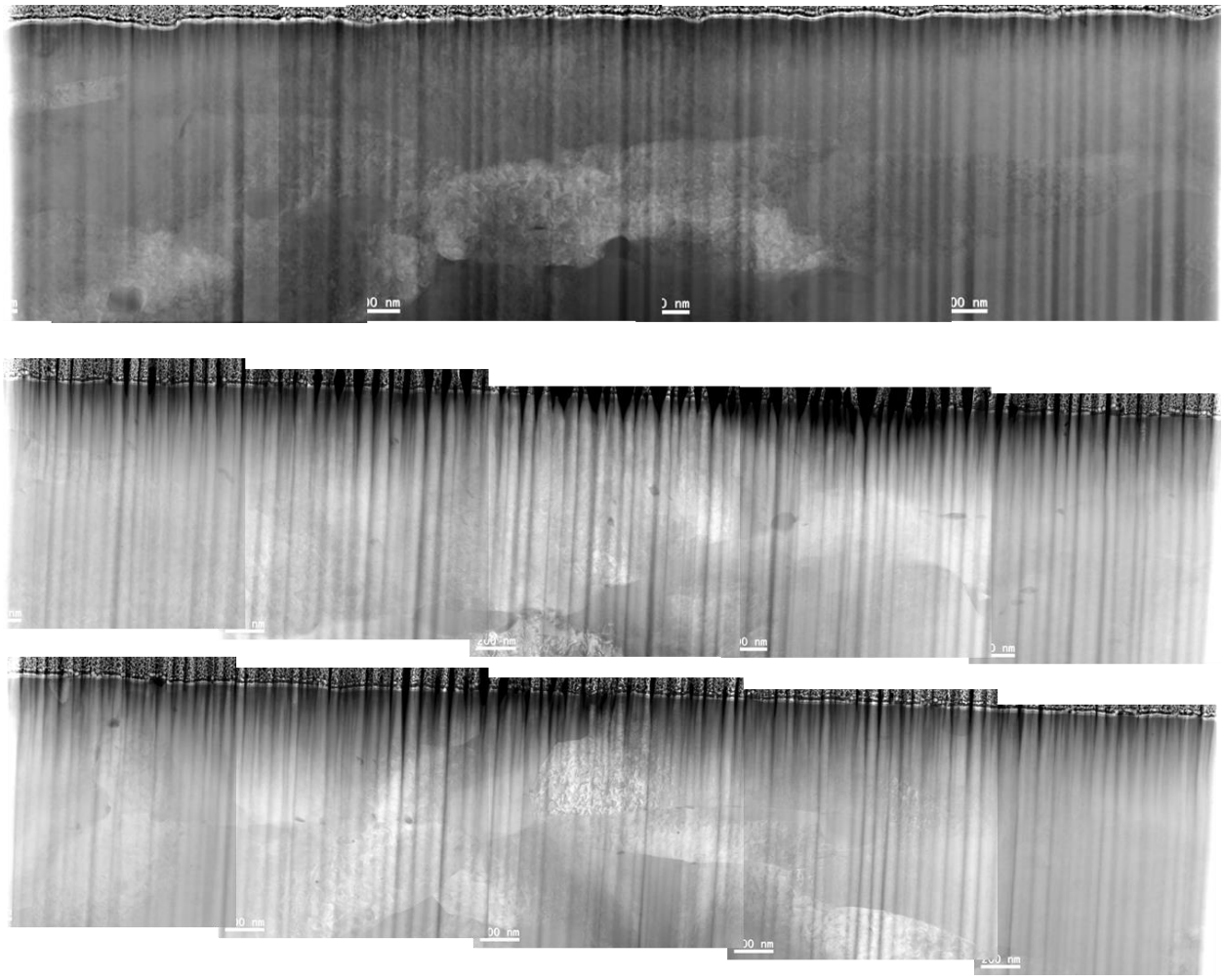

Figure B.12: STEM HAADF Images for liftouts from the irradiation of T91 at 445°C with 0.02 appm He/dpa to 50 dpa.

Figure B.13: STEM HAADF Images for liftouts from the irradiation of T91 at 445°C with 0.02 appm He/dpa to 100 dpa.

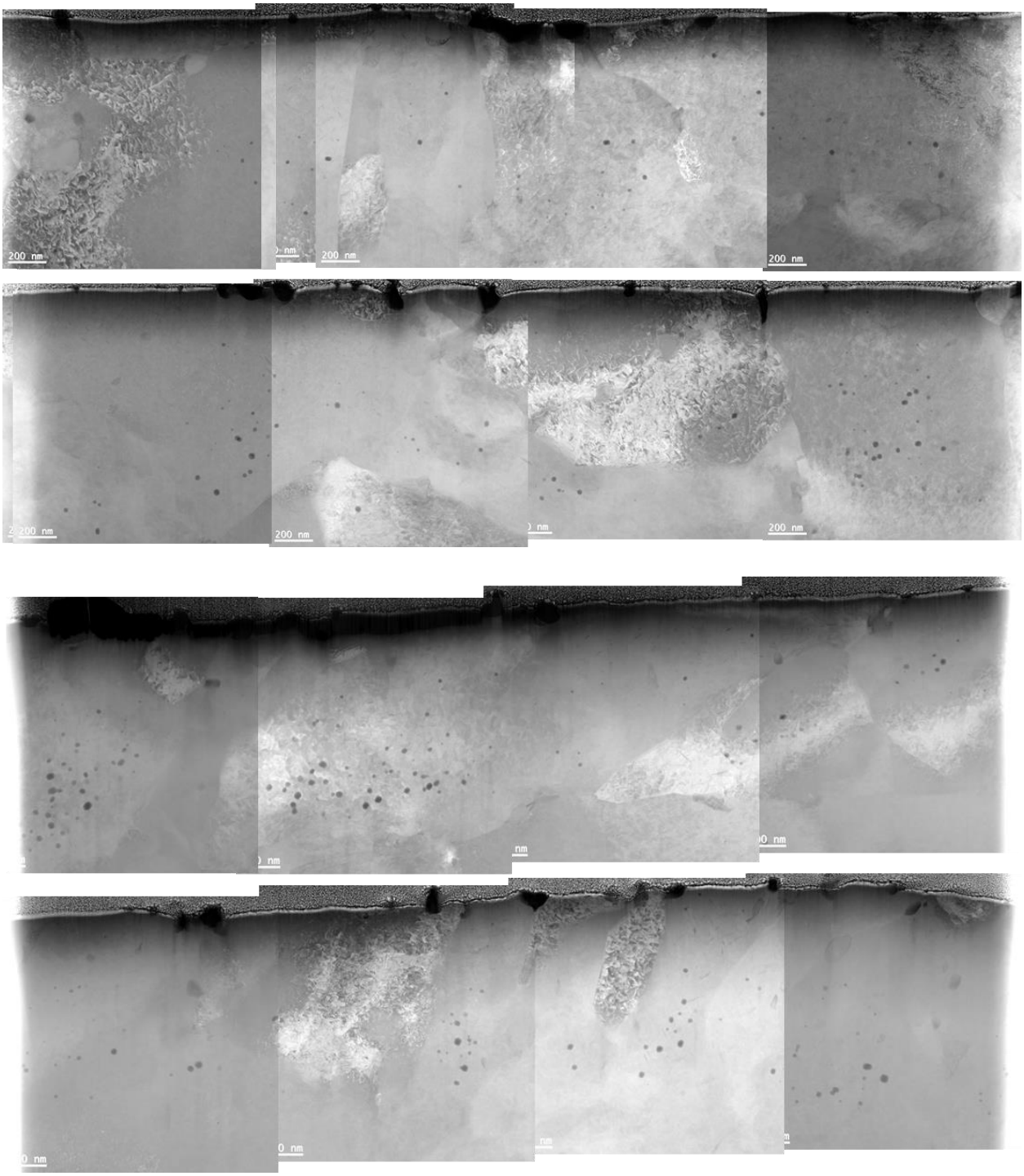

Figure B.14: STEM HAADF Images for liftouts from the irradiation of T91 at 445°C with 0.02 appm He/dpa to 150 dpa.

Figure B.15: STEM HAADF Images for liftouts from the irradiation of T91 at 445°C with 0.2 appm He/dpa to 50 dpa.

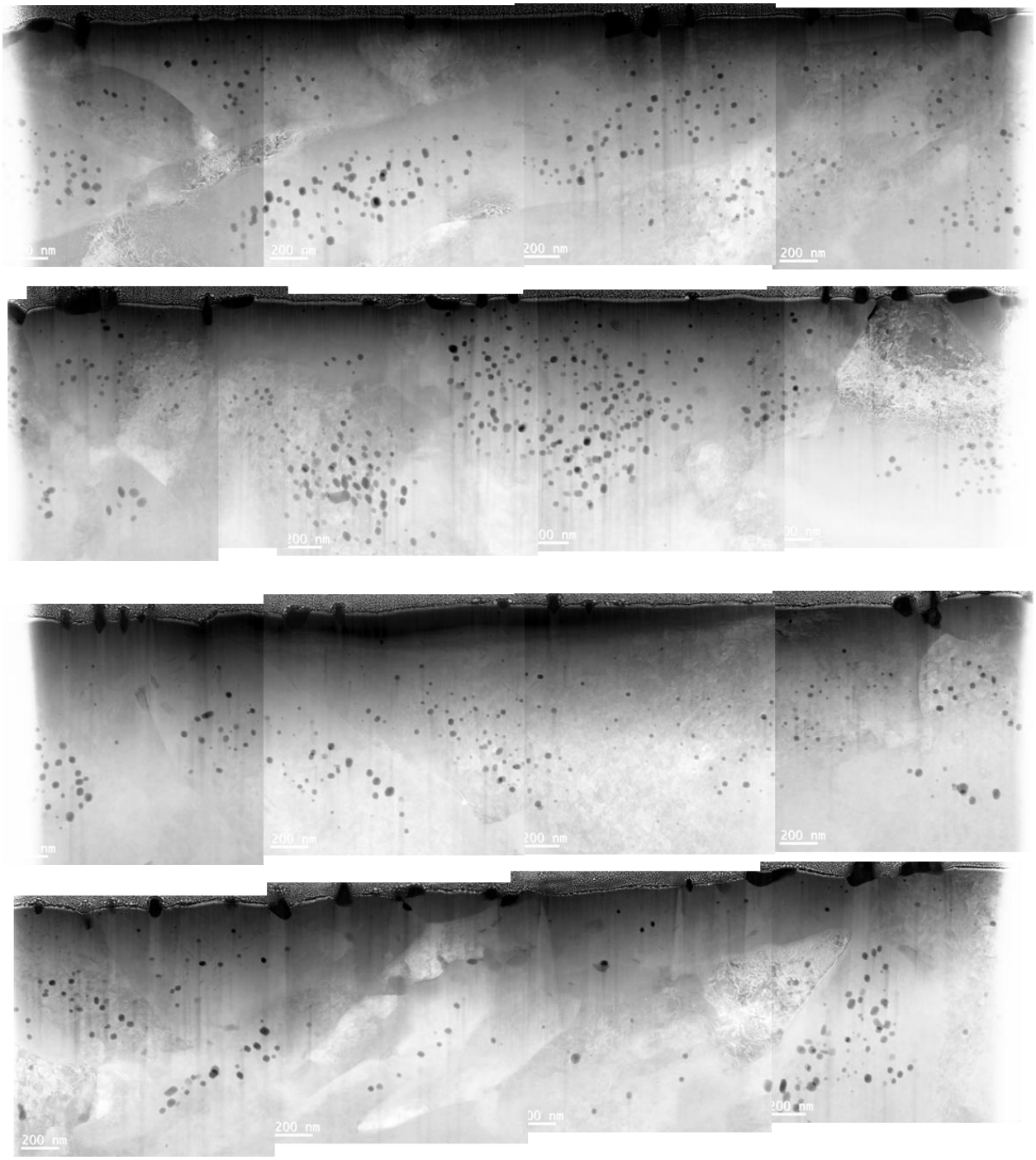

Figure B.16: STEM HAADF Images for liftouts from the irradiation of T91 at 445°C with 0.2 appm He/dpa to 150 dpa.

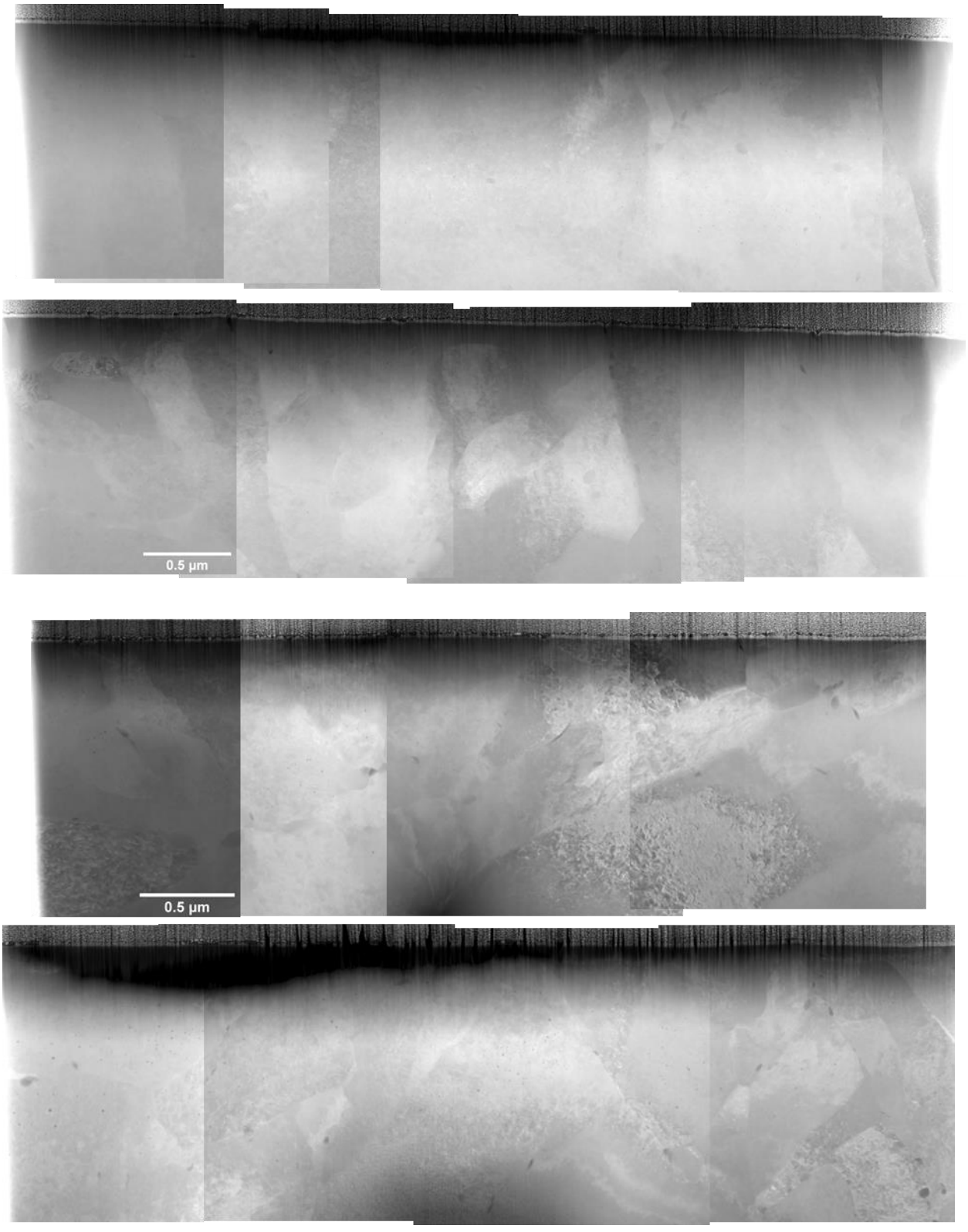

Figure B.17: STEM HAADF Images for liftouts from the irradiation of T91 at 445°C with 4 appm He/dpa to 17 dpa.

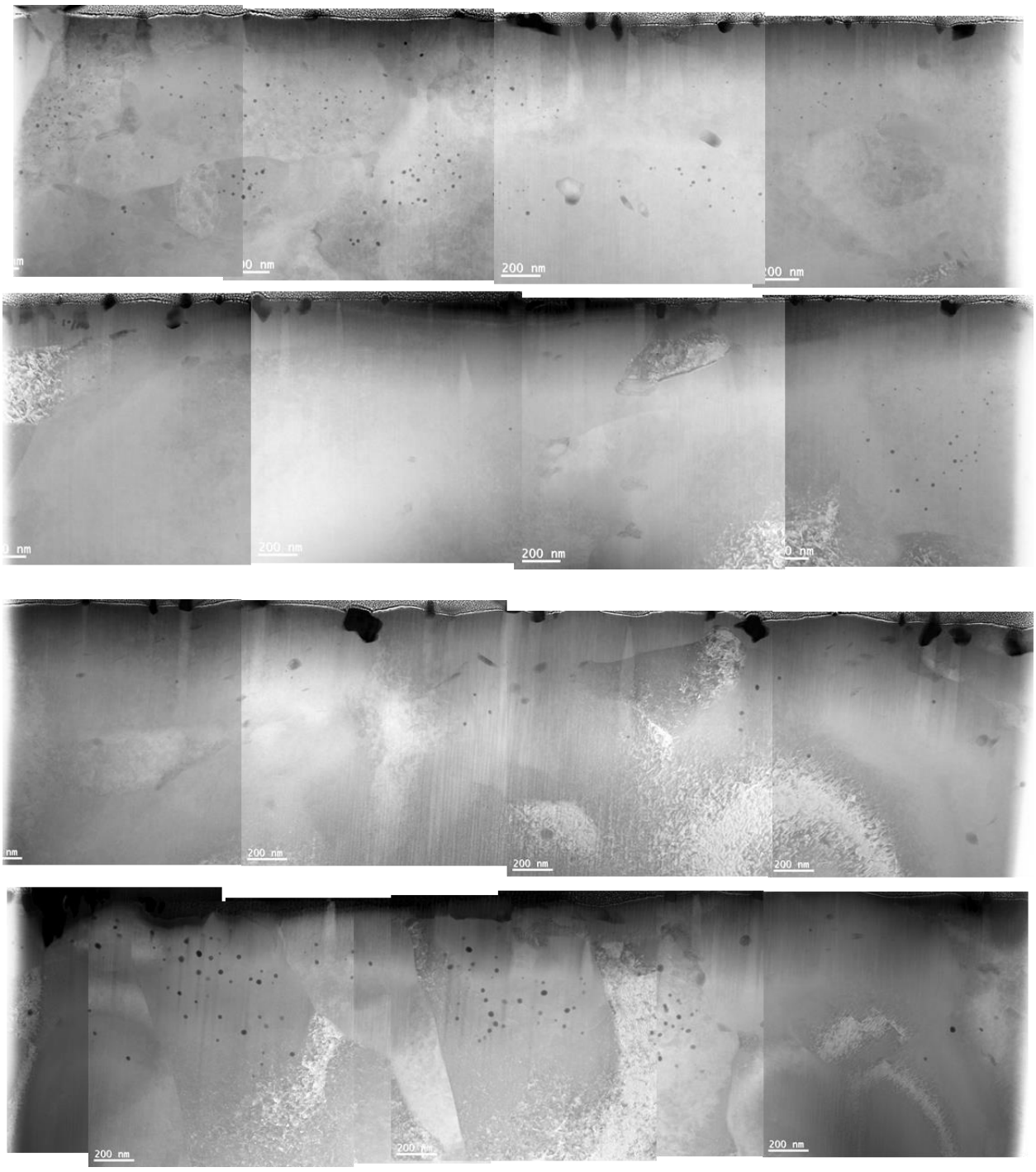

Figure B.18: STEM HAADF Images for liftouts from the irradiation of T91 at 445°C with 4 appm He/dpa to 50 dpa.

Figure B.19: STEM HAADF Images for liftouts from the irradiation of T91 at 445°C with 4 appm He/dpa to 100 dpa.

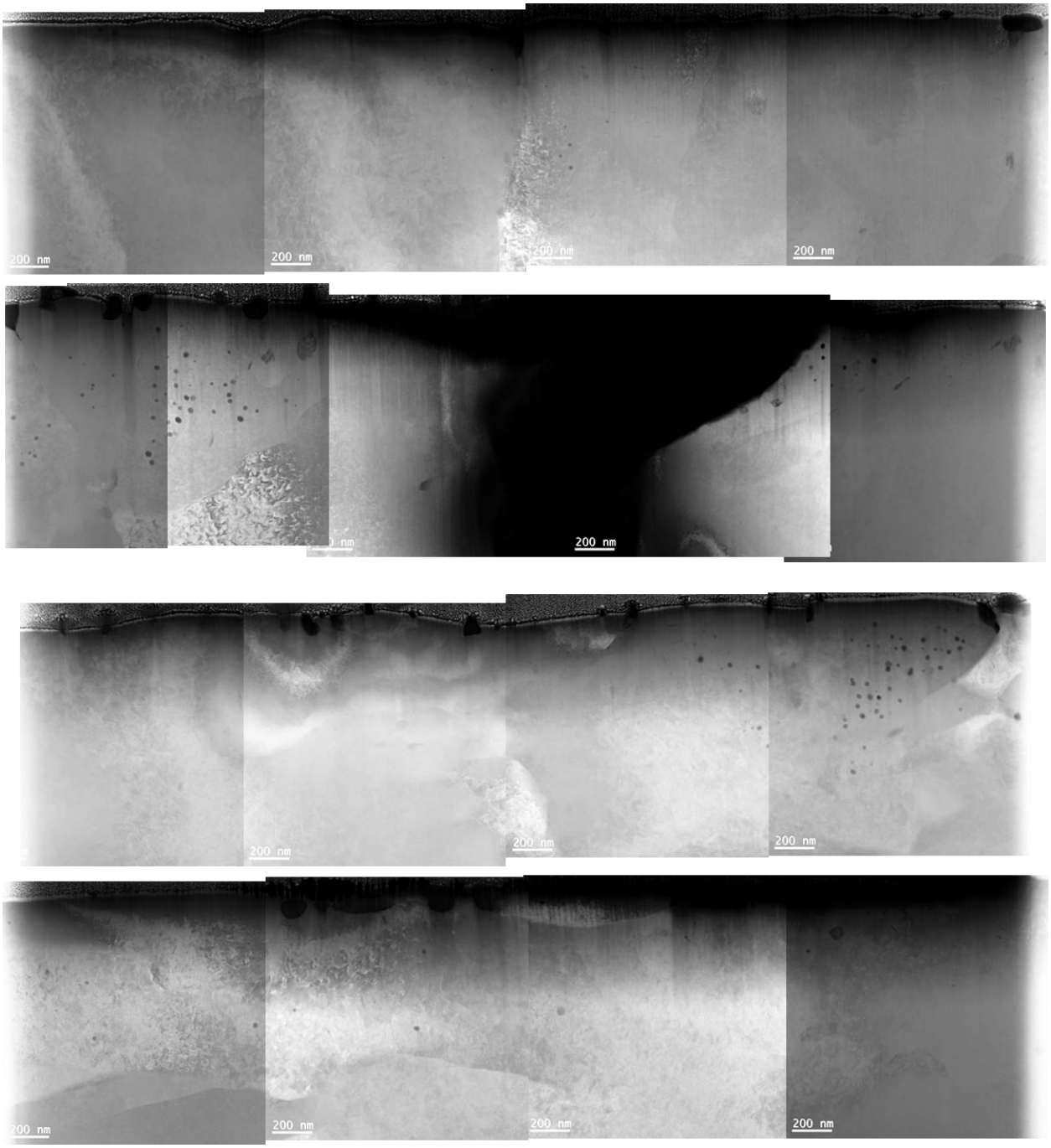

Figure B.20: STEM HAADF Images for liftouts from the irradiation of T91 at 445°C with 4 appm He/dpa to 150 dpa.

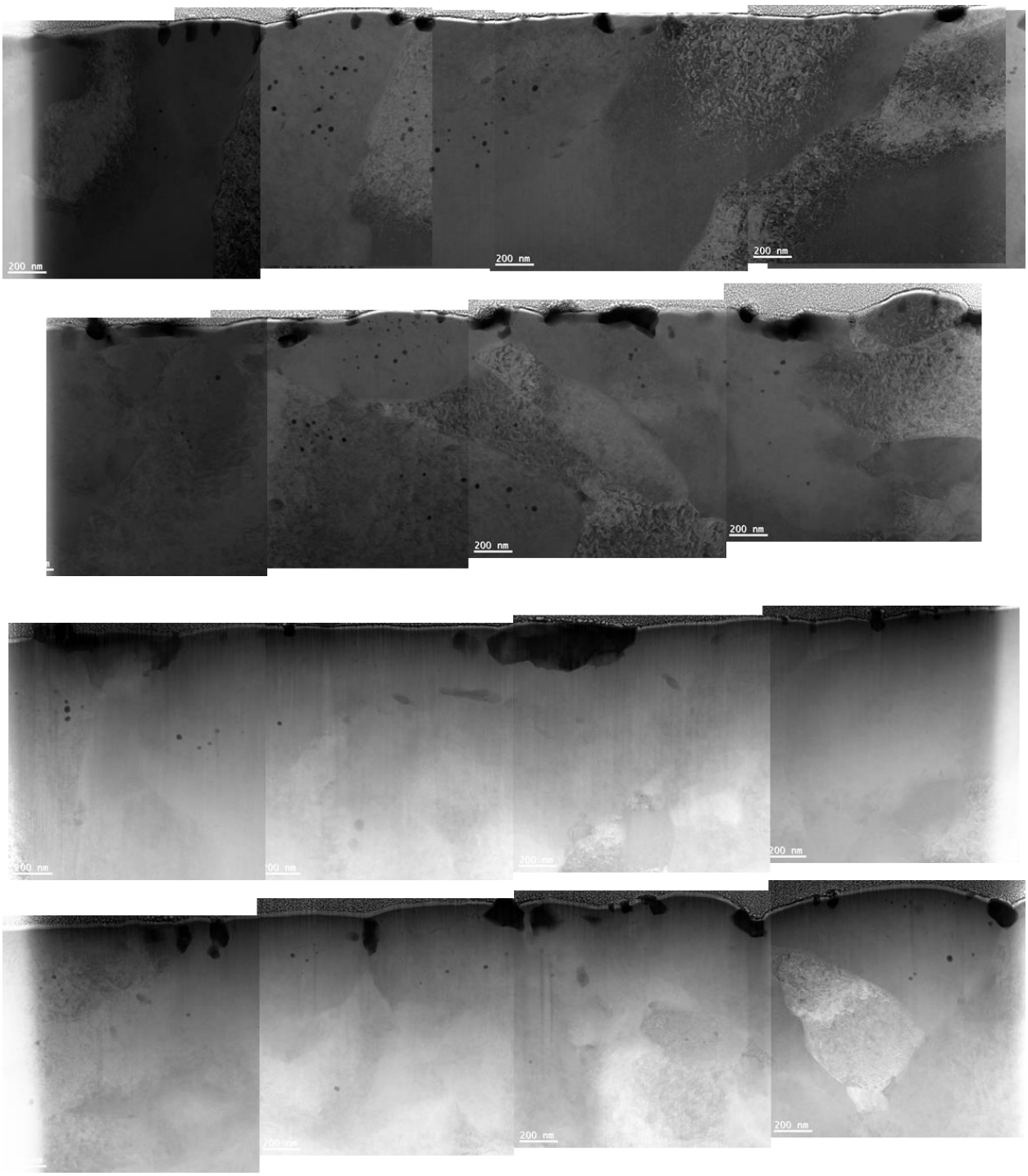

Figure B.21: STEM HAADF Images for liftouts from the irradiation of T91 at 445°C with 4 appm He/dpa to 200 dpa.

Appendix C : **CAVITY SIZE DISTRIBUTION DATA**

Cavity size distribution data is included in the tables in this appendix for each irradiation performed as part of this thesis.

Table C.1: Cavity size distribution data for dual-ion irradiated T91, heat 30176, at 445°C and 17 dpa with co-injected helium.

Cavity Diameter (nm)	Dislocation Density (10^{20} m^{-3})			
Helium-to-dpa Ratio (appm He/dpa)	0 appm He/dpa	0.02 appm He/dpa	0.2 appm He/dpa	4 appm He/dpa
0	0	0	0	0
1	0	0	0	0.02
2	0	0	0.21	73.15
3	0	0.03	3.61	179.00
4	0	0.06	2.14	19.43
5	0	0.02	1.01	1.16
6	0.04	0.03	0.67	0.76
7	0.04	0.05	0.48	0.76
8	0	0.02	0.68	0.71
9	0	0	0.34	0.36
10	0	0	0.26	0.27
11	0	0.03	0.14	0.36
12	0	0	0.06	0.04
13	0	0	0.04	0
14	0	0	0.01	0
15	0	0	0	0
16	0	0	0.01	0
17	0	0	0	0
18	0	0	0	0
19	0	0	0	0
20	0	0	0	0

Table C.2: Cavity size distribution data for dual-ion irradiated T91, heat 30176, at 445°C and 50 dpa with co-injected helium.

Cavity Diameter (nm)	Dislocation Density (10^{20} m^{-3})			
Helium-to-dpa Ratio (appm He/dpa)	0 appm He/dpa	0.02 appm He/dpa	0.2 appm He/dpa	4 appm He/dpa
0	0	0	0	0
1	0.07	118.00	167.00	202.00
2	0.07	23.20	50.80	1020.00
3	0.04	0.12	0.51	127.00
4	0.04	0.15	0.53	9.57
5	0.04	0.15	0.68	7.04
6	0.04	0.12	0.79	0.55
7	0	0.13	0.49	0.41
8	0.04	0.28	0.57	0.19
9	0	0.03	0.55	0.36
10	0.07	0.10	0.53	0.29
11	0	0.15	0.30	0.41
12	0	0.12	0.55	0.23
13	0	0	0.36	0.19
14	0	0.06	0.40	0.30
15	0	0.06	0.32	0.18
16	0	0	0.28	0.19
17	0	0	0.17	0.08
18	0	0.03	0.19	0.11
19	0	0	0.21	0.03
20	0	0	0.25	0.01
21	0	0	0.06	0.03
22	0	0	0.06	0.04
23	0	0	0	0
24	0	0	0.08	0
25	0	0	0.02	0
26	0.04	0	0	0
27	0	0	0	0
28	0.11	0	0	0
29	0	0	0	0
30	0	0	0	0

Table C.3: Cavity size distribution data for dual-ion irradiated T91, heat 30176, at 445°C and 150 dpa with co-injected helium.

Cavity Diameter (nm)	Dislocation Density (10^{20} m^{-3})			
Helium-to-dpa Ratio (appm He/dpa)	0 appm He/dpa	0.02 appm He/dpa	0.2 appm He/dpa	4 appm He/dpa
0	0	0	0	0
1	0	2190.00	3500.00	2660.00
2	0.02	242.00	2510.00	5010.00
3	0.05	0.04	0.04	169.00
4	0.02	0	0	77.10
5	0.02	0.02	0.08	0.10
6	0	0.09	0.04	0.10
7	0.02	0.08	0	0.10
8	0.02	0.19	0.20	0.05
9	0.02	0.16	0.08	0.05
10	0.05	0.06	0.16	0.06
11	0.07	0.26	0.16	0.08
12	0.05	0.09	0.20	0.13
13	0.02	0.09	0.08	0.10
14	0.02	0.14	0.23	0.12
15	0.02	0.09	0.20	0.08
16	0	0.11	0.08	0.05
17	0.09	0.13	0.12	0.07
18	0.02	0.08	0.31	0.07
19	0.07	0.13	0.20	0.05
20	0.05	0.11	0.23	0.12
21	0.07	0	0.20	0.06
22	0.05	0.05	0.27	0.13
23	0.05	0.10	0.27	0.11
24	0.07	0.15	0.23	0.03
25	0.07	0.09	0.12	0.10
26	0.09	0.07	0.08	0.05
27	0.02	0.09	0.23	0.04
28	0.05	0.05	0.08	0
29	0.07	0.05	0.12	0.02
30	0.05	0.05	0.20	0.02
31	0.07	0.02	0.20	0.04
32	0.05	0.06	0.16	0.01
33	0.11	0.04	0.12	0.01
34	0.09	0.03	0.20	0
35	0.05	0.03	0.12	0.01
36	0.07	0.02	0.12	0.01
37	0.21	0	0.04	0
38	0.09	0.03	0.16	0
39	0.05	0.03	0.08	0
40	0.11	0	0.04	0
41	0.07	0.03	0.04	0
42	0.05	0	0	0
43	0.07	0	0	0
44	0	0	0	0
45	0.02	0	0	0
46	0.11	0	0	0
47	0.07	0	0	0
48	0.05	0	0	0
49	0	0	0	0.01
50	0.02	0	0	0
51	0.02	0	0	0
52	0.02	0	0	0
53	0.02	0	0	0

54	0	0	0	0
55	0	0	0	0
56	0	0	0	0
57	0	0	0	0
58	0	0	0	0
59	0	0	0	0
60	0.02	0	0	0

Table C.4: Size distribution data for cavities in dual-ion irradiated HT9, heat 84425, at 460°C and 188 dpa with co-injected helium.

Dislocation Diameter (nm)	Dislocation Density (10^{20} m^{-3})		
Helium-to-dpa Ratio (appm He/dpa)	0 appm He/dpa	0.006 appm He/dpa	4 appm He/dpa
0	0	0	0
5	0.001	49.400	166.000
10	0.015	0.080	14.100
15	0.033	0.109	0.261
20	0.030	0.109	0.301
25	0.045	0.163	0.353
30	0.052	0.153	0.332
35	0.044	0.161	0.246
40	0.068	0.142	0.161
45	0.076	0.096	0.062
50	0.067	0.074	0.024
55	0.062	0.054	0.006
60	0.059	0.033	0
65	0.055	0.021	0.001
70	0.050	0.012	0
75	0.013	0.015	0
80	0.007	0.007	0
85	0.008	0.003	0
90	0.003	0.002	0
95	0	0	0
100	0.002	0	0

Table C.5: Size distribution data for cavities in dual-ion irradiated HT9, heat 84425, at 460°C with 4 appm He/dpa co-injected helium.

Cavity Diameter (nm)	Dislocation Density (1020 m-3 nm-1)				
Damage Level (dpa)	188 dpa	350 dpa	450 dpa	550 dpa	650 dpa
0	0	0	0	0	0
1	34.500	657.000	73.700	58.300	42.800
2	436.000	797.000	377.000	387.000	398.000
3	186.000	356.000	519.000	401.000	283.000
4	87.300	126.000	253.000	227.000	202.000
5	48.300	52.100	65.700	63.000	60.300
6	0.737	14.900	17.100	8.620	0.137
7	0.718	1.120	1.240	0.687	0.137
8	0.621	0.630	0.653	0.477	0.301
9	0.572	0.794	0.721	0.388	0.055
10	0.495	0.411	0.395	0.266	0.137
15	0.588	0.570	0.374	0.204	0.041
20	0.644	0.531	0.323	0.175	0.046
25	0.741	0.509	0.347	0.184	0.037
30	0.654	0.466	0.457	0.242	0.046
35	0.407	0.389	0.368	0.203	0.064
40	0.264	0.257	0.254	0.168	0.082
45	0.093	0.186	0.151	0.095	0.048
50	0.039	0.110	0.089	0.067	0.073
55	0.013	0.071	0.038	0.044	0.049
60	0	0.027	0.039	0.026	0.027
65	0.010	0.027	0.034	0.033	0.055
70	0	0.027	0.029	0.011	0.027
75	0	0.027	0.026	0.013	0
80	0	0.027	0	0	0
85	0	0	0	0.014	0.027
90	0	0.014	0	0	0
95	0	0	0.017	0.011	0.027
100	0	0	0	0	0
105	0	0	0	0	0
110	0	0	0	0	0
115	0	0	0.017	0.018	0.027
120	0	0	0	0	0
125	0	0	0	0	0
130	0	0	0	0	0
135	0	0	0	0	0
140	0	0	0	0	0
145	0.005	0	0	0	0
150	0	0	0	0	0

Appendix D : **DISLOCATION LOOP SIZE DISTRIBUTION DATA**

Dislocation loop size distribution data is included in the tables in this appendix for each irradiation performed as part of this thesis.

Table D.6: Dislocation loop size distribution data for dual-ion irradiated T91, heat 30176, at 445°C and 17 dpa with co-injected helium.

Dislocation Loop Diameter (nm)	Dislocation Density (10^{20} m^{-3})			
Helium-to-dpa Ratio (appm He/dpa)	0 appm He/dpa	0.02 appm He/dpa	0.2 appm He/dpa	4 appm He/dpa
0	0	0	0	0
5	1.44	0.65	1.86	0
10	8.18	6.50	9.29	0.75
15	7.94	6.29	8.18	4.02
20	6.02	6.29	7.81	3.77
25	3.85	3.47	2.97	3.77
30	4.09	3.25	4.09	4.78
35	3.13	1.73	1.86	3.52
40	0.48	0.87	1.12	4.27
45	0.96	0.43	0.37	0.25
50	0.24	0.22	0.74	0.25
55	0.72	0.43	0	0
60	0	0.22	0	0
65	0.24	0	0	0
70	0.24	0.22	0	0
75	0	0	0.37	0.50

Table D.7: Dislocation loop size distribution data for dual-ion irradiated T91, heat 30176, at 445°C with 0.2 appm He/dpa co-injected helium.

Dislocation Loop Diameter (nm)	Dislocation Density (1020 m-3)		
Helium-to-dpa Ratio (appm He/dpa)	17 dpa	50 dpa	150 dpa
0	0	0	0
5	1.86	0	1.90
10	9.29	4.27	6.84
15	8.18	6.60	7.60
20	7.81	5.82	6.84
25	2.97	3.88	3.04
30	4.09	2.72	2.66
35	1.86	0.78	1.14
40	1.12	1.94	1.14
45	0.37	0.78	0.38
50	0.74	0.78	0.76
55	0	1.16	0
60	0	0	0
65	0	0.39	0
70	0	0	0.38
75	0.37	0	0

Table D.8: Dislocation loop size distribution data for dual-ion irradiated HT9, heat 84425, at 460°C and 188 dpa with co-injected helium.

Dislocation Loop Diameter (nm)	Dislocation Loop Density (10^{20} m^{-3})		
Helium-to-dpa Ratio (appm He/dpa)	0 appm He/dpa	0.06 appm He/dpa	4 appm He/dpa
0	0	0	0
5	0	0	0
10	0.42	0	0
15	0.42	0	0
20	2.53	0.05	0
25	2.95	0.16	0.99
30	4.22	0.57	1.98
35	4.64	0.57	2.31
40	2.53	0.47	2.31
45	2.11	0.16	0.66
50	0.84	0.10	0.33
55	0.84	0.26	0.66
60	0	0	0.33
65	0	0	0
70	0	0	0
75	0	0.05	0
80	0	0	0
85	0	0.05	0

References

[1] G.S. Was, Z. Jiao, E. Getto, K. Sun, A.M. Monterrosa, S.A. Maloy, O. Anderoglu, B.H. Sencer, M. Hackett, Emulation of reactor irradiation damage using ion beams, Scr. Mater. 88 (2014) 33–36. https://doi.org/10.1016/j.scriptamat.2014.06.003.

[2] R.L. Klueh, D.R. Harries, High-Chromium Ferritic and Martensitic Steels for Nuclear Applications, 2001. https://doi.org/10.1520/MONO3-EB.

[3] G.S. Was, T. Allen, Radiation-induced segregation in multicomponent alloys: Effect of particle type, Mater. Charact. 32 (1994) 239–255. https://doi.org/10.1016/1044-5803(94)90101-5.

[4] G. Was, Fundamentals of Radiation Material Scence, 1st Editio, Springer, 2007.

[5] O. Anderoglu, J. Van Den Bosch, P. Hosemann, E. Stergar, B.H. Sencer, D. Bhattacharyya, R. Dickerson, P. Dickerson, M. Hartl, S. a. Maloy, Phase stability of an HT-9 duct irradiated in FFTF, J. Nucl. Mater. 430 (2012) 194–204. https://doi.org/10.1016/j.jnucmat.2012.06.038.

[6] J.J. Penisten, The Mechanism of Radiation-Induced Segregation in Ferritic-Martensitic Steels, University of Michigan, 2012. https://deepblue.lib.umich.edu/handle/2027.42/96138.

[7] J. Pešička, A. Aghajani, C. Somsen, A. Hartmaier, G. Eggeler, How dislocation substructures evolve during long-term creep of a 12% Cr tempered martensitic ferritic steel, Scr. Mater. 62 (2010) 353–356. https://doi.org/10.1016/j.scriptamat.2009.10.037.

[8] M. Nastasi, J.W. Mayer, J.K. Hirvonen, Ion-Solid Interactions: Fundamentals and Applications, Cambridge University Press, 1996.

[9] F.. Garner, M.. Toloczko, B.. Sencer, Comparison of swelling and irradiation creep behavior of fcc-austenitic and bcc-ferritic/martensitic alloys at high neutron exposure, J. Nucl. Mater. 276 (2000) 123–142. https://doi.org/10.1016/S0022-3115(99)00225-1.

[10] J.P. Wharry, G.S. Was, The mechanism of radiation-induced segregation in ferritic-martensitic alloys, Acta Mater. 65 (2014) 42–55. https://doi.org/10.1016/j.actamat.2013.09.049.

[11] C. Cawthorne, E.J. Fulton, Voids in Irradiated Stainless Steel, Nature. 216 (1967) 575–576.

[12] K.C. Russell, Nucleation of Voids in Irradiated Metals, Acta Metall. 19 (1971) 753–758.

[13] K.C. Russell, Thermodynamics of gas-containing voids in metals, Acta Metall. 20 (1972) 899–907.

[14] L.K. Mansur, Theory of transitions in dose dependence of radiation effects in structural alloys, J. Nucl. Mater. 206 (1993) 306–323. https://doi.org/10.1016/0022-3115(93)90130-Q.

[15] K. Krishan, Invited review article ordering of voids and gas bubbles in radiation environments, Radiat. Eff. 66 (1982) 121–155. https://doi.org/10.1080/00337578208222474.

[16] K.L. Wong, H.-J. Lee, J.-H. Shim, B. Sadigh, B.D. Wirth, Multiscale modeling of point defect interactions in Fe–Cr alloys, J. Nucl. Mater. 386–388 (2009) 227–230. https://doi.org/10.1016/j.jnucmat.2008.12.092.

[17] A.A. Kohnert, M.A. Cusentino, B.D. Wirth, Molecular statics calculations of the biases and point defect capture volumes of small cavities, J. Nucl. Mater. 499 (2018) 480–489. https://doi.org/10.1016/j.jnucmat.2017.12.005.

[18] W.G. Wolfer, Advances in Void Swelling and Helium Bubble Physics, J. Nucl. Mater. 122 & 123 (1984) 367–378.

[19] a. V. Karasiov, L.R. Greenwood, Neutron flux spectra and radiation damage parameters for the Russian BOR-60 and SM-2 reactors, (n.d.).

[20] J.M. Vitek, R.L. Klueh, Microstructure of 9Cr-1MoVNb Steel Irradiated to 36 dpa at Elevated Temperatures in HFIR, J. Nucl. Mater. 122–123 (1984) 254–259.

[21] E.A. Little, Microstructural evolution in irradiated ferritic-martensitic steels: transitions to high dose behaviour, J. Nucl. Mater. 206 (1993) 324–334. https://doi.org/10.1016/0022-3115(93)90131-H.

[22] E. Wakai, N. Hashimoto, Y. Miwa, J.P. Robertson, R.L. Klueh, K. Shiba, S. Jistukawa, Effect of helium production on swelling of F82H irradiated in HFIR, J. Nucl. Mater. 283–287 (2000) 799–805.

[23] E. Wakai, Y. Miwa, N. Hashimoto, J.. Robertson, R.. Klueh, K. Shiba, K. Abiko, S. Furuno, S. Jitsukawa, Microstructural study of irradiated isotopically tailored F82H steel, J. Nucl. Mater. 307–311 (2002) 203–211. https://doi.org/10.1016/S0022-3115(02)01261-8.

[24] J.J. Kai, R.L. Klueh, Microstructural analysis of neutron-irradiated martensitic steels, J. Nucl. Mater. 230 (1996) 116–123. https://doi.org/10.1016/0022-3115(96)00165-1.

[25] A. Kimura, M. Narui, H. Kayano, Effects of alloying elements on the post-irradiation microstructure of 9%Cr-2%W low activation martensitic steels, J. Nucl. Mater. 191–194 (1992) 879–884. https://doi.org/10.1016/0022-3115(92)90599-G.

[26] B.H. Sencer, J.R. Kennedy, J.I. Cole, S.A. Maloy, F.A. Garner, Microstructural stability of

an HT-9 fuel assembly duct irradiated in FFTF, J. Nucl. Mater. 414 (2011) 237–242. https://doi.org/10.1016/j.jnucmat.2011.03.050.

[27] J. Van Den Bosch, O. Anderoglu, R. Dickerson, M. Hartl, P. Dickerson, J. a. Aguiar, P. Hosemann, M.B. Toloczko, S. a. Maloy, SANS and TEM of ferritic-martensitic steel T91 irradiated in FFTF up to 184 dpa at 413 °c, J. Nucl. Mater. 440 (2013) 91–97. https://doi.org/10.1016/j.jnucmat.2013.04.025.

[28] D.S. Gelles, Microstructural examination of commercial ferritic alloys at 200 dpa, J. Nucl. Mater. 233–237 (1996) 293–298. https://doi.org/10.1016/S0022-3115(96)00222-X.

[29] E. Getto, K. Sun, A.M. Monterrosa, Z. Jiao, M.J. Hackett, G.S. Was, Void swelling and microstructure evolution at very high damage level in self-ion irradiated ferritic-martensitic steels, J. Nucl. Mater. 480 (2016) 159–176. https://doi.org/10.1016/j.jnucmat.2016.08.015.

[30] R. Sindelar, J.J. Kai, D. Plumton, R. Dodd, G. Kulcinski, Microstructural Modification of 21/4 Cr-1Mo Steel by Irradiation with 14 MeV Nickel Ions, Nucl. Instruments Methods Phys. Res. 16 (1986) 260–269.

[31] J.G. Gigax, T. Chen, H. Kim, J. Wang, L.M. Price, E. Aydogan, S.A. Maloy, D.K. Schreiber, M.B. Toloczko, F.A. Garner, L. Shao, Radiation response of alloy T91 at damage levels up to 1000 peak dpa, J. Nucl. Mater. 482 (2016) 257–265. https://doi.org/10.1016/j.jnucmat.2016.10.003.

[32] L. Shao, C.-C. Wei, J. Gigax, A. Aitkaliyeva, D. Chen, B.H. Sencer, F.A. Garner, Effect of defect imbalance on void swelling distributions produced in pure iron irradiated with 3.5 MeV self-ions, J. Nucl. Mater. 453 (2014) 176–181. https://doi.org/10.1016/j.jnucmat.2014.06.002.

[33] G.S. Was, Fundamentals of Radiation Materials Science: Metals and Alloys, Springer, 2007.

[34] A. Hishinuma, L.. Mansur, Critical radius for bias-driven swelling — a further analysis and its application to bimodal cavity size distributions, J. Nucl. Mater. 118 (1983) 91–99. https://doi.org/10.1016/0022-3115(83)90184-8.

[35] A.. Dvoriashin, S.. Porollo, Y.. Konobeev, F.. Garner, Influence of high dose neutron irradiation on microstructure of EP-450 ferritic–martensitic steel irradiated in three Russian fast reactors, J. Nucl. Mater. 329–333 (2004) 319–323. https://doi.org/10.1016/j.jnucmat.2004.04.309.

[36] G. Ayrault, Cavity Formation During Single- and Dual-Ion Irradiation in a 9Cr-1Mo Ferritic Alloy, J. Nucl. Mater. 114 (1983) 34–40.

[37] R. Hide, K. Kusanagi, M. Taguchi, Microstructural Change in Ferritic Steels Under Heavy Ion Irradiation, Eff. Radiat. Mater. 14th Int. Symp. ASTM STP 1046. (1989) 61–72.

[38] G.S. Was, Fundamentals of Radiation Materials Science, Springer Berlin Heidelberg,

Berlin, Heidelberg, NY, 2007. https://doi.org/10.1007/978-3-540-49472-0.

[39] J.J.J. Kai, G.L.L. Kulcinski, 14 MeV nickel-ion irradiated HT-9 ferritic steel with and without helium pre-implantation, J. Nucl. Mater. 175 (1990) 237–243. https://doi.org/10.1016/0022-3115(90)90212-6.

[40] F. a. Schmidt, P.R. Malmberg, J. a. Sprague, J.E. Westmoreland, Swelling Behavior of Commercial Ferritic Alloys, EM-12 and HT-9, as Assessed by Heavy Ion Bombardment, Irradiat. Eff. Microstruct. Prop. Met. (1976) 227.

[41] E. Wakai, T. Sawai, K. Furuya, A. Naito, T. Aruga, K. Kikuchi, S. Yamashita, S. Ohnuki, S. Yamamoto, H. Naramoto, S. Jistukawa, Effect of triple ion beams in ferritic / martensitic steel on swelling behavior, J. Nucl. Mater. 307–311 (2002) 278–282.

[42] E. Getto, Z. Jiao, A.M. Monterrosa, K. Sun, G.S. Was, Effect of pre-implanted helium on void swelling evolution in self-ion irradiated HT9, J. Nucl. Mater. 462 (2015) 458–469. https://doi.org/10.1016/j.jnucmat.2015.01.045.

[43] M.B. Toloczko, F.A. Garner, V.N. Voyevodin, V.V. Bryk, O.V. Borodin, V.V. Mel'nychenko, A.S. Kalchenko, Ion-induced swelling of ODS ferritic alloy MA957 tubing to 500 dpa, J. Nucl. Mater. 453 (2014) 323–333. https://doi.org/10.1016/j.jnucmat.2014.06.011.

[44] N. Hashimoto, R.. Klueh, Microstructural evolution of nickel-doped 9Cr steels irradiated in HFIR, J. Nucl. Mater. 305 (2002) 153–158. https://doi.org/10.1016/S0022-3115(02)01026-7.

[45] K. Asano, Y. Kohno, A. Kohyama, G. Ayrault, Microstructural evolution of HT9 under dual-beam charged particle irradiation, J. Nucl. Mater. 155–157 (1988) 912–915. https://doi.org/10.1016/0022-3115(88)90440-0.

[46] H. Ogiwara, H. Sakasegawa, H. Tanigawa, M. Ando, Y. Katoh, A. Kohyama, Void swelling in reduced activation ferritic/martensitic steels under ion-beam irradiation to high fluences, J. Nucl. Mater. 307–311 (2002) 299–303. https://doi.org/10.1016/S0022-3115(02)01078-4.

[47] E. Wakai, K. Kikuchi, S. Yamamoto, T. Aruga, M. Ando, H. Tanigawa, T. Taguchi, T. Sawai, K. Oka, S. Ohnuki, Swelling behavior of F82H steel irradiated by triple/dual ion beams, J. Nucl. Mater. 318 (2003) 267–273. https://doi.org/10.1016/S0022-3115(03)00122-3.

[48] S. Hiwatashi, Y. Kohno, K. Asakura, A. Kohyama, Microstructural developments in Fe-Cr-W low activation ferritic steels under dual beam charged particle irradiation, J. Nucl. Mater. 179–181 (1991) 709–713. https://doi.org/10.1016/0022-3115(91)90187-C.

[49] T. Yamamoto, Y. Wu, G. Robert Odette, K. Yabuuchi, S. Kondo, A. Kimura, A dual ion irradiation study of helium–dpa interactions on cavity evolution in tempered martensitic steels and nanostructured ferritic alloys, J. Nucl. Mater. 449 (2014) 190–199. https://doi.org/10.1016/j.jnucmat.2014.01.040.

[50] D. Brimbal, E. Meslin, J. Henry, B. Décamps, A. Barbu, He and Cr effects on radiation damage formation in ion-irradiated pure iron and Fe–5.40wt.% Cr: A transmission electron microscopy study, Acta Mater. 61 (2013) 4757–4764. https://doi.org/10.1016/j.actamat.2013.04.070.

[51] Y.E. Kupriiyanova, V.V. Bryk, O.V. Borodin, A.S. Kalchenko, V.N. Voyevodin, G.D. Tolstolutskaya, F.A. Garner, Use of double and triple-ion irradiation to study the influence of high levels of helium and hydrogen on void swelling of 8–12% Cr ferritic-martensitic steels, J. Nucl. Mater. 468 (2016) 264–273. https://doi.org/10.1016/j.jnucmat.2015.07.012.

[52] A. Bhattacharya, E. Meslin, J. Henry, A. Barbu, S. Poissonnet, B. Décamps, Effect of chromium on void swelling in ion irradiated high purity Fe–Cr alloys, Acta Mater. 108 (2016) 241–251. https://doi.org/10.1016/j.actamat.2016.02.027.

[53] Y. Katoh, R.E. Stoller, Y. Kohno, A. Kohyama, Modeling the Effects of Damage Rate and He/dpa Ratio on Microstructural Evolution, J. Nucl. Mater. 194 (1992) 1144–1149.

[54] Y. Katoh, R.E. Stoller, Y. Kohno, A. Kohyama, Numerical Estimation of Synergistic Effects of Displacement Damage and Helium Generation on Microstructural Evolution, Mater. Trans. JIM. 33 (1992) 795–801.

[55] W. V. Green, M. Victoria, T. Leffers, B.N. Singh, eds., No Title, in: Work. Eff. Recoil Energy Spectr. Nucl. Transmutations Evol. Microstruct., Lugano, 1988.

[56] C. Abromeit, Aspects of simulation of neutron damage by ion irradiation, J. Nucl. Mater. 216 (1994) 78–96. https://doi.org/10.1016/0022-3115(94)90008-6.

[57] R.E. Stoller, The influence of helium on microstructural evolution: Implications for DT fusion reactors, J. Nucl. Mater. 174 (1990) 289–310. https://doi.org/10.1016/0022-3115(90)90242-F.

[58] K. Farrell, P.J. Maziasz, E.H. Lee, L.K. Mansur, Modification of radiation damage microstructure by helium, Radiat. Eff. 78 (1983) 277–295. https://doi.org/10.1080/00337578308207378.

[59] K. Farrell, Experimental effects of helium on cavity formation during irradiation—a review, Radiat. Eff. 53 (1980) 175–194. https://doi.org/10.1080/00337578008207114.

[60] W.J. Choyke, J.N. Mcgruer, J.R. Townsend, J.A. Spitznagel, N.J. Doyle, F.J. Venskytis, Helium effects in ion-bombarded 304 stainless steel, J. Nucl. Mater. 85–86 (1979) 647–651. https://doi.org/10.1016/0022-3115(79)90333-7.

[61] J.A. Spitznagel, W.J. Choyke, J. Lauer, B.O. Hall, J.N. McGruer, J.R. Townsend, R.B. Irwin, Evolution of cavity size distributions in dual-ion irradiated austenitic stainless steel and Fe-Cr-Ni ternary alloys, J. Nucl. Mater. 117 (1983) 198–207. https://doi.org/10.1016/0022-3115(83)90024-7.

[62] J.A. Spitznagel, W.J. Choyke, N.J. Doyle, R.B. Irwin, J.R. Townsend, J.N. McGruer,

Critical cavity sizes in dual-ion bombarded 304 SS part I: Experiment, J. Nucl. Mater. 108–109 (1982) 537–543. https://doi.org/10.1016/0022-3115(82)90525-6.

[63] T. Muroga, H. Watanabe, N. Yoshida, H. Kurishita, M.L. Hamilton, Microstructure and Tensile Properties of Neutron-Irradiated Cu and Cu-Sni Containing Isotopically Controlled Boron, J. Nucl. Mater. . 225 (1995) 137–145.

[64] T. Muroga, H. Watanabe, N. Yoshida, Effects of solid transmutants and helium in copper studied by mixed-spectrum neutron irradiation, J. Nucl. Mater. 258–263 (1998) 955–960. https://doi.org/10.1016/S0022-3115(98)00123-8.

[65] T. Muroga, N. Yoshida, The influence of isotopically controlled boron addition on void swelling of nickel irradiated in FFTF, J. Nucl. Mater. 191–194 (1992) 1254–1258. https://doi.org/10.1016/0022-3115(92)90675-B.

[66] J.L. Brimhall, E.P. Simonen, Effect of helium on void formation in nickel, J. Nucl. Mater. 68 (1977) 235–243. https://doi.org/10.1016/0022-3115(77)90242-2.

[67] Q. Xu, T. Yoshiie, K. Sato, Effects of hydrogen and helium produced by transmutation reactions on void formation in copper isotopic alloys irradiated with neutrons, J. Nucl. Mater. 386–388 (2009) 363–366. https://doi.org/10.1016/j.jnucmat.2008.12.127.

[68] S.J. Zinkle, K. Farrell, H. Kanazawa, Microstructure and cavity swelling in reactor-irradiated dilute copper-boron alloy, J. Nucl. Mater. 179–181 (1991) 994–997. https://doi.org/10.1016/0022-3115(91)90258-9.

[69] S.J. Zinkle, K. Farrell, Void swelling and defect cluster formation in reactor-irradiated copper, J. Nucl. Mater. 168 (1989) 262–267. https://doi.org/10.1016/0022-3115(89)90591-6.

[70] B.N. Singh, M. Eldrup, A. Moslang, Effects of hot implantation of helium in copper on bubble formation within grains and on grain-boundaries, in: A.S. Kumar, D.S. Gelles, R.K. Nanstad, E.A. Little (Eds.), Eff. Radiat. Mater. 16th Int. Symp. ASTM STP 1175, American Society for Testing and Materials Special Technical Publication, W Conshohocken, 1994: pp. 1061–1073.

[71] B.N. Singh, A. Horsewell, Effects of fission neutron and 600 MeV proton irradiations on microstructural evolution in OFHC-copper, J. Nucl. Mater. 212–215 (1994) 410–415. https://doi.org/10.1016/0022-3115(94)90095-7.

[72] S.J. Zinkle, Dual Ion Irradiation of Copper, in: Fusion React. Mater. Semiannu. Prog. Rep. Period End. Sept. 30, 1987, DOE/ER-0313/3, 1986: pp. 86–89.

[73] N.H. Packan, K. Farrell, Simulation of first wall damage: Effects of the method of gas implantation, J. Nucl. Mater. 85–86 (1979) 677–681. https://doi.org/10.1016/0022-3115(79)90338-6.

[74] K.C. Russell, The Theory of Void Nucleation in Metals, Acta Metall. 26 (1978) 1615–1630.

[75] C.A. Walsh, J. Yuan, L.M. Brown, A procedure for measuring the helium density and pressure in nanometre-sized bubbles in irradiated materials using electron-energy-loss spectroscopy, Philos. Mag. A. 80 (2000) 1507–1543. https://doi.org/10.1080/01418610008212134.

[76] S. Fréchard, M. Walls, M. Kociak, J.P. Chevalier, J. Henry, D. Gorse, Study by EELS of helium bubbles in a martensitic steel, J. Nucl. Mater. 393 (2009) 102–107. https://doi.org/10.1016/j.jnucmat.2009.05.011.

[77] Y. Wu, G.R. Odette, T. Yamamoto, J. Ciston, P. Hosemann, AN ELECTRON ENERGY LOSS SPECTROSCOPY STUDY OF HELIUM BUBBLES IN NANOSTRUCTURED FERRITIC ALLOYS, 2013.

[78] J.C. Rife, S.E. Donnelly, A.A. Lucas, J.M. Gilles, J.J. Ritsko, Optical Absorption and Electron-Energy-Loss Spectra of Helium Microbubbles in Aluminum, Phys. Rev. Lett. 46 (1981) 1220–1223. https://doi.org/10.1103/PhysRevLett.46.1220.

[79] D. Taverna, M. Kociak, O. Stéphan, A. Fabre, E. Finot, B. Décamps, C. Colliex, Probing Physical Properties of Confined Fluids within Individual Nanobubbles, Phys. Rev. Lett. 100 (2008) 035301. https://doi.org/10.1103/PhysRevLett.100.035301.

[80] L.K. Mansur, E.H. Lee, P.J. Maziasz, A.P. Rowcliffe, Control of helium effects in irradiated materials based on theory and experiment, J. Nucl. Mater. 141–143 (1986) 633–646. https://doi.org/10.1016/0022-3115(86)90066-8.

[81] R.E. Stoller, G.R. Odette, A comparison of the relative importance of helium and vacancy accumulation in void nucleation, Radiation-Induced Chang. {…}. (1987) 358–370.

[82] R.E. Stoller, Y.N. Osetsky, An atomistic assessment of helium behavior in iron, J. Nucl. Mater. 455 (2014) 258–262. https://doi.org/10.1016/j.jnucmat.2014.06.020.

[83] H. Van Swygenhoven, L.M. Stals, The Greenwood-Foreman-Rimmer loop punching mechanism as applied to helium bubble growth in nickel implanted with 5 keV He + ions at 273 K, Radiat. Eff. 78 (1983) 157–163. https://doi.org/10.1080/00337578308207368.

[84] G.W. Greenwood, A.J.E. Foreman, D.E. Rimmer, The role of vacancies and dislocations in the nucleation and growth of gas bubbles in irradiated fissile material, J. Nucl. Mater. 1 (1959) 305–324.

[85] W.D. Wilson, C.L. Bisson, M.I. Baskes, Self-trapping of helium in metals, Phys. Rev. B. 24 (1981) 5616–5624. https://doi.org/10.1103/PhysRevB.24.5616.

[86] C.S. Deo, M.A. Okuniewski, S.G. Srivilliputhur, S.A. Maloy, M.I. Baskes, M.R. James, J.F. Stubbins, Helium bubble nucleation in bcc iron studied by kinetic Monte Carlo simulations, J. Nucl. Mater. 361 (2007) 141–148. https://doi.org/10.1016/j.jnucmat.2006.12.018.

[87] C.S. Deo, M.A. Okuniewski, S.G. Srivilliputhur, S.A. Maloy, M.I. Baskes, M.R. James, J.F. Stubbins, The effects of helium on irradiation damage in single crystal iron, J. Nucl. Mater.

367–370 (2007) 451–456. https://doi.org/10.1016/j.jnucmat.2007.03.117.

[88] R.E. Stoller, G.R. Odette, Analytical solutions for helium bubble and critical radius parameters using a hard sphere equation of state, J. Nucl. Mater. 131 (1985) 118–125. https://doi.org/10.1016/0022-3115(85)90450-7.

[89] Y. Dai, G.R. Odette, T. Yamamoto, The Effects of Helium in Irradiated Structural Alloys, in: Compr. Nucl. Mater., Elsevier, 2012: pp. 141–193. https://doi.org/10.1016/B978-0-08-056033-5.00006-9.

[90] S. Taller, The Role of Damage Rate on Cavity Nucleation with Co-Injected Helium in Dual Ion Irradiated T91 Steel, University of Michigan, 2020. https://deepblue.lib.umich.edu/handle/2027.42/155217.

[91] A.. Dvoriashin, V.D. Dmitriev, V.S. Khabarov, No Title, Eff. Radiat. Mater. 15th Int. Symp. ASTM STP 1125. (1992) 1180–1189. https://compass.astm.org/DIGITAL_LIBRARY/STP/SOURCE_PAGES/STP1125.htm.

[92] T.S. Byun, J.-H. Baek, O. Anderoglu, S.A. Maloy, M.B. Toloczko, Thermal annealing recovery of fracture toughness in HT9 steel after irradiation to high doses, J. Nucl. Mater. 449 (2014) 263–272. https://doi.org/10.1016/j.jnucmat.2013.07.064.

[93] S.A. Maloy, M. Toloczko, J. Cole, T.S. Byun, Core materials development for the fuel cycle R&D program, J. Nucl. Mater. 415 (2011) 302–305. https://doi.org/10.1016/j.jnucmat.2011.04.027.

[94] B.H. Sencer, J.R. Kennedy, J.I. Cole, S. a. Maloy, F. a. Garner, Microstructural analysis of an HT9 fuel assembly duct irradiated in FFTF to 155 dpa at 443 C, J. Nucl. Mater. 393 (2009) 235–241. https://doi.org/10.1016/j.jnucmat.2009.06.010.

[95] T.S. Byun, W. Daniel Lewis, M.B. Toloczko, S.A. Maloy, Impact properties of irradiated HT9 from the fuel duct of FFTF, J. Nucl. Mater. 421 (2012) 104–111. https://doi.org/10.1016/j.jnucmat.2011.11.059.

[96] T.S. Byun, M.B. Toloczko, T.A. Saleh, S.A. Maloy, Irradiation dose and temperature dependence of fracture toughness in high dose HT9 steel from the fuel duct of FFTF, J. Nucl. Mater. 432 (2013) 1–8. https://doi.org/10.1016/j.jnucmat.2012.07.019.

[97] E.M. Getto, The Co-Evolution of Microstructure Features in Self-Ion Irradiated HT9 at Very High Damage Levels, University of Michigan, 2016. https://doi.org/2027.42/135912.

[98] A. Monterrosa, The Role of Pre-Implanted Helium and Carbon on Cavity Evolution in Ion-Irradiated T91, (2018).

[99] S. Taller, D. Woodley, E. Getto, A.M. Monterrosa, Z. Jiao, O. Toader, F. Naab, T. Kubley, S. Dwaraknath, G.S. Was, Multiple ion beam irradiation for the study of radiation damage in materials, Nucl. Instruments Methods Phys. Res. Sect. B Beam Interact. with Mater. Atoms. 412 (2017) 1–10. https://doi.org/10.1016/j.nimb.2017.08.035.

[100] G.S. Was, S. Taller, Z. Jiao, A.M. Monterrosa, D. Woodley, D. Jennings, T. Kubley, F. Naab, O. Toader, E. Uberseder, Resolution of the carbon contamination problem in ion irradiation experiments, Nucl. Instruments Methods Phys. Res. Sect. B Beam Interact. with Mater. Atoms. 412 (2017) 58–65. https://doi.org/10.1016/j.nimb.2017.08.039.

[101] J.F. Ziegler, M.D. Ziegler, J.P. Biersack, SRIM – The stopping and range of ions in matter (2010), Nucl. Instruments Methods Phys. Res. Sect. B Beam Interact. with Mater. Atoms. 268 (2010) 1818–1823. https://doi.org/10.1016/j.nimb.2010.02.091.

[102] ASTM International, E521-16 Standard Practice for Investigating the Effects of Neutron Radiation Damage Using Charged-Particle Irradiation, West Conshohocken, PA, 2016. https://doi.org/10.1520/E0521-16.

[103] S.J. Zinkle, L.L. Snead, Opportunities and limitations for ion beams in radiation effects studies: Bridging critical gaps between charged particle and neutron irradiations, Scr. Mater. 143 (2018) 154–160. https://doi.org/10.1016/j.scriptamat.2017.06.041.

[104] K. Sun, Resolution Limits for JEOL 2100F and JEOL 2010F at the Michigan Center for Materials Characterization, (n.d.).

[105] B. Yao, D.J. Edwards, R.J. Kurtz, G.R. Odette, T. Yamamoto, Multislice simulation of transmission electron microscopy imaging of helium bubbles in Fe, J. Electron Microsc. (Tokyo). 61 (2012) 393–400. https://doi.org/10.1093/jmicro/dfs065.

[106] T. Malis, S.C. Cheng, R.F. Egerton, EELS log-ratio technique for specimen-thickness measurement in the TEM, J. Electron Microsc. Tech. 8 (1988) 193–200. https://doi.org/10.1002/jemt.1060080206.

[107] J. Schindelin, I. Arganda-Carreras, E. Frise, V. Kaynig, M. Longair, T. Pietzsch, S. Preibisch, C. Rueden, S. Saalfeld, B. Schmid, J.-Y. Tinevez, D.J. White, V. Hartenstein, K. Eliceiri, P. Tomancak, A. Cardona, Fiji: an open-source platform for biological-image analysis, Nat. Methods. 9 (2012) 676–682. https://doi.org/10.1038/nmeth.2019.

[108] Z. Chang, D. Terentyev, N. Sandberg, K. Samuelsson, P. Olsson, Anomalous bias factors of dislocations in bcc iron, J. Nucl. Mater. 461 (2015) 221–229. https://doi.org/10.1016/j.jnucmat.2015.03.025.

[109] T. Jourdan, Influence of dislocation and dislocation loop biases on microstructures simulated by rate equation cluster dynamics, J. Nucl. Mater. 467 (2015) 286–301. https://doi.org/10.1016/j.jnucmat.2015.09.046.

[110] W.G. Wolfer, The Dislocation Bias, J. Comput. Mater. Des. 14 (2007) 403–417. https://doi.org/10.1007/s10820-007-9051-3.

[111] F.S. Ham, Stress-Assisted Precipitation on Dislocations, J. Appl. Phys. 30 (1959) 915–926. https://doi.org/10.1063/1.1735262.

[112] S.I. Golubov, B.N. Singh, H. Trinkaus, On recoil-energy-dependent defect accumulation in

pure copper Part II. Theoretical treatment, Philos. Mag. A. 81 (2001) 2533–2552. https://doi.org/10.1080/01418610108217162.

[113] G.R. Odette, On mechanisms controlling swelling in ferritic and martensitic alloys, J. Nucl. Mater. 155–157 (1988) 921–927. https://doi.org/10.1016/0022-3115(88)90442-4.

[114] G.P. Walters, The electron irradiation of pure Fe-Cr-Ni alloys in the temperature range 400 to 700°C, J. Nucl. Mater. 136 (1985) 263–279. https://doi.org/10.1016/0022-3115(85)90014-5.

[115] J.L. Brimhall, L.A. Charlot, E.P. Simonen, Effect of pulsed irradiation on void swelling in nickel, J. Nucl. Mater. 104 (1981) 1147–1150. https://doi.org/10.1016/0022-3115(82)90755-3.

[116] Z. Jiao, S. Taller, K. Field, G. Yeli, M.P. Moody, G.S. Was, Microstructure evolution of T91 irradiated in the BOR60 fast reactor, J. Nucl. Mater. 504 (2018) 122–134. https://doi.org/10.1016/j.jnucmat.2018.03.024.

[117] S. Taller, Z. Jiao, K. Field, G.S. Was, Emulation of fast reactor irradiated T91 using dual ion beam irradiation, J. Nucl. Mater. 527 (2019) 151831. https://doi.org/10.1016/j.jnucmat.2019.151831.

[118] X. Wang, A.M. Monterrosa, F. Zhang, H. Huang, Q. Yan, Z. Jiao, G.S. Was, L. Wang, Void swelling in high dose ion-irradiated reduced activation ferritic–martensitic steels, J. Nucl. Mater. 462 (2015) 119–125. https://doi.org/10.1016/j.jnucmat.2015.03.050.

[119] A.M. Monterrosa, Z. Jiao, G.S. Was, The influence of helium on cavity evolution in ion-irradiated T91, J. Nucl. Mater. 509 (2018) 707–721. https://doi.org/10.1016/j.jnucmat.2018.06.033.

[120] Y.X. Wei, N. Gao, D. Wang, C. Chen, L.P. Guo, Effect of hydrogen atom concentration on hydrogen migration and bubble evolution in bcc iron, Nucl. Instruments Methods Phys. Res. Sect. B Beam Interact. with Mater. Atoms. 461 (2019) 83–87. https://doi.org/10.1016/j.nimb.2019.09.025.

[121] E. Hayward, C. Deo, Energetics of small hydrogen-vacancy clusters in bcc iron., J. Phys. Condens. Matter. 23 (2011) 425402. https://doi.org/10.1088/0953-8984/23/42/425402.